

The Pennsylvania State University

The Graduate School

Eberly College of Science

**APPLICATIONS OF MOLECULAR DYNAMICS, MONTE CARLO AND
METADYNAMICS SIMULATIONS USING REAXFF REACTIVE FORCE FIELDS TO
FLUID/SOLID INTERFACES**

A Dissertation in

Physics

by

Muralikrishna Raju

© 2015 Muralikrishna Raju

Submitted in Partial Fulfillment

of the requirements

for the Degree of

Doctor of Philosophy

May 2015

The dissertation of Muralikrishna Raju was reviewed and approved* by the following:

Adri C T van Duin

Associate Professor of Mechanical Engineering

Dissertation Co-Adviser

Co-Chair of Committee

Kristen Fichthorn

Merrell R. Fenske Professor of Chemical Engineering

Professor of Physics

Dissertation Co-Adviser

Co-Chair of Committee

Milton W Cole

Distinguished Professor of Physics

Jorge O. Sofo

Professor of Physics

Professor of Materials Science and Engineering

James Kubicki

Professor of Geosciences

Richard W. Robinett

Professor of Physics

Director of Graduate Studies

*Signatures are on file in the Graduate School

ABSTRACT

The interaction of dense fluids (water, polar organic solvents, room temperature ionic liquids, etc.) with solid substrates controls many chemical processes encountered in nature and industry. The key features of fluid-solid interfaces (FSIs) are the high mobility and often reactivity of the fluid phase, and the structural control provided by the solid phase. In this dissertation we apply molecular modeling methods to study FSIs in the following systems:

1. Dissociation of water on titania surfaces

We studied the adsorption and dissociation of water at 300 K on the following TiO_2 surfaces: anatase (101), (100), (112), (001) and rutile (110) at various water coverages, using a recently developed ReaxFF reactive force field. The molecular and dissociative adsorption configurations predicted by ReaxFF for various water coverages agree with previous theoretical studies and experiment. ReaxFF predicts a complex distribution of water on these surfaces depending on an intricate balance between the spacing of the adsorption sites (under-coordinated Ti and O surface atoms), water-surface interactions, and water-water interactions. Using molecular dynamics simulations to quantify water dissociation over the TiO_2 surfaces at various water coverages, we find that the extent of water dissociation predicted by the ReaxFF reactive force field is in general agreement with previous density-functional theory studies and experiments. We demonstrate a correlation between the extent of water dissociation on different TiO_2 surfaces and the strength of hydrogen bonding between adsorbed water molecules and water outside the adsorbed layer, as evidenced by the red shift of the O-H vibrational stretching mode of adsorbed water.

2. Mechanisms of Oriented Attachment in TiO_2 nanocrystals

Oriented attachment (OA) of nanocrystals is now widely recognized as a key process in the solution-phase growth of hierarchical nanostructures. However, the microscopic origins of OA

remain unclear. Using the same ReaxFF Ti/O/H reactive force field employed in the previous study, we perform molecular dynamics simulations to study the aggregation of various titanium dioxide (anatase) nanocrystals in vacuum and humid environments. In vacuum, the nanocrystals merge along their direction of approach, resulting in a polycrystalline material. By contrast, in the presence of water vapor, the nanocrystals reorient themselves and aggregate via the OA mechanism to form a single or twinned crystal. They accomplish this by creating a dynamic network of hydrogen bonds between surface hydroxyls and surface oxygens of aggregating nanocrystals. We determine that OA is dominant on surfaces that have the greatest propensity to dissociate water. Our results are consistent with experiment, are likely to be general for aqueous oxide systems, and demonstrate the critical role of solvent in nanocrystal aggregation. This work opens up new possibilities for directing nanocrystal growth to fabricate nanomaterials with desired shapes and sizes.

3. Li interactions in carbon based materials

Graphitic carbon is still the most ubiquitously used anode material in Li-ion batteries. In spite of its ubiquity, there are few theoretical studies that fully capture the energetics and kinetics of Li in graphite and related nanostructures at experimentally relevant length/time-scales and Li-ion concentrations. In this study we describe development and application of a ReaxFF reactive force field to describe Li interactions in perfect and defective carbon based materials using atomistic simulations. We develop force-field parameters for Li-C systems using van der Waals-corrected density-functional theory (DFT). Grand canonical Monte Carlo simulations of Li intercalation in perfect graphite with this new force-field not only gives a voltage profile in good agreement with known experimental and DFT results but also captures the in-plane Li ordering as well as the interlayer separations for stage I and II compounds. In defective graphite, the ratio of

Li/C i.e. the capacitance increases and the voltage shifts, both in proportion to the concentration of vacancy defects and metallic lithium is observed explaining lithium plating seen in recent experiments. We also demonstrate the robustness of the force-field by simulating model carbon nanostructures i.e. both 0D and 1D structures, that can be potentially used as battery electrode materials. While a 0D defective onion-like carbon facilitates fast charging/discharging rates by surface Li-adsorption, a 1D defect-free carbon nanorod requires a critical density of Li for intercalation to occur at the edges. Our force-field approach opens up the opportunity for studying energetics and kinetics of perfect and defective Li/C structures containing thousands of atoms as a function of intercalation. This is a key step towards modeling of realistic carbon materials for energy applications.

4. Transfer of aqueous protons across single layer graphene

Proton transfer across single layer graphene is associated with large computed energy barriers and is therefore thought to be unfavorable at room temperature. Experiments, however, have not yet been performed to test this prediction. Here, we subject a single layer of graphene on fused silica to cycles of high and low pH and show that protons transfer reversibly through the graphene to undergo acid-base chemistry with silica surface hydroxyl groups. After ruling out diffusion through macroscopic pinholes, the protons are found to transfer through rare, naturally occurring atomic defect sites. Computer simulations reveal low energy processes for water-mediated proton transfer across hydroxyl-terminated atomic defect sites that participate in a Grotthuss-type relay mechanism, while defects terminated by pyrylium-like ether bridges shut down proton exchange. Given the unfavorable energy barriers to transfer of helium and H₂, the calculations show that single layer graphene is selectively permeable to aqueous protons.

5. Capacitive mixing

The amount of salinity-gradient energy that can be obtained through capacitive–mixing based on double layer expansion depends on the extent the electric double layer (EDL) is altered in a low salt concentration (LC) electrolyte (e.g., river water). We showed that the electrode-rise potential, which is a measure of the EDL perturbation process, was significantly ($P = 10^{-5}$) correlated to the concentration of strong acid surface functional groups using five types of activated carbon. Electrodes with the lowest concentration of strong acids (0.05 mmol g^{-1}) had a positive rise potential of $59 \pm 4 \text{ mV}$ in the LC solution, whereas the carbon with the highest concentration (0.36 mmol g^{-1}) had a negative rise potential ($-31 \pm 5 \text{ mV}$). Chemical oxidation of a carbon (YP50) using nitric acid decreased the electrode rise potential from $46 \pm 2 \text{ mV}$ (unaltered) to $-6 \pm 0.5 \text{ mV}$ (oxidized), producing a whole cell potential ($53 \pm 1.7 \text{ mV}$) that was $4.4\times$ larger than that obtained with identical electrode materials (from $12 \pm 1 \text{ mV}$). Changes in the EDL were linked to the behavior of specific ions in a LC solution using molecular dynamics and metadynamics simulations. The EDL expanded in the LC solution when a carbon surface (pristine graphene) lacked strong acid functional groups, producing a positive-rise potential at the electrode. In contrast, the EDL was compressed for an oxidized surface (graphene oxide), producing a negative-rise electrode potential. These results established the linkage between rise potentials and specific surface functional groups (strong acids), and demonstrated on a molecular scale changes in the EDL using oxidized or pristine carbons.

Our applications to these five systems clearly demonstrate the capability of ReaxFF-based molecular dynamics simulations to provide a bridge between ab-initio results and experiments.

Contents

List of Figures	viii
List of Tables.....	xiv
Acknowledgement.....	xv
1 Introduction.....	1
2 ReaxFF Reactive Force Field	5
2.1 ReaxFF Formalism.....	6
2.2 Limitations of ReaxFF Method	15
3 ReaxFF Reactive Force Field Study of the Dissociation of Water on Titania Surfaces	20
3.1 Introduction.....	20
3.2 Computational methods	22
3.3 Results and Discussion	24
3.4 Summary and Conclusions.....	54
4 Mechanisms of Oriented Attachment of TiO₂ Nanocrystals in Vacuum and Humid Environments: Reactive Molecular Dynamics	56
4.1 Introduction.....	56
4.2 Computational Methods	57
4.3 Results and Discussion	60
4.4 Summary and Conclusions.....	74
5 A Reactive Force Field study of Li/C Systems for Electrical Energy Storage	75
5.1 Introduction.....	75
5.2 Computational Methods	76
5.3 Results and Discussion	82
5.4 Summary and Conclusions.....	98
6 Transfer of Aqueous Protons Across Single Layer Graphene	100
6.1 Introduction.....	100
6.2 Methods	102
6.3 Results and Discussion	106
6.4 Summary and Conclusions.....	118
7 The effect of strong acid functional groups on electrode rise potential in capacitive mixing by double layer expansion	120
7.1 Introduction.....	120
7.2 Methods	124
7.3 Results and Discussion	129
7.4 Summary and Conclusions.....	146
8 Summary and Future Directions	147
References	152

List of Figures

Figure 1.1. Summary of the spatial and temporal scales spanned by modeling approaches [ab initio molecular dynamics (AIMD); explicit atom, united atom and mesoscale classical molecular dynamics (CMD); mesoscale CMD; Monte Carlo (MC) and continuum models] and experimental probes [inelastic neutron scattering (INS); quasi-elastic neutron scattering (QENS); neutron spin echo spectrometry (NSES); fluorescence probes; second harmonic generation (SHG) and sum frequency generation (SFG) spectrometry; nuclear magnetic resonance (NMR); X-ray reflectivity (XR); crystal truncation rod scattering technique of surface X-ray diffraction (CTR); X-ray standing wave (XSW); and neutron reflectivity (NR)]. Acknowledgement: Prof. Peter Cummings, Vanderbilt University.....	2
Figure 1.2. Elements in the periodic table describe by ReaxFF.	3
Figure 3.1. Oxygen-oxygen radial distribution function for water at 298 K.	23
Figure 3.2. Molecular adsorption over anatase (101). Ti atoms are gray, O atoms in TiO_2 are red, the terminal water oxygen is blue, and H atoms are white. Five-fold Ti surface atoms (Ti_{5c}) and two-fold O surface atoms (O_{2c}) are indicated and the dashed lines indicate hydrogen bonds.	25
Figure 3.3. (2 x 2) overlayer structure of molecular water on anatase (101) at 190 K. Water hydrogen and oxygen atoms inside the dashed box are emphasized in yellow and blue, respectively. The arrow indicates the double periodicity along the [010] direction.....	26
Figure 3.4. Water distribution over anatase (101) at 1.0 ML with the zigzag pattern for molecularly adsorbed water (blue oxygens) interspersed with dissociated water (green oxygens). Dashed lines indicate hydrogen bonds	27
Figure 3.5. (a) Snapshot from an MD simulation of water on anatase (101) at 3.0 ML coverage; (b) Density plot of titanium (red) and oxygen (blue) atoms over anatase (101). The numbers and arrows indicate the heights of the n^{th} water layer; (c) Perpendicular distance of the water-oxygen atoms from the plane containing the surface Ti_{5c} atoms over anatase (101).	28
Figure 3.6. Water bilayer configuration above (a) molecularly adsorbed (blue oxygens) and (b) dissociatively adsorbed (green oxygens) water over anatase (101). The oxygens of water in the second layer and oxygens in TiO_2 slab are shown in red.	29
Figure 3.7. OH coverage (ML) over anatase (101) as a function of temperature.....	31
Figure 3.8. WDP and TWDP on anatase (101) as a function of water coverage.....	32
Figure 3.9. Snapshot from an MD simulation of water on over unreconstructed anatase (001) at 3.0 ML coverage; (b) Density plot of titanium (red) and oxygen (blue) atoms over anatase (001). The numbers and arrows indicate the heights of the n^{th} water layer; (c) Perpendicular distance of the water-oxygen atoms from the plane containing the surface Ti_{5c} atoms on anatase (001).	34

Figure 3.10. Cleavage of the $\text{Ti}_{5c}\text{-O}_{2c}$ bond on unreconstructed anatase (001) due to dissociative adsorption.....	35
Figure 3.11. WDP and TWDP on anatase (001) surface as a function of water coverage.	36
Figure 3.12. Ad-molecule model of the anatase (001) – (1 x 4) reconstructed surface.	37
Figure 3.13. Water dissociation along the ridge at a Ti_{4c} atom site on anatase (001) - (1 x 4)....	37
Figure 3.14. (a) Snapshot from an MD simulation of water on anatase (100) at 3.0 ML coverage; (b) Density plot of titanium (red) and oxygen (blue) atoms over anatase (100). The numbers and arrows indicate the heights of the n^{th} water layer; (c) Perpendicular distance of the water-oxygen atoms O_w from the plane containing the surface Ti_{5c} atoms on anatase (100).	39
Figure 3.15. WDP and TWDP on anatase (100) as a function of water coverage.....	40
Figure 3.16. Molecular adsorption over anatase (112).	42
Figure 3.17. (a) Snapshot from an MD simulation of water on anatase (112) at 3.0 ML coverage; (b) Density plot of titanium (red) and oxygen (blue) atoms over anatase (112). The numbers and arrows indicate the heights of the n^{th} water layer; (c) Perpendicular distance of the water-oxygen atoms O_w from the plane containing the surface Ti_{5c} atoms on anatase (112).	43
Figure 3.18. WDP and TWDP on anatase (112) as a function of water coverage.....	44
Figure 3.19. (a) Snapshot from an MD simulation of water on rutile (110) at 3.0 ML coverage; (b) Density plot of titanium (red) and oxygen (blue) atoms over rutile (110). The numbers and arrows indicate the heights of the n^{th} water layer; (c) Perpendicular distance of the water-oxygen atoms O_w from the plane containing the surface Ti_{5c} atoms on rutile (110).	46
Figure 3.20. WDP and TWDP on rutile (110) surface as a function of water coverage.	47
Figure 3.21. Snapshot from an MD simulation over rutile(110) at (a) 0.5 ML water coverage and (b) 2 ML water coverage.....	48
Figure 3.22. OH coverage (ML) on rutile (110) as a function of temperature.	49
Figure 3.23. Comparison of TWDP on various titania surfaces at 1 ML and 3 ML water coverage.	50
Figure 3.24. Contributions to the stretching band of the VDOS from HA hydrogen atoms. HA hydrogen atoms bridge the adsorbed layer and waters outside the adsorbed layer.	53
Figure 4.1. Equilibrated structures of the large (a) and small (b) symmetric anatase nanoparticles with Wulff shapes, a large nanoparticle that is truncated on the {001} facet (c), and two nanoparticles that are truncated on the {112} facet (d and e).....	59
Figure 4.2. Snapshots of the aggregation of anatase nanocrystals in vacuum. These snapshots were taken at (a) 255 ps; (b) 260 ps; (c) 265 ps and; (d) 270 ps.	61

Figure 4.3. Hydroxyl coverage over the anatase nanocrystal in Figure 4.6(a) as a function of water coverage at 573 K.	62
Figure 4.4. Snapshots of the initial approach of anatase nanocrystals in water. These snapshots were taken at (a) 187.5 ps; (b) 205 ps; (c) 212.5 ps and; (d) 225 ps.....	64
Figure 4.5. Snapshots of the alignment of anatase nanocrystals on {112} facets in water. These snapshots were taken at (a) 275 ps; (b) 300 ps; (c) 350 ps and; (d) 375 ps.	65
Figure 4.6. (a) Network of hydrogen bonds between anatase nanocrystals aligned on {112} facets. The hydrogen-bond network is formed between terminal hydroxyls (in which a hydroxyl from a dissociated water binds to an under-coordinated Ti atom at the surface) or bridging hydroxyls (in which a hydrogen from a dissociated water binds to a bridging, two-fold coordinated surface oxygen) on one nanocrystal and surface oxygens of the adjacent nanocrystal. (b) Density plot of hydrogen (blue) and oxygen (red) atoms in Figure 3(a) obtained as an average over a time period of 250 ps. (c) TEM image of wet SnO ₂ nanocrystals. For synthesis and characterization please refer to Wang <i>et al</i> ¹⁵²	68
Figure 4.7. Translational speeds leading up to the alignment of the anatase nanoparticles in Figure 4.5.....	69
Figure 4.8. Snapshots of the OA of anatase nanocrystals on {101} facets in water. These figures were taken at (a) 737.5 ps; (b) 750.75 ps; (c) 763.75 ps and; (d) 775 ps.....	71
Figure 4.9. Structural analysis of OA aggregates on (a) {112} (b) {112} twin (c) {001} and (d) {101} facets of anatase nanocrystals. Only Ti atoms are shown, with anatase atoms in grey and anatase {112} twins in orange.	72
Figure 5.1. Comparison of potential energy curves of Li diffusion along two paths (a) Hollow–Bridge–Hollow, and (b) Hollow–Top–Bridge–Top–Hollow in graphite at separations of 3.35 Å and 3.7 Å predicted by ReaxFF and DFT calculations.....	82
Figure 5.2. Potential energy curves for lithium diffusion in the direction perpendicular to the graphene sheet for graphene with (a) mono-vacancy and (b) di-vacancy. The blue dashes are DFT values for the Local Minimum, Diffusion Barrier and Position of Local Minimum.....	83
Figure 5.3. (a) In-plane Li ordering in stage I and stage II compounds as seen from above on the carbon honeycomb lattice.(b) Li-C stacking in stage II and (c) stage I.....	84
Figure 5.4. (a) Voltage profile for Li-graphite system obtained by ReaxFF. (b) Clustering of Li up-down pairs in graphite during loading. (red is up and blue is down with respect to graphene)	86
Figure 5.5. Voltage profile for Li intercalation in graphite with single and di-vacancy.	87
Figure 5.6. In-plane Li ordering in stage II compounds in graphite with (a) single and (b) di-vacancy as seen from above on the carbon honeycomb lattice. Li-C stacking in stage II compounds in graphite with (c) single and (d) di-vacancy	89

Figure 5.7. Free-energy surface (FES) for adsorption of lithium on (a) pristine graphite and (b) graphite with divacancy as a function of x and y coordinates of Li with the graphite sheets placed along the xy plane. 90

Figure 5.8. (a) Side view of density plot of Li (blue) during a NVT simulation at 300 K showing Li intercalation in graphite (b) top view 93

Figure 5.9. Formation energy of Li, Li-2, Li-3 and Li-4 clusters over graphene, graphene with single and di-vacancy, 5-8-5 reconstructed graphene, 5-5-5-7-7-7 reconstructed graphene. 94

Figure 5.10. Four Li atoms forming a prismatic cluster over 6-layer graphene. (b) Li atom forming a metallic layer over 6-layer graphene. 95

Figure 5.11. (a) Density plot of Li (purple) during a metadynamics simulation at 600 K. (b) The free energy landscape for Li diffusing out from the OLC through a 12-membered ring. 96

Figure 5.12. Density plot of Li (green) in an OLC during a NVT simulation at 1000 K. The inset shows a Li diffusing through a 16 membered ring. 98

Figure 6.1. (A) Dual-pump flow system employed in the nonlinear optical studies using a waveplate ($\lambda/2$) to set the input polarization of the 600 nm probe light field to plane-polarized parallel to the plane of incidence while detection of the second harmonic generation photons at $\lambda=300$ nm is achieved using a photomultiplier tube (PMT) and single photon counting techniques as described in the Supplementary Information. (B) p-in/all-out Polarized SHG E-field recorded as a function of time from the fused silica/water interface during pH jumps from 7 to 3 to 10 and subsequent pH cycling between 3 and 10 at a bulk aqueous flow of 0.9 mL/sec and an NaCl concentration of 1 mM in the absence (crimson, bottom) and presence (blue, top) of single layer graphene placed between the fused silica substrate and the flowing bulk aqueous phase. (C) Composite of 25 SEM images of single layer graphene on a fused silica substrate, showing 7 macroscopic pinholes, marked by white circles. (D) High resolution aberration-corrected ADF STEM images of defect-free single layer graphene on a TEM grid and (E) of a rarely imaged atomic defect. 101

Figure 6.2. Side and top views of oxygen- (A) and OH-(B) terminated defect models used in the DFT calculations. Snapshots (C, D) and energetics (E, F) from the nudged elastic band calculations for proton transfer through the ether- and OH- terminated defect sites marking (**region I**) release of proton from H_3O^+ to ether and OH group, respectively; (**region II**) relay of proton between ether and OH groups, respectively; (**region III**) release of proton from ether and OH groups to H_3O^+ , respectively. Denotations of spheres: grey=carbon; red=oxygen; white=hydrogen atoms. 109

Figure 6.3. Water channel formation from molecular dynamic simulations using the ReaxFF force field carried out a constant number, volume, and 300 K temperature and water mediated proton transfer through atomic defects terminated in 6 OH groups (A), 4 OH groups and one oxygen atom (B), 2 OH groups and two oxygen atom (C), and three oxygen atoms (D). Denotations of spheres: grey=carbon; red=oxygen; white=hydrogen atoms. 111

Figure 6.4. Density plot of oxygen(blue) and hydrogen(red) in the silica/water/graphene interface, as obtained during a 300K ReaxFF molecular dynamics simulation. (A) structure at high pH (40% SiOH/60% SiO ⁻ ; OH-ions in water solution) – showing very strong local water structure and 20-fold reduced water self diffusion (B) water structure at neutral/low pH (100% SiOH; pure H ₂ O) showing more liquid water structure and water self-diffusion comparable to bulk water. Denotations of spheres: yellow=silicon; red=oxygen; cyan=carbon atoms.	114
Figure 6.5 (a) Graphene/water system used in the ReaxFF/AIMD simulations (b) oxygen number density profiles obtained from the ReaxFF/MD and AIMD simulations (c) hydrogen density profiles obtained from the ReaxFF/MD and AIMD simulations.....	117
Figure 6.6 Heats of formation for various defect terminations on quad-vacancy graphene.	118
Figure 7.1. (A) Four step capacitive mixing based on double layer expansion process. Step 1: electrodes charged in HC. Step 2: under open circuit, LC replaces HC solution, causing the EDL to expand (generating energy). Step 3: electrodes discharged at a higher potential (energy harvesting). Step 4: under open circuit, HC replaces LC, compressing the EDL. (B) Typical voltage response curve during a CDLE cycle with LC steps (2- EDL expansion and 3- Discharge) shaded in light blue, and HC steps (4- EDL compression and 1- Charge shaded in dark blue.	120
Figure 7.2. Snapshot of the simulation cell from a molecular dynamics run with pristine graphene as the cathode and graphene oxide as the anode in the cell.	127
Figure 7.3. (A) Concentration of surface functional groups for various carbons tested, and (B) the individual electrode ($\Delta\phi$) potential rise as a function of the concentration of strong acid surface functional groups for different carbons.	131
Figure 7.4. Concentration of oxygen containing functional groups for various carbon materials	132
Figure 7.5. Potentiometric titration curves for tested carbons (a) pH range from 4 to 10 (b) zoomed in selection (pH from 5 to 8).....	132
Figure 7.6. (a) Whole cell potential rise during CDLE cycle, and (b) Individual electrode (ϕ +) and (ϕ -) potential rise and fall for various activated carbon materials.	133
Figure 7.7. Individual electrode potential rise as a function of (a) total surface area, (b) total pore volume.....	134
Figure 7.8. Individual electrode potential rise as a function of (a) microporous surface area, (b) microporous volume (c) mesoporous surface area, (d) mesoporous volume (e) macroporous surface area (f) macroporous volume.	135
Figure 7.9. (a) Charge versus pH from potentiometric titrations for SX+ and HRD samples, with PZC indicated. (b) GCS modeled potential rise as a function of the base potential for SX+ and HRD samples.	135

Figure 7.10. (a) Whole cell (ϕ_{cell}) and (b) individual electrode ($\phi_{HRD/SX} + \pm$) potentials for asymmetrical CDLE operation using SX+ and HRD activated carbons. (C) Whole cell (ϕ_{cell}) and (d) individual electrode potentials ($\phi_{SX} + /SX + \pm$ and $\phi_{HRD/HRD} \pm$) for a symmetrical CDLE operation using SX+ and HRD. Blue shaded area indicates when seawater was present in the cell (step 1&4), and red shading indicates when river water was present. 137

Figure 7.11. (A) Whole cell CDLE performance with similar and dissimilar electrodes YP50/YP50 ox, YP50 ox/YP50, YP50/YP50, and YP50ox/YP50 ox, (B) individual rise and fall potentials for similar electrodes (YP50/YP50 and YP50 ox/YP50 ox) and (C) individual rise and fall potentials for dissimilar electrodes (YP50/YP50ox and YP50 ox/YP50). 138

Figure 7.12. (a) Capacitance of various activated carbons as a function of CV scan rate and (b) cyclic voltammogram at 2 mV/sec. 140

Figure 7.13. Cyclic voltammogram for dissimilar electrodes SX+/HRD and YP50/YP50 ox.. 140

Figure 7.14. Snapshot from a MD simulation showing the electric double layer (EDL) in the (A) high concentration electrolyte and (B) low concentration electrolyte; the water molecules are not shown explicitly. Free-energy surface (FES) for adsorption of chlorine ion on the pristine graphene (PG) electrode as a function of separation from the electrode and coordination with water for the (C) high concentration electrolyte and (D) low concentration electrolyte when PG is the positive electrode in the cell. Free-energy surface (FES) for adsorption of potassium ion on the graphene oxide (GO) electrode as a function of separation from the electrode and coordination with water for the (E) high concentration electrolyte and (F) low concentration electrolyte when GO is the negative electrode in the cell. The arrows indicate the direction of shift of free-energy basins when changing from high to low concentration electrolyte. Free-energy surface (FES) for adsorption of potassium ion on the graphene oxide (GO) electrode as a function of coordination with surface oxygens and coordination with water for the (G) high concentration electrolyte and (H) low concentration electrolyte when GO is the negative electrode in the cell. 142

Figure 7.15. Free-energy surface (FES) for adsorption of potassium ion on the graphene oxide (GO) electrode as a function of separation from the electrode and coordination with surface oxygens for the (a) high concentration electrolyte and (b) low concentration electrolyte when GO is the anode in the cell. The arrows indicate the direction of shift of free-energy basins when changing from high to low concentration electrolyte. 144

List of Tables

Table 3.1. Average number and length of hydrogen bonds between adsorbed water molecules and waters outside the adsorbed layer at 3 ML coverage.	51
Table 5.1. The fitted parameters optimized in this Li-C force field development study.	79
Table 5.2. Comparison of ReaxFF and DFT values for various adsorption energies of Li in graphene and graphite.	80
Table 6.1. DFT and ReaxFF-calculated activation barriers for proton transfer through different vacancy sites on graphene in water.	109

Acknowledgement

First and foremost, I would like to express my sincere thanks and deep felt gratitude to my advisors, Prof. Adri van Duin and Prof. Kristen Fichthorn for their constant guidance, support, and encouragement. Their patience and support helped me overcome many crisis situations and finish this dissertation. I am grateful to them for guiding me in my research and career. Adri gave me the independence to explore various projects on my own, and at the same time guided me when I lost my way. I am deeply grateful to Kristen for the long insightful discussions and scientific advice about my research. I am also thankful to her for encouraging the use of correct grammar and consistent notation in my writings and for carefully reading and commenting on countless revisions. More importantly I am deeply grateful for the understanding, support and encouragement during the tough times. I feel very fortunate for this opportunity to learn from two incredible mentors.

I am thankful to Dr. David J. Wesolowski, director of FIRST-EFRC for his support, guidance and leadership through all these years. Despite his busy schedule, he has always been available to give suggestions and to help with the scientific, various non-scientific and funding aspects of our research. I am thankful to Dr. Andrew Stack at ORNL for hosting me and guiding me on accelerated MD methods. His guidance has been invaluable to my research and I am grateful for his patience and willingness to spend long hours advising me during my time at ORNL. I would like to acknowledge our collaborators Dr. Ganesh Panchapakesan and Dr. Paul R.C. Kent for their insightful discussions and help with my research. I am grateful to Ganesh for his scientific and general career advice through these years. I am thankful to Prof. Fran Geiger, Prof. Matthew Neurock, Dr. Lucas Vlcek, Jennifer Achtyl, Dr. Lijun Xu and Dr. Yu Cai for their help, guidance

and scientific discussions all through our FIRST projects. I would like to acknowledge all members of the FIRST team for their conscious and unconscious guidance and support.

I am also thankful to the members of my committee Prof. Milton W Cole, Prof. Jorge O. Sofo and Prof. James Kubicki for their time, guidance and help during the course of this work. I am thankful to all my Professors and Teachers for guiding and shaping me. I have been fortunate to learn from many inspiring teachers over the years.

I am grateful to my group members for a number of insightful discussions and all the fun times. It was a great experience to work with you all. Many friends have helped me stay happy and sane through these difficult years. It is difficult to imagine these wonderful years without them. I greatly value their friendship and I deeply appreciate them being there for me.

Most importantly, none of this would have been possible without the love and patience of my mom, dad and sister. They have been my constant source of love, strength, support and motivation all these years. My parents are my heroes and have sacrificed a lot to bring us up and provide us a loving home. My sister is my best friend and I love her for being her and constantly loving, supporting and understanding me. I am grateful to my grandparents and my extended family for their unending love and support. During the course of these years I found my wife and her family and sister extends my circle of love and support. My wife and kid are my most precious gifts and at the end of this journey, we look forward to the next one.

Thank You God.

Fundamental understanding and predictive modeling of fluid-surface interfaces (FSIs) is essential to enable transformative advances in several progressive technologies, including energy storage, solar energy utilization, heterogeneous catalysis, materials synthesis and chemical separations. Interfaces are of particular interest because atoms situated at the interface behave differently from those at the bulk and therefore we should expect the chemistry of the interface to be unique. The truncated solid surface exposes under-coordinated atoms that drive dynamic interactions with the adjacent fluid by local bond relaxation, charge redistribution, dissolution, precipitation, adsorption, etching, porosity development and destruction. The finite size, shape, directional bonding, charge distribution and polarizability of solute and solvent components are further convoluted with their ability to reorient, unmix and react with one another and the surface. Unique FSI properties thus emerge from a complex interplay of short- and long-range forces and reactions among the molecular fluid components, solutes and surfaces. Accurate conceptual and quantitative models of FSI properties and behavior at the atomic to nanoscale are necessary to develop predictive understandings of such systems and guide formulations for specific applications. Atomic-scale investigations with computational methodologies could contribute significantly to understanding origins of interfacial phenomena and furnish many details that are not accessible experimentally.

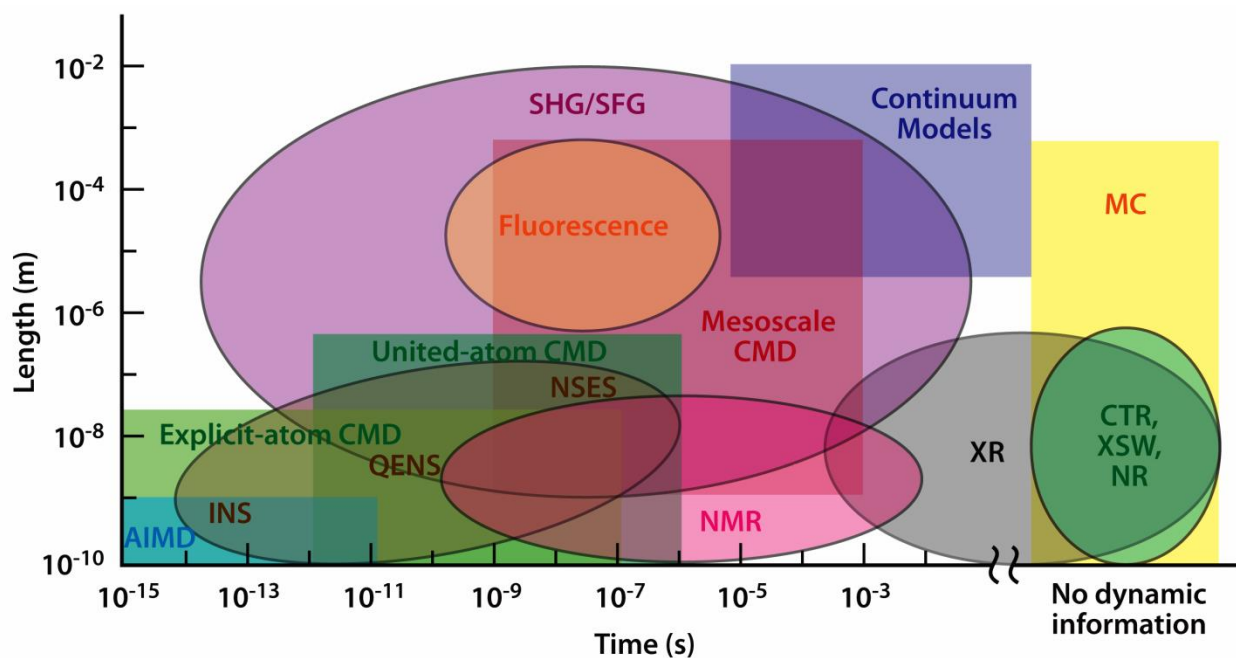


Figure 1.1. Summary of the spatial and temporal scales spanned by modeling approaches [ab initio molecular dynamics (AIMD); explicit atom, united atom and mesoscale classical molecular dynamics (CMD); mesoscale CMD; Monte Carlo (MC) and continuum models] and experimental probes [inelastic neutron scattering (INS); quasi-elastic neutron scattering (QENS); neutron spin echo spectrometry (NSES); fluorescence probes; second harmonic generation (SHG) and sum frequency generation (SFG) spectrometry; nuclear magnetic resonance (NMR); X-ray reflectivity (XR); crystal truncation rod scattering technique of surface X-ray diffraction (CTR); X-ray standing wave (XSW); and neutron reflectivity (NR)]. Acknowledgement: Prof. Peter Cummings, Vanderbilt University.

Figure 1.1 shows the summary of the spatial and temporal scales spanned by various modeling approaches and experimental probes. First-principles calculations can provide detailed and accurate descriptions of binding and interactions at interfaces. However, their substantial computational costs restrict the system sizes and times that can be probed, thus limiting their applicability to study chemical and physical phenomena at interfaces. Empirical force-field methods, on the other hand are faster and can handle larger systems but cannot commonly describe chemical reactions, such as dissociative adsorption on surfaces. Although we can make progress through the use of brute force AIMD methods, we need to use reactive CMD methods in order to be able to access the length and time scales needed for several of the experimental probes. ReaxFF,

a bond-order based empirical reactive force field, can simulate chemical reactions and thus allows for reasonable description of reactivity, structures and transport properties at the interface. ReaxFF thus bridges this gap between methods based in quantum mechanics (QM), such as DFT and empirical force-field methods by being able to handle large simulations while maintaining an accuracy and reactivity that approaches that of QM-based methods. A detailed description of the ReaxFF potential is provided in the next chapter. Figure 1.2 shows the elements currently described by ReaxFF. All these materials are described with exactly the same set of potential functions, enabling ReaxFF to describe material interfaces. The strength and applicability of ReaxFF is in its ability to describe energetics and kinetics of multiphase, multimaterial systems containing thousands of atoms with QM-based accuracy for barriers and reaction energies.

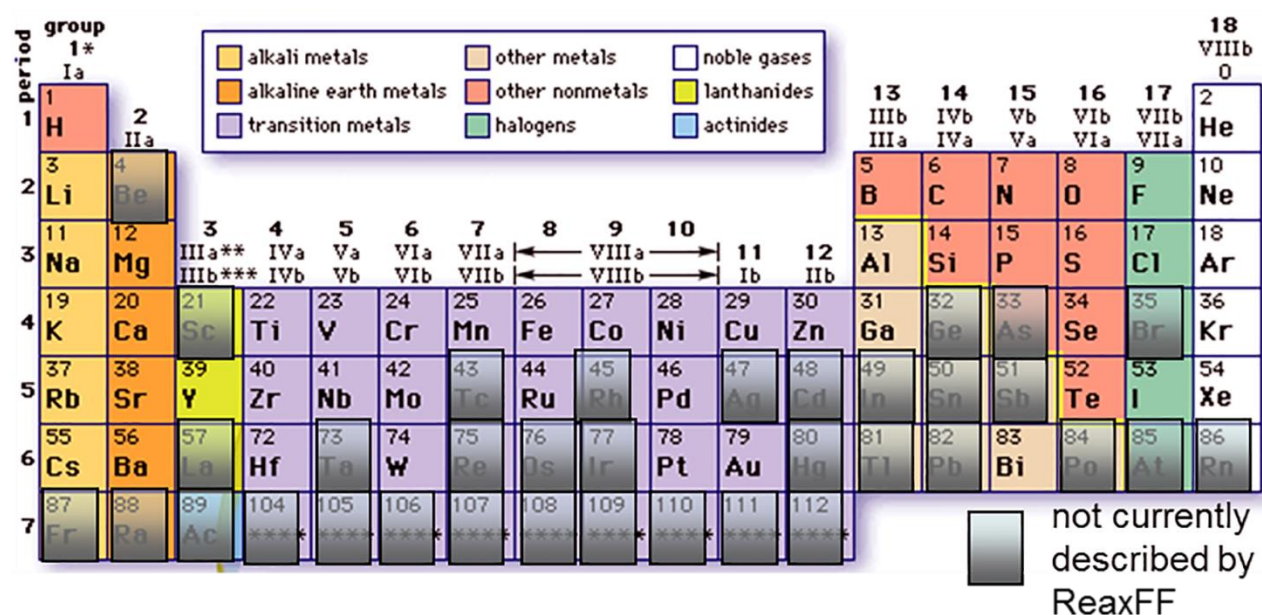


Figure 1.2. Elements in the periodic table describe by ReaxFF.

This dissertation is organized as follows. In chapter 2, we describe the ReaxFF reactive force field method. In chapter 3, we present our results on adsorption and dissociation of water on

the following titania surfaces: anatase (101), (001), (100), (112) and rutile (110) at various water coverages. Chapter 4 discusses the applications of the validated Ti/O/H ReaxFF force field to study the origins of oriented attachment in titania nanocrystals in aqueous environments. Chapter 5 describes the development of a Li/C ReaxFF force field and its application to study energetics and kinetics of Li intercalation in pristine and defective carbon based materials. In chapter 6 we discuss our collaborative experimental and theoretical results on transfer of aqueous protons through single layer graphene. This is followed by description of another collaborative experimental and theoretical study on the effect of functional groups in capacitive mixing by double layer expansion in chapter 7. Chapter 8 discusses impacts and future directions of the projects discussed in the dissertation.

2 ReaxFF Reactive Force Field

ReaxFF¹ is a general bond-order-dependent potential that uses a relationship between bond distance and bond order on one hand and a relationship between the bond order and bond energy on the other to describe bond formation and bond dissociation realistically. This formulation allows ReaxFF to describe under- and over-coordinated systems properly. The bond orders are combined with functions of valence coordinates such as bond angles and torsion angles so that the energy contributions from bonding terms vanish upon bond dissociation. The ReaxFF potential uses central field formalism wherein nonbonded interactions, namely Coulomb and van der Waals interactions, are calculated between every atom pair. Excessively close range interactions are avoided by using a shielding term² in the energy expression for the nonbonded interactions. Atomic charges are calculated using the geometry-dependent charge calculation scheme (EEM scheme) of Mortier et al³. Instead of Ewald summation to calculate long-range Coulomb interactions, ReaxFF uses a seventh-order taper function⁴ with an outer cutoff radius of 10 Å. The system energy in ReaxFF is calculated as the sum of a number of energy terms as:

$$\begin{aligned} E_{system} = & E_{bond} + E_{lp} + E_{over} + E_{under} + E_{val} + E_{pen} + E_{coa} + E_{C2} + E_{triple} \\ & + E_{tors} + E_{conj} + E_{H-bond} + E_{vdWaals} + E_{Coulomb} \end{aligned} \quad (2.1)$$

ReaxFF parameters are optimized against Quantum Chemical (QC) data based on Density Functional Theory (DFT) on relevant systems. Typically, this data consists of atomic charges, geometric parameters such as bond lengths, bond angles, torsions and lattice constants, heats of formations, equation of state data and reaction energies. Once the ReaxFF parameters are developed, they can be employed in molecular dynamics simulations to study the chemistry and dynamics under varied conditions in systems of our interest. An important aspect of ReaxFF

potential is that it can be systematically improved by fitting to new DFT data in an iterative manner as research on a specific problem proceeds.

2.1 ReaxFF Formalism

A Bond Order and Bond Energy

A fundamental assumption of ReaxFF is that the bond order BO'_{ij} between a pair of atoms can be obtained directly from the interatomic distance r_{ij} as given in Equation (2.2). In calculating the bond orders, ReaxFF distinguishes between contributions from sigma bonds, pi-bonds and double pi bonds.

$$BO'_{ij} = BO_{ij}^{\sigma} + BO_{ij}^{\pi} + BO_{ij}^{\pi\pi} = \exp \left[p_{bo1} \cdot \left(\frac{r_{ij}}{r_o^{\sigma}} \right)^{p_{bo2}} \right] + \exp \left[p_{bo3} \cdot \left(\frac{r_{ij}}{r_o^{\pi}} \right)^{p_{bo4}} \right] + \exp \left[p_{bo5} \cdot \left(\frac{r_{ij}}{r_o^{\pi\pi}} \right)^{p_{bo6}} \right] \quad (2.2)$$

Based on the uncorrected bond orders BO' , derived from Equation 2.2, an uncorrected overcoordination Δ' can be defined for the atoms as the difference between the total bond order around the atom and the number of its bonding electrons Val .

$$\Delta'_i = -Val_i + \sum_{j=1}^{neighbour(i)} BO'_{ij} \quad (2.3a)$$

ReaxFF then uses these uncorrected overcoordination definitions to correct the bond orders BO'_{ij} using the scheme described in Equations (2.4a-f). To soften the correction for atoms bearing lone electron pairs a second overcoordination definition Δ'^{boc} (equation 2.3b) is used in equations 2.4e and 2.4f. This allows atoms like nitrogen and oxygen, which bear lone electron pairs after filling their valence, to break up these electron pairs and involve them in bonding without obtaining a full bond order correction.

$$\Delta_i^{'boc} = -Val_i^{boc} + \sum_{j=1}^{neighbour(i)} BO_{ij}' \quad (2.3b)$$

$$\begin{aligned} BO_{ij}^{\sigma} &= BO_{ij}'^{\sigma} \cdot f_1(\Delta_i', \Delta_j') \cdot f_4(\Delta_i', BO_{ij}') \cdot f_5(\Delta_j', BO_{ij}') \\ BO_{ij}^{\pi} &= BO_{ij}'^{\pi} \cdot f_1(\Delta_i', \Delta_j') \cdot f_1(\Delta_i', \Delta_j') \cdot f_4(\Delta_i', BO_{ij}') \cdot f_5(\Delta_j', BO_{ij}') \\ BO_{ij}^{\pi\pi} &= BO_{ij}'^{\pi\pi} \cdot f_1(\Delta_i', \Delta_j') \cdot f_1(\Delta_i', \Delta_j') \cdot f_4(\Delta_i', BO_{ij}') \cdot f_5(\Delta_j', BO_{ij}') \\ BO_{ij} &= BO_{ij}^{\sigma} + BO_{ij}^{\pi} + BO_{ij}^{\pi\pi} \end{aligned} \quad (2.4a)$$

$$f_1(\Delta_i, \Delta_j) = \frac{1}{2} \cdot \left(\frac{Val_i + f_2(\Delta_i', \Delta_j')}{Val_i + f_2(\Delta_i', \Delta_j') + f_3(\Delta_i', \Delta_j')} + \frac{Val_j + f_2(\Delta_i', \Delta_j')}{Val_j + f_2(\Delta_i', \Delta_j') + f_3(\Delta_i', \Delta_j')} \right) \quad (2.4b)$$

$$f_2(\Delta_i', \Delta_j') = \exp(-p_{bod} \cdot \Delta_i') + \exp(-p_{bod} \cdot \Delta_j') \quad (2.4c)$$

$$f_3(\Delta_i', \Delta_j') = -\frac{1}{p_{boc2}} \cdot \ln \left\{ \frac{1}{2} \cdot \left[\exp(-p_{boc2} \cdot \Delta_i') + \exp(-p_{boc2} \cdot \Delta_j') \right] \right\} \quad (2.4d)$$

$$f_4(\Delta_i', BO_{ij}') = \frac{1}{1 + \exp(-p_{boc3} \cdot (p_{boc4} \cdot BO_{ij}' \cdot BO_{ij}' - \Delta_i'^{boc}) + p_{boc5})} \quad (2.4e)$$

$$f_5(\Delta_j', BO_{ij}') = \frac{1}{1 + \exp(-p_{boc3} \cdot (p_{boc4} \cdot BO_{ij}' \cdot BO_{ij}' - \Delta_j'^{boc}) + p_{boc5})} \quad (2.4f)$$

A corrected overcoordination Δ_i can be derived from the corrected bond orders using equation (2.5).

$$\Delta_i = -Val_i + \sum_{j=1}^{neighbour(i)} BO_{ij} \quad (2.5)$$

Equation (2.6) is used to calculate the bond energies from the corrected bond orders BO_{ij} .

$$E_{bond} = -D_e^\sigma \cdot BO_{ij}^\sigma \cdot \exp\left[p_{bel} \left(1 - (BO_{ij}^\sigma)^{p_{be2}}\right)\right] - D_e^\pi \cdot BO_{ij}^\pi - D_e^{\pi\pi} \cdot BO_{ij}^{\pi\pi} \quad (2.6)$$

B Lone pair energy

Equation (2.8) is used to determine the number of lone pairs around an atom. Δ_i^e is determined in Equation (2.7) and describes the difference between the total number of outer shell electrons (6 for oxygen, 4 for silicon, 1 for hydrogen) and the sum of bond orders around an atomic center.

$$\Delta_i^e = -Val_i^e + \sum_{j=1}^{neighbour(i)} BO_{ij} \quad (2.7)$$

$$n_{lp,i} = \text{int}\left(\frac{\Delta_i^e}{2}\right) + \exp\left[-p_{lp1} \cdot \left(2 + \Delta_i^e - 2 \cdot \text{int}\left\{\frac{\Delta_i^e}{2}\right\}\right)^2\right] \quad (2.8)$$

For oxygen with normal coordination (total bond order=2, $\Delta_i^e=4$), equation (2.8) leads to 2 lone pairs. As the total bond order associated with a particular O starts to exceed 2, equation (2.8) causes a lone pair to gradually break up, causing a deviation Δ_i^{lp} , defined in equation (2.9), from the optimal number of lone pairs $n_{lp,opt}$ (e.g. 2 for oxygen, 0 for silicon and hydrogen).

$$\Delta_i^{lp} = n_{lp,opt} - n_{lp,i} \quad (2.9)$$

This is accompanied by an energy penalty, as calculated by equation (2.10).

$$E_{lp} = \frac{p_{lp2} \cdot \Delta_i^{lp}}{1 + \exp(-75 \cdot \Delta_i^{lp})} \quad (2.10)$$

C Overcoordination

For an overcoordinated atom ($\Delta_i > 0$), equations (2.11a-b) impose an energy penalty on the system.

The degree of overcoordination Δ is decreased if the atom contains a broken-up lone electron pair.

This is done by calculating a corrected overcoordination (equation 2.11b), taking the deviation from the optimal number of lone pairs, as calculated in equation (9), into account.

$$E_{over} = \frac{\sum_{j=1}^{nbond} p_{ovun1} \cdot D_e^\sigma \cdot BO_{ij}}{\Delta_i^{lpcorr} + Val_i} \cdot \Delta_i^{lpcorr} \cdot \left[\frac{1}{1 + \exp(p_{ovun2} \cdot \Delta_i^{lpcorr})} \right] \quad (2.11a)$$

$$\Delta_i^{lpcorr} = \Delta_i - \frac{\Delta_i^{lp}}{1 + p_{ovun3} \cdot \exp \left(p_{ovun4} \cdot \left\{ \sum_{j=1}^{neighbour(i)} (\Delta_j - \Delta_j^{lp}) \cdot (BO_{ij}^\pi + BO_{ij}^{\pi\pi}) \right\} \right)} \quad (2.11b)$$

D Undercoordination

For an undercoordinated atom ($\Delta_i < 0$), we want to take into account the energy contribution for the resonance of the π -electron between attached under-coordinated atomic centers. This is done by equations 2.12 where E_{under} is only important if the bonds between under-coordinated atom i and its under-coordinated neighbors j partly have π -bond character.

$$E_{under} = -p_{ovun5} \cdot \frac{1 - \exp(p_{ovun6} \cdot \Delta_i^{lpcor})}{1 + \exp(-p_{ovun2} \cdot \Delta_i^{lpcor})} \cdot \frac{1}{1 + p_{ovun7} \cdot \exp \left[p_{ovun8} \cdot \left\{ \sum_{j=1}^{neighbour(i)} (\Delta_j - \Delta_j^{lp}) \cdot (BO_{ij}^\pi + BO_{ij}^{\pi\pi}) \right\} \right]} \quad (2.12)$$

E Valence Angle Terms

E.1 Angle energy. Just as for bond terms, it is important that the energy contribution from valence angle terms goes to zero as the bond orders in the valence angle goes to zero. Equations (2.13a-g) are used to calculate the valence angle energy contribution. The equilibrium angle Θ_o for Θ_{ijk} depends on the sum of π -bond orders (SBO) around the central atom j as described in Equation (2.13d). Thus, the equilibrium angle changes from around 109.47 for sp^3 hybridization (π -bond=0) to 120 for sp^2 (π -bond=1) to 180 for sp (π -bond=2) based on the geometry of the central atom j

and its neighbors. In addition to including the effects of π -bonds on the central atom j , Equation (2.13d) also takes into account the effects of over- and under-coordination in central atom j , as determined by equation (2.13e), on the equilibrium valency angle, including the influence of a lone electron pair. Val^{angle} is the valency of the atom used in the valency and torsion angle evaluation. Val^{angle} is the same as Val^{boc} used in equation (2.3c) for non-metals. The functional form of Equation (2.13f) is designed to avoid singularities when $SBO=0$ and $SBO=2$. The angles in Equations (2.13a)-(2.13g) are in radians.

$$E_{val} = f_7(BO_{ij}) \cdot f_7(BO_{jk}) \cdot f_8(\Delta_j) \cdot \{p_{val1} - p_{val1} \exp[-p_{val2}(\Theta_o(BO) - \Theta_{ijk})^2]\} \quad (2.13a)$$

$$f_7(BO_{ij}) = 1 - \exp(-p_{val3} \cdot BO_{ij}^{p_{val4}}) \quad (2.13b)$$

$$f_8(\Delta_j) = p_{val5} - (p_{val5} - 1) \cdot \frac{2 + \exp(p_{val6} \cdot \Delta_j^{angle})}{1 + \exp(p_{val6} \cdot \Delta_j^{angle}) + \exp(-p_{val7} \cdot \Delta_j^{angle})} \quad (2.13c)$$

$$SBO = \sum_{n=1}^{neighbor(j)} (BO_{jn}^{\pi} + BO_{jn}^{\pi\pi}) + \left[1 - \prod_{n=1}^{neighbour(j)} \exp(-BO_{jn}^8) \right] \cdot (-\Delta_j^{angle} - p_{val8} \cdot n_{lp,j}) \quad (2.13d)$$

$$\Delta_j^{angle} = -Val_j^{angle} + \sum_{n=1}^{neighbour(j)} BO_{jn} \quad (2.13e)$$

$$SBO2 = 0 \text{ if } SBO \leq 0$$

$$SBO2 = SBO^{p_{val9}} \text{ if } 0 < SBO < 1$$

$$SBO2 = 2 - (2 - SBO)^{p_{val9}} \text{ if } 1 < SBO < 2$$

$$SBO2 = 2 \text{ if } SBO > 2 \quad (2.13f)$$

$$\Theta_0(BO) = \pi - \Theta_{0,0} \cdot \{1 - \exp[-p_{val10} \cdot (2 - SBO2)]\} \quad (2.13g)$$

E.2 Penalty energy. To reproduce the stability of systems with two double bonds sharing an atom in a valency angle, like allene, an additional energy penalty, as described in Equations (2.14a) and

(2.14b), is imposed for such systems. Equation (2.9b) deals with the effects of over/undercoordination in central atom j on the penalty energy.

$$E_{pen} = p_{pen1} \cdot f_9(\Delta_j) \cdot \exp \left[-p_{pen2} \cdot (BO_{ij} - 2)^2 \right] \exp \left[-p_{pen2} \cdot (BO_{jk} - 2)^2 \right] \quad (2.14a)$$

$$f_9(\Delta_j) = \frac{2 + \exp(-p_{pen3} \cdot \Delta_j)}{1 + \exp(-p_{pen3} \cdot \Delta_j) + \exp(p_{pen4} \cdot \Delta_j)} \quad (2.14b)$$

E.3 Three-body conjugation term. The hydrocarbon ReaxFF potential contained only a four-body conjugation term (see section F.2), which was sufficient to describe most conjugated hydrocarbon systems. However, this term failed to describe the stability obtained from conjugation by the $-\text{NO}_2$ -group. To describe the stability of such groups a three-body conjugation term is included (equation 2.15).

$$E_{coa} = p_{coa1} \cdot \frac{1}{1 + \exp(p_{coa2} \cdot \Delta_j^{val})} \cdot \exp \left[-p_{coa3} \cdot \left(-BO_{ij} + \sum_{n=1}^{neighbour(i)} BO_{in} \right)^2 \right] \cdot \exp \left[-p_{coa3} \cdot \left(-BO_{jk} + \sum_{n=1}^{neighbour(k)} BO_{kn} \right)^2 \right] \cdot \exp \left[-p_{coa4} \cdot (BO_{ij} - 1.5)^2 \right] \cdot \exp \left[-p_{coa4} \cdot (BO_{jk} - 1.5)^2 \right] \quad (2.15)$$

F Torsion angle terms

F.1 Torsion rotation barriers. Just as with angle terms we need to ensure that dependence of the energy of torsion angle ω_{ijkl} accounts properly for $\text{BO} \rightarrow 0$ and for BO greater than 1. This is done by Equations (2.16a)-(2.16c).

$$E_{tors} = f_{10}(BO_{ij}, BO_{jk}, BO_{kl}) \cdot \sin \Theta_{ijk} \cdot \sin \Theta_{jkl} \cdot \left[\frac{1}{2} V_1 \cdot (1 + \cos \omega_{ijkl}) + \frac{1}{2} V_2 \cdot \exp \left\{ p_{tor1} \cdot (BO_{jk}^\pi - 1 + f_{11}(\Delta_j, \Delta_k))^2 \right\} \cdot (1 - \cos 2\omega_{ijkl}) + \frac{1}{2} V_3 \cdot (1 + \cos 3\omega_{ijkl}) \right] \quad (2.16a)$$

$$f_{10}(BO_{ij}, BO_{jk}, BO_{kl}) = [1 - \exp(-p_{tor2} \cdot BO_{ij})] \cdot [1 - \exp(-p_{tor2} \cdot BO_{jk})] \cdot [1 - \exp(-p_{tor2} \cdot BO_{kl})] \quad (2.16b)$$

$$f_{11}(\Delta_j, \Delta_k) = \frac{2 + \exp \left[-p_{tor3} \cdot (\Delta_j^{angle} + \Delta_k^{angle}) \right]}{1 + \exp \left[-p_{tor3} \cdot (\Delta_j^{angle} + \Delta_k^{angle}) \right] + \exp \left[p_{tor4} \cdot (\Delta_j^{angle} + \Delta_k^{angle}) \right]} \quad (2.16c)$$

F.2 Four body conjugation term. Equations (2.17a-b) describe the contribution of conjugation effects to the molecular energy. A maximum contribution of conjugation energy is obtained when successive bonds have bond order values of 1.5 as in benzene and other aromatics.

$$E_{conj} = f_{12}(BO_{ij}, BO_{jk}, BO_{kl}) \cdot p_{cot1} \cdot \left[1 + (\cos^2 \omega_{ijkl} - 1) \cdot \sin \Theta_{ijk} \cdot \sin \Theta_{jkl} \right] \quad (2.17a)$$

$$f_{12}(BO_{ij}, BO_{jk}, BO_{kl}) = \exp \left[-p_{cot2} \cdot \left(BO_{ij} - 1\frac{1}{2} \right)^2 \right] \cdot \exp \left[-p_{cot2} \cdot \left(BO_{jk} - 1\frac{1}{2} \right)^2 \right] \cdot \exp \left[-p_{cot2} \cdot \left(BO_{kl} - 1\frac{1}{2} \right)^2 \right] \quad (2.17b)$$

G Hydrogen bond interactions

Equation (2.18) described the bond-order dependent hydrogen bond term for a X-H—Z system as incorporated in ReaxFF.

$$E_{Hbond} = p_{hb1} \cdot \left[1 - \exp(p_{hb2} \cdot BO_{XH}) \right] \cdot \exp \left[p_{hb3} \left(\frac{r_{hb}^o}{r_{HZ}} + \frac{r_{HZ}}{r_{hb}^o} - 2 \right) \right] \cdot \sin^8 \left(\frac{\Theta_{XHZ}}{2} \right) \quad (2.18)$$

H Correction for C₂

ReaxFF erroneously predicts that two carbons in the C₂-molecule form a very strong (triple) bond, while in fact the triple bond would get de-stabilized by terminal radical electrons, and for that reason the carbon-carbon bond is not any stronger than a double bond. To capture the stability of C₂ we introduced a new partial energy contribution (E_{C2}). Equation (2.19) shows the potential function used to de-stabilize the C₂ molecule:

$$\begin{aligned} E_{C2} &= k_{c2} \cdot (BO_{ij} - \Delta_i - 0.04 \cdot \Delta_i^4 - 3)^2 & \text{if } BO_{ij} - \Delta_i - 0.04 \cdot \Delta_i^4 > 3 \\ E_{C2} &= 0 & \text{if } BO_{ij} - \Delta_i - 0.04 \cdot \Delta_i^4 \leq 3 \end{aligned} \quad (2.19)$$

where Δ_i is the level of under/overcoordination on atom i as obtained from subtracting the valency of the atom (4 for carbon) from the sum of the bond orders around that atom and k_{c2} the force field parameter associated with this partial energy contribution.

I Triple bond energy correction.

To describe the triple bond in carbon monoxide triple bond stabilization energy is used, making CO both stable and inert. This energy term only affects C-O bonded pairs. Equation (2.20) shows the energy function used to describe the triple bond stabilization energy.

$$E_{trip} = p_{trip1} \exp[-p_{trip2} (BO_{ij} - 2.5)^2] \cdot \frac{\exp\left[-p_{trip4} \cdot \left(\sum_{k=1}^{(neighbour\ i)} BO_{ik} - BO_{ij}\right)\right] + \exp\left[-p_{trip4} \cdot \left(\sum_{k=1}^{(neighbour\ j)} BO_{jk} - BO_{ij}\right)\right]}{1 + 25 \cdot \exp[p_{trip3} (\Delta_i + \Delta_j)]} \quad (2.20)$$

J Nonbonded interactions

In addition to valence interactions which depend on overlap, there are repulsive interactions at short interatomic distances due to Pauli principle orthogonalization and attraction energies at long distances due to dispersion. These interactions, comprised of van der Waals and Coulomb forces, are included for *all* atom pairs, thus avoiding awkward alterations in the energy description during bond dissociation.

J.1 Taper correction. To avoid energy discontinuities when charged species move in and out of the non-bonded cutoff radius ReaxFF employs a Taper correction, as developed by de Vos Burchart⁵. Each nonbonded energy and derivative is multiplied by a Taper-term, which is taken from a distance-dependent 7th order polynomial (equation 2.21)).

$$Tap = Tap_7 \cdot r_{ij}^7 + Tap_6 \cdot r_{ij}^6 + Tap_5 \cdot r_{ij}^5 + Tap_4 \cdot r_{ij}^4 + Tap_3 \cdot r_{ij}^3 + Tap_2 \cdot r_{ij}^2 + Tap_1 \cdot r_{ij} + Tap_0 \quad (2.21)$$

The terms in this polynomial are chosen to ensure that all 1st, 2nd and 3rd derivatives of the non-bonded interactions to the distance are continuous and go to zero at the cutoff boundary. To that

end, the terms Tap_0 to Tap_7 in equation (2.21) are calculated by the scheme in equation (2.22), where R_{cut} is the non-bonded cutoff radius.

$$\begin{aligned}
Tap_7 &= 20/R_{cut}^7 \\
Tap_6 &= -70/R_{cut}^6 \\
Tap_5 &= 84/R_{cut}^5 \\
Tap_4 &= -35/R_{cut}^4 \\
Tap_3 &= 0 \\
Tap_2 &= 0 \\
Tap_1 &= 0 \\
Tap_0 &= 1
\end{aligned} \tag{2.22}$$

J.2 van der Waals interactions. To account for the van der Waals interactions we use a distance-corrected Morse-potential (Equations. 2.23a-b). By including a shielded interaction (Equation 2.23b) excessively high repulsions between bonded atoms (1-2 interactions) and atoms sharing a valence angle (1-3 interactions) are avoided.

$$E_{vdWaals} = Tap \cdot D_{ij} \cdot \left\{ \exp \left[\alpha_{ij} \cdot \left(1 - \frac{f_{13}(r_{ij})}{r_{vdW}} \right) \right] - 2 \cdot \exp \left[\frac{1}{2} \cdot \alpha_{ij} \cdot \left(1 - \frac{f_{13}(r_{ij})}{r_{vdW}} \right) \right] \right\} \tag{2.23a}$$

$$f_{13}(r_{ij}) = \left[r_{ij}^{P_{vdW1}} + \left(\frac{1}{\gamma_w} \right)^{P_{vdW1}} \right]^{\frac{1}{P_{vdW1}}} \tag{2.23b}$$

J.3 Coulomb Interactions

As with the van der Waals-interactions, Coulomb interactions are taken into account between *all* atom pairs. To adjust for orbital overlap between atoms at close distances a shielded Coulomb-potential is used (Equation 2.24).

$$E_{coulomb} = Tap \cdot C \cdot \frac{q_i \cdot q_j}{\left[r_{ij}^3 + (1/\gamma_{ij})^3 \right]^{1/3}} \tag{2.24}$$

Atomic charges are calculated using the Electron Equilibration Method (EEM)-approach³. The EEM charge derivation method is similar to the QEq-scheme; the only differences, apart from parameter definitions, are that EEM does not use an iterative scheme for hydrogen charges (as in QEq) and that QEq uses a more rigorous Slater orbital approach to account for charge overlap.

2.2 Limitations of ReaxFF Method

A No Explicit Electrons

ReaxFF reactive force field method can describe reactions in a complex chemical environment, however, the ReaxFF method does not contain an explicit electron or hole description. This limits the applicability of the ReaxFF method to calculate electronic properties and to investigate processes driven by explicit electron flow such as in semiconductor junctions, molecular memories, fuel cells, batteries, photosynthesis etc.

Although the current version of ReaxFF method does not include electron explicitly, it has several energy terms which implicitly accounts for the effects of explicit electrons. Over- or under-coordination terms works by comparing number of electrons around an atom involved in bonded interactions to its number of valence electrons. Polarizable charge calculation scheme, EEM method³ calculate charges on every atom based on electronegativity and hardness, and lone-pair terms is used to include the energy-effects of breaking up a lone-electron pairs on an atom⁶. However, existing ReaxFF method possesses limitations in studying electrochemical processes. For example, ReaxFF has difficulty in capturing correct electron affinity of the Ethyl carbonate (EC) electrolyte molecules and significantly underestimates the reduction potential of the EC molecule⁷. This results in extremely fast EC reduction reactions at Li-metal/electrolyte interface. ReaxFF exhibited poor energy conservation in NVE simulations of ionic liquid system when charge constraint was imposed⁸. Therefore, it is evident that current version of ReaxFF requires

further improvement to investigate electrochemical processes. At the current status of computational methods in chemistry, an effective way to fill the gap is to extend the capability of the ReaxFF method to incorporate explicit -electron or -hole description. This implementation would enhance its reactive capability to include redox chemistry. There is ongoing effort in the van Duin research group to implement explicit electron description within the current framework of the ReaxFF method.

B Electron Equilibrated Method (EEM)

Sanderson's principle of electronegativity equalization states that, upon the formation of a molecule, electrons flow until all electronegativities are equalized⁹. Essentially the same principle is found in density functional theory (DFT), stating that the electronic ground state has a constant chemical potential^{9, 10}. Starting from basic DFT equations, Mortier *et al.*³ derived the electronegativity equalization method (EEM) providing an elegant mathematical reformulation of Sanderson's principle. EEM assumes a quadratic model for the molecular energy as function of the atomic charges. A minimization of this energy (with a constraint on the total charge) leads to a set of linear electronegativity equations, whose solution yields ab initio quality atomic charges at minimal computational cost.

EEM has two major fundamental limitations, which become problematic in simulations of extended systems or when one studies atomic charges during chemical reactions. The first problem is that EEM always predicts a cubic scaling of the dipole polarizability with system size, while dielectric systems exhibit a linear scaling in the macroscopic limit. The second problem is that EEM yields, in general, fractional molecular charges for a system with two or more molecules, even when these molecules are well separated. For such systems, one expects integer-charged molecules because the energy of an isolated molecule is a piece-wise linear function of the

molecular population with derivative discontinuities at integer populations. Both problems boil down to one general weakness: EEM always allows long-range (even through-space) charge transfer, while this is only realistic inside conductor-like systems, e.g., metals or conjugated hydrocarbons.

A new polarizable force field (PFF), namely atom-condensed Kohn-Sham density functional theory approximated to second order¹¹ (ACKS2), surmounts two major shortcomings of EEM: ACKS2 predicts a linear size-dependence of the dipole polarizability in the macroscopic limit and correctly describes the charge distribution when a molecule dissociates. ACKS2 is currently implemented in the serial ReaxFF source code and will be parallelized in the future. As an illustration, a hydrogen atom at a perpendicular distance of 100 Å from a periodic (6 x 6) pristine graphene sheet acquires a charge of + 0.027e in the EEM scheme. In the ACKS2 scheme, for the same case, both the hydrogen atom and pristine graphene sheet has a charge of 0.0e. The details of the ReaxFF reactive force field employed for the above calculation is described in Chapter 6: ‘Transfer of Aqueous Protons Across Single Layer Graphene’. ACKS2 is essentially an extension of EEM and is derived from Kohn-Sham density functional theory (KS-DFT), making use of two novel ingredients in the context of PFFs: (i) constrained atomic populations and (ii) the Legendre transform of the Kohn-Sham kinetic energy. For details on derivation and implementation of ACKS2, refer to Verstraelen *et al.*¹¹. The implementation of ACKS2 is very similar to that of EEM, with only a small increase in computational cost. ACKS2 is a quadratic PFF and has its inherent limitations: ACKS2 cannot describe redox reactions or different ions of a given molecule with a single set of parameters.

C. Many-Body Effects in van der Waals Interactions

ReaxFF employs pair-wise potentials to calculate van der Waals interactions⁶. Pair-wise potentials are a commonly employed approximation to evaluate van der Waals interactions.

Several studies¹²⁻¹⁷ report on the inadequacies of the additive approximation and significant many-body effects are reported for various species in wide variety of configurations. The many-body effects increase as the species become more polarizable, is geometry dependent and can be either repulsive or attractive. A plausible approach to include many-body effects in physical adsorption is to develop two-body approximations in terms of a ‘renormalized substrate atom’ by choosing an effective van der Waals coefficient for the interaction between the gas and substrate atoms as employed in several recent studies¹⁸⁻²⁰. This implicitly takes into account the effects of the environment the atom experiences in a solid. However, this approach neglects the screening of the pair-potential by the environment. Hence, this procedure has the fundamental limitation that it neglects electromagnetic screening effects in van der Waals interactions which are important and inherently geometry dependent^{12, 17}. This implies that there is no transferability in van der Waals interactions. van der Waals interactions are weaker compared to covalent and electrostatic interactions and therefore many-body effects in van der Waals interactions are not significant in systems dominated by covalent and electrostatic interaction. However, reliable determination of many-body effects is essential in systems dominated by van der Waals interactions, for e.g., physisorption of inert gases, benzene on metal surfaces.

D. Spin-Excitations

In ground state systems -- and excited state systems between curve crossings -- the Born-Oppenheimer approximation applies, and the electronic wavefunction is set by the instantaneous position of the nuclei. In conventional force fields, including ReaxFF, the total energy is parameterized as a function of the nuclear coordinates alone. Since a wavefunction does not need to be explicitly computed, a significant time savings over quantum mechanics methods is possible, and the dynamics of large systems can be simulated in a practical way. However this approach

fails to describe highly excited systems, where there may be many curve crossings and a high density of states, causing the Born-Oppenheimer approximation to break down over long time intervals. Also, in many situations, when the molecular system owns enough energy to explore unusual regions of the configuration space, the Born-Oppenheimer approximation may fail. In such regions, the adiabatic surface driving the time evolution of the system branches and the nuclear wavepacket will split among a manifold of states. The occurrence of these nonadiabatic effects is not only common for a large number of problems, ranging from collision reactions to photochemistry, and is the basis for key biochemical phenomena, such as light detection and the photostability of the genetic code. The ReaxFF method cannot be applied to investigate these systems/problems, since it lacks an explicit electron description and is parameterized against QC data corresponding to the lowest energy spin-state. A plausible approach to incorporate excited-state dynamics in ReaxFF is to have different atom types for the same element parameterized to different low lying spin-states.

3

ReaxFF Reactive Force Field Study of the Dissociation of Water on Titania Surfaces

3.1 Introduction

Titanium dioxide (TiO_2) is a technologically important material that is widely used in many environment and energy related applications, such as solar cells²¹, water/air purification²², photocatalysis²³⁻²⁵, gas sensors²⁶ and biomaterials^{27, 28}. Most of these applications involve an aqueous or humid environment, where the structure and dynamics of water adsorption play an important role. From a fundamental perspective, the interaction of water with titania surfaces is fascinating because a complex interplay between diverse factors brings the H_2O - TiO_2 interface to a dynamic equilibrium with many interesting properties that are important for applications. For these reasons, the H_2O - TiO_2 interaction has been the subject of several experimental and theoretical studies for decades. The interaction of water with titania surfaces has been studied theoretically using various methods, including molecular mechanics (MM)^{29, 30}, semiempirical molecular orbital (MO) methods, Hartree-Fock (HF)^{31, 32}, Moller-Plesset second order perturbation theory (MP2)³³ and density functional theory (DFT)³⁴ methods employing various exchange-correlation functionals including PW-II³⁵, PW91³⁶, PBE³⁷, RPBE³⁸ and B3LYP^{39, 40}.

First-principles calculations can provide detailed and accurate descriptions of binding and interactions in metal-oxide/water systems. However, their substantial computational costs restrict the system sizes and times that can be probed, thus limiting their applicability to study solid surfaces in aqueous environments. Empirical force-field methods, on the other hand are faster and can handle larger systems but cannot commonly describe chemical reactions, such as dissociative adsorption on metal surfaces. However, ReaxFF, a bond-order based empirical reactive force field, can simulate chemical reactions and thus allows for a dissociable model for water, enabling a

reasonable description of proton-exchange dynamics and H-bond configurations at the interface. ReaxFF thus bridges this gap between methods based in quantum mechanics (QM), such as DFT and empirical force-field methods by being able to handle large simulations while maintaining an accuracy and reactivity that approaches that of QM-based methods. It is therefore of interest to investigate the behavior of TiO_2 in aqueous systems using a ReaxFF reactive force field. We studied the interaction of water with rutile (110), as well as the (101), (001), (112), (100) surfaces of anatase using a ReaxFF force field.

The adsorption of water on TiO_2 depends critically on the coordination of the surface atoms and their mutual separations and arrangement in space. Molecular or associative adsorption corresponds to the formation of a covalent bond between under-coordinated titanium atoms at the surface and the oxygen of a water molecule [referred to as the terminal (O_{TW}) oxygen site]. The two-coordinated bridging oxygen atoms on the surface [the bridging oxygen (O_{B}) site] can form hydrogen bonds with a water-hydrogen atom and induce the dissociation of an adsorbed water molecule. Dissociative adsorption involves a proton transfer from a chemisorbed water molecule to a bridging oxygen introducing $-\text{OH}$ and $-\text{H}$ functional groups at the surface. Here, we are interested in understanding the extent to which H_2O will dissociate on various TiO_2 surfaces. This is of importance because the dissociation state of water on the surface can significantly impact the water structure and surface chemistry on TiO_2 . At a microscopic level, the answer to this question lies in the subtle interplay among forces produced by hydrogen bonds and water dissociation governed by several underlying factors such as surface structure, water coverage, water-surface interactions and water-water interactions.

When water dissociates on TiO_2 surfaces, two surface hydroxyls form: a terminal hydroxyl, in which the hydroxyl from water binds to an under-coordinated Ti atom at the surface via its

oxygen [referred to as the terminal (O_{TH}) oxygen site], and a bridging hydroxyl, in which the hydrogen in water binds to a bridging (2-fold coordinated) surface oxygen [the bridging oxygen (O_B) site]. The dissociated state is the result of a dynamic equilibrium arising from hydrogen bonding between the surface atoms, the adsorbed water molecules and the hydration layer over the adsorbed water molecules. We investigate the dynamical aspect of this equilibrium between associative and dissociative adsorption over various titania surfaces and quantify the amount of water dissociated using a ReaxFF reactive force field. We proceed to describe the computational methods used and then we discuss the results of the simulations.

3.2 Computational methods

In this work we employed the recently developed Ti/O/H ReaxFF parameter set, as recently employed to the glycine/TiO₂ interface by Monti *et al.*⁴¹. This force field was fit to a large, DFT-based, training set, including equations of state for bulk anatase, rutile, brookite and higher-energy TiO₂ crystals, as well as surface energies and water-dissociation energy barriers. The force field was validated by comparisons to DFT/MD simulations of water-dissociation reactions on the rutile (110) surface, in which excellent agreement was achieved between ReaxFF/MD and DFT/MD for the extent of water dissociation at 1 and 3 monolayer (ML) coverages. This force field uses the same general and O/H ReaxFF parameters as employed in a number of previous ReaxFF descriptions, including proteins⁴², alcohols and organic acids⁴³, inorganic acids⁴⁴, phosphates^{42, 45, 46}, zinc oxides^{47, 48}, iron oxides⁴⁹, copper oxides⁵⁰, aluminium⁵¹, silica⁵² and aluminosilicates⁵³, thus allowing straightforward transferability to multicomponent liquids and mixed metal oxide materials. The oxygen-oxygen radial distribution function (rdf) given by ReaxFF for water at 298K is in good agreement with neutron diffraction studies by Soper *et al.*⁵⁴ as seen in **Error! Reference source not found.**. The self-diffusion coefficient of water at 298K given by ReaxFF (0.2106

$\text{\AA}^2/\text{ps}$) is comparable to the values given by diaphragm-cell technique⁵⁵ ($0.2299 \text{ \AA}^2/\text{ps}$) and pulsed magnetic field gradient (PFG) NMR ($0.2299 \text{ \AA}^2/\text{ps}$) studies⁵⁶. A full description of the Ti/O/H force field development will be published separately.

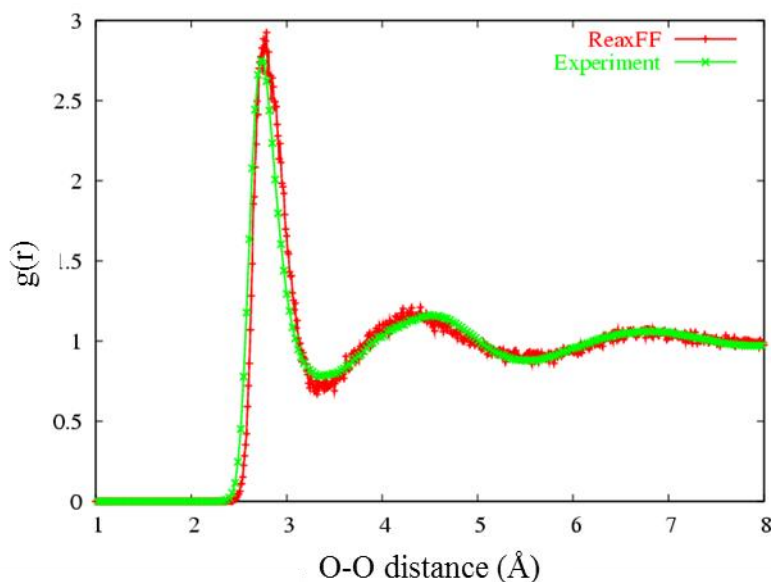


Figure 3.1. Oxygen-oxygen radial distribution function for water at 298 K.

We perform energy minimization calculations with convergence criterion of 0.25 kcal/\AA to obtain binding energies and conformations, and MD simulations to study water adsorption and structural properties of water multilayers over various titania surfaces. The ReaxFF reactive force field implementation in the ADF computational chemistry package⁵⁷ has been used for these calculations. We use periodic slabs to describe various titania surfaces and their lateral dimensions and vacuum spacing are specified below. All MD simulations have been performed in the canonical (NVT) ensemble, with a time step of 0.25 fs using the Berendsen thermostat with a coupling time constant of 100 fs to control temperature of the entire system.

For all following discussions, one monolayer (ML) is defined with respect to the number of five-fold coordinated Ti surface atoms (Ti_{5c}). To study H_2O adsorption we place water molecules in random configurations over various titania surfaces at 0.50, 0.75, 1.0, 1.5, 2.0 and

3.0 ML coverages. We then perform MD simulations for 500 ps at 300K to quantify water dissociation. In these simulations the equilibration time was 100 ps and the subsequent production run was 400 ps. As we will discuss below, we also studied cases where the vacuum spacing, lateral dimensions of the simulation box, water coverage, and temperature have been adjusted to match corresponding DFT calculations or experiments.

3.3 Results and Discussion

H₂O-Anatase interaction

i. H₂O-Anatase (101)

Anatase (101) is the lowest-energy surface of the anatase polymorph of TiO₂ and so its interface with water has been the subject of several studies^{25, 58-72}. In our simulations we used a periodic anatase (101) slab with (9 x 9) unit cells parallel to the surface that contains 4 layers of TiO₂. The dimensions of the simulation cell are 61.44 Å x 68.13 Å parallel to the surface and 25 Å in the direction perpendicular to the surface. From MD simulations performed at 300 K for various water coverages, we find that on anatase (101) molecular adsorption is preferred over dissociative adsorption for coverages up to 0.75 ML, which is supported by previous DFT studies⁵⁸⁻⁶¹. In molecular or associative adsorption, the surface is terminated by chemisorbed terminal water molecules, in which the oxygen forms a dative bond with a Ti_{5c} atom and the hydrogens are stabilized by forming hydrogen bonds with the two-fold coordinated surface bridging O_{2c} atoms in the adjacent row as seen in Figure 3.2.

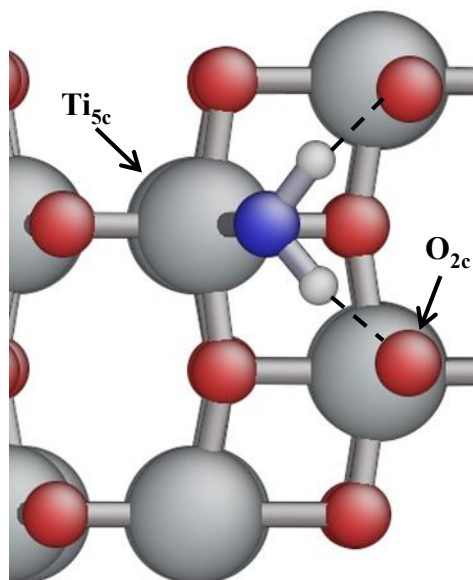


Figure 3.2. Molecular adsorption over anatase (101). Ti atoms are gray, O atoms in TiO_2 are red, the terminal water oxygen is blue, and H atoms are white. Five-fold Ti surface atoms (Ti_{5c}) and two-fold O surface atoms (O_{2c}) are indicated and the dashed lines indicate hydrogen bonds.

Scanning Tunneling Microscopy (STM) studies by He *et al.*⁶² show that over anatase (101) water adsorbs molecularly to form a locally ordered (2 x 2) structure at a coverage of 0.24 ML and 190 K. In the same study, the (2 x 2) superstructure was probed using DFT calculations based on the PBE exchange-correlation functional. It was proposed that charge rearrangement at the water-anatase interface affects the adsorption of further water molecules, resulting in short-range repulsive and attractive interactions along the [010] and $[11\bar{1}]/[1\bar{1}\bar{1}]$ directions, respectively, that produce a locally ordered (2 x 2) structure. This influence of adsorbed water molecules on further adsorption of water due to substrate-mediated interactions leads to the formation of the (2 x 2) superstructure. To match the experimental conditions, we performed a MD simulation with the above anatase (101) slab at 190 K with 0.24 ML water coverage. The simulation was run with an equilibration time of 50 ps and a subsequent production run of 200 ps and we obtained the configuration in Figure 3.3. In Figure 3.3, we can see the (2 x 2) overlayer structure on anatase (101) surface, as proposed by He *et al.*⁶².

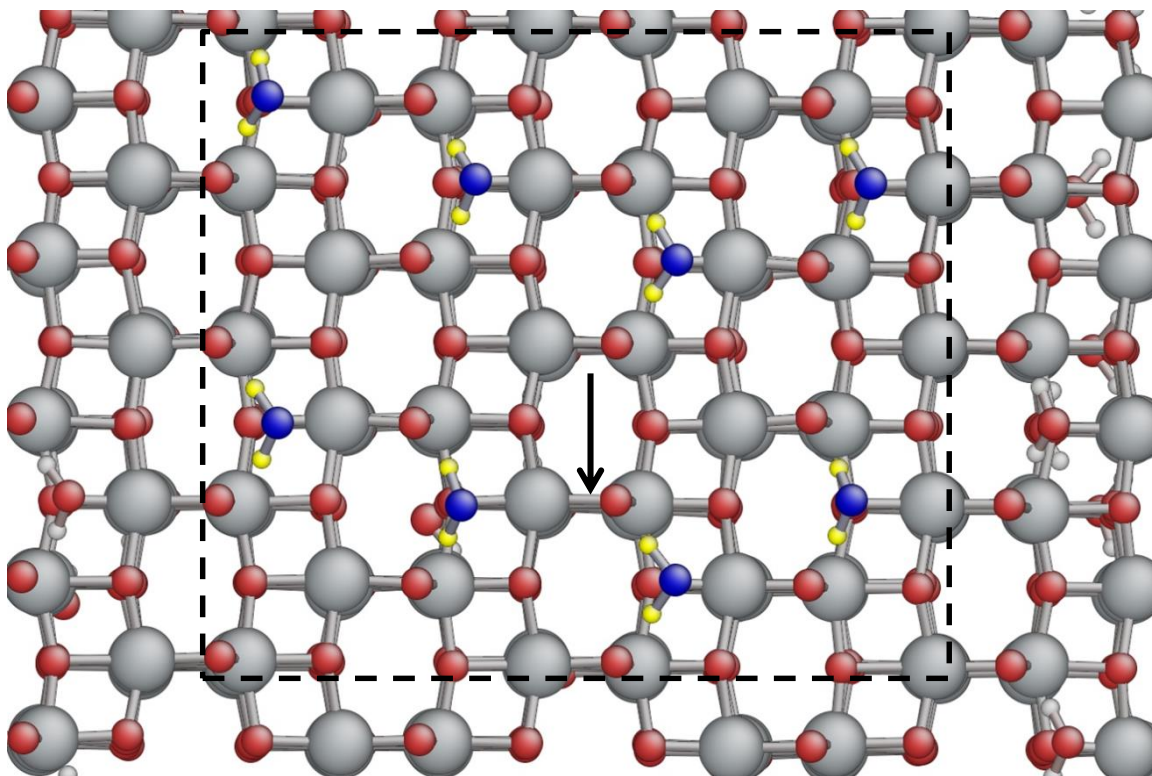


Figure 3.3. (2 x 2) overlayer structure of molecular water on anatase (101) at 190 K. Water hydrogen and oxygen atoms inside the dashed box are emphasized in yellow and blue, respectively. The arrow indicates the double periodicity along the [010] direction.

In our ReaxFF simulations we see dissociative adsorption over anatase (101) at 300 K for water coverages of 0.75 ML and higher, resulting in mixed molecular and dissociative adsorption. This is contradictory to the prevailing view of pure molecular adsorption on anatase (101)^{58-61, 66, 73}. Tilocca *et al.*⁵⁸ proposed that the hydrogen bonds between water and O_{2c} atoms play a critical role in the distribution of water on anatase (101) surface, stabilizing molecular adsorption and also leading to local ordering of adsorbates in which the water dipoles are oriented to form a zigzag pattern along the [-101] direction at 1 ML. We observe this zigzag pattern for molecularly adsorbed water molecules at 300 K along with dissociated water. From

Figure 3.4. Water distribution over anatase (101) at 1.0 ML with the zigzag pattern for molecularly adsorbed water (blue oxygens) interspersed with dissociated water (green oxygens). Dashed lines indicate hydrogen bonds

we can see that the dissociated water molecule causes rearrangement of the ‘zigzag’ hydrogen bonded network formed at the surface by molecularly adsorbed water molecules. Recent surface-sensitive photoelectron spectroscopy studies by Sandell *et al.*⁷⁴ indicate that the formation of a water ML over anatase (101) involves both molecular and dissociative adsorption, which agrees with our observations. Dissociative adsorption is observed at higher coverages (>0.75 ML), indicating that surrounding water molecules assist in dissociation of terminal water molecules. Figure 3.5(a) shows a snapshot from a simulation of water on anatase (101) at 3.0 ML coverage, which distinguishes the oxygens of the terminal hydroxyls (O_{TH}) from the oxygens of terminal water molecules (O_{TW}).

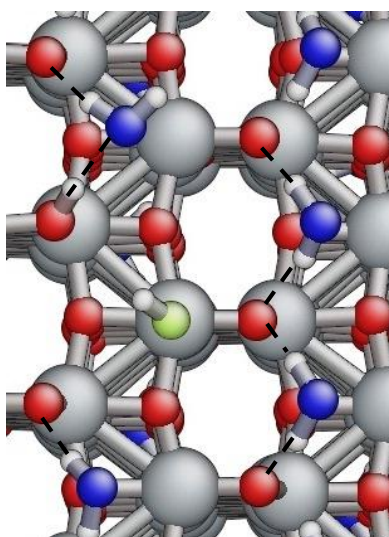


Figure 3.4. Water distribution over anatase (101) at 1.0 ML with the zigzag pattern for molecularly adsorbed water (blue oxygens) interspersed with dissociated water (green oxygens). Dashed lines indicate hydrogen bonds

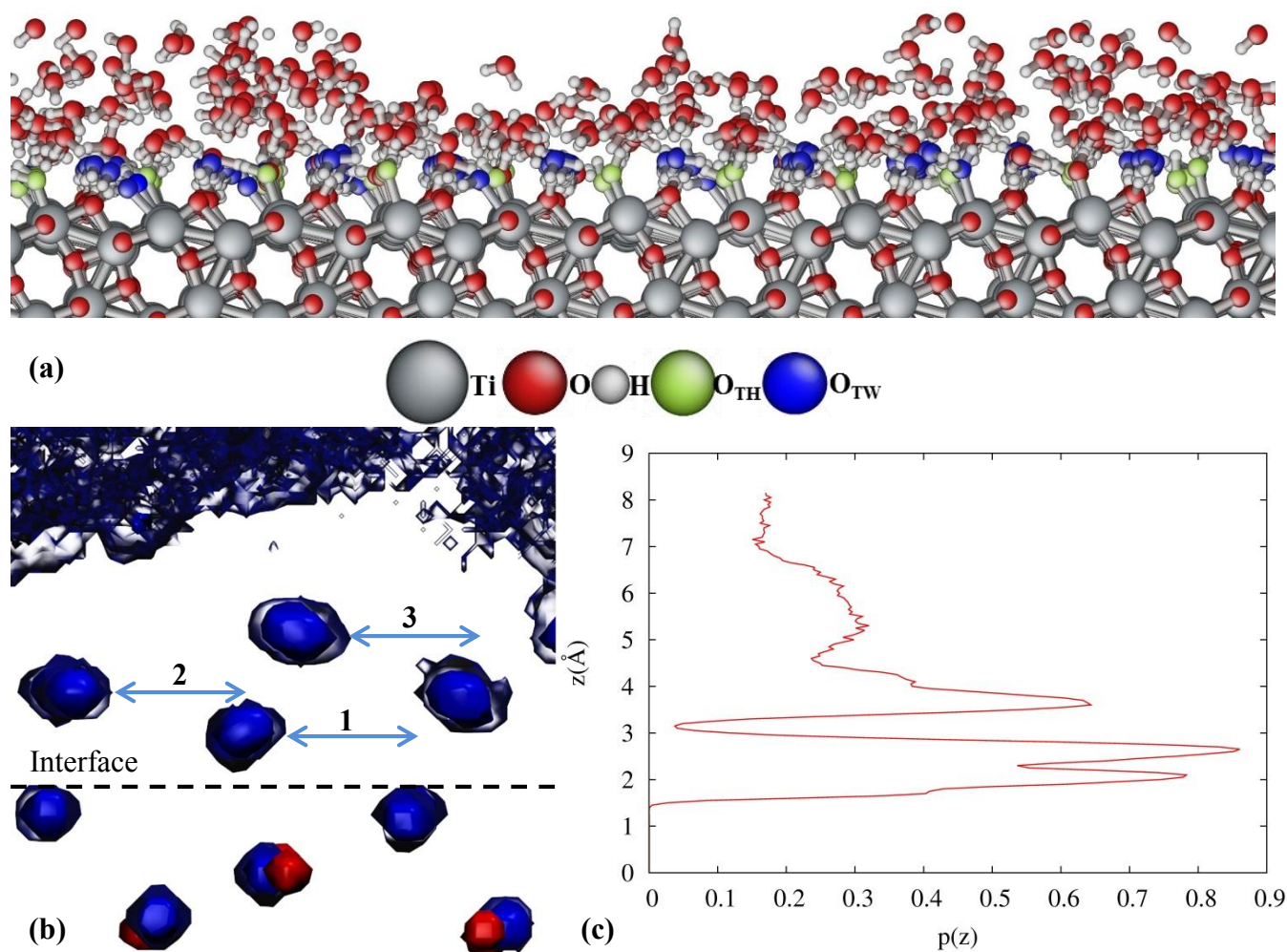


Figure 3.5. (a) Snapshot from an MD simulation of water on anatase (101) at 3.0 ML coverage; (b) Density plot of titanium (red) and oxygen (blue) atoms over anatase (101). The numbers and arrows indicate the heights of the n^{th} water layer; (c) Perpendicular distance of the water-oxygen atoms from the plane containing the surface Ti_{5c} atoms over anatase (101).

Figure 3.6 shows the binding configurations for the water bilayer adsorbed over a molecularly adsorbed water molecule and a dissociated water molecule over a periodic (2 x 1) anatase (101) slab with 4 layers of titanium and vacuum spacing of 25 Å perpendicular to the surface.^{75, 76} Mattioli *et al.*^{75, 76} studied these configurations by performing total-energy calculations and *ab initio* MD simulations at different temperatures and found that these structures are characterized by short H bonds, both between the two water molecules ($\text{H}-\text{O}_w$, where O_w is the

oxygen in a water molecule) and between the water molecules and the bridging O_{2c} ($H-O_{2c}$) atoms in the surface. From Figure 3.6, it is clearly seen that the nature of first layer predetermines the structure of the second layer. The distribution of water on the (101) surface thus results from interactions between bound water molecules, bridging O_{2c} atoms, and surrounding water molecules.

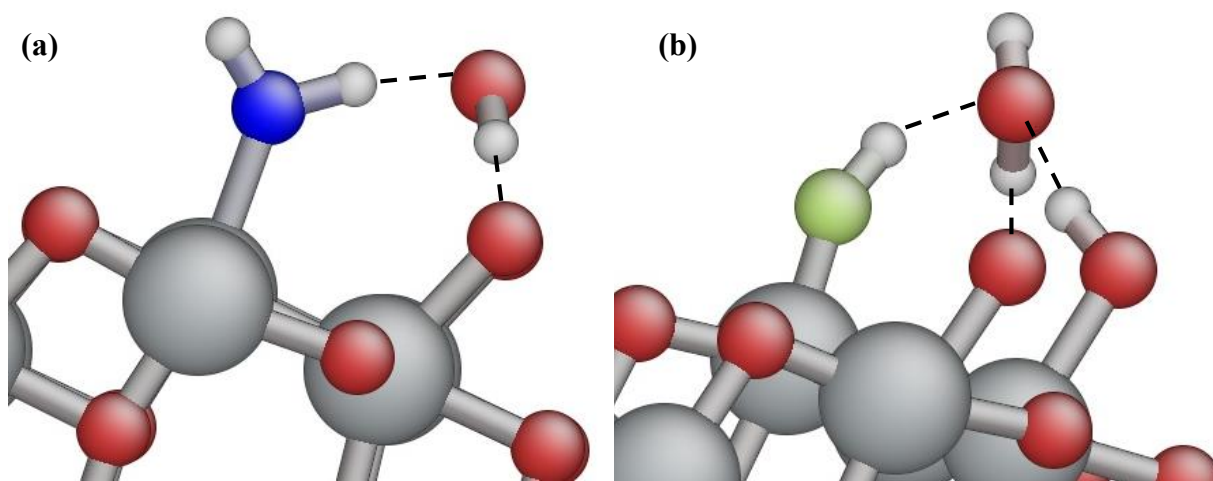


Figure 3.6. Water bilayer configuration above (a) molecularly adsorbed (blue oxygens) and (b) dissociatively adsorbed (green oxygens) water over anatase (101). The oxygens of water in the second layer and oxygens in TiO₂ slab are shown in red.

Water multi-layers have a well-defined structure close to the anatase (101) surface. Figure 5(b) gives the density plot of titanium (red) and oxygen (blue) atoms in the simulation box during a 500-ps NVT run at 300 K with 3 ML water. To obtain the density plot, we first divided the simulation cell into a mesh of cubic boxes with dimensions ($0.30 \text{ \AA} \times 0.30 \text{ \AA} \times 0.30 \text{ \AA}$). We then counted the number of times a particular atom type (*e.g.*, oxygen) was located in each of the grids through the entire length of simulation and normalized these numbers by the highest count recorded in any of the grids. We used these values to obtain the resulting density plot in Figure 3.5(b). From Figure 3.5(b) we can see the positions of the first three water layers on the anatase (101) surface and the transition to the bulk water phase, indicating that at the interface, water forms

well defined structural layers up to 3 layers. The distribution $p(z)$ of the perpendicular distances of the water-oxygen atoms from the plane containing the surface Ti_{5c} atoms is given in Fig. 5(c). The peaks in the distribution (~ 2 Å, ~ 2.65 Å and two broad peaks centered at ~ 4 Å and ~ 5.5 Å) are comparable to the peaks calculated by Tilocca and Selloni^{58, 73} (~ 2 Å, ~ 2.75 Å, ~ 4 Å and ~ 5.5 Å) using DFT calculations based on the PBE exchange-correlation functional for a water trilayer.

Synchrotron radiation core level photoelectron spectroscopy studies by Sandell *et al.*⁷⁴ show that on heating the anatase (101) sample, the OH coverage at the surface goes through a maximum with increasing temperature. To study the variation of terminal hydroxyl coverage with temperature, we performed MD simulations for 500 ps at temperatures ranging from 100 K to 1500 K at regular intervals of 200 K. Figure 3.7 shows the variation of terminal OH coverage with temperature during the temperature-ramp MD simulation. We can see that on heating the OH coverage increases initially and then decreases due to desorption of OH groups by recombining with a neighboring proton to form a water molecule. The variation of terminal OH coverage over anatase (101) with temperature is qualitatively similar to what is seen experimentally⁷⁴. However the temperature at which the OH coverage begins to decrease is higher than what is seen experimentally. This is likely because our heating rate is significantly faster than that in the experiments, so that water cannot recombine and desorb on the MD time scale at low temperatures.

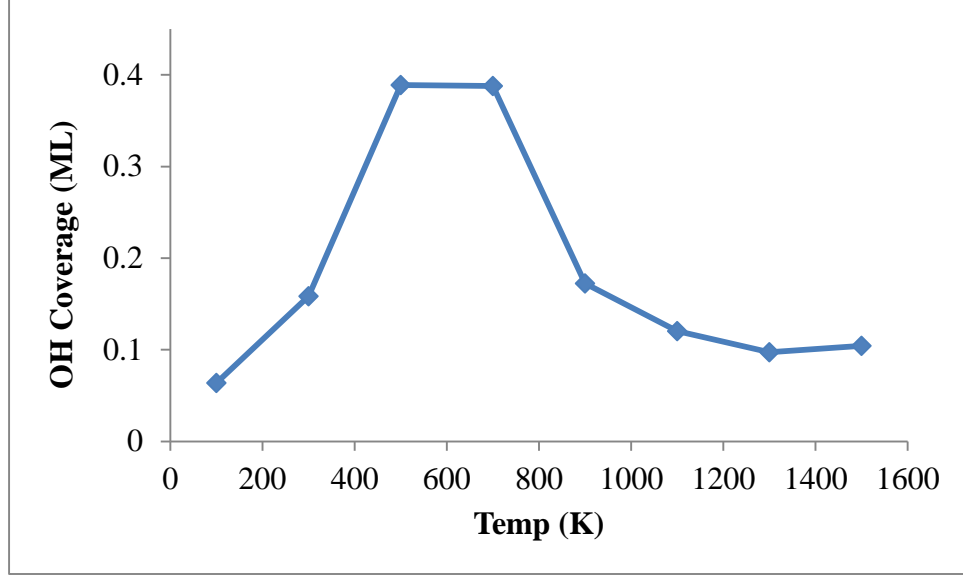


Figure 3.7. OH coverage (ML) over anatase (101) as a function of temperature.

To quantify water dissociation we calculated the water dissociation percentage (WDP), which is the percent of water molecules that have dissociated in the whole simulation box, and to quantify the fraction of dissociated water at the interface we compute the terminal water dissociation percentage (TWDP), which we define as

$$TWDP = \frac{\text{Number of terminal } [OH]}{\text{Number of terminal } [OH] + \text{Number of terminal } H_2O} \quad (3.1)$$

Figure 3.8 gives the WDP and TWDP over anatase (101) for various water coverages. As the coverage increases, the WDP increases until a coverage of ~ 2.0 ML, after which it decreases slightly. The TWDP is equal to the WDP up to a coverage of 1 ML, after which it continues to increase with increasing water coverage. This indicates that non-interfacial water molecules aid in the dissociation of water at the surface. As we will discuss below, the increase in TWDP with coverage is observed for all the studied anatase surfaces and it arises from stabilization of dissociated water molecules by hydrogen bonding or from surrounding water molecules aiding in

dissociation by mediating proton transfer between the terminal water molecule and surface bridging oxygens.

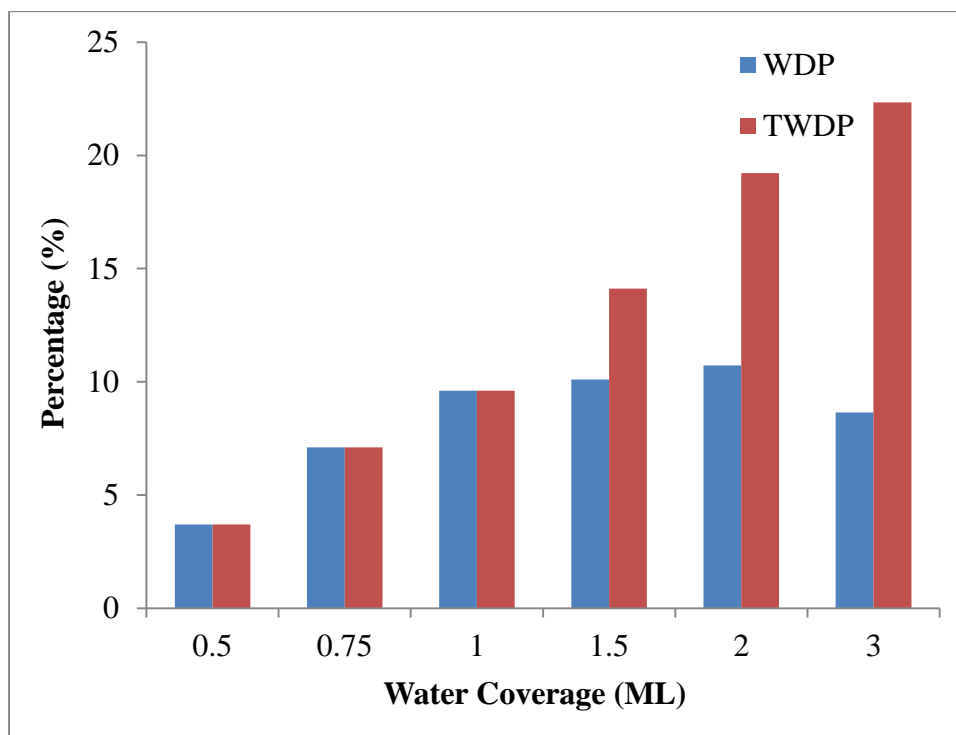


Figure 3.8. WDP and TWDP on anatase (101) as a function of water coverage.

ii. H₂O-Anatase (001)

The unreconstructed anatase (001) surface presents both Ti_{5c} and O_{2c} sites to water molecules. Since all the surface atoms (Ti_{5c} and O_{2c}) are under-coordinated, anatase (001) has a higher surface energy and a higher reactivity than anatase (101). In this simulation we used a 4-layer anatase (001) slab with (9 x 9) unit cells parallel to the surface. The dimensions of the simulation cell are 68.13 Å x 68.13 Å parallel to the surface and 25 Å in the direction perpendicular to the surface. From our MD simulations at 300 K for various coverages we observe that at low coverages (<1.0 ML) dissociative adsorption occurs and hydroxyl groups are formed within clusters of adsorbed water molecules, suggesting that clustering plays a role in dissociative

adsorption. In regions without clusters, the water molecules hydrogen bond to the surface O_{2c} atoms.

At higher coverages (> 1 ML), mixed molecular/dissociative adsorption is observed. This result is supported by DFT calculations (PBE) by Gong *et al.*⁷⁷, who investigated water dissociation on anatase (001) at 1 ML coverage and observed mixed molecular/dissociative adsorption. **Error! Reference source not found.**(a) shows a snapshot from a MD simulation of water on anatase (001) at 3.0 ML coverage, which distinguishes the oxygens of the terminal hydroxyls (O_{TH}) from the oxygens of terminal water molecules (O_{TW}). In molecular adsorption, the oxygen atom of the water molecule binds to a Ti_{5c} atom, while in dissociative adsorption there is an additional proton transfer from the chemisorbed water molecule to a bridging surface O_{2c} atom in the adjacent row. During our MD simulations we observe that dissociative adsorption can lead to the cleavage of Ti_{5c} - O_{2c} bonds on unreconstructed anatase (001), by the formation of Ti-OH bonds, as shown in Figure 3.10, thus stabilizing two Ti_{5c} atoms. This cleavage of Ti_{5c} - O_{2c} bonds was also observed in previous DFT studies by Gong *et al.*⁷⁷. At 1 ML water coverage, ~33% of dissociative adsorption leads to cleavage of Ti_{5c} - O_{2c} bonds during MD simulations at 300 K.

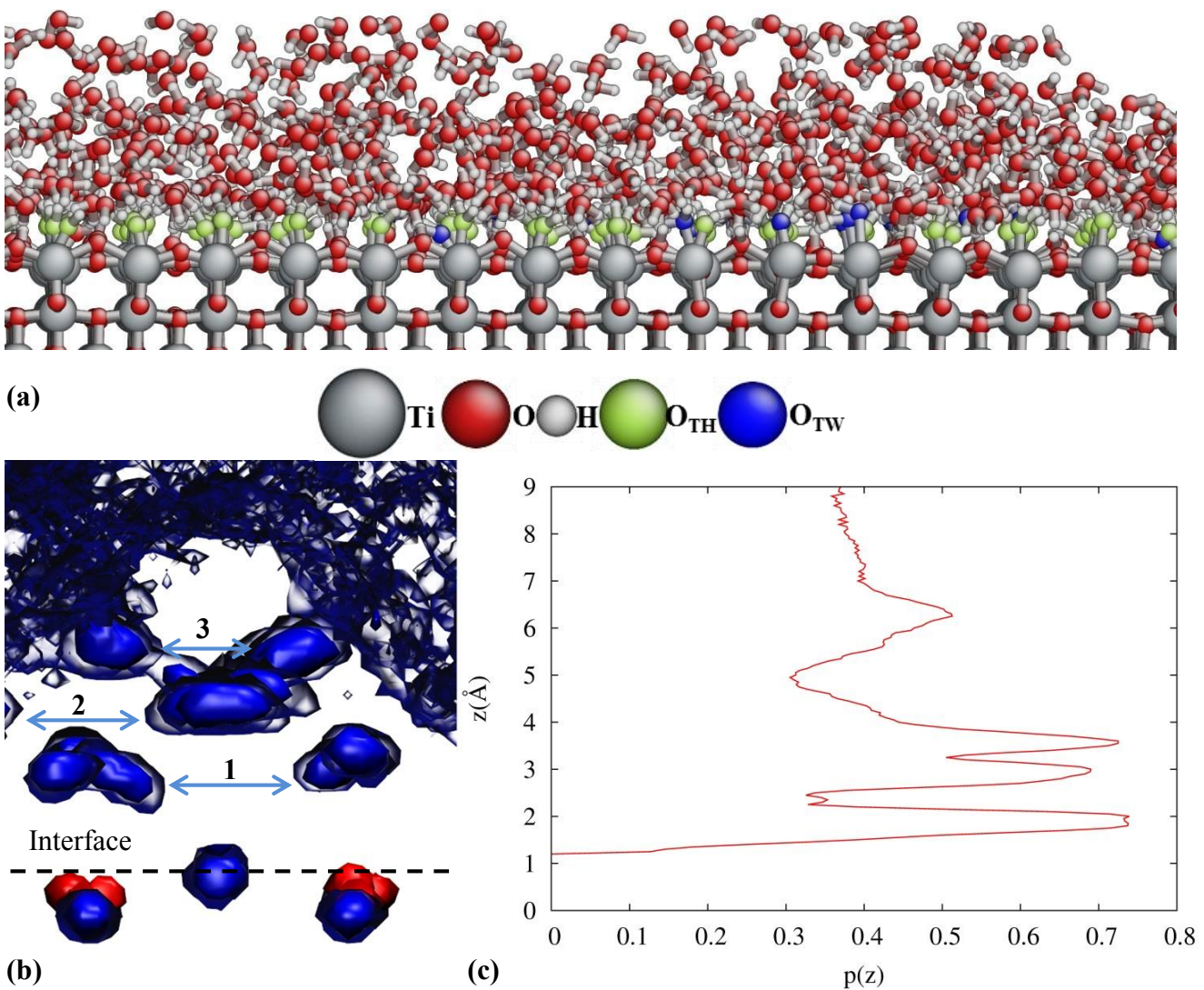


Figure 3.9. Snapshot from an MD simulation of water on over unreconstructed anatase (001) at 3.0 ML coverage; (b) Density plot of titanium (red) and oxygen (blue) atoms over anatase (001).

The numbers and arrows indicate the heights of the n^{th} water layer; (c) Perpendicular distance of the water-oxygen atoms from the plane containing the surface Ti_{5c} atoms on anatase (001).

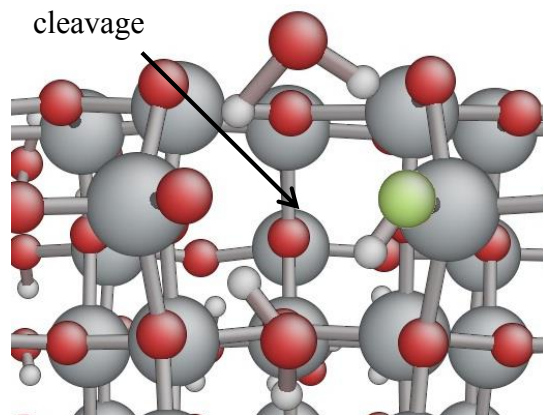


Figure 3.10. Cleavage of the $\text{Ti}_{5c}\text{-O}_{2c}$ bond on unreconstructed anatase (001) due to dissociative adsorption.

Figure 3.11 gives the WDP and TWDP on unreconstructed anatase (001) as a function of water coverage. The WDP increases until 1.0 ML, then it decreases with increasing water coverage which simply reflects that an increasing fraction of the water cannot contact the surface at the higher coverages. We note that the maximum in the DWP for anatase (001) occurs at a lower coverage than on anatase (101) because the (001) surface has a higher reactivity. The TWDP increases with coverage past 1 ML, indicating that non-surface water assists in dissociation.

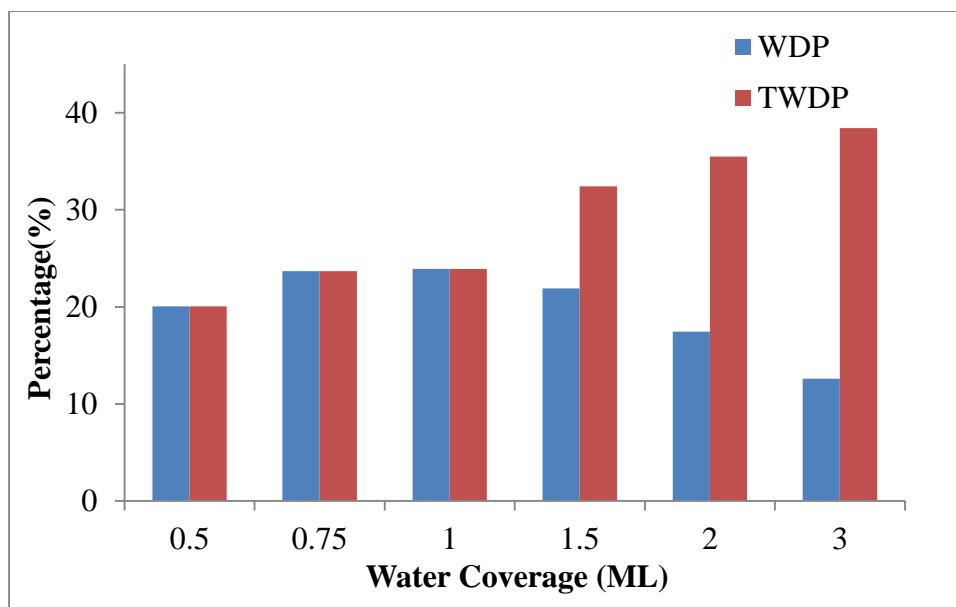


Figure 3.11. WDP and TWDP on anatase (001) surface as a function of water coverage.

The structure of the first three layers of water adsorbed on anatase (001) is shown in **Error! Reference source not found.**(b). The distribution $p(z)$ of the perpendicular distances of the water-oxygen atoms from the plane containing the surface Ti_{5c} atoms is given in **Error! Reference source not found.**(c). The distance distribution has peaks at $\sim 2 \text{ \AA}$, $\sim 3 \text{ \AA}$, $\sim 3.55 \text{ \AA}$ and a broad peak around $\sim 6.25 \text{ \AA}$.

Anatase (001) undergoes a (1×4) surface reconstruction under ultra-high vacuum (UHV) conditions^{78, 79}. The structure of the reconstructed surface has been derived from STM studies by Liang *et al.*^{79, 80} in conjunction with first-principles DFT calculations (PBE) by Lazzeri and Selloni⁸¹. We use the ‘ad-molecule’ model (ADM) proposed by Lazzeri and Selloni to study water dissociation on the reconstructed (1×4) surface. The surface can be described as consisting of valleys and ridges.

Figure 3.12. Ad-molecule model of the anatase (001) – (1×4) reconstructed surface.

shows the structure of the (1×4) reconstructed surface used in our calculations. We find that anatase (001) (1×4) dissociates water, but only at the ridges and the dissociation always led

to cleavage of $\text{Ti}_{4c}\text{-O}_{2c}$ bonds along the ridges, as shown in Figure 3.13. This agrees with the first-principles calculations of Vittadini and Selloni⁸² and also with experimental studies using photoelectron spectroscopy by Sandell *et al.*⁸³. Since water dissociates only at the ridges, the anatase (001) – (1 x 4) reconstructed surface dissociates less water than the clean anatase (001) surface. This is reflected in the higher WDP over the clean anatase(001) surface (23.9%) compared to the WDP over the anatase(001) (1 x 4) reconstructed surface (12.1%).

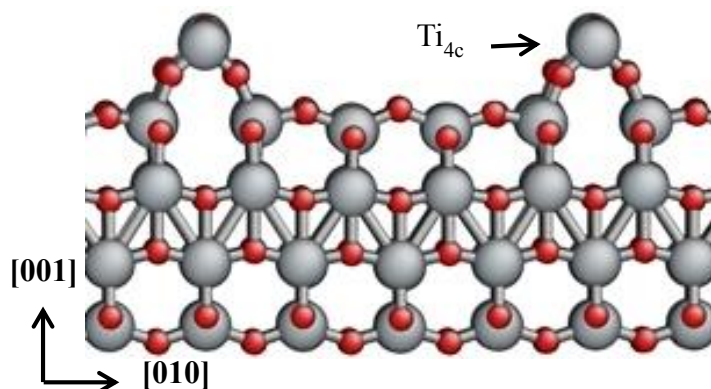


Figure 3.12. Ad-molecule model of the anatase (001) – (1 x 4) reconstructed surface.

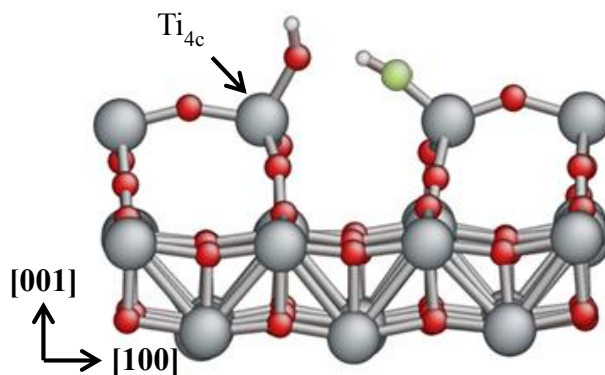


Figure 3.13. Water dissociation along the ridge at a Ti_{4c} atom site on anatase (001) - (1 x 4).

iii. H_2O -Anatase (100)

The anatase (100) surface has Ti_{5c} , O_{2c} and O_{3c} sites, which make it slightly less stable than the majority (101) surface, but more stable than the minority (001) surface. In this simulation we

used an anatase (100) slab with (9 x 9) unit cells parallel to the surface and 4 layers of TiO₂. The dimensions of the simulation cell are 68.04 Å x 86.31 Å parallel to the surface and 25 Å perpendicular to the surface. From the MD simulations at various coverages we observe that dissociative adsorption is favorable on anatase (100) and it occurs for all the studied water coverages. This is consistent with previous DFT studies^{64, 84-87}. Figure 3.14(a) shows a snapshot from an MD simulation of water on anatase (100) at 3.0 ML coverage that shows both molecularly and dissociatively adsorbed water.

The density plot of oxygen and titanium atoms in the simulation box during a 500-ps NVT simulation at 300 K indicates the structure of the first three layers of water adsorbed over anatase (100) and is shown in Figure 3.14(b). Figure 3.14(c) gives the vertical distribution of the water-oxygen atoms from the plane containing the surface Ti_{5c} atoms. The distribution has peaks at ~1.55 Å, ~2.25 Å and two broad peaks about ~4 Å and ~5.6 Å. The peak at ~1.55 Å which is shorter than Ti-O bond distance corresponds to the water molecules hydrogen bonded over the O_{2c} trenches on the surface.

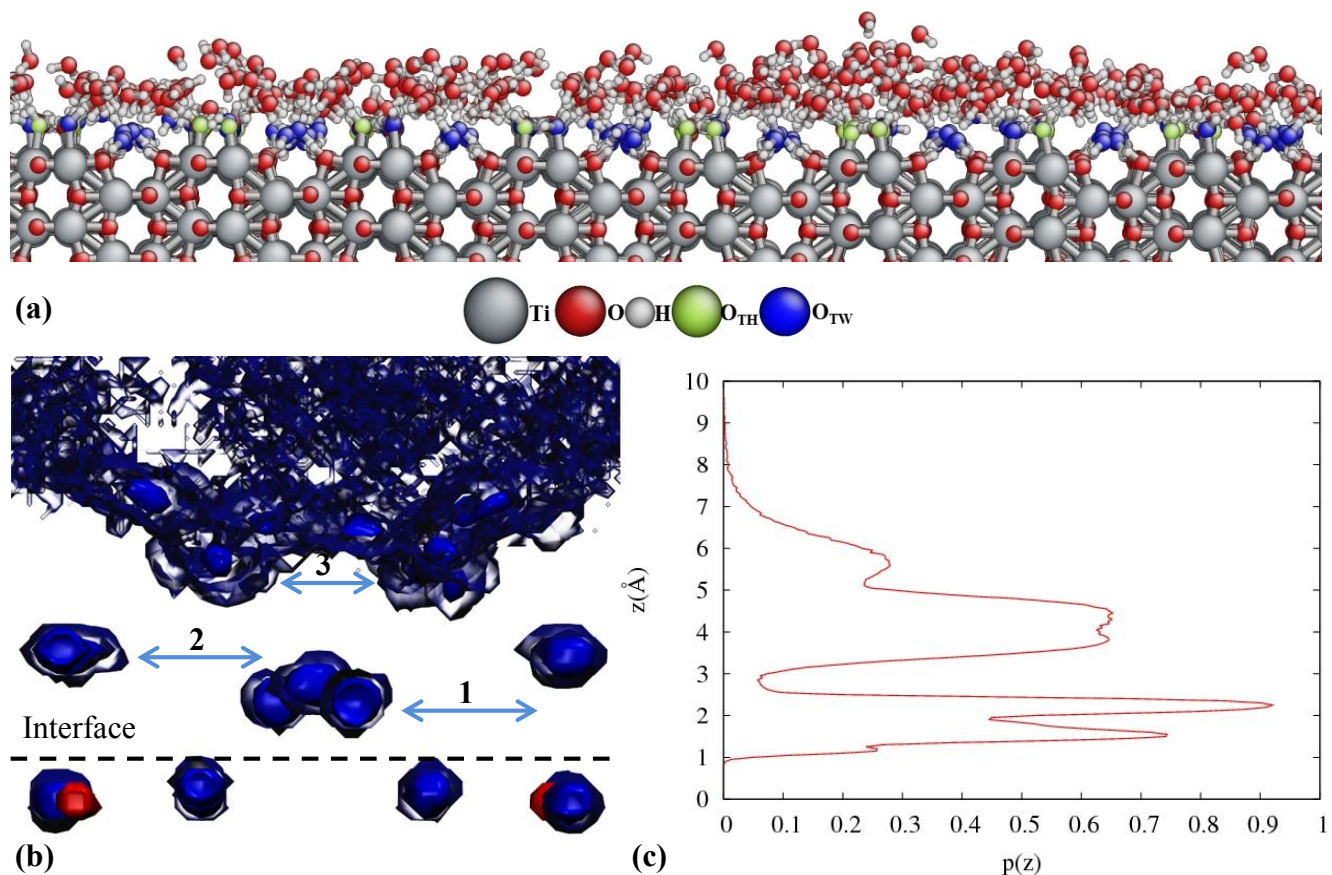


Figure 3.14. (a) Snapshot from an MD simulation of water on anatase (100) at 3.0 ML coverage; (b) Density plot of titanium (red) and oxygen (blue) atoms over anatase (100). The numbers and arrows indicate the heights of the n^{th} water layer; (c) Perpendicular distance of the water-oxygen atoms O_w from the plane containing the surface Ti_{sc} atoms on anatase (100).

Figure 3.15 gives the WDP and TWDP as a function of coverage and we can see that as the water coverage increases, the TWDP increases, suggesting that surrounding water molecules assist in water dissociation. In their DFT study, Arrouvel *et al.*⁸⁴ found that pure dissociative adsorption is favored at low coverages, while a mixed adsorption occurs at higher coverages. The DFT studies by Ignatchenko *et al.*⁸⁵ also support the view of mixed associative and dissociative adsorption over anatase (100). The WDP increases until a coverage of 1.5 ML and then decreases with coverage. This is because the increase in TWDP is overshadowed by the number of water molecules added in the second and third layers which do not contact the surface.

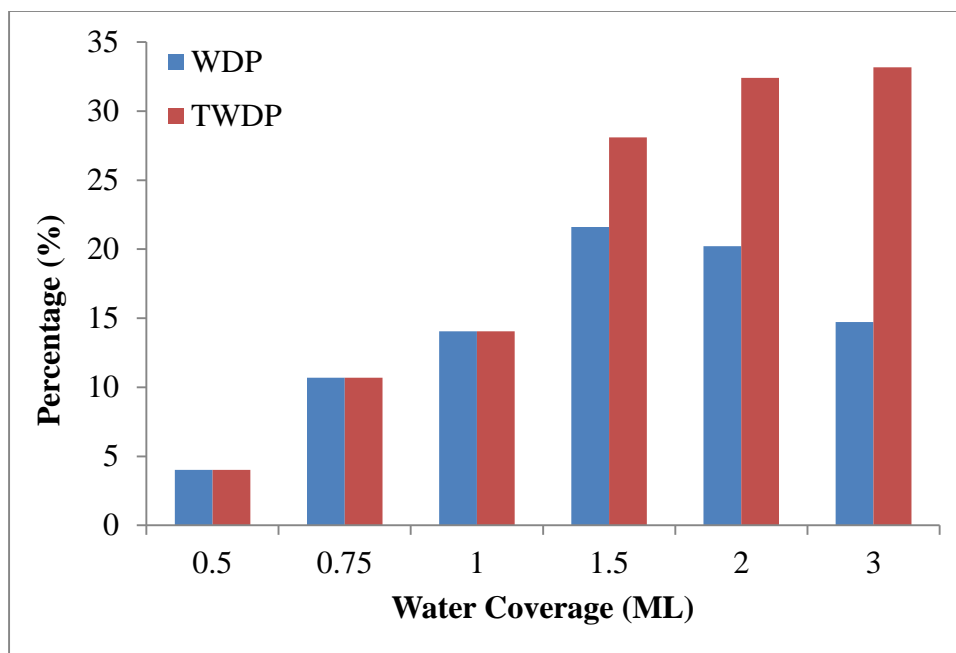


Figure 3.15. WDP and TWDP on anatase (100) as a function of water coverage.

iv. H₂O-Anatase(112)

The anatase (112) surface has a higher surface energy and reactivity than anatase (100), but is more stable than anatase (001). Anatase (112) twins form easily at surfaces and interfaces of nanocrystal aggregates⁸⁸ by the oriented attachment mechanism and it is observed that the anatase-to-rutile phase transformation is nucleated at these anatase (112) twin boundaries^{88, 89}. These interesting processes at the nanoscale regime involve the anatase (112) surface and so it is important to understand the behavior of water on this surface.

Previous theoretical studies^{30, 67} predict that water prefers to adsorb molecularly over anatase (112) at a coverage of 0.25 ML. Water adsorbs molecularly over the anatase (112) surface by binding to the surface Ti_{5c} atoms and the water hydrogens form hydrogen bonds with the bridging O_{2c} surface atoms, as shown in Figure 3.16. In dissociative adsorption, there is proton transfer to the bridging O_{2c} atoms in the adjacent row. To test the potential, we study water adsorption on a periodic (2 x 1) slab with four layers of titanium and dimensions 10.70 Å x 5.49

Å parallel to the surface and vacuum spacing of 15 Å. The dimensions were chosen to match those in previous DFT studies (PBE) by Gong and Selloni⁶⁷. The adsorption of one water molecule on this slab corresponds to a coverage of 0.25 ML. We calculate the adsorption energy E_a using the expression

$$E_a = E_{S+W} - E_S - E_W \quad , \quad (3)$$

where E_{S+W} is the energy of a slab with water adsorbed on it, E_S is the energy of the bare relaxed slab, and E_W is the energy of an isolated water molecule. The binding configuration predicted by our force field is given in Fig. 16 and is similar to that predicted by DFT studies⁶⁷. The values given by the ReaxFF reactive force field for the adsorption energy, the $\text{Ti}_{5c}\text{-O}_w$ distance and the $\text{H}_w\text{-O}_{2c}$ distance are 1.36 eV, 2.32 Å and 1.57 Å, respectively, and are in good agreement with the DFT values⁶⁷ of 1.18 eV, 2.13 Å and 1.57 Å, respectively. After structural optimization we subsequently performed a MD simulation in the NVT ensemble for 75 ps at a temperature of 300 K and found that the adsorbed water molecule remained in the same binding configuration without dissociating at this coverage (0.25 ML).

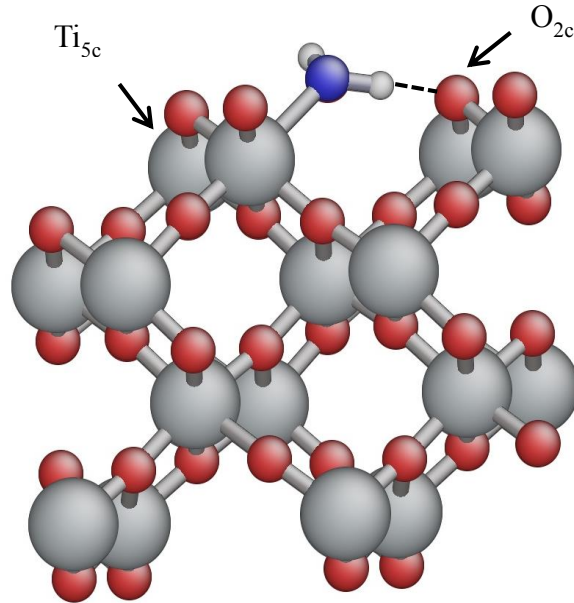


Figure 3.16. Molecular adsorption over anatase (112).

For the MD simulations at various water coverages, we used an anatase (112) slab with (9 x 9) unit cells parallel to the surface and 4 layers of TiO_2 . The dimensions of the periodic slab are 96.30 Å x 49.41 Å parallel to the surface with a vacuum spacing of 25 Å perpendicular to the surface. On anatase (112), water exhibits a mixed adsorption trend, with both molecular and dissociative adsorption, for all studied coverages from 0.5 to 3.0 ML. Figure 3.17(a) shows the water distribution over anatase (112) surface at 3.0 ML coverage.

Figure 3.17(b) gives the density plot of oxygen and titanium atoms in the simulation box during a 500-ps NVT simulation at 300K and indicates the structure of the first four layers of water adsorbed over anatase (112). On anatase (112), bridging O_{2c} atoms are located over the Ti_{5c} atoms and the surface is characterized by ‘V’ shaped ridges as seen in Figure 3.16 and Figure 3.17(a). The surface Ti_{5c} atoms bind with the water-oxygen atoms at an angle such that the $\text{Ti}_{5c}\text{-O}_w$ bond is not perpendicular to the surface. Thus, in the distribution $p(z)$ of the perpendicular distances of the water oxygen atoms from the plane containing the Ti_{5c} atoms we can see a peak at ~ 1.05 Å corresponding to the bridging oxygen atoms and a peak at ~ 1.45 Å (< Ti-O bond length) corresponding to the first layer of adsorbed water molecules. The second layer of adsorbed water molecules forms a network of hydrogen bonds with the bridging oxygens and this corresponds to the peak at 3.2 Å. Figure 3.17(c) gives the distribution $p(z)$ of the perpendicular distances of the water oxygen atoms from the plane containing the surface Ti_{5c} atoms.

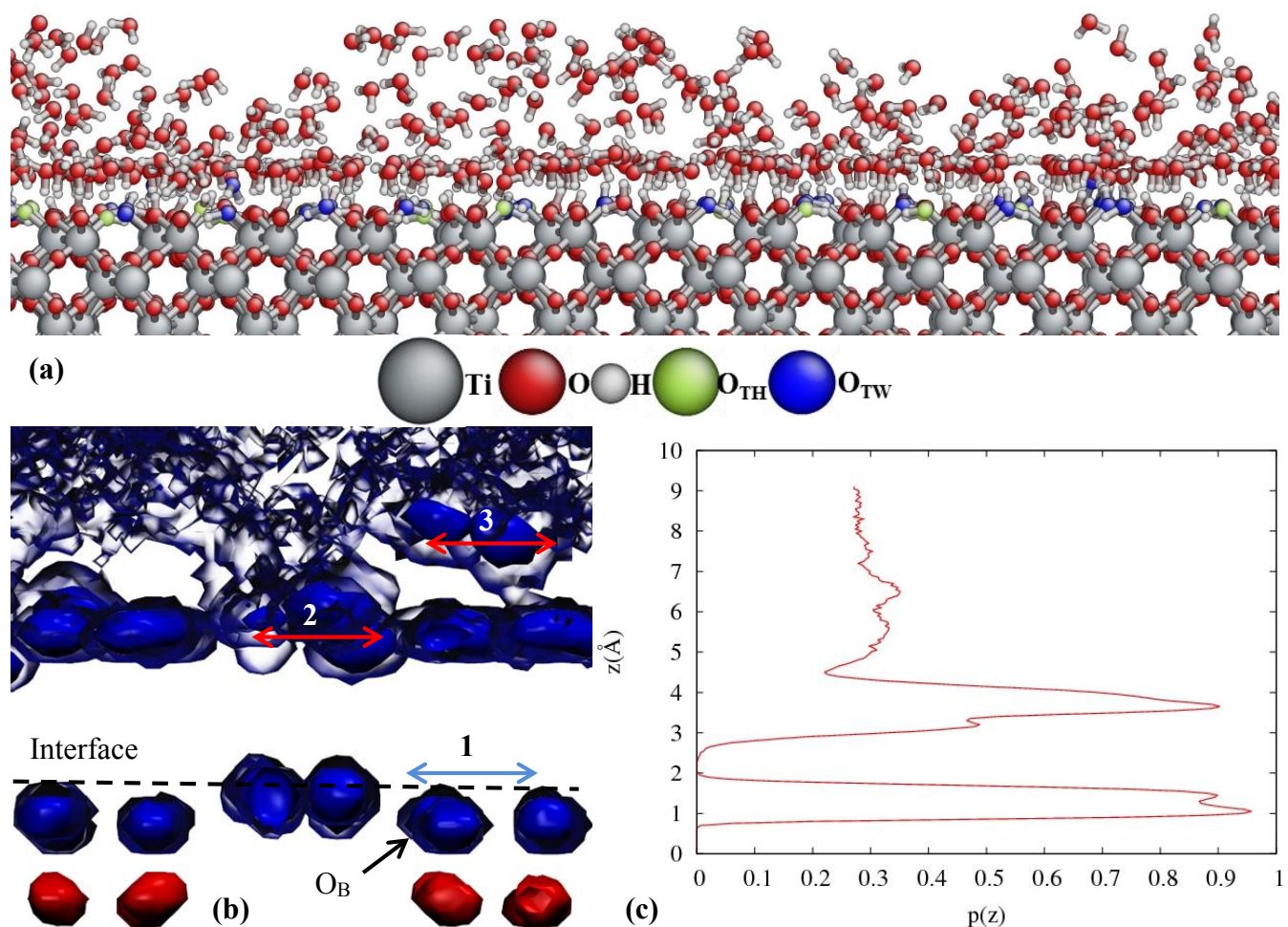


Figure 3.17. (a) Snapshot from an MD simulation of water on anatase (112) at 3.0 ML coverage; (b) Density plot of titanium (red) and oxygen (blue) atoms over anatase (112). The numbers and arrows indicate the heights of the n^{th} water layer; (c) Perpendicular distance of the water-oxygen atoms O_w from the plane containing the surface Ti_{sc} atoms on anatase (112).

Figure 3.18 gives the WDP and TWDP as function of coverage. We can see that over anatase (112), the TWDP increases with coverage. This observation is consistent with the behavior on other anatase surfaces investigated in this study and we can infer that the surrounding water molecules aid in the dissociation of terminal water molecules. The WDP increases until a water coverage of 1.0 ML and then decreases with increasing coverage because water in the second and third layers does not tend to be dissociated.

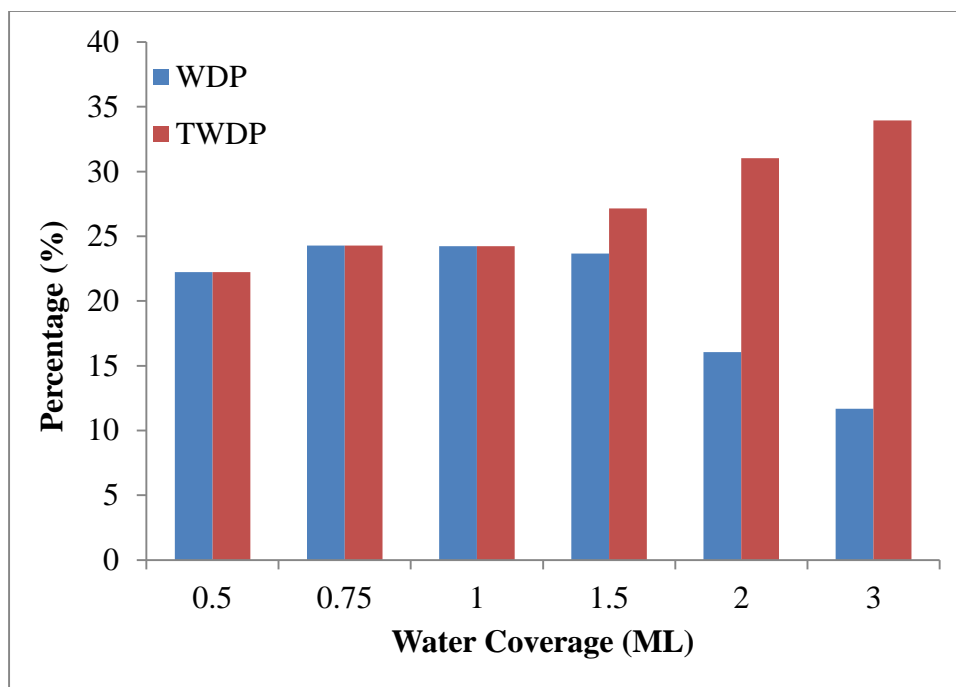


Figure 3.18. WDP and TWDP on anatase (112) as a function of water coverage.

v. H₂O-Rutile (110) interaction

Rutile (110) is the lowest-energy surface of rutile. This surface has been extensively studied both experimentally⁹⁰⁻⁹⁷ and theoretically⁹⁸⁻¹¹⁹ over the past several decades. The rutile (110) surface undergoes a (1 x 2) reconstruction under reducing conditions and various models have been suggested for this reconstruction based on theoretical and experimental studies⁶³. However, according to theoretical calculations and ultra-high vacuum based measurements, the rutile (110) surface in deionized water (DIW) at room temperature and one atmosphere pressure should not be reconstructed¹²⁰. Therefore, we consider the non-reconstructed rutile (110) (1x1) surface for studying the rutile (110)/water interface. In these simulations, we used a rutile (110) slab with (12 x 6) unit cells parallel to the surface and 4 layers of TiO₂. The dimensions of the simulation cell are 71.34 Å x 78.96 Å parallel to the surface and 25 Å in the direction perpendicular to the surface. Both molecular and dissociative adsorptions are observed on rutile (110). Figure 3.19(a) shows the water distribution over rutile (110) at 3.0 ML coverage. Here, we see that for

molecular adsorption, the water oxygen forms a dative bond with the surface Ti_{5c} atom and in a dissociation event there is a proton transfer between the terminal water molecule and the bridging oxygen. Water also adsorbs by hydrogen bonding to the surface O_{2c} atoms. This configuration is observed at low coverages and is less favorable at higher coverages.

The density plot of titanium atoms (red) and oxygen atoms (blue) in the simulation box during a 500-ps NVT simulation at 300 K is shown in Figure 3.19(b). We can see three distinct layers of adsorbed water-oxygens and the perpendicular distances of the water-oxygens from the plane containing the surface Ti_{5c} atoms is given in Figure 3.19(c). The perpendicular distribution of water-oxygens from the surface Ti_{5c} atoms has peaks at ~ 2.2 Å, ~ 3.65 Å, ~ 5.5 Å and a broad peak about ~ 8 Å. This is in good agreement with crystal truncation rod (CTR) studies by Zhang *et al.*^{119, 120} which gives the location of the first two peaks at 2.12 Å and 3.8 Å. MD studies by Predota *et al.*¹¹⁸ give the location of these peaks at ~ 2.2 Å, ~ 3.8 Å. For the third layer, they predict the peak position to be at ~ 4.8 Å for a surface with fully associated water and ~ 6 Å for a surface with fully dissociated water.

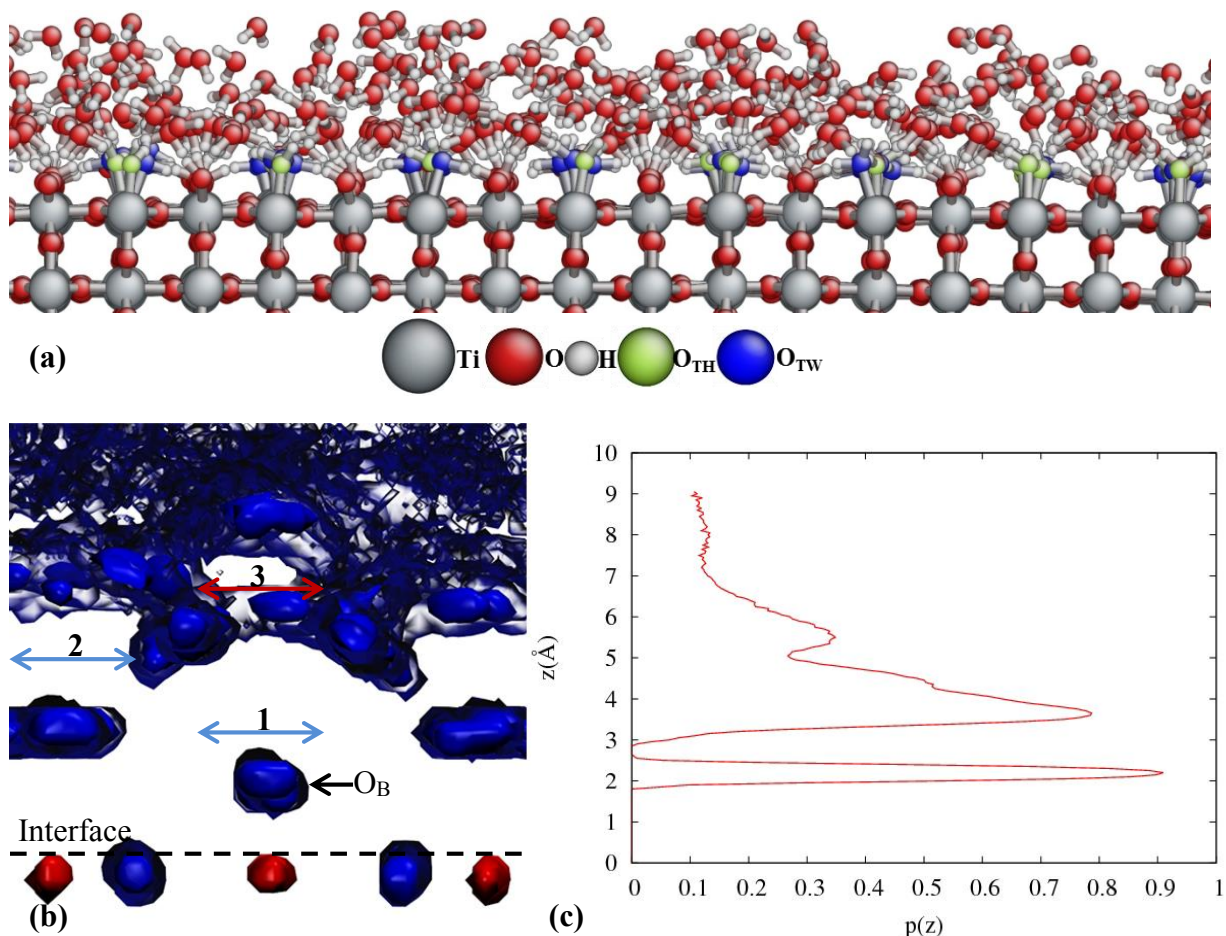


Figure 3.19. (a) Snapshot from an MD simulation of water on rutile (110) at 3.0 ML coverage; (b) Density plot of titanium (red) and oxygen (blue) atoms over rutile (110). The numbers and arrows indicate the heights of the n^{th} water layer; (c) Perpendicular distance of the water-oxygen atoms O_w from the plane containing the surface Ti_{5c} atoms on rutile (110).

Figure 3.20 shows the WDP and TWDP as a function of water coverage. The TWDP at 1 ML is $33.50 \pm 0.53\%$ and at 3 ML, it is $22.90 \pm 0.67\%$, in good agreement with DFT studies^{99, 121-123} which predict $\sim 33\%$ dissociation at 1 ML coverage and $\sim 25\%$ dissociation at 3 ML coverage. X-ray CTR studies by Zhang et.al^{119, 120} indicate a $30 \pm 15\%$ TWDP in deionized water, which is in the range predicted by our simulations. As the coverage increases the WDP decreases and this can be partly explained by the fact that as coverage increases the water in the higher layers does not contact the surface. However the interesting point to note is that the TWDP decreases, as well. This means that less water dissociates in the first layer closest to the surface. This behavior is in

contrast with the behavior on the anatase surfaces investigated in this study, where the TWDP increases with coverage.

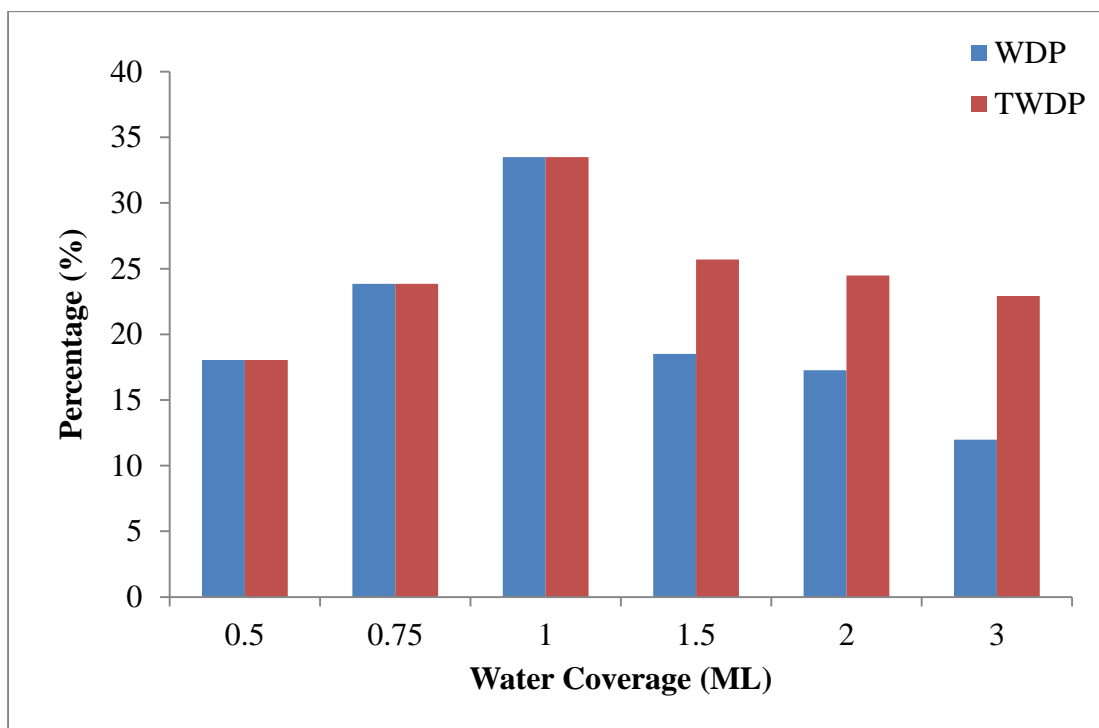


Figure 3.20. WDP and TWDP on rutile (110) surface as a function of water coverage.

The trend in the TWDP on rutile (110) is consistent with the previous *ab initio* MD simulations of Bandura *et al.*¹¹¹ and Kumar *et al.*^{99, 123} and can be explained as follows. At low coverages, terminal water molecules are stabilized by forming hydrogen bonds with bridging O_{2c} surface atoms or with neighboring adsorbed molecules, as shown in Figure 3.21(a). In a dissociation event at low coverages (<1 ML), there is a direct proton transfer between the terminal water molecule and a nearby surface bridging oxygen. At higher coverages (>1 ML), the terminal water molecule does not form a direct hydrogen bond with the bridging oxygen and is usually stabilized by forming hydrogen bonds with the surrounding water molecules above the adsorbed layer as shown in Figure 3.21(b). Thus, a dissociation event requires an indirect proton transfer between the terminal water and the bridging oxygen mediated by the water layer above the surface.

This indirect proton transfer involves at least two proton transfers, whose sequential occurrence is less likely than a direct proton transfer event at low coverages (<1 ML). DFT studies (PW91) by Bandura *et al.*¹¹¹ also report the absence of this indirect proton transfer on rutile (110). The obstruction of direct proton transfer from water to bridging oxygen and the decreased likelihood of indirect proton transfer mediated by water in the second layer at higher water coverages can explain the decrease in TWDP with water coverage on rutile (110). As we will discuss below, the absence of this indirect proton transfer over rutile (110) arises because of weak hydrogen bonding between waters in the first adsorbed layer and waters outside the adsorbed layer.

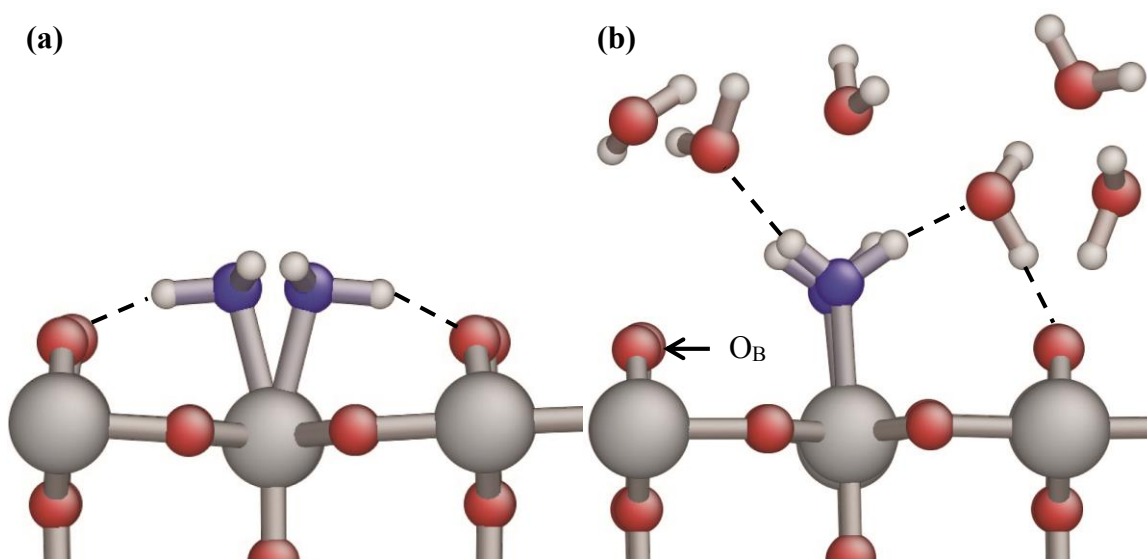


Figure 3.21. Snapshot from an MD simulation over rutile(110) at (a) 0.5 ML water coverage and (b) 2 ML water coverage.

Photoelectron spectroscopy studies by Sandell *et al.*⁹⁷ show both molecular and dissociative adsorption occur in a monolayer of water on rutile (110). This agrees with the mixed adsorption picture predicted by ReaxFF. Also Sandell *et al.* observed that on heating the sample, the OH coverage decreases due to desorption of water from the surface by the combination of a terminal hydroxyl group with a proton on the bridging oxygen. We performed MD simulations in the NVT ensemble for 500 ps at temperatures ranging from 100 K to 1500 K at regular intervals

of 200 K to obtain the terminal OH coverage at these temperatures. Figure 3.22 shows the terminal hydroxyl coverage as a function of temperature and we can see that the OH coverage increases and then decreases with temperature, as seen experimentally. The temperature at which the OH coverage begins to decrease is higher than is seen experimentally (210 K). This is likely because our heating rate is significantly faster than that in the experiments, so that water cannot recombine and desorb on the MD time scale at low temperatures. The temperature dependence of OH coverage on rutile (110) is qualitatively similar to that for anatase (101) (cf., Fig. 7).

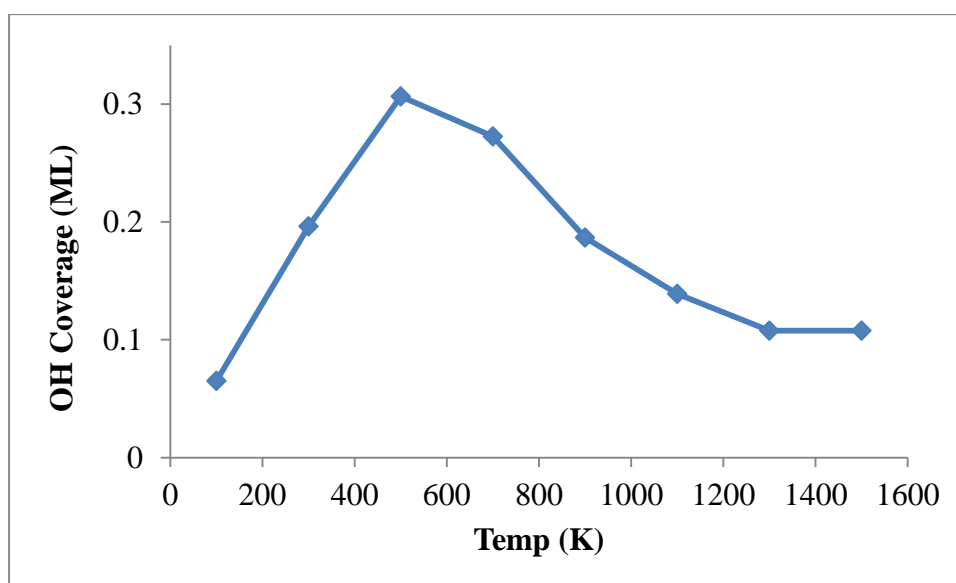


Figure 3.22. OH coverage (ML) on rutile (110) as a function of temperature.

Comparison of surface reactivities

Figure 3.23 show a comparison of the TWDP on the studied surfaces at 1 ML and 3 ML, respectively. The order of reactivity from low to high at 1 ML is anatase (101), anatase (100), anatase (112), anatase (001) and rutile (110). As the coverage increases to 3 ML, the reactivity of rutile (110) decreases and the order of reactivity from low to high is anatase (101), rutile (110), anatase (100), anatase (112), anatase (001). This change in reactivity of rutile (110) has been reported in previous DFT studies^{98, 99}. The order of reactivity follows the expected trend based on

surface energies and previous DFT studies. For the anatase surfaces the surface energy has the following trend anatase (101) < anatase (100) < anatase (112) < anatase (001),⁶⁸ which is seen in the TWDP, as well. Rutile (110) is the most stable rutile surface and has a low terminal water dissociation percentage.

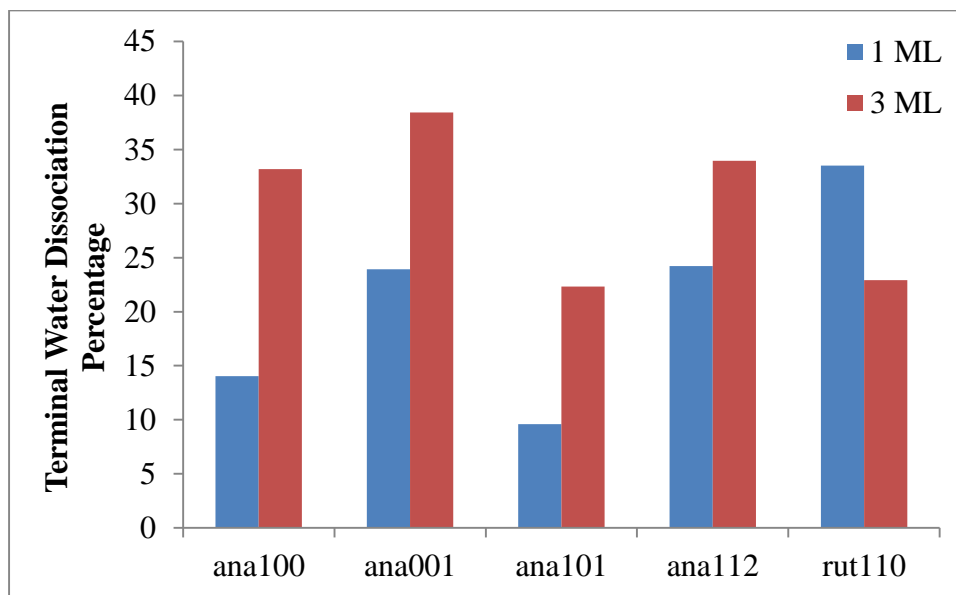


Figure 3.23. Comparison of TWDP on various titania surfaces at 1 ML and 3 ML water coverage.

Hydrogen bonds and water dissociation

Interestingly, the TWDP goes through a maximum with water coverage on rutile (110), whereas it increases with water coverage over all the studied anatase surfaces. To understand this contrasting behavior, we note that there are changes at the interfaces as water coverage increases. Below 1 ML water coverage, the distribution of water molecules at the surface is dominated by hydrogen bonding between the adsorbed water molecules and surface oxygens. As the water coverage increases to one ML and beyond, a hydration layer of structurally perturbed and dynamically hindered water molecules forms and covers the adsorbed water molecules. As a result, at water coverages greater than a monolayer, the dissociation state is a dynamic equilibrium dominated by hydrogen bonding between the adsorbed water molecules, the surface atoms, and

also this hydration layer. The strong attraction provided by hydrogen bonding weakens the O-H covalent bond in a water molecule and this paves the way to the dynamical process of water dissociation over these surfaces. Different surfaces of anatase and rutile have exposed oxygens in different bonding situations and three-dimensional arrangements and thereby can create hydrogen-bond networks of disparate configurations and strengths. To characterize the interaction of the hydration layer with adsorbed water molecules, we calculate the average number and average length of hydrogen bonds formed between the adsorbed layer of water molecules and water outside the adsorbed layer at 3 ML water coverage over all the studied surfaces. A hydrogen bond is considered to exist if the distance between the acceptor oxygen and hydrogen covalently bonded to a donor oxygen is less than 2.3 Å and the angle among the hydrogen, the donor oxygen, and the acceptor oxygen is less than 30°^{124, 125}. These quantities are given in

Table 3.1.

Surface	Anatase (101)	Anatase (100)	Anatase (112)	Anatase (001)	Rutile (110)
Number	1.64±0.06	1.19±0.07	1.11±0.03	1.96±0.05	0.95±0.02
Length	1.61±0.01	1.62±0.01	1.61±0.01	1.68±0.01	1.71±0.03

Table 3.1. Average number and length of hydrogen bonds between adsorbed water molecules and waters outside the adsorbed layer at 3 ML coverage.

For convenience, we designate the hydrogen atoms bridging the adsorbed layer and water outside the adsorbed layer as ‘HA hydrogen atoms’ and the hydrogen bonds formed by them as ‘HA hydrogen bonds’. As we see in

Table 3.1, the average number of HA hydrogen bonds formed is higher for the anatase surfaces than it is for rutile (110). MD studies by Kavathekar *et al.*¹²⁶ based on a non-reactive force field also report this striking difference in the average number of HA hydrogen bonds for rutile (110) (~0.91 Å) and anatase (101) (~1.59 Å). This arises because of the more open nature

of the anatase surfaces, which allows for greater hydrogen bonding contact of adsorbed water molecules with those outside the first layer. As seen in Figure 3.21, the rutile surface is characterized by bridging O_{2c} atoms rising over the plane of surface Ti atoms, which restricts hydrogen-bonding contact between adsorbed water molecules and water outside this adsorbed layer. DFT studies by Bandura *et al.*¹¹¹ also observed that over rutile (110) water in the second layer forms hydrogen bonds with the bridging O_{2c} atoms only and not with the terminal H_2O molecules.

From

Table 3.1 we also see that the average length of HA hydrogen bonds is the longest for rutile (110), implying weaker HA hydrogen bonds. The presence of stronger and higher numbers of HA hydrogen bonds is one of the reasons for the increase in the TWDP with water coverage over the anatase surfaces and the weak HA hydrogen bonds over rutile (110) can explain the decrease in TWDP with water coverage.

The differences in the strengths of the hydrogen bonds are reflected in their effects on the vibrational frequencies of the O-H bond. For an isolated water molecule, the vibrational frequency of the stretching mode is a well-defined peak at about 105 THz. In the liquid, hydrogen bonding with other water molecules provides a strong attraction force that weakens the covalent O-H bond and lowers the stretching-band frequency of the O-H bond. Stronger hydrogen bonds weaken the covalent O-H bond to a greater extent than weak hydrogen bonds and thereby lower the vibrational frequencies to a greater extent. By calculating the Fourier transform of the velocity autocorrelation function, we obtain the vibrational density of states (VDOS) of the systems studied here. To investigate the strengths of the hydrogen bonds between the adsorbed layer and waters outside the

adsorbed layer over the studied TiO₂ surfaces, we obtained the contribution of HA hydrogen atoms to the stretching band of the VDOS and these are shown in Figure 3.24.

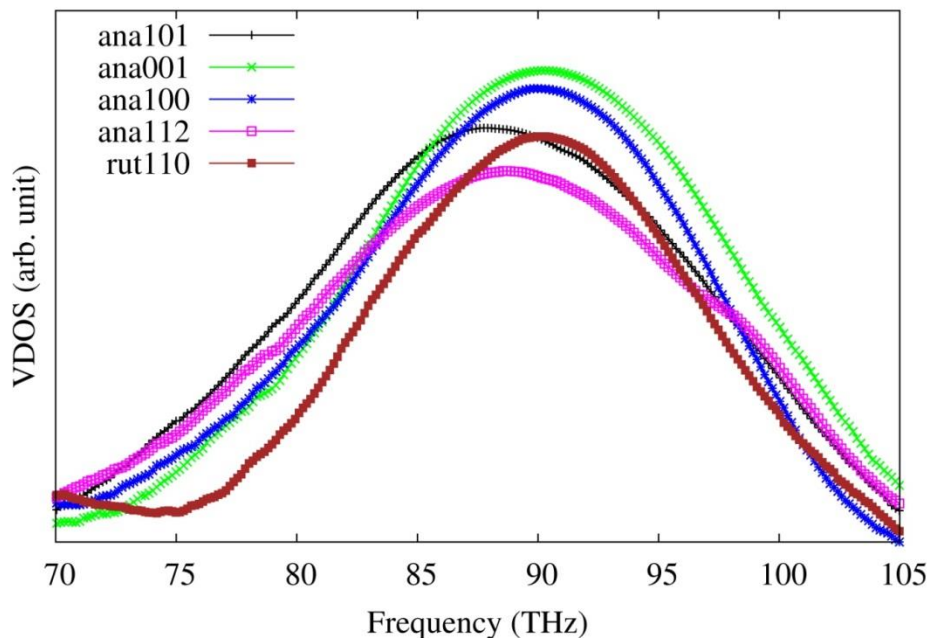


Figure 3.24. Contributions to the stretching band of the VDOS from HA hydrogen atoms. HA hydrogen atoms bridge the adsorbed layer and waters outside the adsorbed layer.

Inelastic neutron scattering (INS) studies by Levchenko *et al.*¹²⁷ show a broad band of the O-H stretching modes at 330-470 meV (~80-114 THz) for water adsorbed on anatase nanoparticles at 4 K and INS studies by Spencer *et al.*¹²⁸ show O-H stretching modes at 350-470 meV (~85-114 THz) for water adsorbed on rutile nanoparticles at 4 K. As we see in Figure 3.24, the O-H stretching modes obtained from our MD simulations fall in the same frequency range as the INS experiments. From Figure 3.23 we can see that the O-H vibrational frequency is red-shifted the least for rutile (110), indicating that rutile (110) contains the weakest HA hydrogen bonds. The presence of stronger HA hydrogen bonds over the anatase surfaces can explain the increase in the TWDP with water coverage over these surfaces. Together, Figure 3.24 and

Table 3.1 show a strong correlation between the acceptor-hydrogen distance and the vibrational frequency associated with that hydrogen bond. We thus demonstrate a correlation

between the strengths of HA hydrogen bonds and the variation of the TWDP over the studied TiO_2 surfaces. Deconvolution of the vibrational spectrum to contributions from different individual atoms can thus be a useful tool to analyze the hydrogen bond dynamics at the interface.

3.4 Summary and Conclusions

In summary, we tested the capability of the ReaxFF reactive force field to describe water binding and dissociation on relevant anatase [anatase (101), anatase (100), anatase (001), anatase (112)] and rutile (110) surfaces. We investigated water binding conformations (both molecular and dissociative) and water dissociation percentages on these surfaces for various coverages from 0.25 to 3.0 ML and find good agreement with experiments and previous DFT studies. The ability of the ReaxFF force field to accurately describe water dissociation and render this chemistry is desirable for some applications.

The force field predicts mixed molecular and dissociative adsorption on anatase (101), which is contrary to previous DFT studies, but in agreement with recent photoelectron spectroscopy experiments. For all the surfaces, we find that water has a well-defined structure close to the surface and this is evident from the density plots given above. The perpendicular distribution of water oxygens and surface Ti_{5c} atoms was in good agreement with previous DFT studies. The ReaxFF reactive force field is able to reproduce the variation of OH coverage on anatase (101) and rutile (110) surfaces with temperature, the formation of (2 x 2) overlayer structure on anatase (101) at low coverages, and water dissociation on the reconstructed anatase (001) (1 x 4) surface in good agreement with experimental results.

Interestingly, we find that water in the hydration layer immediately adjacent to the adsorbed water layer enhances water dissociation on the studied anatase surfaces, such that the TWDP increases with water coverage. In contrast, the TWDP goes through a maximum with water

coverage over rutile (110). Stronger hydrogen bonding between the adsorbed water layer and the hydration layer covering this adsorbed layer can account for the increase in TWDP with water coverage over the anatase surfaces. Thus the ReaxFF reactive force field is robust in being able to describe water binding and dissociation on various titania surfaces for a range of water coverages and temperatures and is therefore suitable for large-scale simulation of TiO_2 -water interfaces.

4 Mechanisms of Oriented Attachment of TiO₂ Nanocrystals in Vacuum and Humid Environments: Reactive Molecular Dynamics

4.1 Introduction

The ability to direct and control crystal growth by the oriented attachment (OA) mechanism, whereby nanocrystals interact and aggregate along specific crystallographic directions to form single- or twinned-crystal structures, is an exciting prospect that could allow the design and synthesis of hierarchical nanocrystal structures for functional devices. Crystallization by aggregation and coalescence of nanocrystal occurs frequently in natural processes as applied by organisms during biomineralization^{129, 130}, in morphosynthesis of biomimetic inorganic materials¹³¹ and in controlled synthesis of nanocrystals and nanowires¹³²⁻¹³⁵. Remarkably, growth by OA occurs in wide variety of organic and inorganic materials exhibiting diverse particle morphologies including spheres^{135, 136}, ellipsoids¹³⁷, cubes¹³², platelets^{138, 139}, wires¹⁴⁰, and hybrids¹⁴¹, resulting in complex architectures ranging from quasi-one dimensional nanowires and nanorods to hierarchical two- or three-dimensional superstructures^{142, 143}. However, the origins and mechanisms of OA remain unresolved. Atomic-scale investigations with molecular dynamics (MD) simulations could contribute significantly to understanding growth by OA and furnish many details of this mechanism that are not accessible experimentally.

OA was first observed by Penn and Banfield¹⁴⁴ in nanocrystalline anatase synthesized under hydrothermal conditions via the sol-gel method. In the case of hydrothermally coarsened anatase, the nanocrystals assemble into twinned or single-crystalline structures composed of several primary crystallites, suggesting a sequence of whole-particle alignment followed by interface elimination. In colloidal systems, OA could originate from intrinsic interactions between nanocrystals, such as dipole-dipole interactions, solvent-mediated interactions, such as selective

adsorption and surface chemistry of liquid-phase molecules at the nanocrystal-liquid interface, or a combination of the two. By studying the aggregation in both vacuum and aqueous environments, we can isolate the roles of intrinsic forces between the nanocrystals and those mediated by the solvent and, thus, clarify the pathway by which OA occurs.

4.2 Computational Methods

Reactive force-field methods, such as ReaxFF, can simulate chemical reactions with higher efficiencies than *ab initio* MD, making them a suitable choice to model nanometer-sized particles in solvent. Here we employ the recently developed Ti/O/H ReaxFF parameter set, as described in Kim *et al.*¹⁴⁵ and as recently applied to describe the glycine/TiO₂ interface by Monti *et al.*⁴¹ and to various water/TiO₂ interfaces by Raju *et al.*¹⁴⁶. This force field was fit to a large, density functional theory (DFT) based, training set, including equations of state for bulk anatase, rutile, brookite and higher-energy TiO₂ crystals, as well as surface energies and water-dissociation energy barriers. As described in more detail in Kim *et al.*¹⁴⁶ and Raju *et al.*¹⁴⁶, this force field was validated by comparisons to DFT/MD simulations and experimental results on water-dissociation reactions on various anatase and rutile surfaces of titania. This force field uses the same general and O/H ReaxFF parameters as employed in a number of previous ReaxFF descriptions¹⁴⁶, including proteins, alcohols and organic acids, inorganic acids, phosphates, zinc-oxides, iron-oxides, copper-oxides, aluminium, silica and aluminosilicates, thus allowing straightforward transferability to multicomponent liquids and mixed metal-oxide materials.

The O/H ReaxFF parameters used in this study were trained against a substantial DFT-based training set containing, among others, water binding energy for clusters containing 2–35 water molecules, bond dissociation energies in H₂O, O₂, and H₂, concerted proton transfer barriers in [H₂O]_x clusters ($x = 2-6$), proton transfer reactions in OH⁻/H₂O and H₃O⁺/H₂O clusters, H–O–

H and H–O–OH angular distortions, H₂O monomer and dimer vibrational frequencies, and equations of state for various ice crystals. A detailed discussion on the development, fitting and validation of the Ti–O–H ReaxFF parameters is available in Kim *et al.*¹⁴⁵ and detailed descriptions of the ReaxFF potential functions are available in van Duin *et al.*¹ and Russo *et al.*¹⁴⁷. As reported in Raju *et al.*¹⁴⁶ the Ti/O/H ReaxFF reactive force field describes water binding conformations (both molecular and dissociative), water dissociation percentages, and structure of adsorbed water layers on various surfaces of titania [anatase (101), (100), (112), (001) and rutile (110)] in good agreement with experiments and DFT studies. The force field also describes the variation of OH coverage on anatase (101) and rutile (110) surfaces with temperature, the formation of (2 x 2) overlayer structure on anatase (101) at low coverages, and water dissociation on the reconstructed anatase (001) (1 x 4) surface in good agreement with experimental studies¹⁴⁶. ReaxFF incorporates a bond-order dependent hydrogen bond term and as reported in Raju *et al.*¹⁴⁶, the Ti/O/H force field reproduces the hydrogen bond distribution over various surfaces of titania in agreement with previous theoretical studies and also reproduces the vibrational density of states (VDOS) for these systems in agreement with inelastic neutron scattering (INS) studies.

Nanocrystalline anatase has been experimentally observed to possess a tetragonal bipyramidal morphology down to sizes of 3-5 nm¹³⁴. Indeed, density-functional theory (DFT) calculations predict that anatase nanocrystals have this tetragonal bipyramidal shape, as given by the standard Wulff construction¹⁴⁸. We consider symmetric, charge-neutral, Wulff-shaped anatase nanocrystals of two different sizes: large nanocrystals containing 2691 Ti and O atoms and small nanocrystals consisting of 840 atoms. As shown in **Error! Reference source not found.a-b**, Wulff-shaped anatase crystals have two surfaces exposed to vacuum: the {101} and {001} surfaces. In addition to Wulff shapes, we consider three asymmetric nanocrystals shown in **Error!**

Reference source not found.c-e, which mimic possible off-Wulff shapes that could occur during crystal growth.

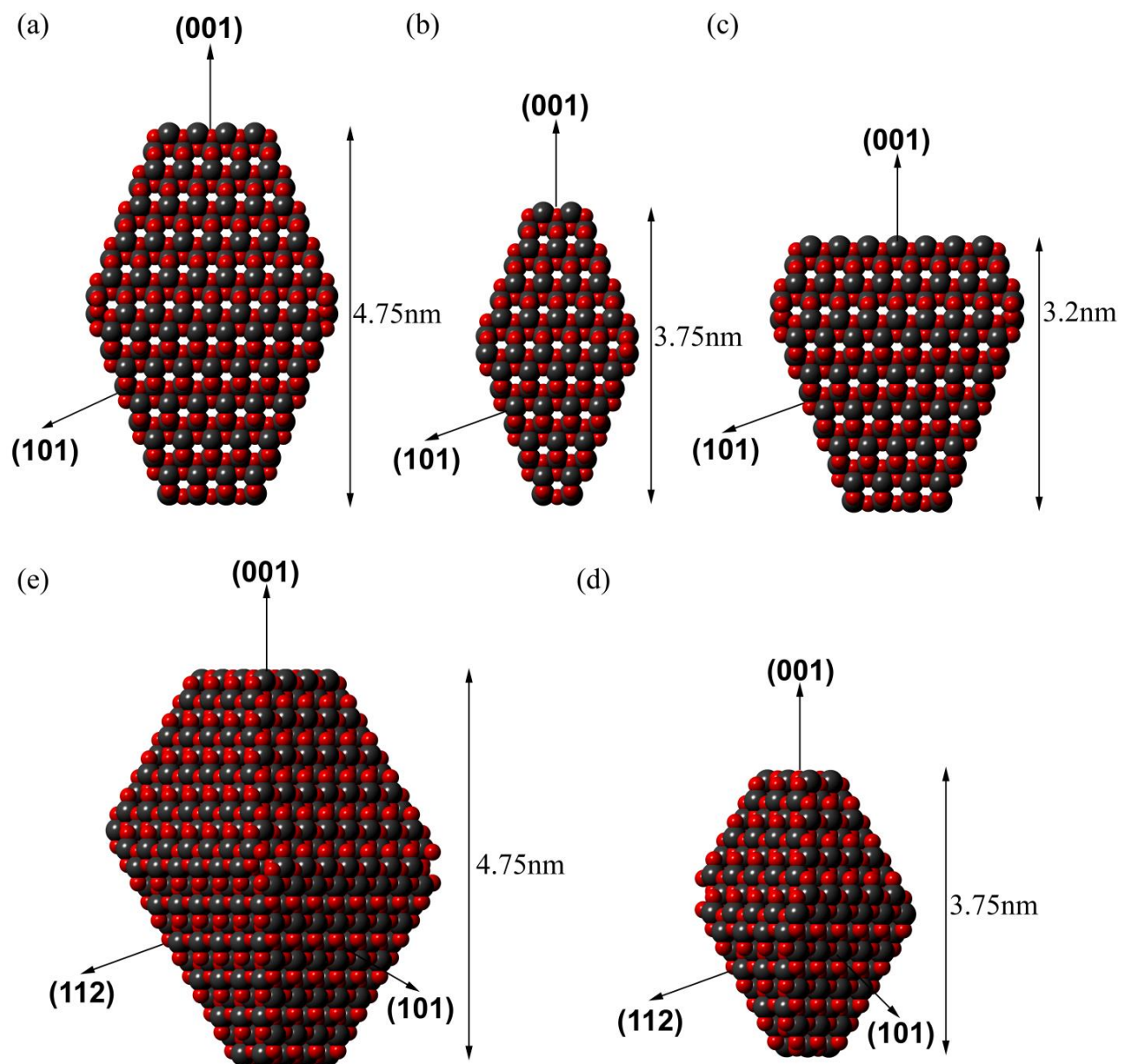


Figure 4.1. Equilibrated structures of the large (a) and small (b) symmetric anatase nanoparticles with Wulff shapes, a large nanoparticle that is truncated on the $\{001\}$ facet (c), and two nanoparticles that are truncated on the $\{112\}$ facet (d and e).

We replicated the equilibrated nanocrystals and placed eight nanocrystals in a simulation cell with dimensions of 125 Å x 325 Å x 125 Å in different initial configurations corresponding to various center-of-mass separations and orientations relative to one another. In this way, we allow for the possibility that many-body interactions could influence nanoparticle aggregation – although our observations indicate that OA is mediated by nanocrystal-pair interactions. Initially the crystals were at least 30 Å apart, so they could rotate freely without touching each other. We simulated the system in the canonical (NVT) ensemble at 573 K, to correspond to the temperature in experimental studies¹³⁴. The total simulation time ranged from 1.0 - 2.0 ns, which is long enough to observe the approach and aggregation of the nanocrystals. A typical simulation box contains ~15000-18000 atoms and the simulations were run as parallel, eight-processor jobs using the ReaxFF reactive force field implementation in the ADF computational chemistry package⁵⁷.

4.3 Results and Discussion

We do not observe aggregation by OA in vacuum, consistent with the results of Alimohammadi and Fichthorn¹⁴⁹. The aggregation of nanocrystals in **Error! Reference source not found.** is representative of the aggregation mechanism observed in vacuum. In vacuum, absence of adsorbed surface species allows the nanocrystals to aggregate along their direction of approach (**Error! Reference source not found.**).

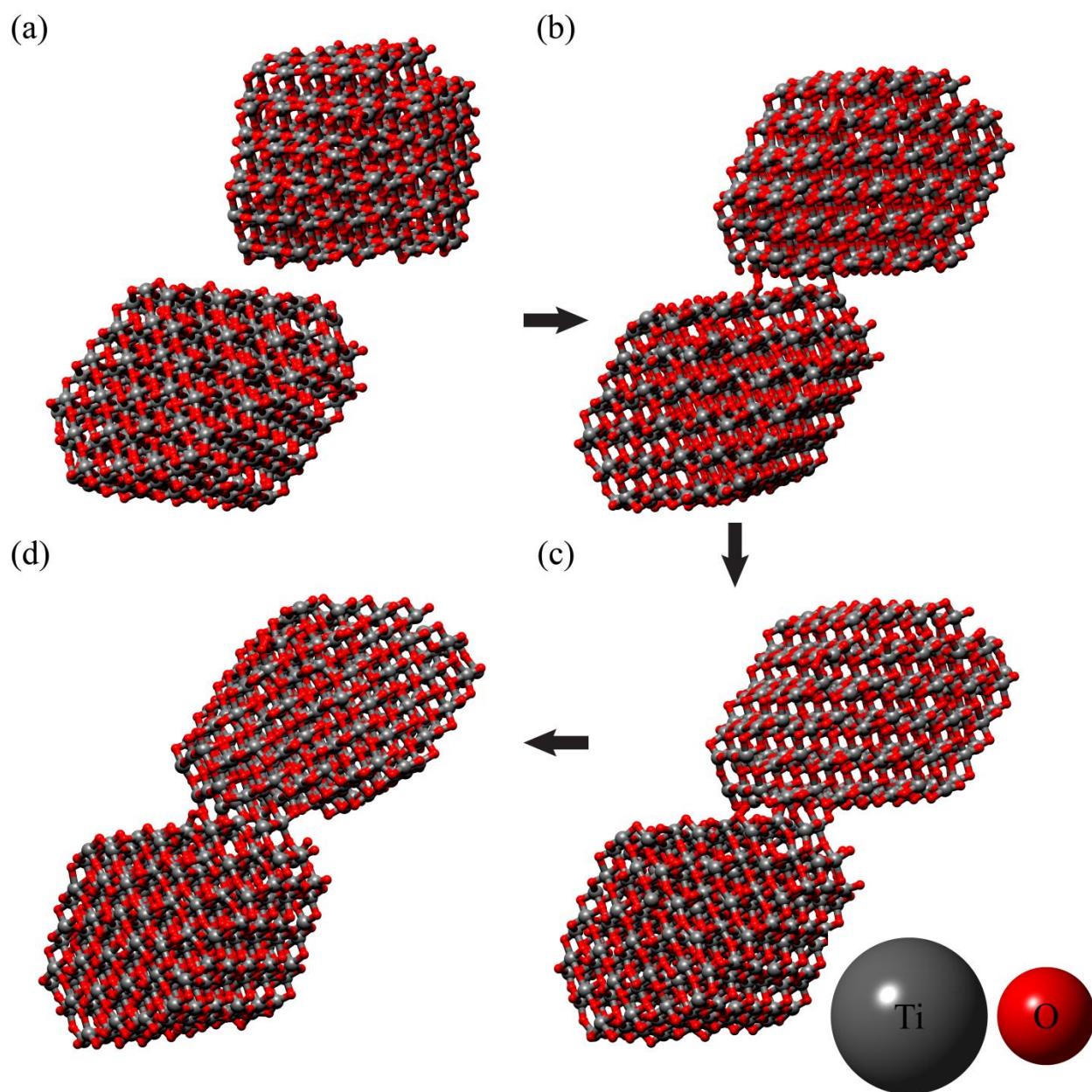


Figure 4.2. Snapshots of the aggregation of anatase nanocrystals in vacuum. These snapshots were taken at (a) 255 ps; (b) 260 ps; (c) 265 ps and; (d) 270 ps.

The absence of OA in vacuum led us to hypothesize that water mediates growth by OA through adsorbed surface groups: molecularly or dissociatively adsorbed water, in this case. Because MD simulations of nanocrystals at hydrothermal conditions are prohibitively slow, our aim was to achieve an aqueous environment, representative of bulk water, within the interparticle

gap at close proximities. We, thus, investigated the amount of water needed to saturate the nanocrystal surfaces with hydroxyl groups at a temperature of 573 K, to correspond to the temperature in experimental studies¹³⁴. We found that the hydroxyl coverage on the nanoparticle surfaces saturates when the total number of water molecules corresponds to 5 ML of water coverage on all the nanoparticle surfaces at 573 K (**Error! Reference source not found.**). Thus, we performed MD simulations in the NVT ensemble at this coverage and a temperature of 573 K. By simulating nanocrystals in water vapor, we facilitate their fast diffusion as they approach one another and we aim to capture their (water-mediated) interactions at sub-nanometer separations, where just a few water layers reside in the inter-particle gap. It is observed experimentally^{150, 151} [also see below in Figure 4.6(c)] that nanoparticles associate at these close separations before aggregating, so that our simulations may describe this associated state and subsequent aggregation.

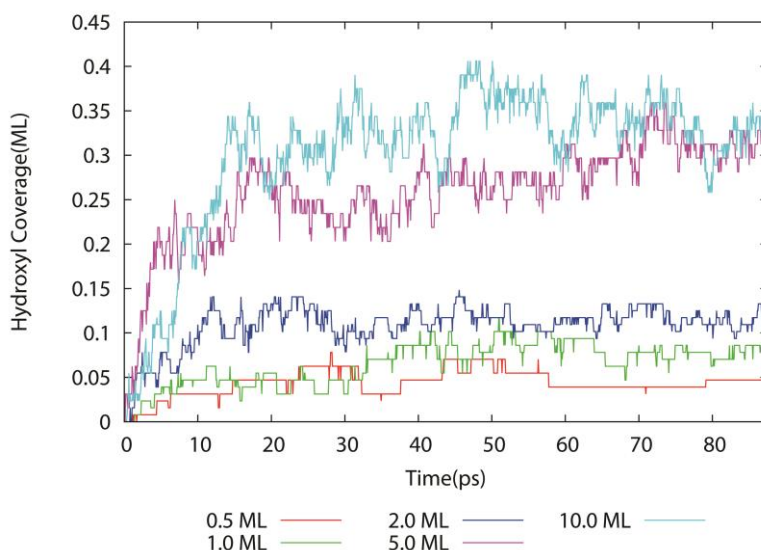


Figure 4.3. Hydroxyl coverage over the anatase nanocrystal in **Error! Reference source not found.**(a) as a function of water coverage at 573 K.

We observe numerous instances of OA in simulations including water. We find that water plays multiple roles in mediating OA, which is a two-step process consisting of the initial alignment of nanocrystals, followed by their coalescence to form a single or twinned crystal.

Figure 4.4 shows a typical initial approach of two nanocrystals in water. Here, the presence of adsorbed surface species (molecularly and dissociatively adsorbed water) prevents immediate aggregation of the nanocrystals (

Figure **4.4**. Snapshots of the initial approach of anatase nanocrystals in water. These snapshots were taken at (a) 187.5 ps; (b) 205 ps; (c) 212.5 ps and; (d) 225 ps.

4). This starkly contrasts their behavior in vacuum (cf., **Error! Reference source not found.**). The approaching nanocrystals, which are initially at least 30 Å apart, associate at separations of ~5 Å. At these close separations, they interact via the first and second water layers adsorbed on their surfaces. As shown in Figure 4.5 and Figure **4.6**, we have dense water coverage in the inter-particle gap at these separations.

Once in close vicinity, the nanocrystals continuously diffuse and rotate relative to each other, making transient contacts at many points until they fall into alignment (Figure 4.5). In all the trajectories, the nanocrystals interact in close proximity for significant periods of time and explore multiple configurations before alignment occurs. When the nanocrystals align, their separation reduces to ~2.8 Å and they are separated by the first water layer adsorbed on their surfaces. When they achieve alignment, the nanocrystals remain aligned until coalescence is initiated at a contact point.

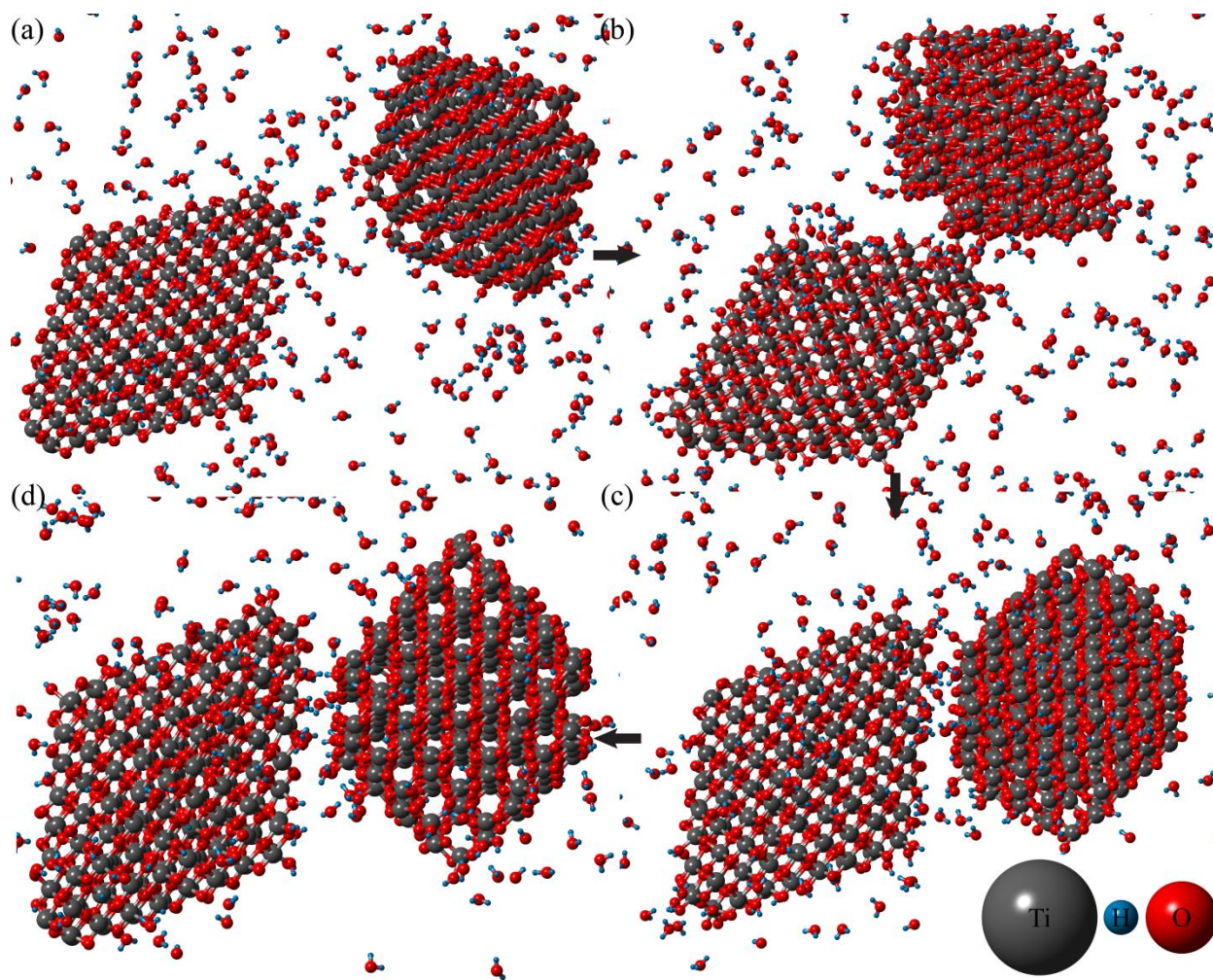


Figure 4.4. Snapshots of the initial approach of anatase nanocrystals in water. These snapshots were taken at (a) 187.5 ps; (b) 205 ps; (c) 212.5 ps and; (d) 225 ps.

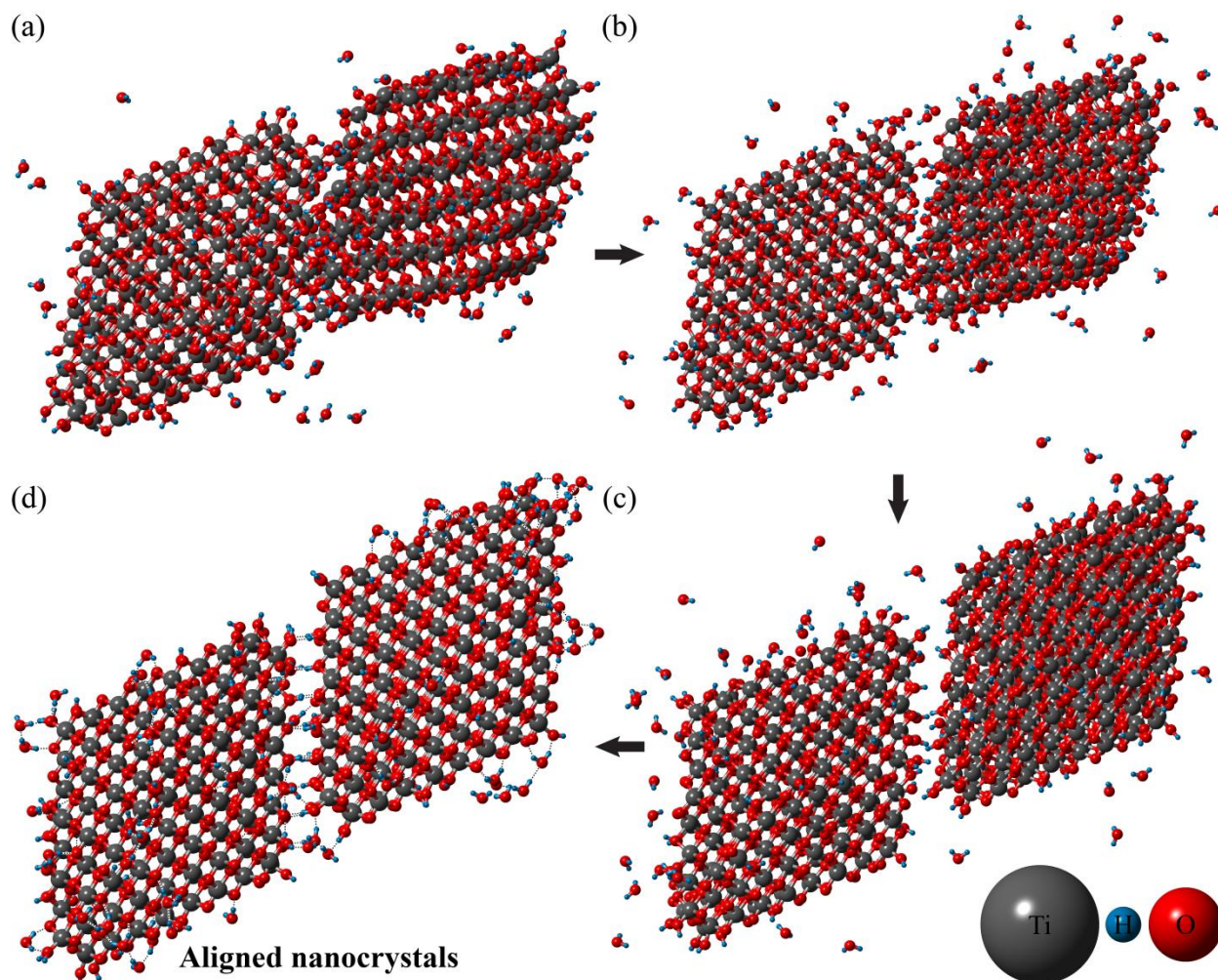


Figure 4.5. Snapshots of the alignment of anatase nanocrystals on $\{112\}$ facets in water. These snapshots were taken at (a) 275 ps; (b) 300 ps; (c) 350 ps and; (d) 375 ps.

To understand the origins of the alignment mechanism, we studied the interface between various aligned nanocrystals. Figure 4.6(a) shows the interface between two nanocrystals aligned on $\{112\}$ facets. The area between the aligned nanocrystals is characterized by a network of hydrogen bonds between the bridging or terminal hydroxyls on one nanoparticle and the surface oxygens of the other nanoparticle. Water, thus, mediates the alignment of the nanocrystals along specific crystallographic directions through the formation of inter-particle hydrogen bonds. This network of hydrogen bonds provides the long-range ordering necessary to bring and hold the nanocrystals in alignment and is formed when the nanocrystals align along a specific

crystallographic direction. This hydrogen-bonding-mediated, long-range ordering of anatase nanocrystals can be likened to the structure of DNA, in which two strands of DNA are held together by hydrogen bonds that occur between complementary nucleotide base pairs. This illustrates how weak bonds, such as hydrogen bonds, can play a major role in the structure and stability of natural systems. The interface is devoid of associatively adsorbed water molecules and contains only hydroxyls and as discussed later has implications on which surfaces have propensity to exhibit OA. The interface in **Figure 4.6(a)** consists of 30 hydrogen bonds with an average hydrogen bond length of 1.70 Å, providing a total binding energy of 3.70 eV. **Figure 4.6(c)** is a transmission electron microscopy (TEM) image of wet SnO₂ nanocrystals¹⁵², which have a crystal structure similar to TiO₂. Here, we see that aligned SnO₂ nanocrystals are separated by spacing of the order of 1-2 lattice constants, which is consistent with the observation from our simulations that aligned nanocrystals are separated by a network of inter-particle hydrogen bonds. We also note that recent cryogenic TEM experiments by Yuwano *et al.*¹⁵⁰ suggest that the growth of goethite nanowires in water via OA is preceded by ferrihydrite mesocrystals, or aligned crystallites with water in the inter-particle gap.

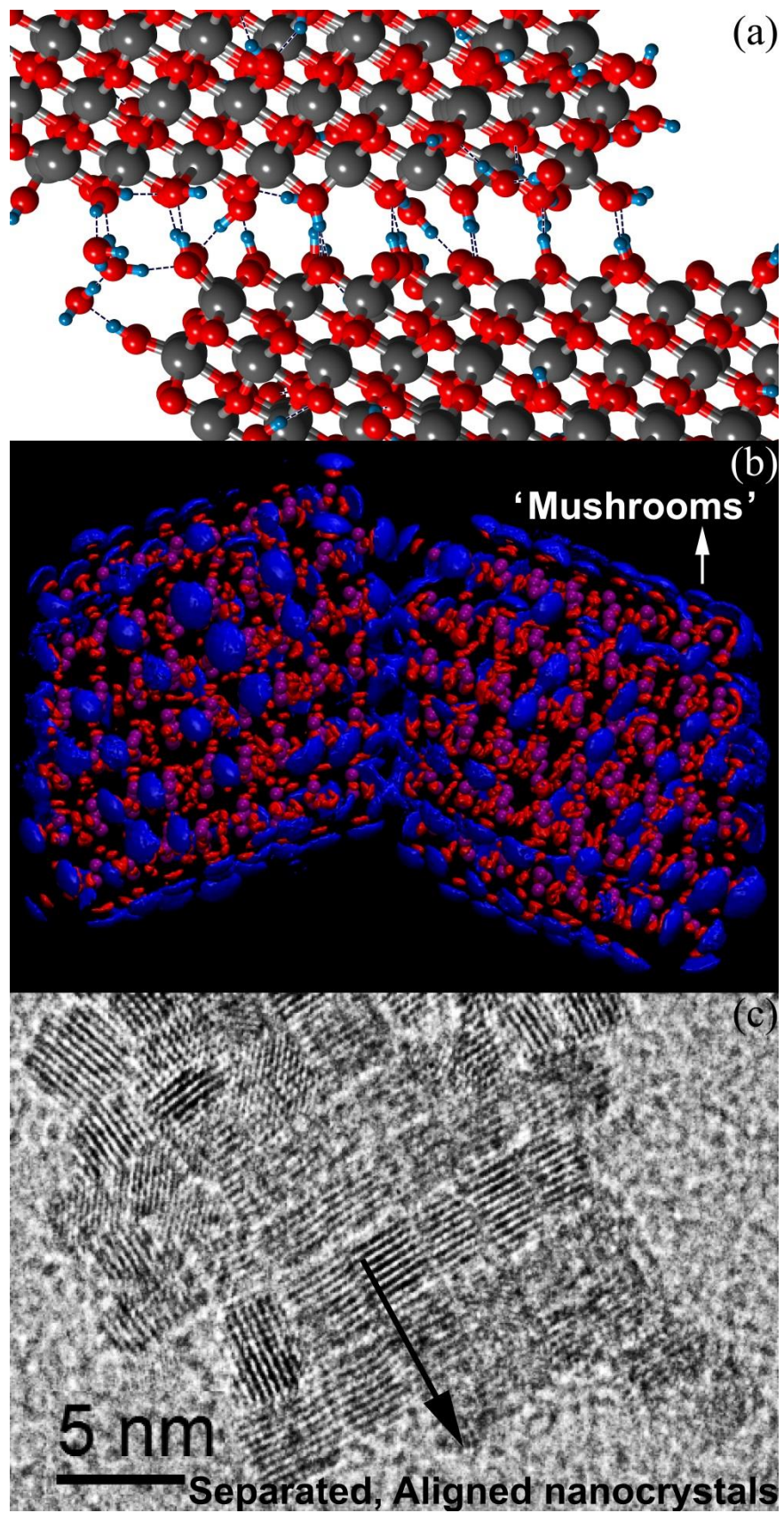


Figure 4.6. (a) Network of hydrogen bonds between anatase nanocrystals aligned on {112} facets. The hydrogen-bond network is formed between terminal hydroxyls (in which a hydroxyl from a dissociated water binds to an under-coordinated Ti atom at the surface) or bridging hydroxyls (in which a hydrogen from a dissociated water binds to a bridging, two-fold coordinated surface oxygen) on one nanocrystal and surface oxygens of the adjacent nanocrystal. (b) Density plot of hydrogen (blue) and oxygen (red) atoms in Figure 3(a) obtained as an average over a time period of 250 ps. (c) TEM image of wet SnO₂ nanocrystals. For synthesis and characterization please refer to Wang *et al*¹⁵².

Analysis of particle motion leading to alignment shows that the translational speed increases as the particles approach one another and decreases once they align. For example, at center-of-mass separations greater than 30 Å, the nanocrystals in **Figure 4.6(a)** diffuse with a relatively constant translational speed of 0.35 Å/ps. However, within center-of-mass separations of 25 Å, the translational component increases to 0.7 Å/ps as they explore different configurations and later decreases to 0.3 Å/ps after alignment (**Error! Reference source not found.**). This is in agreement with experimental observations indicating that translational speeds of the nanocrystals increase by 2-3 times as they approach each other^{151, 153}. The higher speeds in our simulations compared to those in experiment arise from the low water density in our simulations, which allows us to observe nanocrystal aggregation over the MD time scale. Figure 4.6(b) shows the density plot of hydrogen (blue) and oxygen (red) atoms in Figure 4.6(a), which was obtained as an average over a time period of 250 ps. Away from the inter-particle gap, the density of the adsorbed hydrogen atoms forms mushroom-shaped regions as they explore localized areas on the particle surfaces. However, in the area between the aligned nanocrystals, the mushroom-shaped regions crisscross, indicating that the nanocrystals continuously exchange hydrogens at the particle-particle interface. The inter-particle region is dynamic, with hydrogen transfers between various surface groups (bridging hydroxyls, terminal hydroxyls and bridging oxygens) and this paves way for the aggregation of nanocrystals through expulsion of inter-particle hydroxyls by regenerating water.

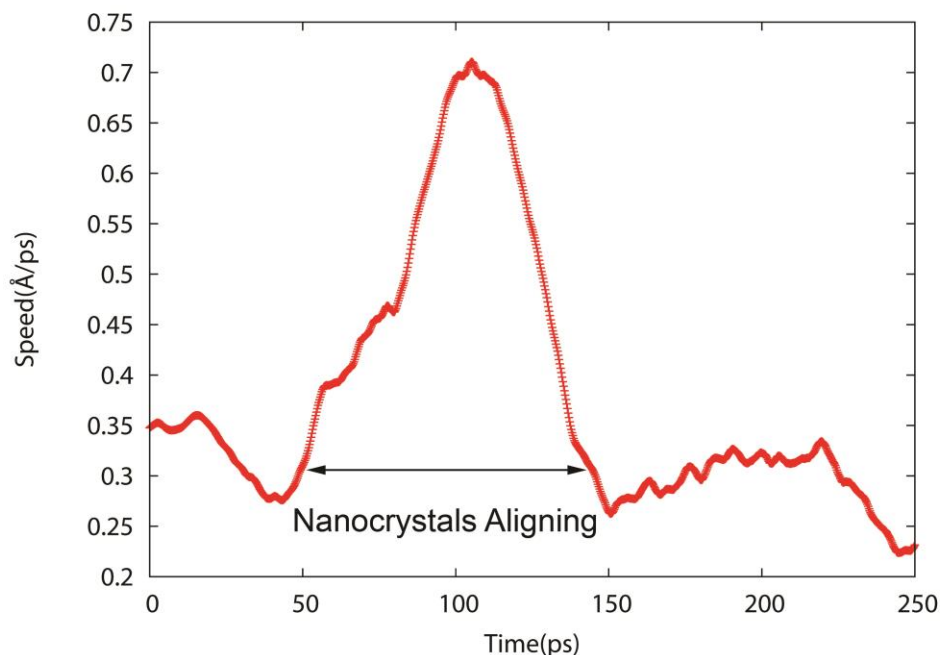


Figure 4.7. Translational speeds leading up to the alignment of the anatase nanoparticles in Figure 4.5

Once aligned, the nanocrystals stay in alignment and the inter-particle region is static with respect to the relative orientation of the nanocrystals. The dynamics at this interface can be reduced to hydrogen transfers between the various surface groups and the surrounding water. Aggregation occurs when surface hydroxyls combine with protons and evacuate the interparticle gap as water, leaving bare TiO_2 surfaces to associate. The time scale over which all the inter-particle surface hydroxyls desorb as water by recombining with protons is not accessible in our MD simulations at temperatures of 573 K. Thus, we ran NVT simulations at 1100 K to accelerate the kinetics of proton transfer for aligned nanocrystals. At these elevated temperatures, we observe aggregation of the aligned nanocrystals. The aggregation initiates at a contact point and proceeds rapidly in a zipper-like fashion, closing down the inter-particle gap (Figure 4.8). The aggregation mechanism shown in Figure 4.8 is representative of the aggregation mechanism observed in water. The nanocrystals in Figure 4.8 stay in alignment for 250 ps until aggregation is initiated at a contact

point, after which aggregation proceeds rapidly, finishing in 40 ps. Although we consider nanocrystals in vapor, we note that surrounding water molecules can play an important role in aggregation. In previous theoretical studies,^{99, 146} it was observed that water in higher layers can assist in the dissociation of water adsorbed on titania surfaces by mediating proton transfer. It is thus conceivable that surrounding water molecules could facilitate the proton-hydroxyl recombination reaction that proceeds prior to nanoparticle aggregation. Additionally, water surrounding the nanocrystals could stabilize ejected water molecules through hydrogen bonding. The observed aggregation mechanism can therefore be expected to take place in bulk water, as well.

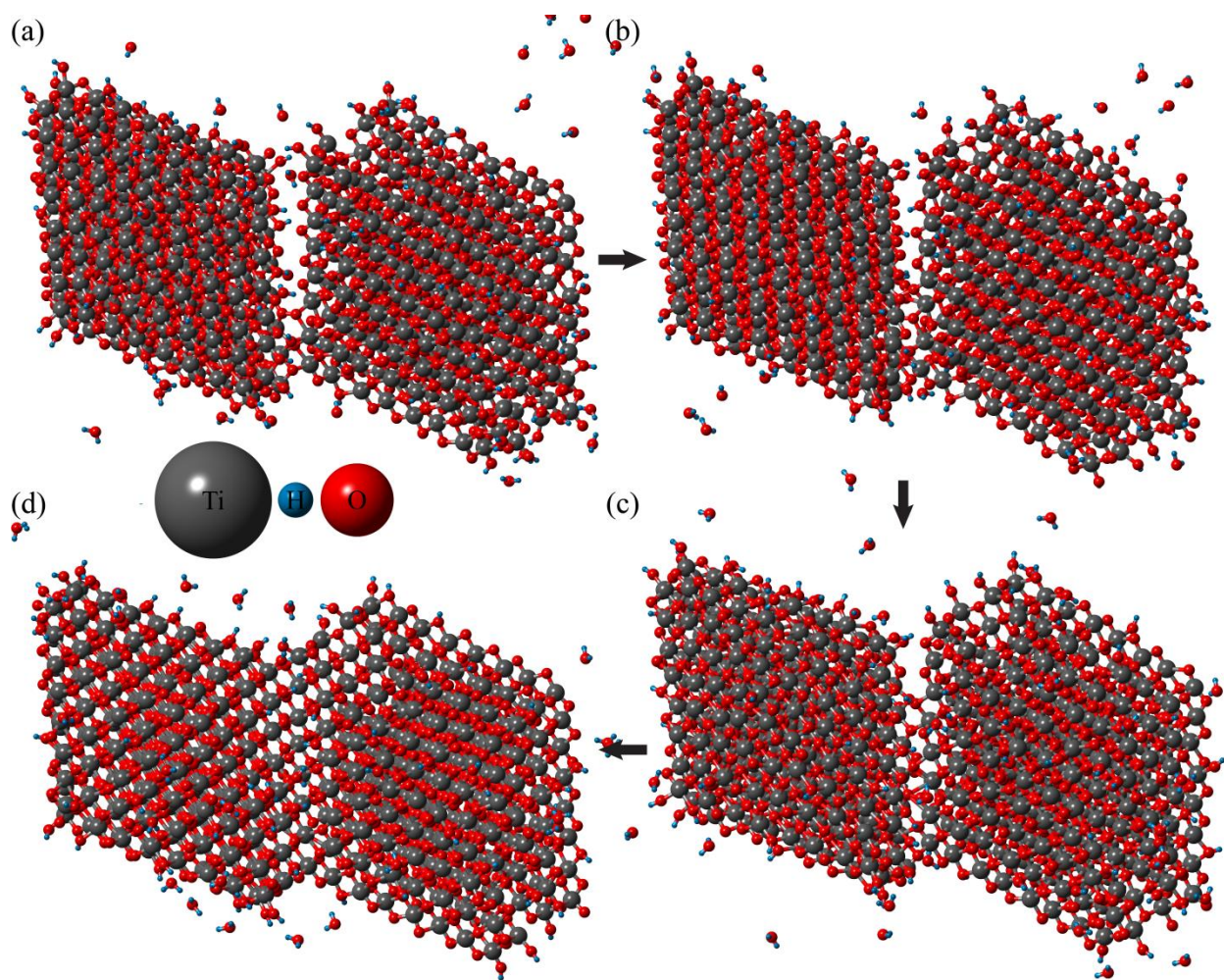


Figure 4.8. Snapshots of the OA of anatase nanocrystals on {101} facets in water. These figures were taken at (a) 737.5 ps; (b) 750.75 ps; (c) 763.75 ps and; (d) 775 ps.

We observe OA on the {112}, {001}, and {101} surfaces, as is also seen experimentally¹³⁴ and representative cases are shown in **Figure 4.9**. To analyze the structure of the aggregates, we employ the ‘local order parameter’ developed by Zhou and Fichthorn⁸⁹. The local order parameter can differentiate titanium atoms in anatase, anatase {112} twin, or rutile environments, and can be used to study the crystallinity of the resulting aggregates. The local order parameter analysis establishes that aggregates obtained from our simulations are single crystals for coalescence on the {112}, {001}, and {101} surfaces, as shown in **Figure 4.9**. In addition, we observe the formation of anatase {112} twins, which has also been observed in experimental studies by Penn and Banfield¹³⁴.

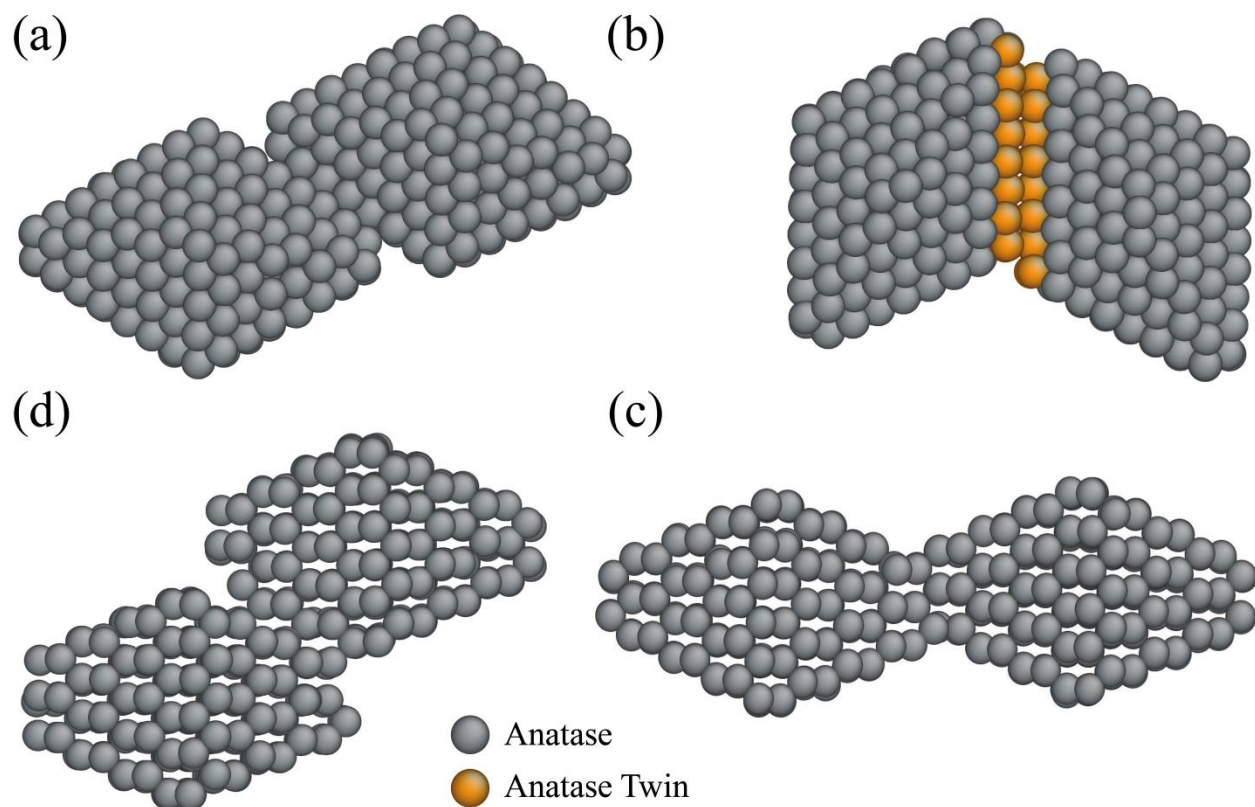


Figure 4.9. Structural analysis of OA aggregates on (a) {112} (b) {112} twin (c) {001} and (d) {101} facets of anatase nanocrystals. Only Ti atoms are shown, with anatase atoms in grey and anatase {112} twins in orange.

In 24 aggregation events, we observed OA 14 times on anatase {112}, 8 times on anatase {001}, and 2 times on anatase {101}. Experimentally OA has been observed to occur most commonly on {112}, occasionally on {001}, and rarely on {101}¹³⁴. We find that OA most frequently involves the surfaces that have the highest propensity to dissociate water. Our previous studies demonstrated that the anatase {112} and {001} surfaces dissociate water to a greater extent than the {101} surface for water coverages up to 3.0 ML, which implies a higher hydroxyl coverage on the {112} and {001} facets than on {101}¹⁴⁶. Also, the alignment of nanocrystals involves the formation of a network of hydrogen bonds directed normal to the nanocrystal surfaces and this requires the presence of facets with adsorbed hydroxyls. As shown in Figure 4.6(a) the interface between aligned nanocrystals contains hydroxyls and is devoid of molecularly adsorbed water molecules. The hydrogen bonds formed by molecularly adsorbed water are not directed normal to the surface, which explains the low frequency of OA on the {101} surface. Our results may explain the occurrence of OA in oxides that are known to dissociate water to a significant extent, such as SnO₂^{111, 154} and ZnO^{133, 155}. SnO₂ and ZnO surfaces ionize to a greater extent than TiO₂ in response to bulk solution pH¹⁵⁶ and this may affect their aggregation mechanism. OA growth of SnO₂¹⁵² shows a sequence of particle alignment followed by interface elimination. Figure 4.6(c) shows aligned SnO₂ nanocrystals associating at very close separations of 2-3 Å without aggregating. At these close separations, only a single layer of water could be present on the nanoparticle surfaces and can be conceived to consist only of adsorbed hydroxyls or molecular water. The water layer can facilitate the creation of hydrogen bonds which in turn bridges the adjacent nanoparticles, yielding the OA growth mechanism upon elimination of adsorbed species.

This suggests a similar mechanism of alignment followed by coalescence in SnO_2 . This mechanism is also observed in iron oxyhydroxide nanocrystals^{150, 151}.

The anatase nanocrystal surfaces are susceptible to protonation whereby the surfaces adsorb or desorb protons in response to the bulk solution pH. The room temperature pH_{pzc} (point of zero charge) of nanocrystalline anatase is reported¹⁵⁷ to range from pH 5 to 7. We calculated the surface charge density using the charge description scheme in ReaxFF for the anatase nanoparticle shown in **Error! Reference source not found.**(d), which was equilibrated in 5 ML of water for 75 ps at 573 K. We find a negative value ($\sim -0.022 \text{ C/m}^2$), suggesting that the force field is able to reproduce deprotonation at $\text{pH} > \text{pH}_{\text{pzc}}$. The observed surface charge density in our simulations is reasonable, since experiments report the surface charge density at 298 K and pH 7 of anatase^{158, 159} as $\sim -0.01 \text{ C/m}^2$ and of rutile¹⁶⁰ as $\sim -0.02 \text{ C/m}^2$. Comparing the surface charge density predicted by the force field with experiments is non-trivial since it is dependent on temperature, the size and facets of the nanoparticle, the density of water in the simulations and the electrolyte¹⁵⁸. Previous MD studies^{156, 161} investigated the effect of temperature and pH on surface protonation and solvation structure at the rutile(110) surface and showed that surface protonation can modify the hydrogen-bonding network and thus the interfacial water structure. On silica nanoparticle surfaces, the degree of ionization has been shown to modify the interfacial water structure by changing the fraction of ions adsorbed on the surfaces¹⁶². Similarly on anatase nanoparticles surface ionization may affect the penetration of protons into solution and modify the number of freely dissociated, mobile protons present near the surface. The effects of surface ionization on OA are not known and investigating the variation in surface ionization of anatase nanocrystals with pH and its effects on interfacial structures of water may provide a way to probe the effects of pH on OA.

Penn and Banfield¹³⁴ observe OA in titania hydrothermally coarsened in deionized (DI) water as well as in acidic conditions. The frequency of observed attachments in the most acidic solutions (pH 1-2) as well as in solutions adjusted using NaOH (pH 8 -11) is similar to that observed in DI water. However at a pH around 3, an increased frequency of OA is observed. Our simulations are representative of the aggregation mechanism observed in DI water and the effect of buffers and pH of solution on OA may be addressable in future studies. Also of importance is the role of structure directing agents (SDA). These agents ranging from small monomer molecules to heavy-molecular-weight polymers and organic ligands are known to modify and direct OA^{163, 164}. Future studies could target the mechanisms of OA in such systems.

4.4 Summary and Conclusions

The OA pathway observed in our simulations is consistent with the pathway observed in TEM studies of OA for iron oxyhydroxide nanocrystals by Li *et al.*¹⁵¹. TEM images from that study show a sequence of whole-particle alignment followed by coalescence initiated at a contact point. The iron oxyhydroxide nanocrystals continuously rotate and interact until they find a perfect lattice match. Thereafter, aggregation proceeds rapidly after a sudden jump to contact. Thus, the OA pathway observed in our simulations is likely generic to aqueous oxide materials and indicates the important role played by water and hydrogen bonding in mediating crystal growth by OA.

5

A Reactive Force Field study of Li/C Systems for Electrical Energy Storage

5.1 Introduction

Graphitic carbon is the most ubiquitously used anode material in Li-ion batteries¹⁶⁵⁻¹⁶⁹ (LIBs). This is due to its low cost, its low voltage with respect to lithium that allows higher cell voltages when paired with oxide cathodes, reasonable capacity, and modest volume expansion on lithiation. Yet, the achievable rates in graphite, determined by the diffusion of lithium, are lower than desired ($D_{\text{Li}} \sim 10^{-6} \text{ cm}^2 \text{ s}^{-1}$)¹⁷⁰. Lithium insertion into graphite further produces ordered solid phases that lead to significant strain and latent heat induced losses and mechanical damage during cycling¹⁷¹⁻¹⁷³. Ideally one would like to improve capacity and rates without any loss in cyclability leading to a longer lifetime. Most of the simulations of Li-graphite systems to date have focused on defect-free graphite with no rigorous treatment of vacancies, even though experiments show that defective graphite can indeed allow increased rates¹⁷⁴. Recent theoretical studies in graphene and graphite indicate that defects/vacancies and curvature strongly affect lithium adsorption energies^{175, 176}. Defective graphene also enhances reduction of oxygen, a key step in Li-air batteries¹⁷⁷. This suggests urgency in improving our microscopic understanding of the Li intercalation process in graphitic systems and a need to explore the degree of variability in the voltage/rates/capacity/cyclability for defective graphite.

The challenge in modeling Li intercalations comes from the coupling between the weakly van der Waals bonded graphite and the charge-transfer of the lithium metal atoms to the graphite¹⁷⁸. This coupling, combined with the electrostatic interaction of the ions in the solid, gives rise to many different types of ordered solid phases. Density functional theory (DFT) calculations with

van der Waals corrections are able to predict theoretical voltage curves and diffusion barriers for a single lithium ion in experimentally known solid phases¹⁷⁰ as well as in nanotubes^{179, 180}. However, DFT rapidly becomes prohibitively computationally costly¹⁸¹ at the large system sizes and timescales needed to study defective materials, nanoscale materials, phase transitions or lithium intercalation and charge-discharge dynamics at realistic concentrations. Force-field methods are required to study this regime. Due to the charge-transfer nature of this system, a reactive force field is required to study the phenomenon.

In this work we fit a reactive force field for the Li/C system using the ReaxFF formalism and study the microscopic features of lithium intercalation/deintercalation using a grand canonical Monte Carlo simulation involving about a thousand atoms in a variety of carbon structures. We differentiate atomistic processes that occur in single-layer graphene and bulk graphite with those occurring on surfaces and edges and capture the staging effect seen in graphite^{169, 182}. We study graphite with realistic concentrations of both point and topological defects (1-2% defect density), and determine quantitatively how the staging effects are changed. Finally we perform simulations for two carbon nanostructures, a 0D carbon-onion and a 1D carbon nano-rod. The novel insights we gain about Li-intercalation in these carbon nanostructures with/without defects demonstrates the utility of reactive force-fields in gaining a microscopic understanding of processes in energy materials by atomistic simulations of thousands of atoms in a reactive environment.

5.2 Computational Methods

Computationally the ReaxFF formalism is fast enough to permit calculations of thousands of atoms on modest computational resources. For example, the molecular dynamics simulations of onion-like carbons described later, involved 6475 atoms. We were able to obtain 118 steps per minute on a 4 processing core workstation, while the equivalent DFT calculation would not be

possible even using the largest supercomputers. Parallel molecular dynamics simulators like LAMMPS¹⁸³ and ADF⁵⁷ allows atomistic simulations of hundreds of thousands of atoms on high performance computing systems enabling modeling of realistic carbon materials.

A. Fitting the ReaxFF parameters for Li/C systems

In the current study, we develop optimized force-field parameters for Li/C systems. The training set of data used to fit these parameters is a collection of results (energies, geometries, charges etc.) derived from quantum-mechanical (QM) calculations. The parameters for pure carbon were previously used in Yang *et al.*¹⁸⁴ and Huang *et al.*¹⁸⁵.

Ab initio calculations

The force field is trained against a set of density functional theory based datasets. The long ranged van der Waals interactions between carbon atoms is captured via the Grimme parameterization¹⁸⁶ using the DFT-D2 formalism as implemented in the VASP package^{187, 188}. All calculations use the PBE functional and a converged **k**-point mesh corresponding to one point per 0.0008 Å⁻³. Lithium polarizability is set to zero (i.e. $C_6^{\text{Li}} = 0$) as was shown to be necessary to capture lithium diffusion barriers in graphite as well as the structural parameters of fully lithiated graphite – LiC₆^{178, 189}. The following data are used to train the force field: (1) cohesive energy and elastic constants of AA, AB, rhombohedral graphite and LiC₆, (2) the lithium diffusion barriers in AA graphite at inter-planar spacings of 3.35, 3.52 and 3.706 Å, (3) lithium adsorption energies on perfect and single-vacancy defect graphene and (4) the different types of lithium clusters on graphene and defective graphene (different reconstructions of vacancies and divacancies). This data is chosen to be representative of the geometries and electronic configurations likely to be found in pure and defective graphite for varying local lithium concentrations while remaining small enough to be suitable for force-field training.

On pristine graphene, two Li-atoms form a dimer with $d(\text{Li-Li})=2.91\text{\AA}$, with one of the Li-atoms on the hollow hexagonal site 1.91\AA above the graphene plane. Three Li-atoms form a coplanar, isosceles triangle of side 2.86\AA perpendicular to the graphene plane with two of the atoms on the hollow site at a height of 1.93\AA . Four Li-atoms form a prismatic cluster with three coplanar atoms at the hollow site of graphene at a height of 1.86\AA . For a single atom vacancy defect, Li-atoms bind to the under bonded $\text{sp}^3\text{-C}$ atom with a bond distance of $d(\text{Li-C})\sim 2.08\text{\AA}$ with up to 2 Li-atoms per under-bonded $\text{sp}^3\text{-C}$. Cluster formation begins at three Li-atoms, similar to the case of pristine graphene, with four atoms forming an interesting inverted prismatic cluster at the center of the defect with a $d(\text{Li-Li})\sim 1.98\text{\AA}$. For a 5-8-5 reconstructed graphene due to a divacancy, single lithium is at a height of 1.43\AA at the center of the octagon with very little puckering of the graphene layer. Presence of two lithium atoms leads to strong puckering when one of the Li atom form bonds with the atoms around the defect and a $d(\text{Li-Li}) = 2.33\text{\AA}$. The bonded Li atom substitutes for the missing two carbon atoms giving rise to the puckering due to a non-zero curvature effect. But this type of Li-atom arrangement is higher in energy by 0.6 eV than a coplanar arrangement with one Li at the center of the octahedral site and another at the pentagonal site with a $d(\text{Li-Li})=2.964\text{\AA}$ with no puckering of graphene. This suggests that the Li-C interaction dominates over metallic interactions between Li-atoms, possibly due to local charge transfer processes. But with an extra Li-atom, formation of a 3D cluster through the defect is more stable than an arrangement with adsorbed geometries of individual Li-atoms. With four atoms, Li-atoms forms a trigonal pyramidal Li cluster with one atom at the center of the octahedral site suggesting a strong tendency to form metal clusters instead of ion adsorption on graphene. For a 5-5-5-7-7-7 reconstruction of the graphene defect, a single Li-atom sits on the C-atom at the intersection of the 7-7-7 rings at a distance of 2.04\AA . Interestingly, two Li-atoms form a dimer above this C-atom

with a $d(\text{Li-Li})=3.10\text{\AA}$. Three Li-atoms form an isosceles triangular geometry with the other two atoms on top of the pentagonal sites.

Forcefield Optimization

To optimize the bond parameters for Li-C we utilize a successive one-parameter search technique to minimize the sum-of-squares error function

$$Error = \sum_i^n \left[\frac{(\chi_{i,qm} - \chi_{i,ReaxFF})}{\sigma_i} \right]^2 \quad (5.1)$$

where $\chi_{i,qm}$ is a QM value, $\chi_{i,ReaxFF}$ is a ReaxFF calculated value, and σ_i is a weight assigned to data point i . We fit a total of 10 parameters (**Table 5.1**) to a training set containing 389 data points using a successive single-parameter search method, using multiple cycles to account for parameter correlation. The fitted Li/C parameters are presented in **Table 5.1**.

Bond parameters (Li-C parameters)					
Sigma-bond dissociation energy (Edis1) 82.8122	Bond energy (pbe1) 0.9497	Bond energy (pbe2) 0.1520	Pi bond order (pbo3) -0.2500	Sigma bond order (pbo1) -0.1991	Sigma bond order (pbo2) 5.1849
Off diagonal parameters (Li-C parameters)					
Ediss 0.2964	Rvdw 1.9000	Alfa 10.8828		Cov.r 1.5947	

Table 5.1. The fitted parameters optimized in this Li-C force field development study.

Forcefield Validation

In this section, we compare ReaxFF with the training set DFT data corresponding to structures and energies of Li adsorption and diffusion in graphene and graphite.

We consider three sites with high symmetry to analyze the adsorption of Li on graphene: the site in the center of a hexagon (Hollow), the site at the midpoint of a carbon-carbon bond (Bridge), and the site on top of a carbon atom (Top). **Table 5.2** gives the comparison of ReaxFF

and DFT values for Li adsorption on graphene at these sites. The adsorption energy E_{ad} is defined as

$$E_{ad} = E_{Li+g} - E_g - nE_{Li} \quad (5.2)$$

where E_{Li+g} is the energy of graphene with Li adsorbed on it, E_{Li} is the energy of one metallic (body-centered cubic) Li atom, E_g is the energy of the isolated graphene, and n is the number of adsorbed Li atoms. The Li reference state is the stable bulk phase (bcc-Lithium) and hence the adsorption energy measures the stability of Li adsorbed single layer graphene (SLG) against isolated SLG and metallic Li. The geometry structure and energies are obtained after the positions of all atoms have been relaxed.

	ReaxFF (kcal/mol)	DFT (kcal/mol)
Li adsorption energy (AE) on Hollow site in graphene	12.63	12.08
Li AE on Hollow Site – Li AE on Bridge site in graphene	-7.07	-7.00
Li AE on Bridge Site – Li AE on Top site in graphene	-2.30	-2.40
Li in Graphite (Formation energy of LiC_6)	-2.74	-2.76

Table 5.2. Comparison of ReaxFF and DFT values for various adsorption energies of Li in graphene and graphite.

The force field was also parameterized against the dissociation pathways of C-Li bond in CH_3 -Li, C_6H_5 -Li. The ReaxFF values for bond dissociation energy and equilibrium bond length of the C-Li bond in CH_3 -Li (2.31 eV, 1.9616Å) and C_6H_5 -Li (2.33 eV, 1.9663Å) are in good agreement with the DFT values of (2.39 eV, 1.9119Å) and (2.60 eV, 1.9730Å) respectively. We

observed that ReaxFF reproduces the equilibrium distance and the overall bond strength accurately, but that the bond dissociates more quickly in the ReaxFF description, compared to the DFT results. This set of non-periodic DFT calculations were performed using the B3LYP functional as implemented in the Gaussian package¹⁹⁰.

To further validate the forcefield we investigated Li intercalation and diffusion in pure graphite. When multiple graphene sheets are stacked to form graphite, the only binding forces between adjacent layers are due to weak Van der Waals (vdW) interactions. As Li is intercalated, the C-C vdW bonds are perturbed and screened by the hybridization between the Li ions and carbon atoms. This is evidenced in the change from *AB* hexagonal stacking (graphite) to *AA* stacking in stage I compounds^{169, 182}. As shown in **Table 5.2** ReaxFF gives the formation energy of stage I (LiC_6) compounds in good agreement with DFT calculations indicating that the hybridization is accurately captured by ReaxFF. To investigate Li diffusion we considered separations between graphene layers of 3.35 Å and 3.7 Å in *AA* graphite. **Figure 5.1**, shows the comparison of potential energy curves of Li diffusion along two symmetrical paths: Hollow-Bridge-Hollow, and Hollow-Top-Bridge-Top-Hollow. ReaxFF shows very good agreement with DFT calculations for the studied diffusion paths: for the first path, the transition state energies are 27.20 vs 12.70 kcal/mol while for the second the transition energies are 32.87 vs 15.33 kcal/mol at separations of 3.35 Å and 3.7 Å respectively.

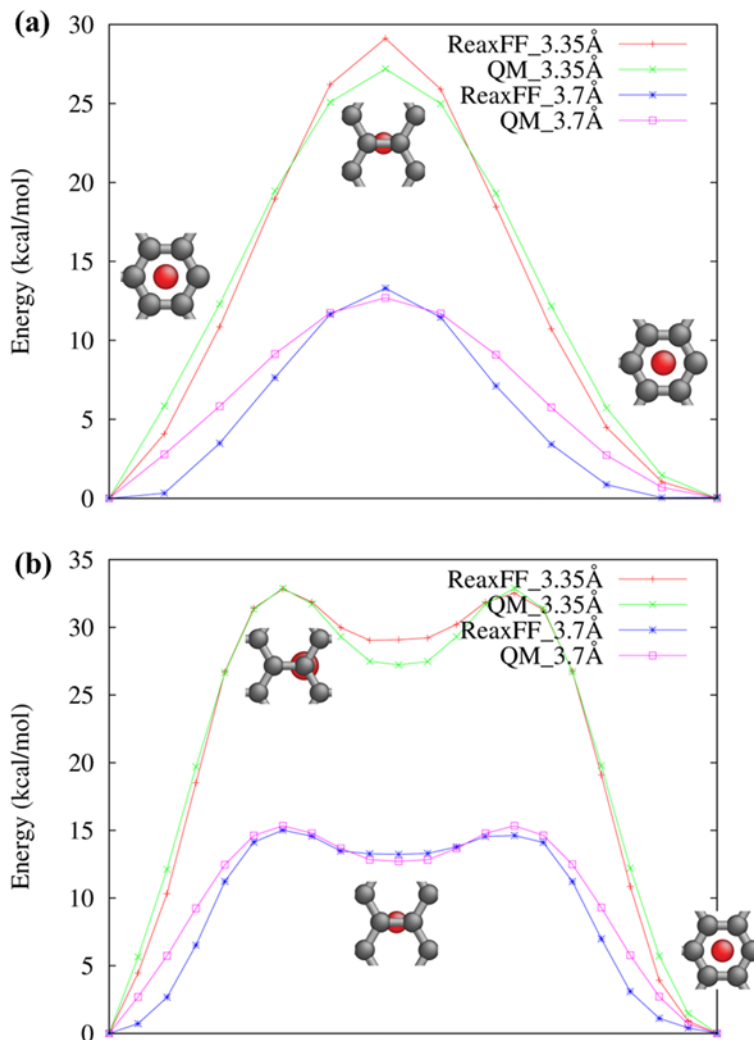


Figure 5.1. Comparison of potential energy curves of Li diffusion along two paths (a) Hollow-Bridge-Hollow, and (b) Hollow-Top-Bridge-Top-Hollow in graphite at separations of 3.35 Å and 3.7 Å predicted by ReaxFF and DFT calculations.

5.3 Results and Discussion

A. Adsorption and Diffusion of Lithium on Defective Graphene

Lithium motion on pristine graphene is restricted to two-dimensional diffusion. Lithium diffusion in the direction perpendicular to the graphene sheet is extremely unfavorable energetically. The diffusion barrier for Li in the direction perpendicular to pristine graphene given by ReaxFF (8.87 eV) is in good agreement with DFT (8.74 eV)¹⁹¹. Intuitively, defects in graphene

can reduce the diffusion barrier of lithium. We investigate the diffusion of Li in the direction perpendicular to the graphene sheet for two cases: graphene with single-vacancy, and graphene with di-vacancy. **Figure 5.2** shows the energy landscape for lithium diffusion in the direction perpendicular to the graphene sheet for graphene with single vacancy and graphene with di-vacancy. The ReaxFF values for the local minimum, diffusion barrier and position of local minimum for the two cases are in good agreement with the corresponding DFT values¹⁹¹, suggesting the general applicability of our force-field method to defective carbonaceous materials in general.

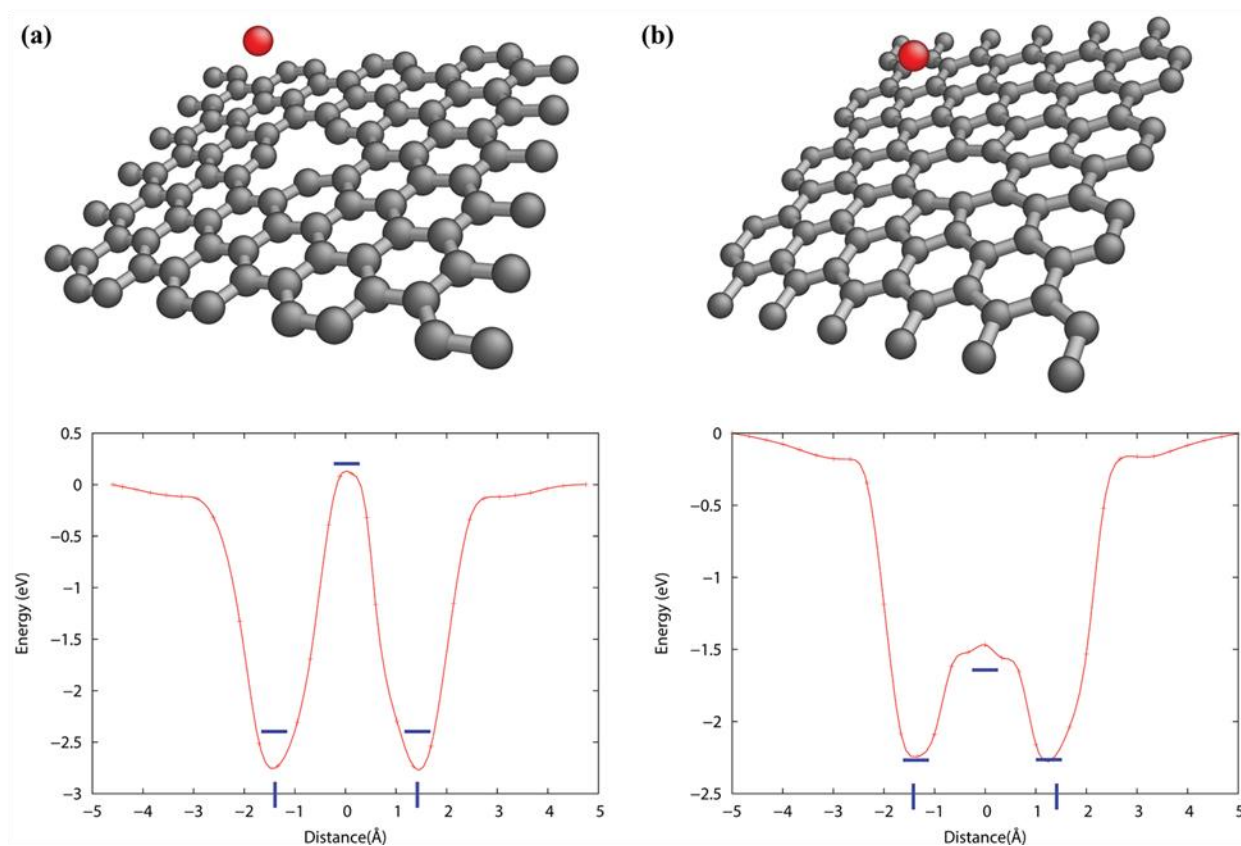


Figure 5.2. Potential energy curves for lithium diffusion in the direction perpendicular to the graphene sheet for graphene with (a) mono-vacancy and (b) di-vacancy. The blue dashes are DFT values for the Local Minimum, Diffusion Barrier and Position of Local Minimum.

B. Li intercalation in pristine and defective graphite – voltage profile

We apply Grand canonical Monte Carlo (GCMC) simulations based on the Metropolis algorithm to obtain a set of ground states consistent with first principles data. The GCMC temperature scans at constant chemical potential are combined with molecular dynamics runs of 12.5 ps in the NVT ensemble for every 50 successful GCMC moves.

Bulk Graphite

To explore Li loading in bulk graphite we used a periodic (6 x 6 x 8) supercell, corresponding to 8 graphene layers. GCMC simulations were performed at constant external chemical potential of Li at a temperature of 300 K till maximum Li loading. The external chemical potential of Li was fixed at the total energy of a single lithium atom in body-centered cubic lithium. **Figure 5.3(a)** shows the in-plane Li ordering (checkerboard pattern) for stage II and stage I compounds predicted by ReaxFF in agreement with previous DFT calculations¹⁶⁹. ReaxFF also reproduces the Li-C stacking sequence in stage II and stage I compounds as shown in Figure 5.3(b).

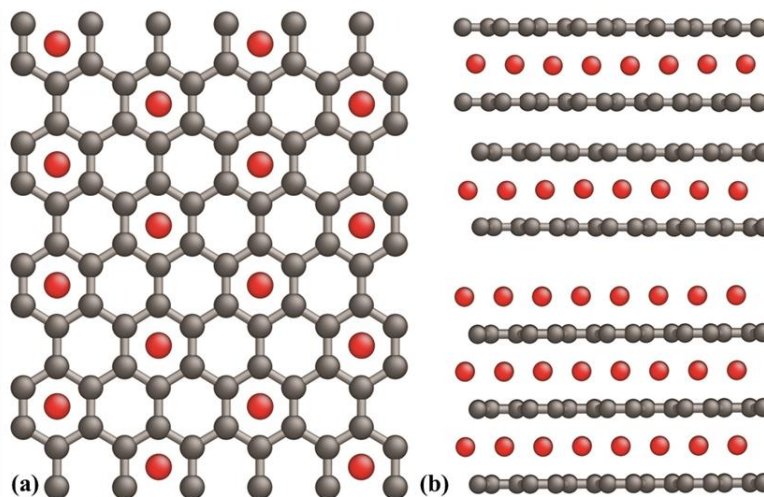


Figure 5.3. (a) In-plane Li ordering in stage I and stage II compounds as seen from above on the carbon honeycomb lattice. (b) Li-C stacking in stage II and (c) stage I.

The average potential as a function of Li intercalation content in a material is calculated as

$$V(x) = - \frac{G(\text{Li}_{x+\Delta x}\text{C}_6) - G(\text{Li}_x\text{C}_6) - \Delta x G(\text{Li})}{\Delta x} \quad (5.3)$$

where G is the Gibbs free energy of the compound. We replace the Gibbs free energy by the internal energy. **Figure 5.4(a)** shows the voltage profile in Li_xC_6 obtained using ReaxFF as a function of x in Li_xC_6 which is in good agreement with the experimental voltage profile¹⁹². The voltage profile reflects the sequence of phase transitions in the system, because the coexistence of two stable phases gives rise to plateaus. The three regions of two-phase coexistence in lithium intercalated graphite correspond to voltage plateaus at regions of A, B and C as shown in **Figure 5.4(a)**. The first lithiated phase to become thermodynamically stable is a stage III + dilute stage II compound at $0.12 < x < 0.25$ followed by a dilute stage II + stage II compound at $0.25 < x < 0.5$ and the stage I + stage II two-phase region starts at $x=0.5$. The Li concentration at the phase transitions and the phase sequence with increasing Li concentration is comparable with experiments.

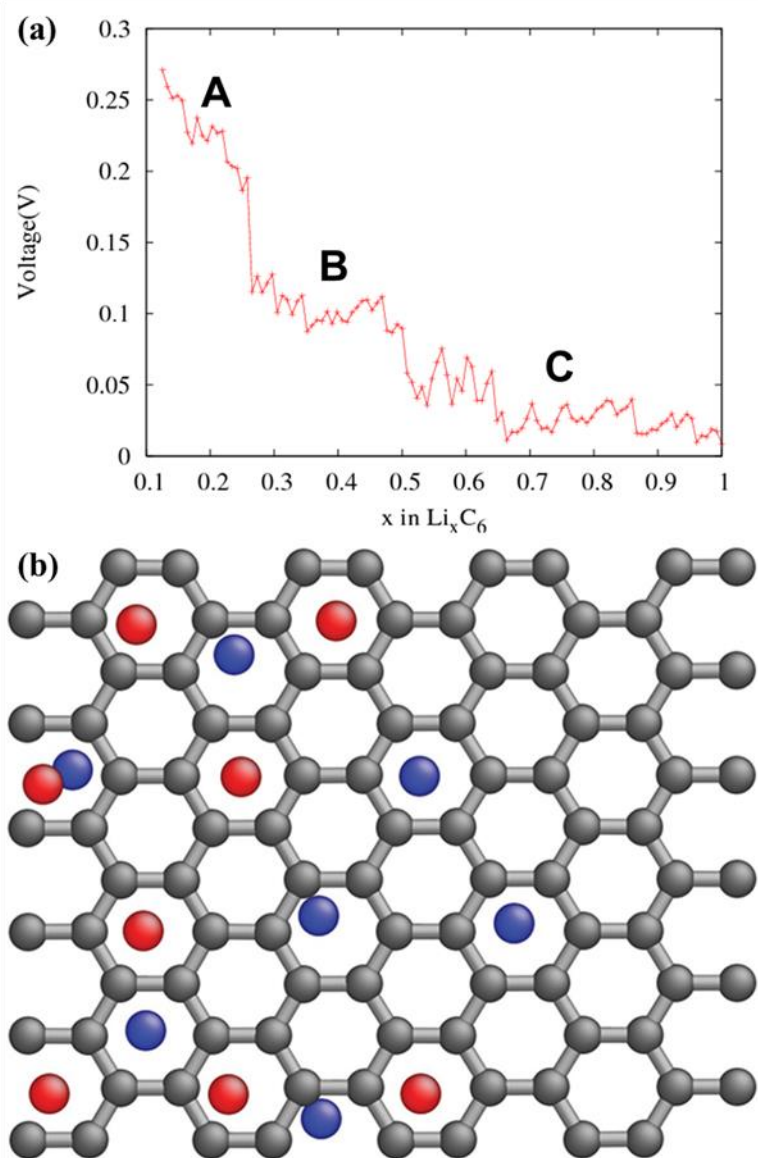


Figure 5.4. (a) Voltage profile for Li-graphite system obtained by ReaxFF. (b) Clustering of Li up-down pairs in graphite during loading. (red is up and blue is down with respect to graphene)

Experimentally, it has been deduced that Li screens the C-C van der Waals interactions^{192, 193}. Thus there is a competition between the attractive C-C van der Waals interactions that prefers to keep the planes free of Li, the attractive Li-C interactions that promotes Li intercalation and Li-Li repulsions which prefer to put Li ions as far apart as possible. This delicate interplay between the three interactions result in a critical Li concentration for which there is enough driving force

to open up and start populating an empty graphite layer giving rise to plateaus in the voltage profile. The layer spacing increased continuously with Li concentration corresponding to the decreases in the voltage profile. The average spacing between graphite layers for fully lithiated stage II compound is 3.7 Å and stage I compound is 3.9 Å which is in good agreement with experimental values of 3.55 Å and 3.7 Å respectively. In the stage II + stage I two-phase region Li starts intercalating in adjacent graphite layers and we observe clustering of up-down Li pairs as show in **Figure 5.4(b)**. As Li concentration in adjacent graphite planes increases they start sliding from the AB stacking in stage II to the AA stacking in stage I.

Graphite with single and di-vacancy

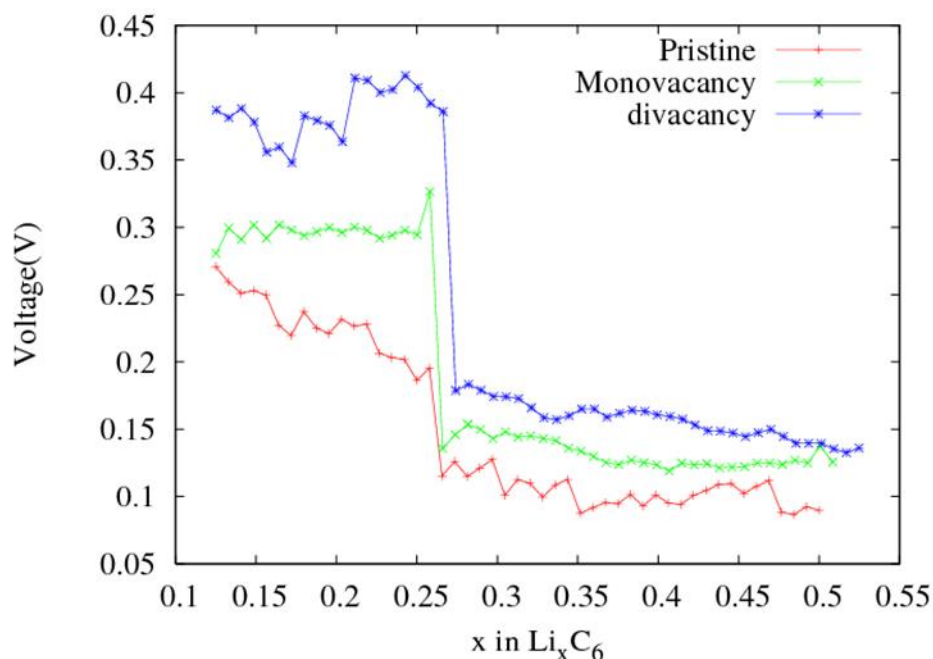


Figure 5.5. Voltage profile for Li intercalation in graphite with single and di-vacancy.

To explore Li loading in graphite with single and di-vacancy we used a periodic (6 x 6 x 8) supercell with a single and di-vacancy respectively in one of the 8 graphene layers. This corresponds to a defect density of 1.05% for the single vacancy and 2.01% for the di-vacancy case in the defect containing graphene layer. GCMC simulations were performed at constant external

chemical potential of Li at a temperature of 300 K till maximum stage II loading. The adsorption energy of Li on single and di-vacancy is larger than the adsorption energy of Li on hollow site in graphite. This increases the voltage for Li intercalation in defective graphite and the increase in voltage is proportional to the size of the defect as shown in **Figure 5.5**. DFT calculations of Li adsorption on defective graphene by Datta *et al.*¹⁹⁴ reports an upward shift in lithiation potential with increase in defect density. The enhanced adsorption energy also increases the Li/C ratio. The presence of defects disturbs the in-plane ordering (checkerboard pattern) in stage II and stage I compounds (cf. **Figure 5.3a**) as shown in **Figure 5.6** and we can observe the formation of metallic Li bonds. For graphite with single vacancy the checkerboard pattern is retained away from the vacancy whereas in presency of di-vacancy the checkerboard pattern is lost up to the second neighboring ring from the defect.

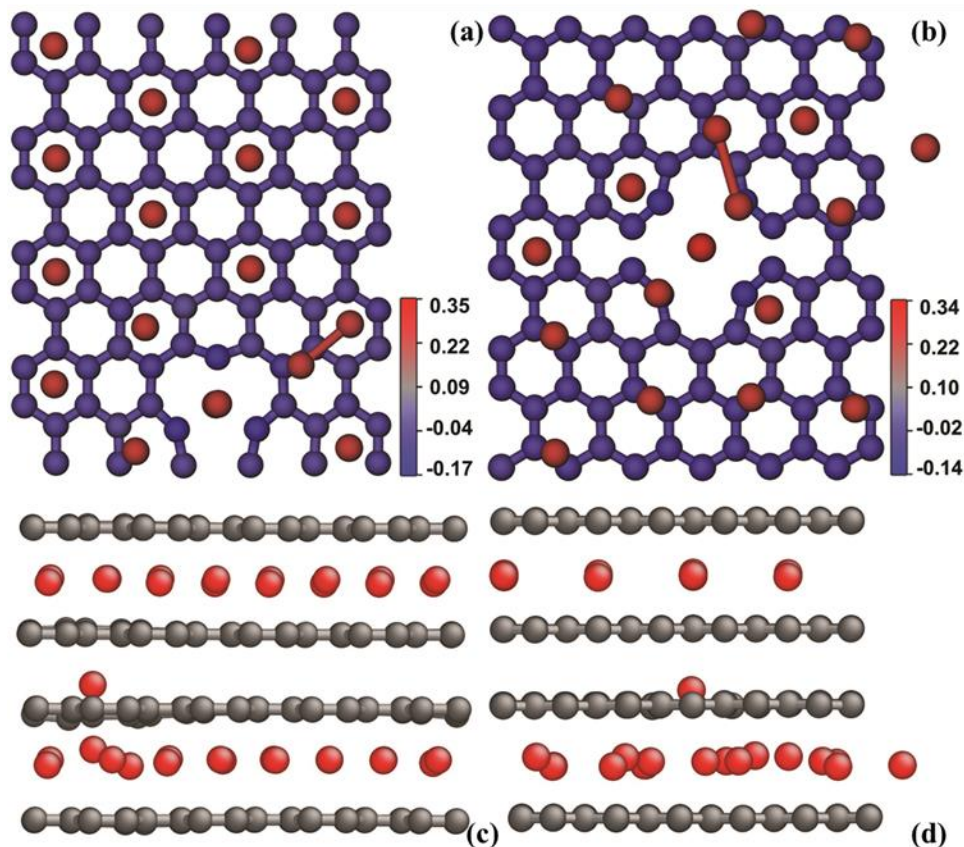


Figure 5.6. In-plane Li ordering in stage II compounds in graphite with (a) single and (b) di-vacancy as seen from above on the carbon honeycomb lattice. Li-C stacking in stage II compounds in graphite with (c) single and (d) di-vacancy

C. Lithium plating

The recent study by Rahul *et al.*¹⁹⁵ reports the plating of lithium metal within the interior of porous graphene networks resulting in very high specific capacities in excess of 850 mAh g⁻¹. DFT calculations from the same study show that presence of 25% divacancy defects induces the formation of Li₃C₈ in the graphene lattice which could act as seed points for subsequent plating of lithium metal.

Using a well-tempered metadynamics simulation, we obtain the free-energy surface (FES) of Li on pristine graphite and graphite with a divacancy site, as shown in **Figure 5.7**. Metadynamics is performed using version 1.3 of PLUMED¹⁹⁶ (called using a “fix” routine from

LAMMPS¹⁸³). The collective variables are the x and y coordinates of Li over the graphite xy-plane. We use a hill height of 0.5 kcal/mol and a width of 0.35 Å, and at every 100 timesteps hills are added. FES's are reconstructed from the Gaussian bias potentials added during the metadynamics trajectory.

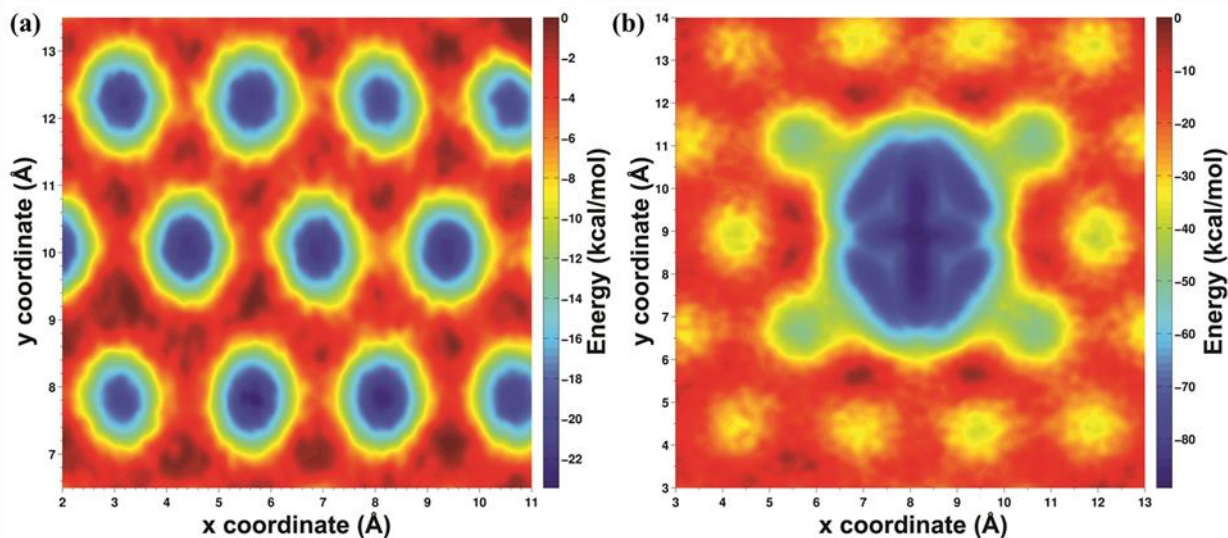


Figure 5.7. Free-energy surface (FES) for adsorption of lithium on (a) pristine graphite and (b) graphite with divacancy as a function of x and y coordinates of Li with the graphite sheets placed along the xy plane.

We can see from **Figure 5.7** that divacancy sites provide a deeper and wider ‘potential-well’ for adsorption of Li with respect to hollow sites on a pristine graphite sheet enabling graphite sheets with divacancy sites to store more Li than pristine graphite. Even at low defect density of 2.1% we observe a maximum capacity of $\sim 428 \text{ mAh g}^{-1}$, which corresponds to Li/C ratio of 0.19 and $\sim 15\%$ increase with respect to pristine graphite. We investigate the Li clusters formed near the divacancy site as shown in Fig. 6(b) and observe that Li in these clusters are closely packed than Li in LiC_6 compounds in pristine graphite. The average Li-Li separation in these clusters is 3.3 Å with an average charge of $+0.279e$ on Li, as compared to an average Li-Li separation of 4.35 Å and an average charge of $+0.29e$ on Li in stage I compounds (LiC_6) in pristine graphite. The Li

separation in these clusters is only 0.28Å greater than Li separation of 3.03Å in body-centered cubic lithium¹⁹⁷. These Li also have a lower charge than LiC₆ (t-test, p<0.001). Therefore it is reasonable to suggest that these localized high lithium content clusters could initiate subsequent plating of lithium metal at these defect sites and explain Li plating in porous graphene networks.

D. Li intercalation in pristine graphite nanorod– intercalation mechanism

Atomic-scale investigations with molecular dynamics (MD) simulations could contribute significantly to understanding Li intercalation in graphite with free edges and furnish many details of this mechanism that are not accessible experimentally. In batteries, Li is intercalated into graphite in the presence of an electrolyte that could undergo reactions at the graphite edges to form solid-electrolyte interphases¹⁹⁸. Here we study intercalation at perfect edges in vacuum, thereby isolating the role of Li-Li and Li-C intercalations. Lithium atoms were placed randomly on both sides of pristine graphite at least ~5Å away and the system was simulated in the canonical (NVT) ensemble at 300 K, to correspond to the temperature in experimental studies. The total simulation time ranged from 500-750 ps, which is long enough to observe the intercalation of Li in graphite.

Li-Li repulsive intercalations are found to play a major role in facilitating Li intercalation in graphite. Li atoms at the Li-graphite interface are pushed into graphite as a result of repulsive Li-Li intercalations. The attractive Li-C interactions facilitate intercalation by opening up the graphite layers. Li intercalation in graphite requires the presence of a cloud of Li atoms at the Li-graphite interface. In the presence of multiple Li atoms near the interface, Li atoms at the interface are pushed in by surrounding Li atoms and the surrounding Li atoms also open up the graphite layer by pulling the carbon atoms at the interface. To illustrate this we simulate the system with a low concentration of Li atoms (Li/C ratio of 0.104) so that a cloud of Li atoms is present only at some graphite layers. **Figure 5.8(a)** shows the density plot of Li atoms (blue) during a NVT

simulation over a time period of 0.5ns. To obtain the density plot, we first divided the simulation cell into a mesh of cubic boxes with dimensions ($0.30 \text{ \AA} \times 0.30 \text{ \AA} \times 0.30 \text{ \AA}$). We then count the number of times a lithium atom was located in each of the grids through the entire length of simulation and normalized these numbers by the highest count recorded in any of the grids. We used these values to obtain the resulting density plot in Fig. 8. The blue color represents all grids (regions) which registered a Li count during the simulation. As shown in **Figure 5.8(a)** Li intercalates only into the layers near which a cloud of Li atoms was present. The intercalation stops when only a single row of Li atoms are present at the interface because of lack of surrounding Li atoms which can push the Li into graphite.

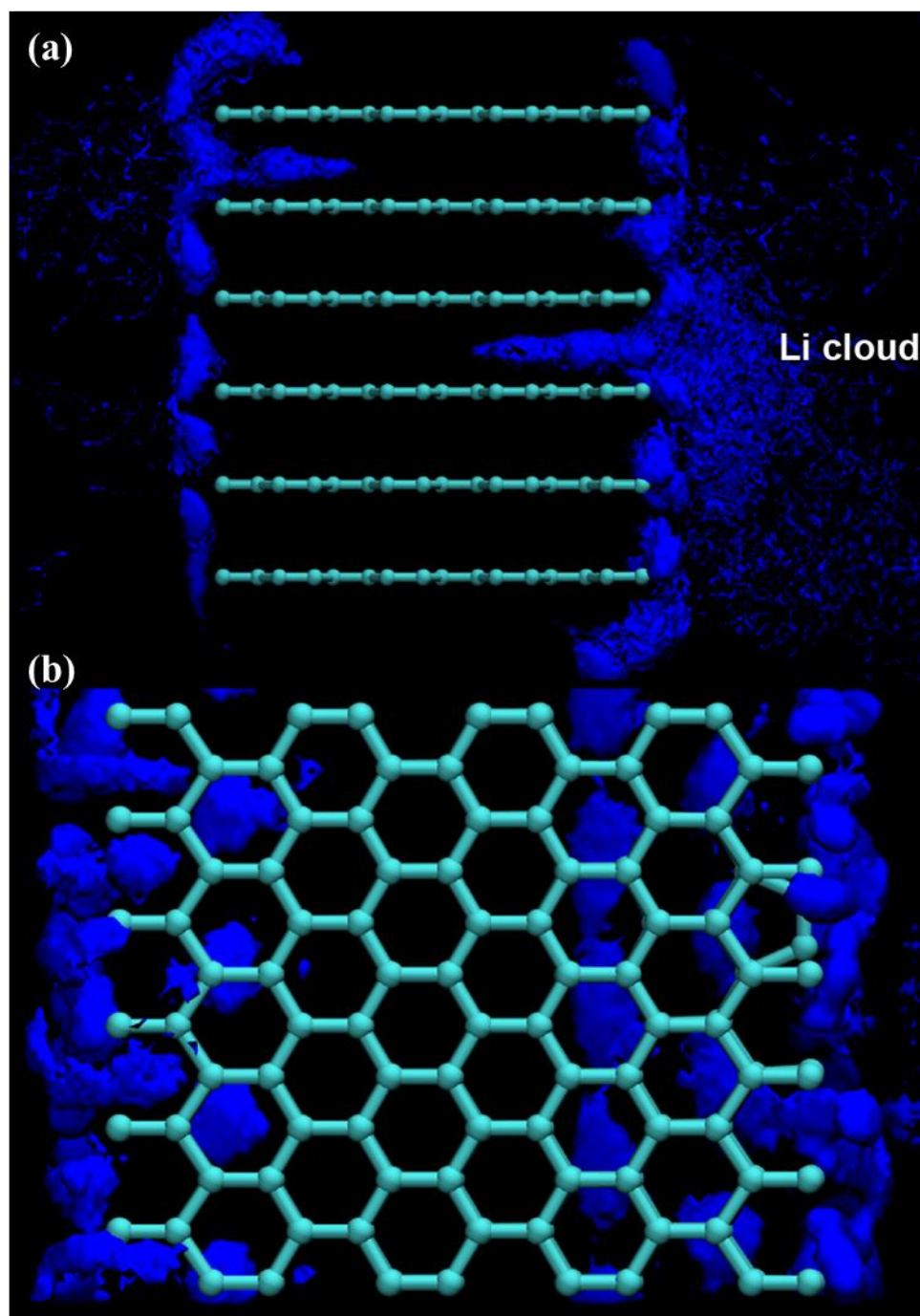


Figure 5.8. (a) Side view of density plot of Li (blue) during a NVT simulation at 300 K showing Li intercalation in graphite (b) top view

E. Adsorption of Li clusters on top of graphene, defective graphene, reconstructed graphene and graphite

We investigate the formation energy of 1, 2, 3 and 4 Li atom clusters adsorbed over pristine graphene, graphene with mono and di-vacancy, 5-8-5 reconstructed graphene and 5-5-5-7-7-7 reconstructed graphene. The formation energies given by ReaxFF are in good agreement with our DFT results as shown in **Figure 5.9**.

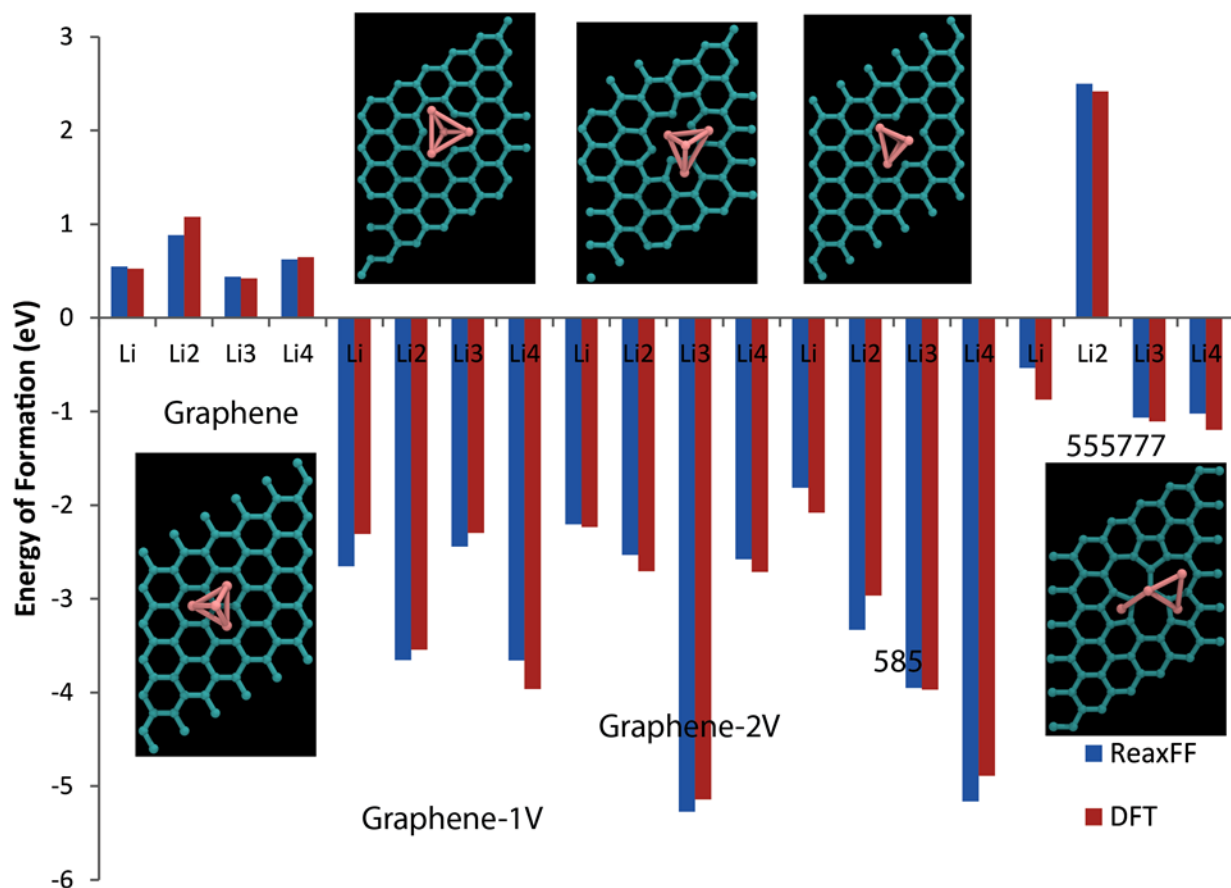


Figure 5.9. Formation energy of Li, Li-2, Li-3 and Li-4 clusters over graphene, graphene with single and di-vacancy, 5-8-5 reconstructed graphene, 5-5-5-7-7-7 reconstructed graphene.

We investigate Li adsorption on top of single and multi-layer graphene using GCMC simulations. We observe that Li does not adsorb on defect-free single layer graphene (SLG), which makes it unsuitable for anode applications. This is in agreement with DFT studies^{189, 199} which reports positive adsorption energies for Li over graphene for Li content ranging from Li_{0.1}C₆ to Li₆C₆. We observe the formation of metallic Li clusters over graphene at concentrations as low as

$x = 0.25$ in Li_xC_6 with 4 Li atoms forming a prismatic cluster as shown in **Figure 5.10**. At higher concentrations Li forms a metallic layer over single and multi-layer graphene and doesn't exhibit the in-plane checkerboard ordering seen in graphite (cf., **Figure 5.3a**).

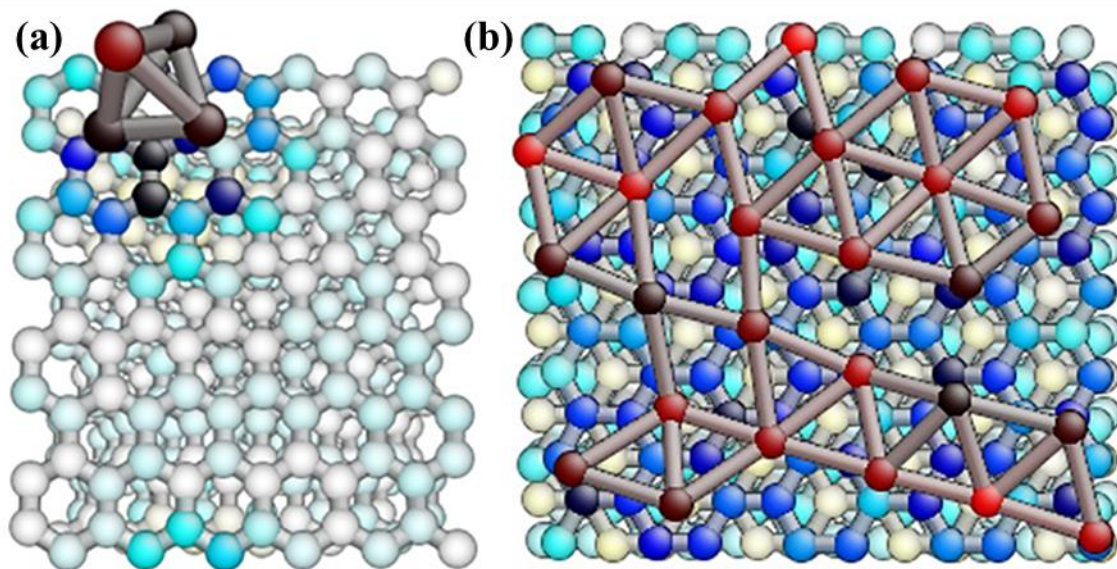


Figure 5.10. Four Li atoms forming a prismatic cluster over 6-layer graphene. (b) Li atom forming a metallic layer over 6-layer graphene.

F. Li intercalation in onion-like carbon nanostructures (OLCs)

We investigate Li intercalation and diffusion in OLCs and explore its possibility as a LIB anode material. Understanding Li diffusivity limitations in OLCs is imperative in order to optimize them for charging/discharging rate performance. The OLC structures were obtained from MD simulations by Ganesh *et al.*²⁰⁰. We perform metadynamics simulations to obtain barriers for Li to diffuse out from an OLC. Intuitively, Li should diffuse from within the OLC to its exterior through defects. We consider an OLC with a diameter of 2 nm and explore the free energy surface of a Li adsorbed between a 12 membered ring in the outer layer and a 6-membered ring in the inner layer of the OLC using metadynamics simulations as implemented in the Plumed package in lammps¹⁹⁶. The collective variable is the distance of the Li atom from the center of the 6 membered ring it is

adsorbed on and the metadynamics simulation is run in the NVT ensemble at 600 K. A hill height of 0.50 kcal/mol and width of 0.35 Å were used, and hills were added every 100 timesteps. FES's were reconstructed from the Gaussian bias potentials added during the metadynamics trajectory. The free energy landscape of Li diffusing out from the OLC is shown in the inset in **Figure 5.11**. The x-axis is the distance of Li from the center of mass of the 6-membered ring within the OLC it is adsorbed on and has an initial value of 2.15 Å. Even though the free-energy minimum of Li is within the OLC, Li has a high energy barrier of ~24.8 kcal/mol to diffuse into the OLC. The high barrier for Li diffusion into OLC suggests that the interior of OLC's do not offer any accessible storage capacity for Li.

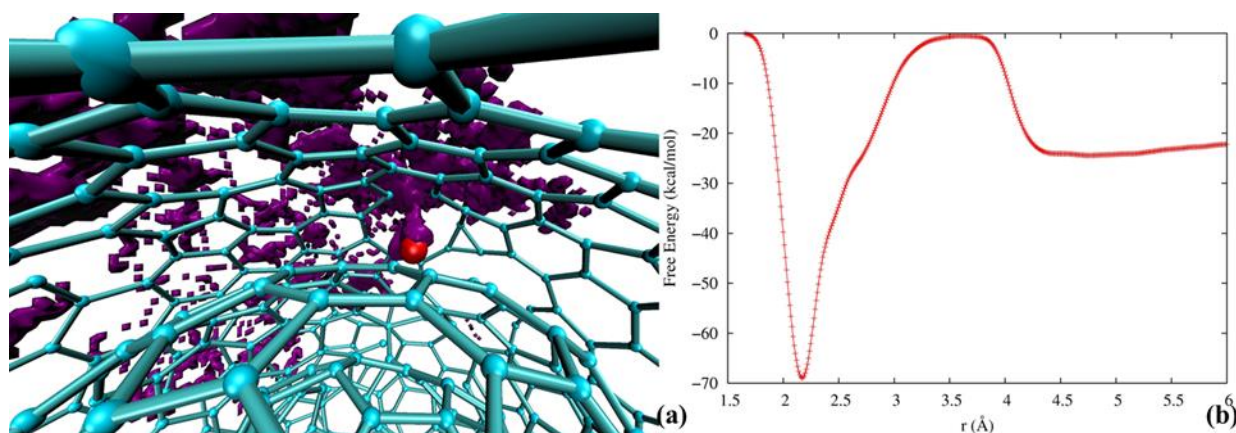


Figure 5.11. (a) Density plot of Li (purple) during a metadynamics simulation at 600 K. (b) The free energy landscape for Li diffusing out from the OLC through a 12-membered ring.

We perform molecular dynamics simulations with Li placed manually within the OLC as well as on its outer surface to investigate Li migration patterns. **Figure 5.12** shows the density plot of Li (green) atoms in the simulation box during a NVT simulation at 1000 K obtained as an average over a time-period of 250 ps. As discussed earlier, the green color represents all grids (regions) which registered a Li count during the simulation. Due to high barriers for Li diffusion between the layers of OLCs we need high temperatures to observe Li diffusion between OLC

layers. We can see that Li outside the OLC have a higher diffusion constant than Li within the OLC and migrates freely on the outer surface of the OLC. However most of the Li within the OLC is confined near its initial position and a few diffuse between the OLC layers. This reiterates the observation from metadynamics simulations that because of high diffusion barriers the interior of OLC's is inaccessible for energy applications and implies lower Li storage capacities in carbon onions. However the outer surface of OLC's offers sites for fast Li adsorption/desorption and is suitable for applications as electrode materials in supercapacitors as is also demonstrated experimentally²⁰¹.

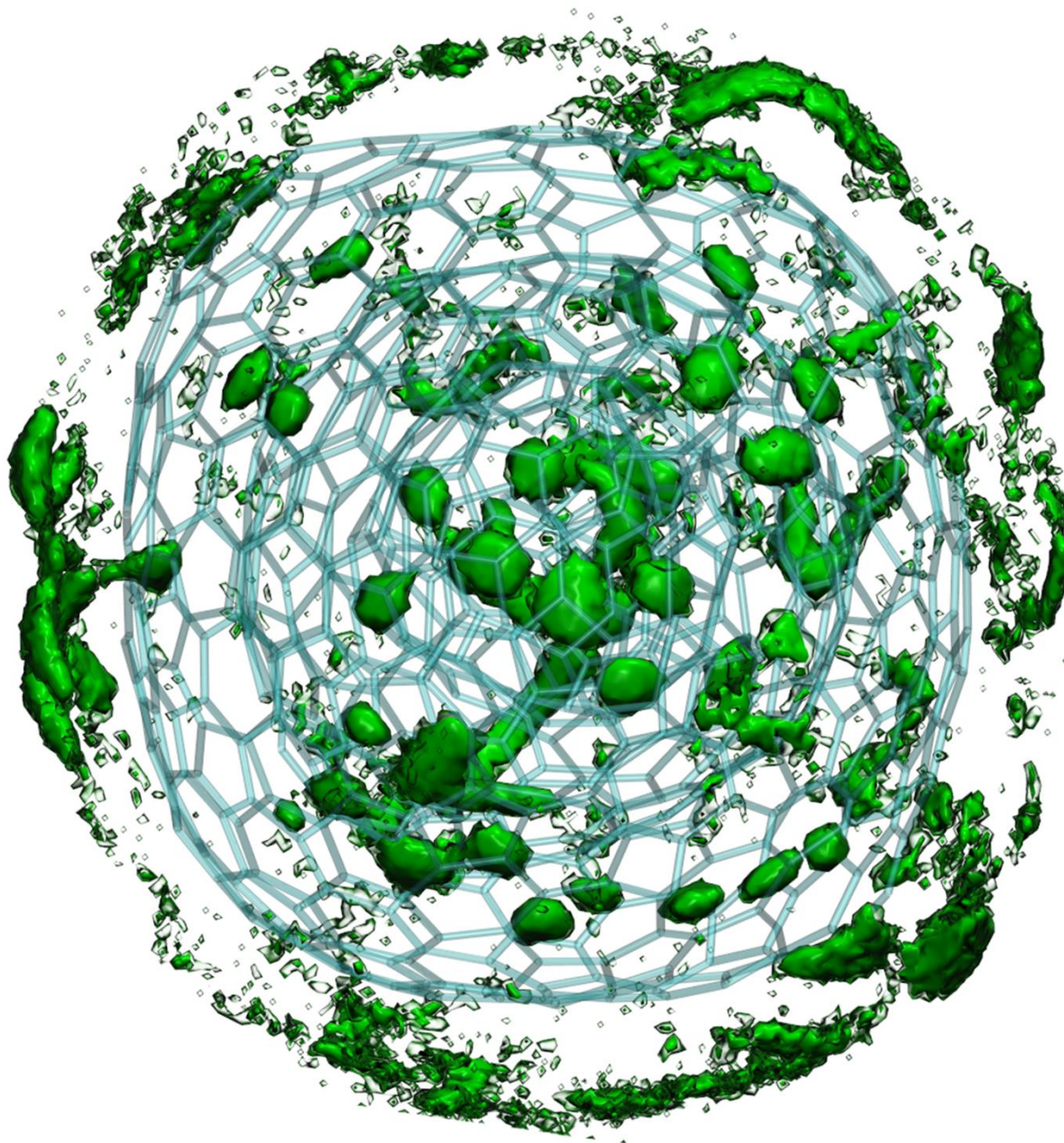


Figure 5.12. Density plot of Li (green) in an OLC during a NVT simulation at 1000 K. The inset shows a Li diffusing through a 16 membered ring.

5.4 Summary and Conclusions

To conclude, we have developed and applied a ReaxFF reactive force field to describe Li/C interactions in carbon based materials with and without defects. The Li/C ReaxFF reactive force field is able to describe energetics of Li adsorption as well as Li migration barriers in

pristine/defective graphene and graphite. Molecular dynamics simulations suggest that a critical Li density is required to enable Li intercalation into graphite. The force field successfully obtains the stepped voltage profile of Li intercalation in graphite seen in experiment¹⁹². In the presence of vacancy defects we observe an increase in the Li/C ratio and an upward shift in the voltage profile, both in proportion to the number of vacancy defects. The larger adsorption energy of Li in defects explains the upward shift as well as the increase in Li/C ratio in presence of defects. The Li-Li separation in Li clusters adsorbed on divacancy defect sites approaches Li-Li separation in bcc-Li metal and should initiate subsequent plating of Li metal at these sites as observed experimentally¹⁹⁵ in porous graphene networks. In carbon onions we observe that the outer-surface provide sites for Li adsorption with fast charging/discharging rates. However the inner volume is inaccessible for Li intercalation due to high diffusion barriers.

We have successfully demonstrated that our force field enables investigation of energetics as well as kinetics of Li intercalation in carbon based materials with/without defects using large-scale atomistic simulations and can be a useful tool for an atomistic understanding of novel processes in carbon nanostructures as well as designing improved carbon (nano)-materials for energy applications.

6 Transfer of Aqueous Protons Across Single Layer Graphene

Please note that the experiments and DFT calculations in this work were performed by our collaborators. Raju M performed the ReaxFF calculations

6.1 Introduction

Brick-and-mortar networks of stacked graphene oxide nanosheets, can act as effective membranes for separating certain atoms, ions, and molecules from one another²⁰²⁻²⁰⁹. In contrast, single layer graphene exhibits dramatically lower permeability towards gases^{205, 210} and is thought to be unfit for proton transfer, which is associated with computed gas phase energy barriers exceeding 1.4 eV²¹¹ unless dopants or nanoscale openings are externally introduced^{207, 208, 211, 212}. To test this prediction experimentally, we placed well-characterized single-layer graphene prepared as previously described^{213, 214} on top of a fused silica substrate and cycled the bulk pH of an aqueous solution above the graphene layer between basic and acidic. We tested for proton exchange through graphene by probing the underlying silica surface with an interfacial potential-dependent version of second harmonic generation (SHG, **Figure 6.1a**)^{215, 216} using 120 fsec input pulses at energies well below the graphene damage threshold^{213, 214}. With a detection limit of 10^{-5} to 10^{-6} V²¹⁷, the method is sensitive enough to follow protonation or deprotonation of as little as 1% of the available silanol groups present in the area probed by SHG. The interfacial potential vanishes at the point of zero charge (PZC of fused silica ~ 2.5)²¹⁸ and the SHG signal intensity is small^{215, 219, 220}. Increasing the pH at constant ionic strength shifts the relevant interfacial acid-base equilibria $\text{SiOH}_2^+ + \text{OH}^- \rightleftharpoons \text{SiOH} + \text{H}_2\text{O}$ and $\text{SiOH} + \text{OH}^- \rightleftharpoons \text{SiO}^- + \text{H}_2\text{O}$ ($\text{pK}_a \sim 4.5$ and ~ 8.5)^{215, 219, 221} to the right and the resulting interfacial potential polarizes the interfacial water molecules such that the SHG signal intensity increases^{215, 219}. Intuitively, the close proximity of the graphene layer and the charged fused silica surface, combined with the sensitivity of the

method, make our approach akin to an Å-scale voltmeter for detecting even rare occurrences of proton exchange.

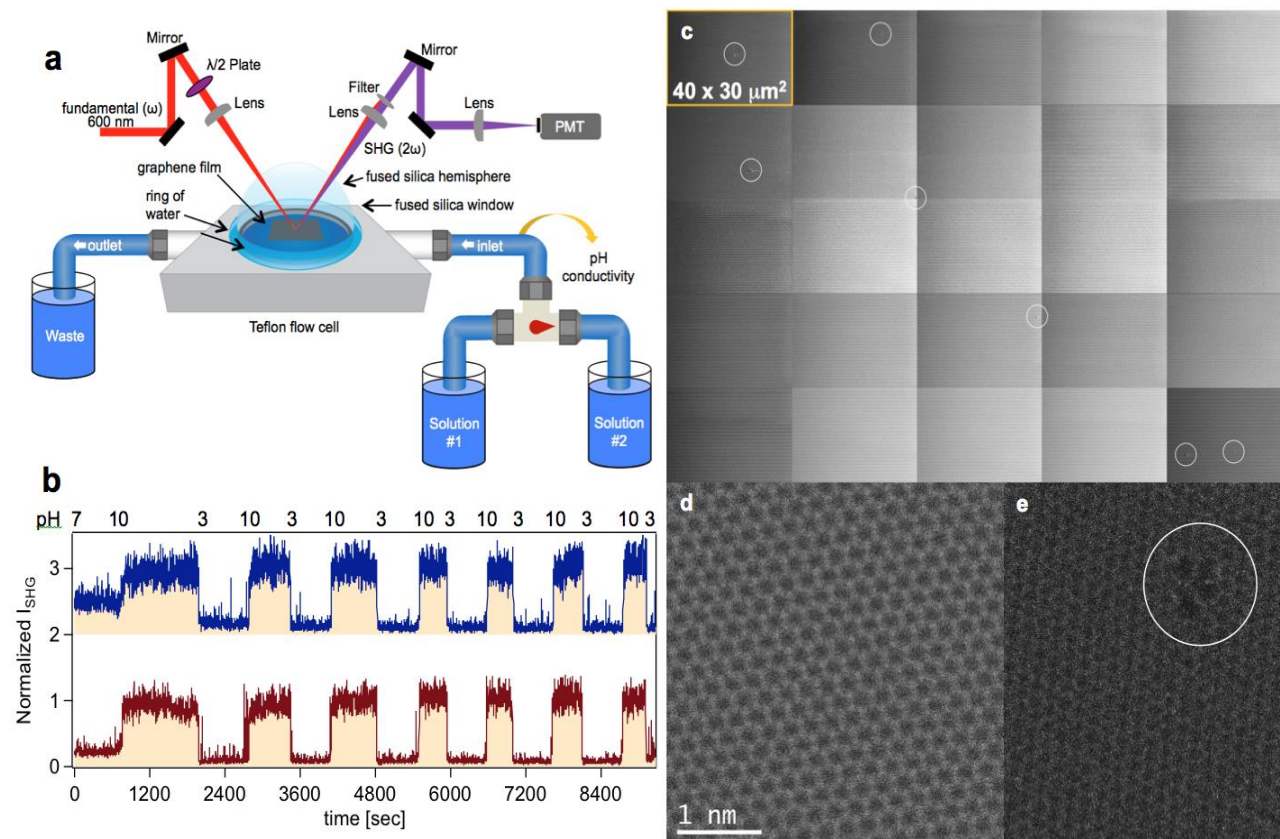


Figure 6.1. (A) Dual-pump flow system employed in the nonlinear optical studies using a waveplate ($\lambda/2$) to set the input polarization of the 600 nm probe light field to plane-polarized parallel to the plane of incidence while detection of the second harmonic generation photons at $\lambda=300$ nm is achieved using a photomultiplier tube (PMT) and single photon counting techniques as described in the Supplementary Information. (B) p-in/all-out Polarized SHG E-field recorded as a function of time from the fused silica/water interface during pH jumps from 7 to 3 to 10 and subsequent pH cycling between 3 and 10 at a bulk aqueous flow of 0.9 mL/sec and an NaCl concentration of 1 mM in the absence (crimson, bottom) and presence (blue, top) of single layer graphene placed between the fused silica substrate and the flowing bulk aqueous phase. (C) Composite of 25 SEM images of single layer graphene on a fused silica substrate, showing 7 macroscopic pinholes, marked by white circles. (D) High resolution aberration-corrected ADF STEM images of defect-free single layer graphene on a TEM grid and (E) of a rarely imaged atomic defect.

Experimental Methods

A detailed description of the Second Harmonic Generation (SHG) setup has been described previously.²²²⁻²²⁵ Briefly, a regeneratively amplified Ti:sapphire system (Hurricane, Spectra Physics) operates at kHz repetition rate producing 120 femtosecond pulses to pump an optical parametric amplifier (OPA-CF, Spectra Physics) tuned to produce 600 nm light. After exiting the OPA, the beam is then directed through a variable density filter to attenuate the pulse energy to either $0.3 \pm 0.05 \mu\text{J/pulse}$ for bare silica studies, or $0.15 \pm 0.05 \mu\text{J/pulse}$ per pulse for graphene studies. The pulse energy used for the graphene films equates to a power density of $2.1(7) \times 10^4 \mu\text{J/cm}^2$ per pulse with a $30 \mu\text{m}$ focal spot, which is well below the damage threshold of graphene as previously reported.^{213, 226} At an angle just below total internal reflection, the p-polarized attenuated fundamental light is then directed through a fused silica hemisphere and focused at the graphene/water or silica/water interface. The reflected fundamental and second harmonic lights are directed through a Schott filter and a monochromator to remove the any contributions at the fundamental frequency before amplification with a PMT and detection using a gated single photon counting system.

The pH jump experiments were carried out using both a fused silica hemisphere (ISP Optics, 1" diameter, QU-HS-25) along with either a fused silica window (ISP Optics, 1" diameter, QI-W-25-1), or a CVD prepared graphene film transferred onto a silica window in an experimental setup previously reported.^{213, 226} The hemisphere and fused silica window were cleaned prior to experiments by first treating the surface of interest with NoChromix (Godax Laboratories) for 1 hour, rinsing with Millipore water and then storing in Millipore water overnight for SHG experiments the next day. The day of the experiment, the bare silica window and hemisphere were

sonicated in methanol for 6 minutes, dried in a 110°C oven for 30 minutes, oxygen plasma cleaned (Harric Plasma) on high for 30 seconds, and then stored in Millipore water until the experiment. The graphene samples were not cleaned with this procedure, and were instead cleaned by flushing with approximately 2 L of Millipore water before each experiment. A schematic of the experimental setup is shown in **Figure 6.1A**. In the experimental setup the graphene sample or silica window was clamped face down against a Viton O-ring on the Teflon flow cell^{213, 226} so that the surface of interest was in contact with the aqueous phase. The fused silica hemisphere was then clamped on top of the window with a Millipore water layer in between in order to minimize the change of refractive index between the phases and to avoid use of an index-matching fluid. Throughout the duration of the experiment it was also necessary to maintain a ring of Millipore water around the bottom of the hemisphere in order to avoid evaporation of the sandwiched water layer.

The aqueous solutions were prepared with Millipore water, prepared the day prior to an experiment and left open to air overnight to equilibrate with atmospheric CO₂, and NaCl (Alfa Aesar, 99+%). The concentration of NaCl was confirmed using a conductivity meter (Fisher Traceable Conductivity and TDS meter, Fisher Scientific). Solution pH was adjusted with minimum amounts of dilute solutions of ~1M NaOH (Sigma-Aldrich, 99.99%) and HCl (EMD ACS grade).

All of the experiments were completed with a 0.9 mL/sec flow using variable flow peristaltic pumps as previously reported.^{213, 226} Using the flow system as depicted in **Figure 6.1A** of the main text, the pumps were switched to pull solutions from two different reservoirs. For the experiments reported here, the two reservoirs contained 1mM NaCl Millipore solutions adjusted to either pH 3 or pH 10. At the start and end of each pH jump experiment, a 1 mM NaCl aqueous

solution adjusted to pH 7 was pumped through the system and the SHG signal was collected until it reached steady state. It is assumed that steady-state conditions were reached once the SHG signal remained at a stable intensity for a minimum of 300 seconds. After the system reached steady-state at pH 7, the flow was switched back and forth between the pH3 and pH10 aqueous solutions, each time allowing the SHG signal to reach steady-state before switching to the next pH. After several pH 3 to 10 and pH 10 to 3 jumps were completed, the pH was adjusted back to pH 7, and the SHG signal was collected until steady-state was reached one last time. A plot of the SHG signal intensity (I_{SHG}) vs time and pH is shown in **Figure 6.1B**.

Computational Methods

In the DFT calculations, the reaction systems were modeled by optimizing a water phase above and below a single graphene sheet. The simulations were carried out in a 5×5 supercell comprised of 50 carbon atoms, was extended infinitively in the x and y dimensions. A 15 Å gap was inserted between the graphene layer perpendicular to the surface. The gap was subsequently filled with enough water molecules to match the overall density of water at $1.0 \times 10^3 \text{ kg/m}^3$. The initial simulations were carried out with water on both side of the graphene layer. The lower SiO_2 substrate was simplified by using additional water. Subsequent calculations were carried out with more realistic slabs comprised of water/graphene/water/ SiO_2 substrates. The reaction rates and mechanisms of proton transfer through the graphene were described in the framework of transition state theory and within the harmonic approximation, which is robust for systems of high densities.

The activation barriers and energies were calculated using periodic density functional theory calculations using the Vienna Ab Initio Simulation Package (VASP). All of the calculations were carried out within the Generalize Gradient Approximation using Perdew-Burke-Ernzerhof (PBE) functional to treat exchange and correlation gradient corrections and PAW

pseudopotentials²²⁷ to describe the electron-ion interactions. Plane wave basis sets with a cutoff energy of 400 eV were used to solve the Kohn–Sham equations for calculations for systems without water. Calculations for systems that include water solvation were carried out with cutoff energies for C and O of 283 eV. The surface Brillouin zone was sampled using a Monkhorst-Pack mesh of $3\times3\times1$. All electronic energies were converged to within a tolerance of 1×10^{-5} eV. All of the atoms were allowed to relax in the geometry optimizations until the forces on each atom were less than 0.03 eV/Å. Spin polarization was examined for all of the systems explored and applied when needed. Transition states were isolated using the nudged elastic band (NEB) method together with the dimer method. The NEB method was used to provide a initial transition state structure that was used in the subsequent dimer simulations to isolate the transition state. The reaction barrier was defined as the energy difference between the transition state and the reaction state minimum. The intrinsic barrier is defined as the energy gap between a transition state and its immediate reaction state.

The ReaxFF simulations were performed using the stand-alone ReaxFF implementation to study proton transfer through pristine graphene and graphene with di- and quad- vacancies. In our simulations we used a (6x6) periodic graphene sheet with water molecules placed in random configurations on either side of the graphene sheet. The dimensions of the simulation cell are 15.01 Å x 17.83 Å parallel to the sheet and 30 Å in the direction perpendicular to the sheet. All MD simulations have been performed in the canonical (NVT) ensemble, with a time step of 0.25 fs using the Berendsen thermostat with a coupling time constant of 100 fs to control temperature of the entire system. To obtain the density plots in Figure 6.3, we first divided the simulation cell into a mesh of cubic boxes with dimensions (0.30 Å x 0.30 Å x 0.30 Å). We then counted the number of times a particular atom type (*e.g.*, oxygen) was located in each of the grids through the entire

length of simulation and normalized these numbers by the highest count recorded in any of the grids. We used these normalized values to obtain the resulting density plots in Figure 6.3.

6.3 Results and Discussion

As shown in **Figure 6.1b**, we find no significant difference between the SHG vs. time traces recorded in the presence and absence of graphene, and no statistically significant differences in the kinetic rates and jump durations. Porous graphene multilayers do not inhibit proton transfer either. The SHG response to pH changes of the bulk solution are consistent with the two well-known^{215, 216, 220, 228} acid-base equilibria of the fused silica/water interface, indicating the SHG experiments do not track merely ion adsorption to the graphene/water interface but acid-base chemistry at the fused silica surface underneath the graphene film, for which proton transfer across the membrane is a necessary condition.

Scanning electron microscopy (SEM) images of graphene single layers deposited on fused silica windows show a low density of macroscopic pinholes-and that the graphene is free of cracks or folds (**Figure 6.1c**). Using 2D proton diffusion coefficients that account for proton trapping^{229, 230} by the surface silanol groups^{231, 232}, we estimate a 4% to 21% likelihood of focusing the 30 μm diameter laser beam onto an area that is subject to two-dimensional proton diffusion around a given pinhole. Additional computer simulations reveal slow water-self diffusion and a strongly enhanced local water structure at high pH near the silica surface, and fast protonation of surface SiO^- groups, indicating negligible 2D proton mobility under basic conditions. The diffusion of protons from the few macroscopic pinholes that are present in our samples, or from the sample edge, to the area probed by the laser can therefore not explain our observations of proton transfer through graphene.

Scanning transmission electron microscopy (STEM) was then used to search for atomic defects using annular dark field (ADF) STEM imaging at 60 kV. The majority of the images show

perfect six-fold symmetry in the position of the carbon atoms and vast areas that lack grain boundaries and atomic, or vacancy, defects (**Figure 6.1d**). Nevertheless, similar to prior reports of atomic scale vacancy point defects^{233, 234}, we find, albeit rarely, atomic defects (**Figure 6.1e**). These defects could originate from the synthesis process or cosmic rays, as the STEM experiments are carried out below the knock-on damage threshold for graphene²³⁵, while the femtosecond laser pulses are attenuated below the onset of processes other than SHG^{213, 214}.

We then used density functional theory (DFT) calculations (**Figure 6.2**) and ReaxFF reactive force field molecular dynamics simulations (**Figure 6.3**)²³⁶⁻²³⁸, respectively, to elucidate the mechanisms for proton transfer. DFT simulations track the detailed changes in the electronic structure and quantify corresponding activation barriers as protons transfer from the water layer through the graphene interface and exit into solution on the opposite side of the surface, whereas the ReaxFF simulations provide a more detailed representation of the interfaces and more rigorous accounting of the dynamics. We find that the main restriction for aqueous proton transfer through pristine, defect-free graphene is the energy required to push the proton into the center of the graphene. The water molecules above and below the graphene layer are unavailable for participation in this process as the non-defective graphene surface is hydrophobic. The energy difference that is reported is due to the initial reference (or reactant) state. Release of the proton from an aquated hydronium ion towards the graphene layer is associated with an energy penalty of ~ 0.65 eV as the initial O-H bond needs to be broken.

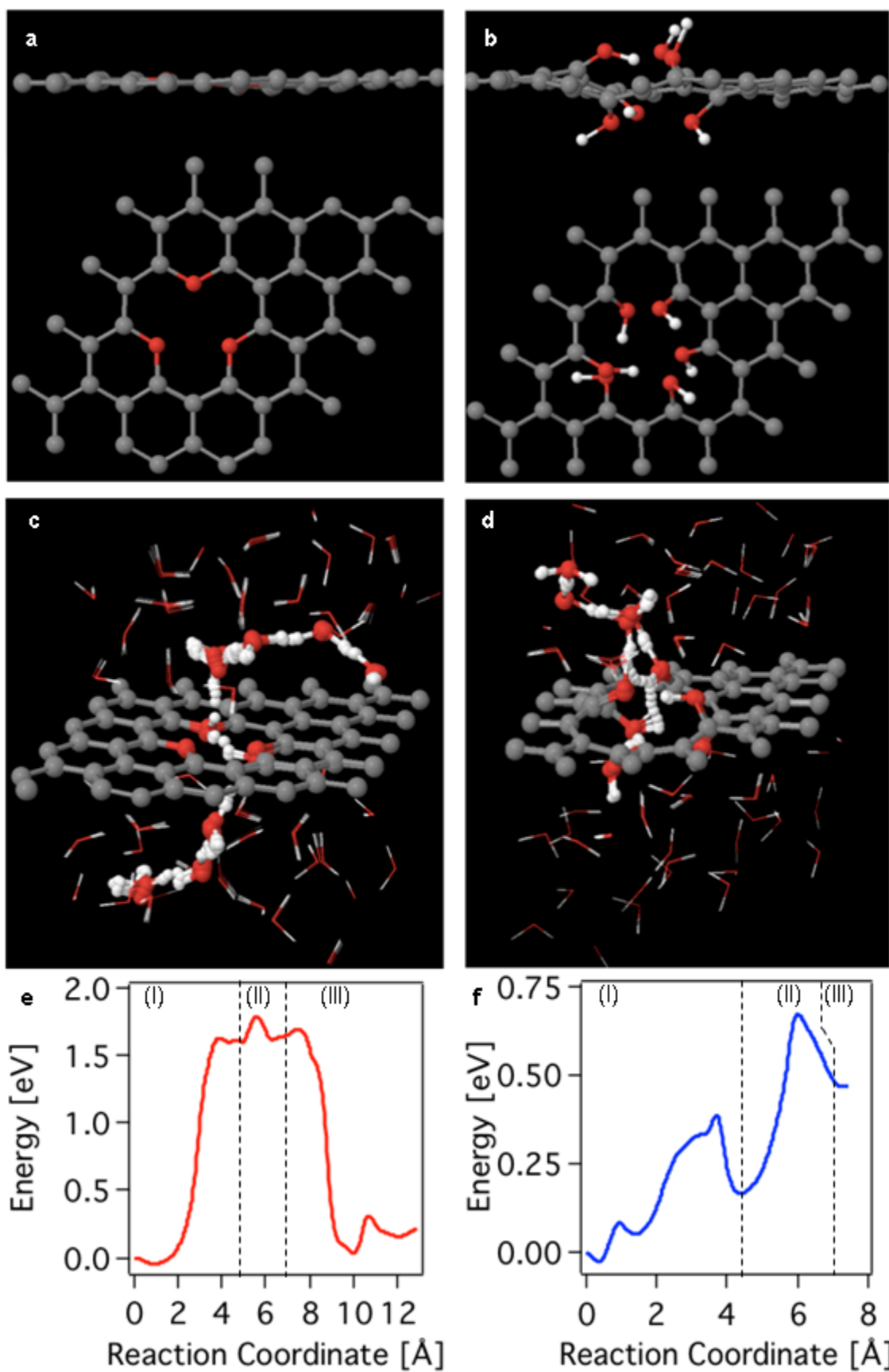


Figure 6.2. Side and top views of oxygen- (**A**) and OH- (**B**) terminated defect models used in the DFT calculations. Snapshots (**C**, **D**) and energetics (**E**, **F**) from the nudged elastic band calculations for proton transfer through the ether- and OH- terminated defect sites marking (**region I**) release of proton from H_3O^+ to ether and OH group, respectively; (**region II**) relay of proton between ether and OH groups, respectively; (**region III**) release of proton from ether and OH groups to H_3O^+ , respectively. Denotations of spheres: grey=carbon; red=oxygen; white=hydrogen atoms.

The activation barrier for proton transfer through graphene was calculated to decrease from over 3.0 eV to less than 1.0 eV in the presence of atomic scale defect sites (**Error! Reference source not found.**). DFT and ReaxFF simulations indicate that the proton transfers from the solution phase to the surface through the center of the defect site and into the solution on the opposite side of the membrane via a Grotthuss²³⁹ mechanism involving proton shuttling. The solution phase proton shuttling paths occur with barriers of < 0.2 eV whereas the barrier to transfer through a given defect site is somewhat higher due to limited access of water and OH groups required for proton shuttling.

Table 6.1. DFT and ReaxFF-calculated activation barriers for proton transfer through different vacancy sites on graphene in water.

Graphene Surface	Bottom Layer	Defect Termination	Activation Barrier	Reax
No vacancy	water	No termination	3.9 eV	6.20 eV
1V	water	No termination	> 2.0 eV	3.54 eV
4V	water	No termination	0.25 eV	0.22 eV
4V	water	3O ether capped	1.8 eV	1.7 eV
4V	water	6OH hydroxyl capped	0.68 eV	0.61 eV
4V	SiO_2	3O ether capped	2.5 eV	2.53 eV
4V	SiO_2	6OH hydroxyl capped	0.7 eV	0.75 eV

The quad vacancy site (4V) was found to be the smallest defect site large enough to facilitate proton transfer through graphene (**Error! Reference source not found.**). This site is comprised of 6 coordinatively unsaturated carbon atoms that are either terminated with 3 oxygen atoms in epoxide-like arrangements reminiscent of pyrylium cations, or with 6 hydroxide groups. Proton transfer through the epoxide-terminated 4V site requires 1.7 eV (**Figure 6.2a**), which we attribute to the fact that the pyrylium-like oxygen atoms are not protophilic and, furthermore, lie in the plane of the graphene, thus leaving a 3.4 Å gap between water and the graphene substrate that prevents proton transfer. The hydroxyl-terminated site, however, provides hydrogen bonding conduits via a Grotthuss mechanism that lowers the barrier to proton transfer to just 0.65 eV (**Figure 6.2b**), indicating it will occur at room temperature. ReaxFF simulations show that a water channel, which establishes itself as proton transfer occurs, thins when the three pairs of OH groups terminating the defect site are replaced, one by one, with oxygen atoms (**Figure 6.3a-c**). The proton transfer channel is fully disrupted when the defect site is terminated by three oxygen atoms (**Figure 6.3**). These transfer paths are selective to aqueous protons as helium and H₂ transfer involve barriers exceeding 1.9 eV.

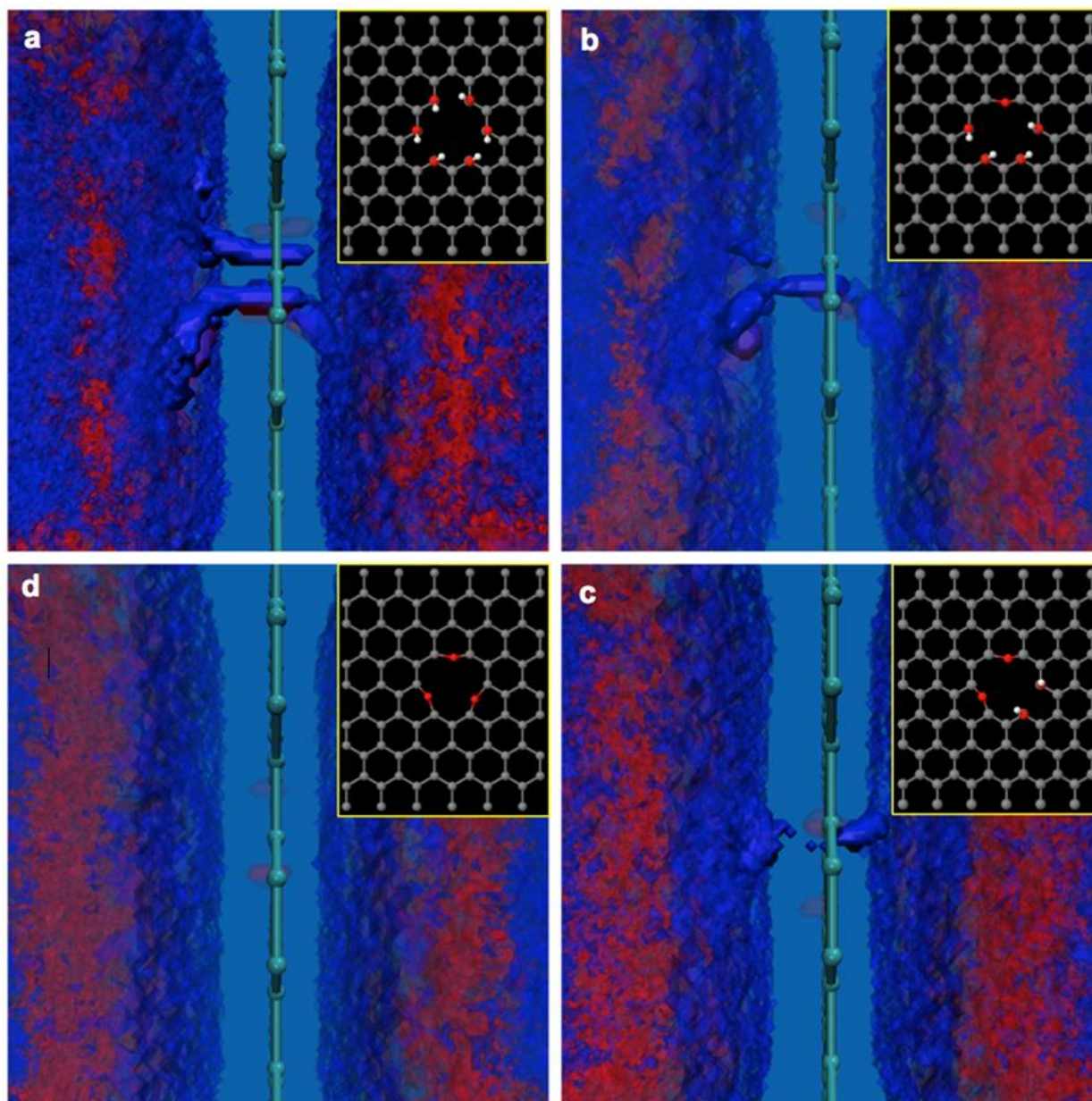


Figure 6.3. Water channel formation from molecular dynamic simulations using the ReaxFF force field carried out a constant number, volume, and 300 K temperature and water mediated proton transfer through atomic defects terminated in 6 OH groups (A), 4 OH groups and one oxygen atom (B), 2 OH groups and two oxygen atom (C), and three oxygen atoms (D).

Denotations of spheres: grey=carbon; red=oxygen; white=hydrogen atoms.

ReaxFF Force Field Validation for Proton Transfer Barriers.

Table 6.1 gives the comparison of activation barriers for proton transfer through different vacancy sites on graphene in water calculated by ReaxFF and DFT. ReaxFF over predicts the

barriers for proton transfer in the pristine and 1V case. However the barriers given by DFT for the pristine and 1V case are high (3.9 eV and >2.0 eV respectively) and are unsurmountable during MD simulations at 300 K. The relevant systems are the 4V cases and the barriers given by ReaxFF are in good agreement with DFT for these systems. As discussed in the main text, our MD simulations are performed for these relevant systems involving various terminations of 4V graphene and we observe proton transfer channels in the presence of hydroxyl group terminations. Note that ReaxFF was not specifically trained against any of these barriers.

The self-diffusion coefficient of water at 298K given by ReaxFF ($2.1 \times 10^{-5} \text{ cm}^2/\text{s}$) is comparable to the values given by diaphragm-cell technique⁵⁵ ($2.272 \times 10^{-5} \text{ cm}^2/\text{s}$) and pulsed magnetic field gradient (PFG) NMR ($2.299 \times 10^{-5} \text{ cm}^2/\text{s}$) studies.⁵⁶ ReaxFF also reproduces the proton diffusion constant ($9.04 \times 10^{-5} \text{ cm}^2/\text{s}$) in water at 298 K in good agreement with experimental studies²⁴⁰ ($9.31 \times 10^{-5} \text{ cm}^2/\text{s}$). DFT and ReaxFF calculations predict water dissociation on a 1V site in graphene to be exothermic with an activation barrier of 47.79 kcal/mol and 36.83 kcal/mol respectively.

ReaxFF simulations of Proton Diffusion.

For complex systems with multiple potential proton transfer sites, ReaxFF provides a suitable alternative to the multistate empirical valence bond (MS-EVB) method developed by Voth and coworkers that can successfully describe the proton transport in water and biomolecular systems.²⁴¹ For extremely complicated system with multiple potential reactions under consideration here, the MS-EVB is no longer applicable because this approach requires a combination of states, which represent the chemical bonding topologies involving the proton. In our applications, we have used the ReaxFF method for water/proton/silica systems.²⁴² In addition, ReaxFF also reproduces experimental results for both water self-diffusion and proton diffusion in

water.²⁴³ We therefore employed ReaxFF MD simulations to calculate proton and water self-diffusion constants in water confined between graphene and α -quartz(001) surface. The diffusion constants provide an estimate of the area accessible via proton diffusion during a time t from which we compute the probability that the rise and drop of the SHG response over graphene is due to pinholes.

ReaxFF, being a reactive force field, takes chemical reactivity into account, which, as discussed below, is of significance in describing proton diffusion in the presence of surface SiO^- species. The simulated system consists of water molecules sandwiched between graphene and quartz surfaces separated by 1.4 nm as shown in **Error! Reference source not found.** In our simulations we used a periodic quartz (001) slab with (6 x 4) unit cells parallel to the surface with 2 layers of SiO_2 and a periodic graphene sheet with (10 x 5) unit cells parallel to the surface. Water molecules and protons were placed in random configurations between the quartz and graphene surfaces. The dimensions of the simulation cell are 24.73 Å x 13.84 Å parallel to the surface and 25 Å in the direction perpendicular to the surface.

The system was energy minimized with convergence criterion of 0.5 kcal/Å and equilibrated in the canonical (NPT) ensemble for 100 ps at 300K, with a time step of 0.25 fs using the Berendsen thermostat with a coupling time constant of 100 fs and Berendsen barostat with a coupling time constant of 500 fs to control temperature and pressure of the entire system. We perform MD simulations on the equilibrium configuration for 125 ps at 300K to calculate the proton and water self-diffusion constants. In these simulations the equilibration time was 25 ps and the subsequent production run was 100 ps.

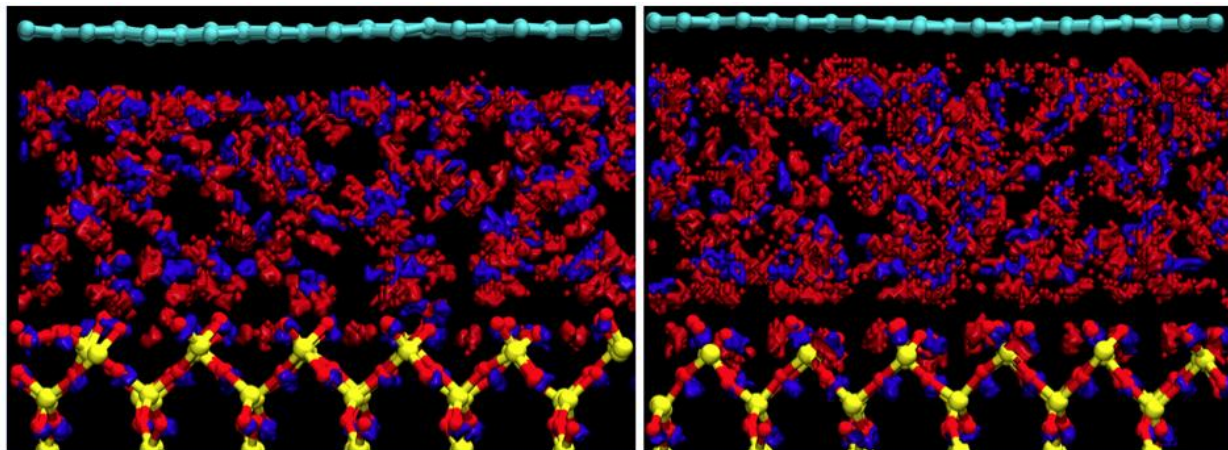


Figure 6.4. Density plot of oxygen(blue) and hydrogen(red) in the silica/water/graphene interface, as obtained during a 300K ReaxFF molecular dynamics simulation. (A) structure at high pH (40% SiOH/60% SiO⁻; OH-ions in water solution) – showing very strong local water structure and 20-fold reduced water self diffusion (B) water structure at neutral/low pH (100% SiOH; pure H₂O) showing more liquid water structure and water self-diffusion comparable to bulk water. Denotations of spheres: yellow=silicon; red=oxygen; cyan=carbon atoms.

We consider two cases; partially hydroxylated (40% SiOH) and fully hydroxylated (100% SiOH) α -quartz(001) surfaces for calculation of the diffusion constants. The self-diffusivity of nano-confined water is reduced roughly by a factor of 24 for the partially hydroxylated ($9.537 \times 10^{-7} \text{ cm}^2/\text{s}$) case and is comparable to liquid water for the fully hydroxylated ($2.892 \times 10^{-5} \text{ cm}^2/\text{s}$) case. **Error! Reference source not found.** gives the density plot of oxygen (blue) and hydrogen (red) atoms in the simulation box during a NVT run at 300 K for (a) partially-hydroxylated and (b) fully-hydroxylated case. As shown in **Error! Reference source not found.** A the partially hydroxylated case shows a strongly enhanced ‘ice-like’ local water structure close to the silica surface whereas the fully hydroxylated case shows a more diffuse water structure similar to liquid water. The O-O separation (2.47 \AA) for SiO⁻...HOH hydrogen bonds at the partially hydroxylated quartz surface is significantly shorter than O-O separation in bulk water (2.83 \AA) indicating the presence of strong hydrogen bonds at the partially hydroxylated quartz/water interface. These strong hydrogen bonds give rise to the ‘ice-like’ water structure at the partially-hydroxylated

quartz/water interface and leads to very low water self-diffusion near the silica surface. The silanol groups on the fully hydroxylated surface forms intralayer hydrogen bonds with surface O atoms on the adjacent row in the V-shaped ridges and doesn't interact with the water phase above giving rise to a vacuum gap between the fully hydroxylated quartz surface and the water phase as shown in **Error! Reference source not found.B**. This explains the absence of local water structure and faster self-diffusivity at the fully hydroxylated quartz/water interface.

In simulations containing partially hydroxylated quartz surfaces the proton diffusion is quickly terminated by protonation of the surface SiO^- groups. This indicates that proton diffusion is significantly slower in the presence of surface anionic species due to proton trapping at these sites and the slower water self-diffusion (~factor 24 reduction compared to liquid water). XPS studies by Duval *et. al*²⁴⁴ reports that surface SiO^- species is present on quartz in the pH range 1 to 10 indicating that proton diffusion is significantly lowered for the entire studied experimental pH range. For the fully hydroxylated case the proton diffusion constant is reduced roughly by a factor of 2 compared to bulk water ($4.944 \times 10^{-5} \text{ cm}^2/\text{s}$).

Since the Grotthuss mechanism plays a key role in the proton transport in solution, we evaluated the sequence of proton transport events in our system.²⁴⁵ In the present work, the oxygen (O^*) of the water with an excess proton is distinguished from the neutral water molecules. The same index number of O^* between two adjacent frames from MD trajectory indicates the vehicular transport without proton hopping. If the O^* index changes between frames, it indicates Grotthuss hopping transport. Using a time-dependent trajectory of O^* , the diffusion constant of proton transport is calculated based on mean-square displacement and Einstein relation.

Validation of ReaxFF for water/graphene interfaces.

To validate the ReaxFF graphene/water molecular dynamics, we compare results from molecular dynamics simulations of water on graphene (Figure 6.5a) between our reax force-field to long *ab initio* molecular dynamics (AIMD) to validate predictions of force-field in describing water/graphene systems. Figure 6.5b and c shows the number density profile of oxygen and hydrogen, comparing AIMD results with our ReaxFF force field. While the strength of the first peak is significantly higher using Reax, the position of the first peak compares very well between the two methods. In addition, the $n_H(r)$ profile shows the presence of a $\sim 1\text{\AA}$ hydrophobic gap, in good agreement with AIMD as well as existing experiments^{246, 247}. The peak is around $\sim 2.4\text{\AA}$ from the graphene surface using both AIMD and reax, suggesting that the water orientation is captured properly using reax at the interface. Beyond $\sim 7\text{\AA}$, water fluctuates about its bulk density.

AIMD was performed using the VASP²³⁶ code and a PBE exchange correlation functional with Grimme parametrization to describe the van der Waals interaction¹⁸⁶. The AIMD was performed at $T=300\text{K}$, with a time step of 0.5 fs, for 43 ps. ReaxFF molecular dynamics were performed for over 150 ps at $T=300\text{K}$. All simulations are for an NVT ensemble at a density of 1g/cc with a hundred water molecules.

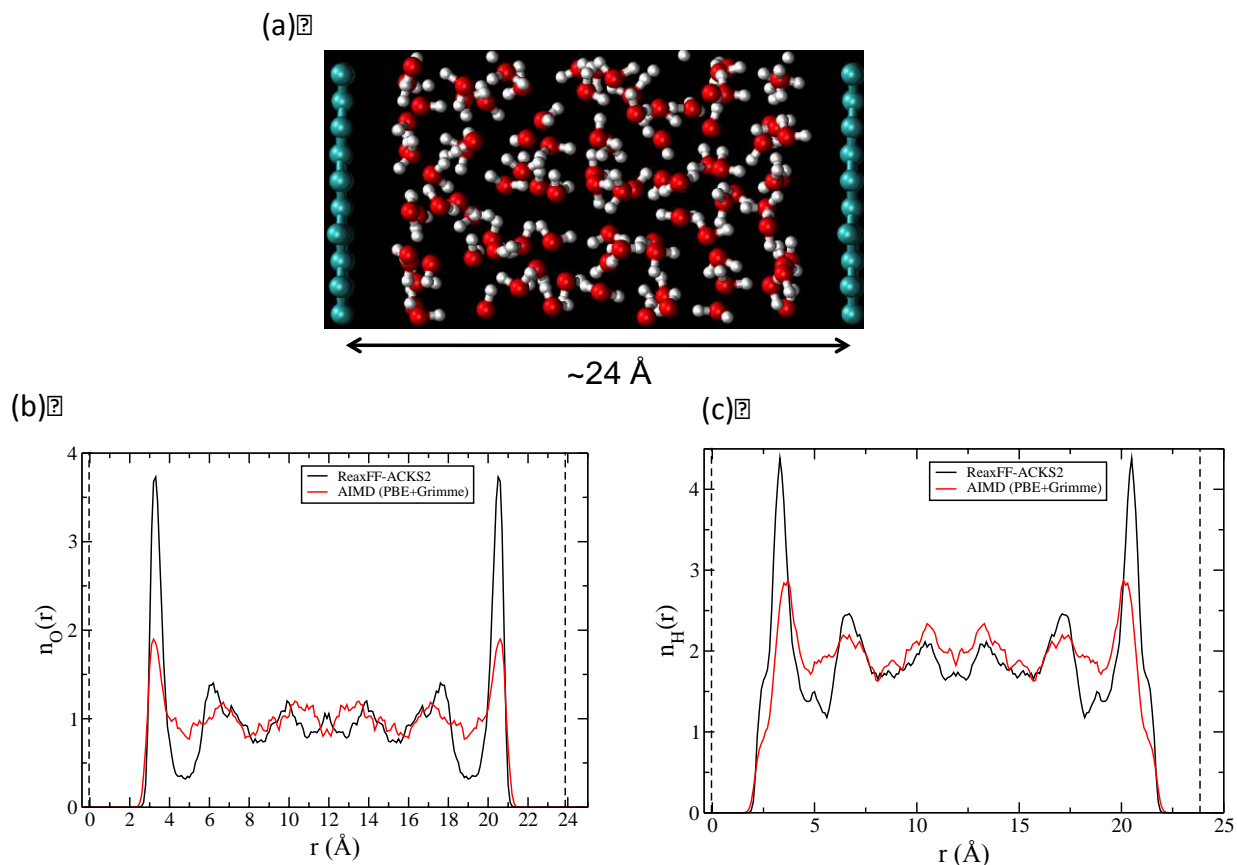


Figure 6.5 (a) Graphene/water system used in the ReaxFF/AIMD simulations (b) oxygen number density profiles obtained from the ReaxFF/MD and AIMD simulations (c) hydrogen density profiles obtained from the ReaxFF/MD and AIMD simulations.

Heats of Formation for the considered ether/hydroxyl defect terminations

We perform MD-NVT simulations for the various ether/hydroxyl group terminations (3ether, 2ether +2OH, 1ether+4OH, 6OH) considered in this study in the presence of a bulk aqueous phase to investigate their relative stabilities at room temperature. We consider a periodic bare quad-vacancy graphene sheet with (10 x 5) unit cells parallel to the surface in contact with a bulk aqueous phase containing 96 water molecules as the reference state. The bare quad-vacancy graphene/water system is considered as the reference state since the graphene sheet utilized in the experimental studies contains defect sites. The various defect terminations were manually prepared by introducing the various terminations at the defect site and solvating the excess protons in the

aqueous phase. The systems were energy minimized with convergence criterion of 0.5 kcal/Å and equilibrated in the canonical (NVT) ensemble for 100 ps at 298.15K, with a time step of 0.25 fs using the Berendsen thermostat with a coupling time constant of 100 fs. The total system energy averaged over the final 20 ps of the NVT simulation was used to calculate the heats of formation as shown in Figure 6.6. Figure 6.6 gives the heats of formation for the various defect terminations, obtained by considering the bare quad-vacancy graphene/water system as the reference state. The 2ether+2OH termination is the most stable state followed by 3ether, 1ether+4OH and 6OH terminations. However all the considered defect terminations are energetically favorable as compared to the bare quad-vacancy system.

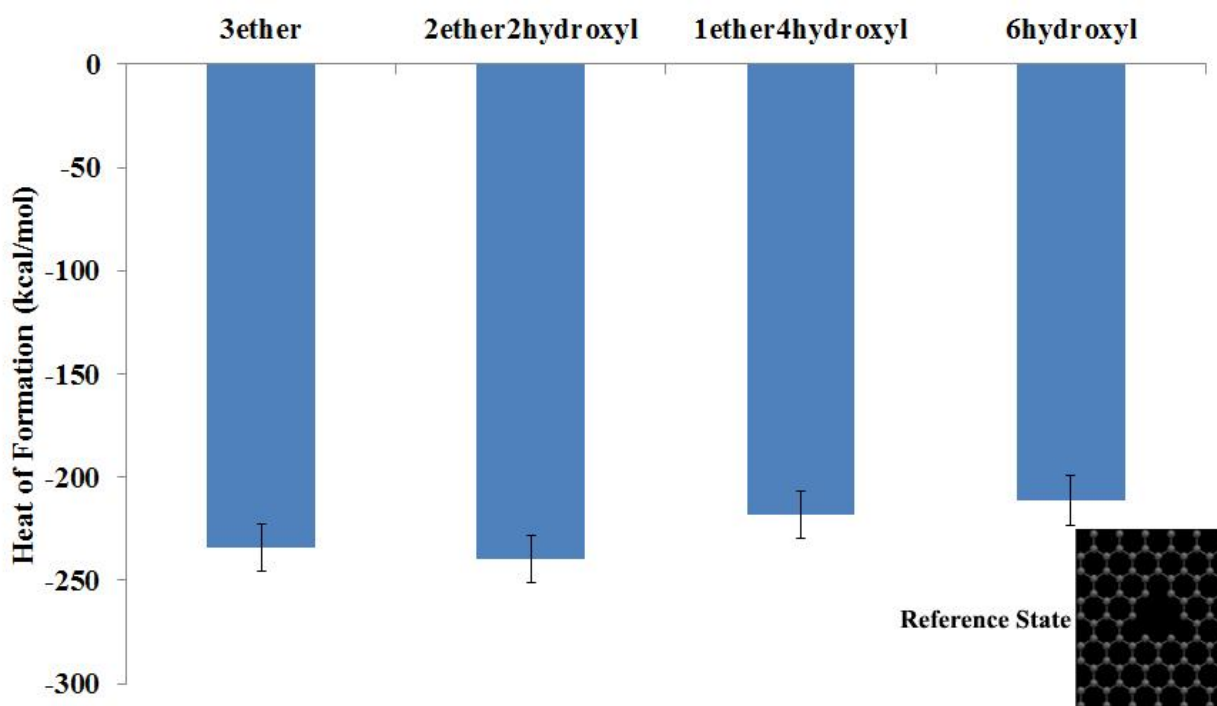


Figure 6.6 Heats of formation for various defect terminations on quad-vacancy graphene.

6.4 Summary and Conclusions

We conclude that aqueous protons transfer through single layer graphene via rare, OH-terminated atomic defects. From the SHG signal jump rates and the times required for 2D proton

diffusion, we estimate that just one atomic defect in the 30 μm laser spot is enough to allow for the apparent unimpeded protonation and deprotonation of the interfacial silanol groups. While the rarity of the atomic defect sites would make it challenging to follow proton exchange across graphene using pH-sensitive electrodes, the close proximity of the graphene layer and the charged fused silica surface, where the experimental observation of surface protonation and deprotonation is made by SHG, allows for the experimental observation of proton exchange across these rare defects. The identification of low barriers specifically for water-assisted transfer of protons through OH-terminated atomic defects in graphene, and high barriers for oxygen-terminated defects could be a first step toward the preparation of zero-crossover proton-selective membranes.

7 The effect of strong acid functional groups on electrode rise potential in capacitive mixing by double layer expansion

Please note that the experiments in this work were performed by our collaborators. Raju M performed the ReaxFF calculations

7.1 Introduction

Between 0.8-2.6 TW of power could be captured globally at estuaries through the natural mixing of sea and river water.^{248, 249} Capacitive mixing based on double layer expansion (CDLE), is an electricity-producing salinity gradient energy (SGE) technology that can harvest mixing energy using capacitive electrodes. Current competing pilot phase SGE technologies, pressure retarded osmosis (PRO) and reverse electrodialysis (RED), require the use of membranes, which increases capital costs²⁴⁹⁻²⁶⁰. CDLE utilizes only low cost activated carbon electrodes, potentially making CDLE the most sustainable conversion technique available for extracting energy from natural mixing processes²⁶¹⁻²⁶⁸.

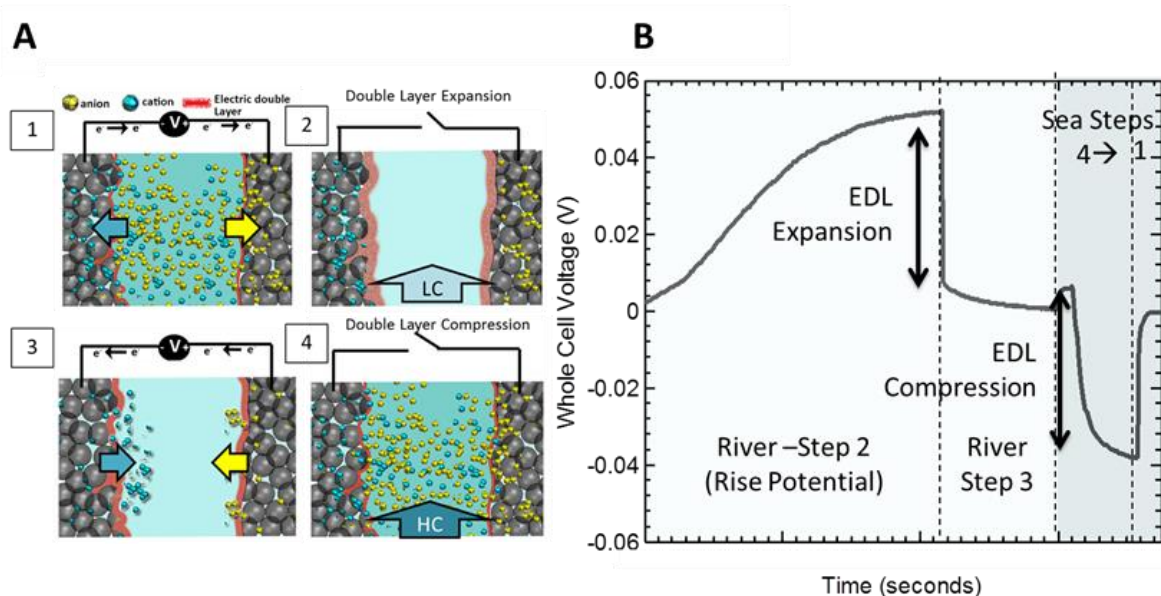


Figure 7.1. (A) Four step capacitive mixing based on double layer expansion process. Step 1: electrodes charged in HC. Step 2: under open circuit, LC replaces HC solution, causing the EDL to expand (generating energy). Step 3: electrodes discharged at a higher potential (energy

harvesting). Step 4: under open circuit, HC replaces LC, compressing the EDL. (B) Typical voltage response curve during a CDLE cycle with LC steps (2- EDL expansion and 3- Discharge) shaded in light blue, and HC steps (4- EDL compression and 1- Charge shaded in dark blue.

CDLE is the reverse of an emerging desalting technique termed capacitive deionization (CDI)²⁶⁹⁻²⁷³. Energy is used in CDI to extract ions from a concentrated salt solution using supercapacitor-based electrodes, while energy can be produced using CDLE from the mixing of high and low salt concentration solutions. Energy extraction with CDLE takes place through four-steps (

Figure 7.1. (A) Four step capacitive mixing based on double layer expansion process. Step 1: electrodes charged in HC. Step 2: under open circuit, LC replaces HC solution, causing the EDL to expand (generating energy). Step 3: electrodes discharged at a higher potential (energy harvesting). Step 4: under open circuit, HC replaces LC, compressing the EDL. (B) Typical voltage response curve during a CDLE cycle with LC steps (2- EDL expansion and 3- Discharge) shaded in light blue, and HC steps (4- EDL compression and 1- Charge shaded in dark blue.). Initially, electrodes are placed in a high salt concentration (HC, e.g. seawater) and they spontaneous charge (zero charging), although charge can be increased using an external power supply (force charging)^{262-264, 274, 275} (step 1). Zero charging is favored because this alleviates the need for an initial investment of energy into the system, and there is minimal charge leakage. Once this surface charge is established, the electrodes are placed in open circuit (no external load), and a low concentration (LC, e.g. river water) displaces the HC solution. The change in concentration results in a perturbation of the electric double layer (EDL) on each electrode. The change in the EDL thickness, typically evaluated in terms of changes in the Debye length (λ), increases the potential drop through the diffuse portion of the EDL [$\varphi_{EDL}^{\pm} = f(\lambda)$], elevating the whole cell potential (φ_{cell}) (step 2). The capacitive electrodes are then discharged (at the higher potential), and energy

is harvested through an external circuit (step 3). The cycle is completed when HC displaces the LC under open circuit (fixed surface charge) conditions, compressing the EDL (step 4)²⁶².

The extent of the EDL expansion and material capacitance (C) dictate how much energy is generated during the CDLE process [$E_{CDLE} = \frac{1}{2}C(2\phi_{EDL})^2$]. From the Poisson-Boltzmann equation and the Gouy–Chapman–Stern (GCS) model, the potential distribution in the diffuse portion of the EDL is:

$$\phi_{EDL} = \frac{2k_bT}{e} \sinh^{-1} \left(\frac{\sigma}{\sqrt{8C_s N_A \epsilon_0 \epsilon_r k_b T}} \right) \quad (7.1)$$

where k_b is the Boltzmann constant, T the temperature, e the electron charge, σ the surface charge density, C_s the salt concentration, N_A Avogadro's constant, ϵ_0 the electric constant, and ϵ_r the relative dielectric constant. The potential distribution (ϕ_{EDL}) increases, as the surface charge density (σ) increases and the solution concentration decreases. During 'zero-charging', the material properties dictate the surface charge density, whereas with 'force-charging' the external power supply provides the surface charge density. Methods that increase the activated carbon's intrinsic charge density are needed in order to capture a significant amount of energy through the 'zero-charging' method.

From the GCS model, an individual electrode operated with a seawater and river water at the electrode's spontaneous potential could approach $\phi_{EDL} \approx 60-90$ mV ($\phi_{Cell} = 2\phi_{EDL}$). In practice, individual electrodes have approached the theoretical predictions, but the whole cell potential has not. The whole cell potential has remained low, typically between $\phi_{Cell} \approx -30$ to 30 mV²⁶²⁻²⁶⁵. This is because each individual electrode's rise potential is similar if the electrodes (positive and negative) have the same material properties. To avoid this, it has been shown that materials with dissimilar rise potentials can be paired together to increase the whole cell voltage^{261, 262}. Ideally,

the greatest whole cell potential rise occurs when one electrode decreases in potential ($\Delta\varphi^{\pm} < 0$) and the other increases in potential ($\Delta\varphi^{\pm} > 0$) when exposed to an LC solution. Through the use of electrodes with the most dissimilar rise potentials, the whole cell potential has approached $\varphi_{\text{Cell}} \approx 100 \text{ mV}^{262}$. Although many different carbons have been examined in CDLE cells for the rise potentials, the physical and chemical characteristic that promote more positive or negative rise potentials have not been well explored.

The objective of this study was to examine the relationships between activated carbon chemical, physical and electrochemical properties and the voltage rise (energy generation phase) that occurs in a CDLE cycle. It was previously shown that the rise potential was related to the point zero charge (PZC) of different types of carbonaceous materials²⁶², but the specific functional groups responsible for these differences were not explored. We hypothesized that the abundance and type (weak versus strong) of acid groups on the carbon surface were primarily responsible for the different behavior of the carbon materials. To examine the specific role of carbon surface chemistry on the rise potential, activated carbons (ACs) that were derived from five different precursor materials were characterized using potentiometric titrations to quantify the concentration of acidic surface functional groups.²⁷⁶ The materials were further examined in terms of their electrochemical (capacitance) and physical (pore size distribution, and total surface area) properties. The voltage rise ($\Delta\varphi^{\pm} > 0$) or fall ($\Delta\varphi^{\pm} < 0$) of each material was determined at its spontaneous potential. To demonstrate the importance of acid functional groups, we oxidized one of the carbons (using nitric acid) to show that this would alter the rise potential in a predictable direction. We measured the resulting whole cell potentials that could be produced using carbons with these different concentrations of surface acid groups in capacitive mixing tests based on a ‘zero charging’ CDLE process. Molecular dynamics and metadynamics simulations were

performed using an idealized system to show that the responses of the EDL on plain carbon (pristine graphene) were different from those on a carbon surface containing a high abundance of oxygen groups (graphene oxide). This linkage between the specific surface chemistry and rise potentials has not previously been examined through both experimental and simulation approaches.

7.2 Methods

Capacitive Mixing System. The CDLE device was manufactured from antistatic clear cast acrylic (McMasterCarr, IL). The endplates ($5.1 \times 5.1 \times 0.95$ cm) and a middle chamber ($5.1 \times 5.1 \times 0.25$ cm) were machined. Each endplate had a 0.64 cm hole drilled and tapped so that a polypropylene tube fitting (0.64 cm tube OD \times 0.64 cm male pipe) could be screwed into the endplate. Fine extruded graphite rods (0.64 cm diameter, Graphitestore.com, Inc.) were fitted into the polypropylene tube fitting, and sealed using Loctite epoxy (McMasterCarr, IL). The graphite rods served as the current collector for the capacitive electrodes. The middle chamber was hollowed out and this served as the flow cell (empty bed volume ~ 2 mL). Tube fittings were glued to the top and bottom of the middle chamber, allowing for flow into and out of the cell. A reference electrode (Ag/AgCl +0.205 versus SHE) (BASi, West Lafayette, IN) was placed in the middle chamber to measure individual electrode potentials.

Electrode Preparation, Treatment and Characterization. Capacitive electrodes were prepared from five commercially available activated carbon (AC) powders based on different precursor materials: peat (SX+) (Norit, USA); coconut shell (YP50, Kuraray Chemical, Japan); phenolic resin (RP-20, Kuraray Chemical, Japan); bituminous coal (BC, Carbon Resources, USA); and hardwood (HRD, MeadWestvaco, USA). To demonstrate

that a carbon rise potential could be modified by chemical oxidation, YP50 was treated (YP50 ox) with nitric acid (0.5 M, Sigma–Aldrich, St. Louis MO) for 12 h.

Capacitive electrodes were prepared through combining the AC powder with 10 wt% polyvinylidene fluoride (PVDF) (Sigma–Aldrich, St. Louis MO). The mixture was homogenized with a sonifier in 2 mL of dimethylformamide (DMF) (Sigma–Aldrich, St. Louis MO), and the slurry was cast onto graphite rods ($\sim 3.2 \text{ mg cm}^{-2}$). Electrodes were dried overnight, washed with ethanol, and then soaked in 0.5 M sodium chloride before use in the CDLE system.

Cyclic voltammograms (CVs) of each electrode were collected using a potentiostat (Biologic VMP-3, USA). The electrodes were scanned from 0 to 0.5 V at 2, 5, 10, 20, 50 and 100 mV sec^{-1} , and the capacitance calculated by:

$$C_{sp} = \frac{2}{\Delta U} \cdot \frac{\int i dU}{\nu \cdot m} \quad (7.2)$$

where ΔU is the width of the voltage scan, i the discharge current, U the voltage, ν the scan rate, and m the mass of carbon on one electrode. Electrodes properties for surface area, pore volume distribution, and strong acid surface functional groups were derived from experimental data previously collected to study oxygen reduction by these activated carbons.²⁷⁶

Spontaneous Potential Measurements. The spontaneous potential of each electrode was obtained through stepping the whole cell voltage from 0 to 1 V at 0.2 V increments, where each voltage was held constant for 10 minutes to ensure steady conditions. The positive, negative, and whole cell voltage was monitored with Ag/AgCl reference electrodes. Step voltages were run three times to ensure repeatability. The potential of the individual electrodes measured at 0 V corresponded to the electrode's spontaneous potential.

Gouy–Chapman–Stern Model. The individual electrode potentials in different solutions ($\varphi_{LC/HCl}^{\pm}$), and the resulting electrode potential rise or fall ($\Delta\varphi^{\pm} = \varphi_{LC}^{\pm} - \varphi_{HC}^{\pm}$) were

estimated using GCS theory (Eq 1).²⁶¹ These calculations produced curves of a rise/fall potentials which were used to evaluate CDLE performance.²⁶² The vanishing point, defined as the zero rise potential, differed based on solution concentration and the material properties of the activated carbons. We expected that the vanishing point would occur at the material's point of zero charge (PZC), so that it could be using the potentiometric titration data for each carbon ().

Capacitive Mixing Performance. Capacitive mixing cycle tests were conducted to evaluate at the whole cell and individual electrode potential rise with carbons with different surface chemistries when solutions were changed. The salt solutions were 0.5 M NaCl (HC) and 0.011 M NaCl (LC). These salt solutions were continuously pumped (peristaltic pump, Cole Parmer, IL) through the test cell at a flowrate of 5 mL min⁻¹. During energy extraction tests with the HC solution, the electrodes were connected to a 10 Ω resistor and charged to ~0.0 V. Then the LC solution was flushed through the cell. When the potential rise reached a plateau, the electrodes were discharged through a 100 Ω resistor until the whole cell reached ~0.0 V. The HC was then pumped through the cell, and this cycle was repeated five times to ensure repeatability.

Molecular Dynamics (MD) Simulations. ReaxFF molecular dynamics (MD) simulations were used to calculate changes in EDL thicknesses that would occur during capacitive-mixing tests with HC or LC solutions. ReaxFF reactive force field calculations were implemented using the ADF computational chemistry package⁵⁷.

Pristine graphene (PG) sheets were used to model electrodes with a low concentration of strong acid functional groups, and graphene oxide (GO) sheets were used to model electrodes with high concentration of strong acid functional groups (**Error! Reference source not found.**). The atomic structure of GO sheets used in the simulations were obtained from MD studies by Bagri *et al.*²⁷⁷. In these simulations we used periodic slabs with dimensions 43.35 Å x 40.04 Å parallel

to the surface to describe the electrodes. Water molecules, potassium, and chlorine atoms were placed in random configurations between the electrodes separated by 16 Å to represent the 2.4 M KCl solution which was used as a representative high concentration solution in all simulations. The ReaxFF force parameters for C/H/O were the same as those used by Rahaman *et al.*²⁷⁸ to describe graphene-water/graphene oxide-water interactions, and the same as Rahaman *et al.*²⁷⁹ for Cl/O/H to describe chloride-water interactions.

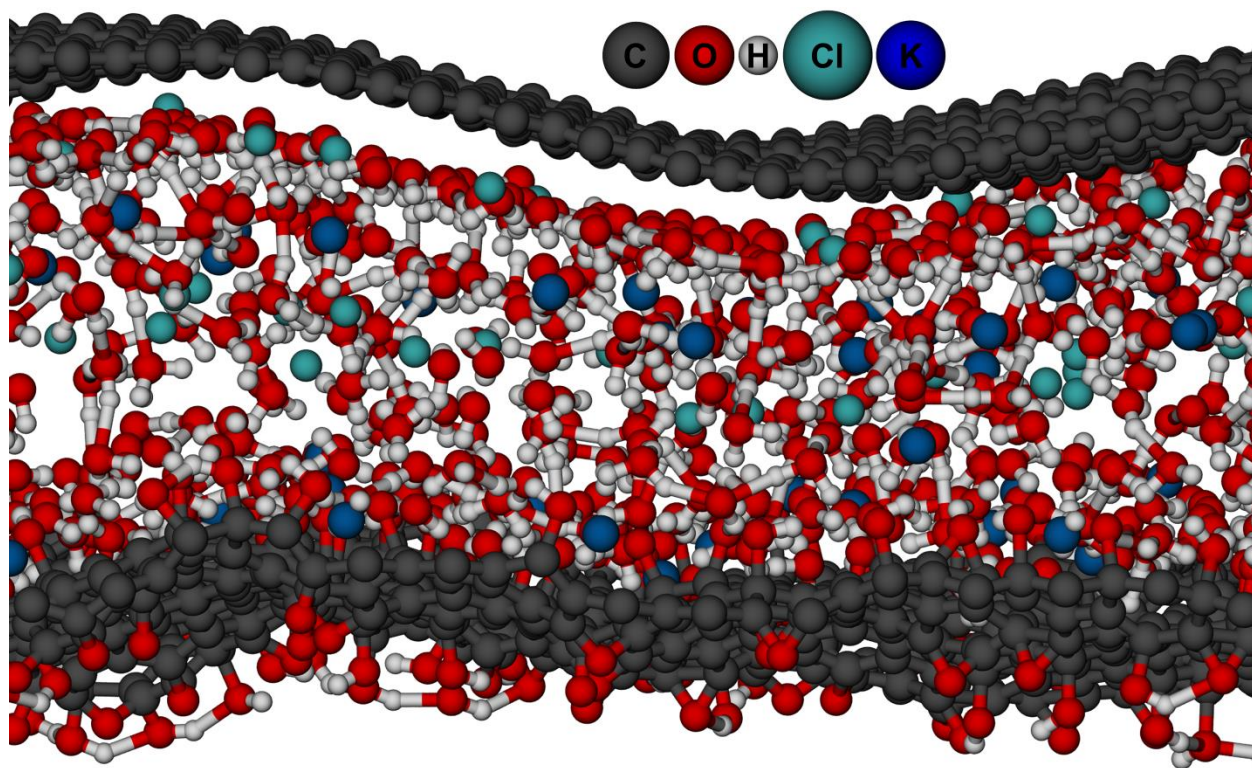


Figure 7.2. Snapshot of the simulation cell from a molecular dynamics run with pristine graphene as the cathode and graphene oxide as the anode in the cell.

All MD simulations were performed in the canonical (NPT) ensemble, with a time step of 0.25 fs using the Berendsen thermostat with a coupling time constant of 100 fs, and Berendsen barostat with a coupling time constant of 500 fs to control temperature and pressure of the entire system. The system was energy minimized with convergence criterion of 0.25 kcal/Å and equilibrated in the canonical (NPT) ensemble for 50 ps at 300K. The EDL thickness at the

electrode surface for the HC electrolyte case was estimated as the equilibrium configuration based on simulations for 50 ps at 300K. The potassium and chlorine ions that were not part of the EDL at the electrodes were removed manually to simulate the change from the HC to LC electrolytes. The resulting 0.9 M KCl solution was used as a representative LC solution in all simulations, and the EDL for this condition was obtained from MD simulations for 100 ps at 300K. In these simulations the equilibration time was 50 ps and the subsequent production run was 50 ps.

Metadynamics was performed using version 1.3 of PLUMED²⁸⁰ (called using a “fix” routine from lammmps). We used the May 5th, 2012 version of the lammmps software package¹⁸³ and version 1.3 of PLUMED¹⁹⁶ for the metadynamics calculations. Metadynamics simulations were performed to calculate the free-energy surface (FES) of ion adsorption/desorption to the electrode surface. For most adsorbates, the vertical distance of adsorbate to the surface (z) is expected to be a reasonable collective variable that distinguishes the adsorbed and desorbed states. However computing the adsorption FES as a function of z alone is not always reliable. When the adsorbate is charged, its binding to the surface involves displacement of the surface layer of water molecules and desolvation of its coordination shell. Therefore, a reliable description of the free energy landscape associated with ion adsorption requires explicit consideration of its desolvation as part of the reaction coordinate. We therefore consider the coordination number of the adsorbing ion with surrounding water molecules (s) as a second collective variable in our calculations. The two collective variables, the separation of ion from the electrode along the z direction (z) and solvation of ion in water (s), are defined as

$$z = z_{ion} - z_{electrode} \quad (7.3)$$

and

$$s = \sum_{i \in \text{ion}} \sum_{j \in \text{O}_{\text{water}}} s_{ij} \quad (7.4)$$

respectively. Here z_{ion} is the z coordinate of the adsorbing ion, $z_{\text{electrode}}$ is the average z coordinate of the electrode and

$$s_{ij} = \begin{cases} 1 & \text{for } r_{ij} \leq 0 \\ 1 - \left(\frac{r_{ij}}{r_0}\right)^6 & \text{for } r_{ij} \geq 0 \\ 1 - \left(\frac{r_{ij}}{r_0}\right)^{12} & \end{cases} \quad (7.5)$$

where $r_{ij} = |r_i - r_j| - d_0$ and d_0, r_0 is set to 3.05 Å and 0.2 Å respectively. For ion adsorption on the graphene oxide (GO) electrode we also consider the coordination of adsorbing ion with surface oxygens as a collective variable as defined in equations (2) and (3) with O_{water} replaced by $\text{O}_{\text{surface}}$. This is important since near the GO electrode the surface oxygens can provide part of the solvation shell for the adsorbing ions. A hill height of 0.10 kcal/mol and width of 0.35 Å were used, and hills were added every 100 timesteps. FES's were reconstructed from the Gaussian bias potentials added during the metadynamics trajectory.

7.3 Results and Discussion

Surface Chemistry of the Carbon Electrodes. Based on potentiometric titrations the concentration of acidic (**Error! Reference source not found.**A) and oxygen containing () functional groups was highest for the HRD sample, and lowest the SX+ (peat based) carbon. The remaining carbons (YP50, BC and RP20) all contained intermediate concentration of strong acid groups. The strong acid functional groups measured for the HRD sample were primarily oxygen containing acids (e.g. phenolic, carboxylic, and lactonic).²⁷⁶ Surface functional groups can act as a source of surface charge, as the functional groups can undergo dissociation or protonation.²⁸¹ The HRD sample had the largest quantity of strong acid surface functional groups around the

operating electrolyte's pH (e.g. pH=7), whereas SX^+ has the lowest concentration of functional groups at pH=7 (

Figure 7.5). The groups that could potentially dissociate or protonate at pH 7 were carboxylic acid groups, and thus the concentration of these acid groups was of most interest relative to electrode rise/fall tests.

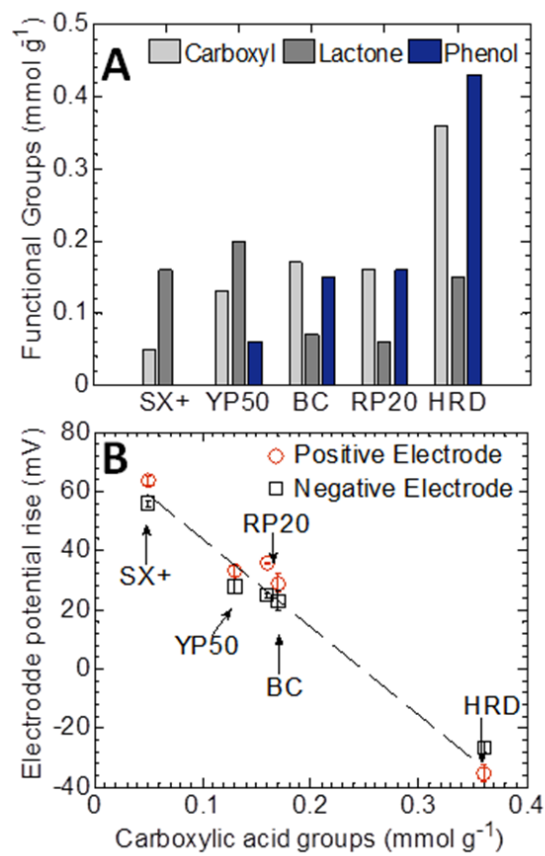


Figure 7.3. (A) Concentration of surface functional groups for various carbons tested, and (B) the individual electrode ($\Delta\phi$) potential rise as a function of the concentration of strong acid surface functional groups for different carbons.

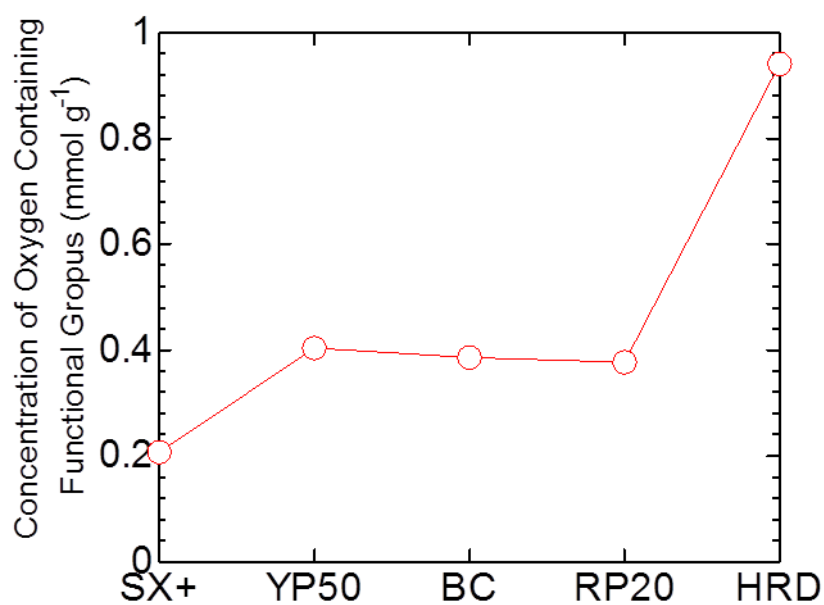


Figure 7.4. Concentration of oxygen containing functional groups for various carbon materials

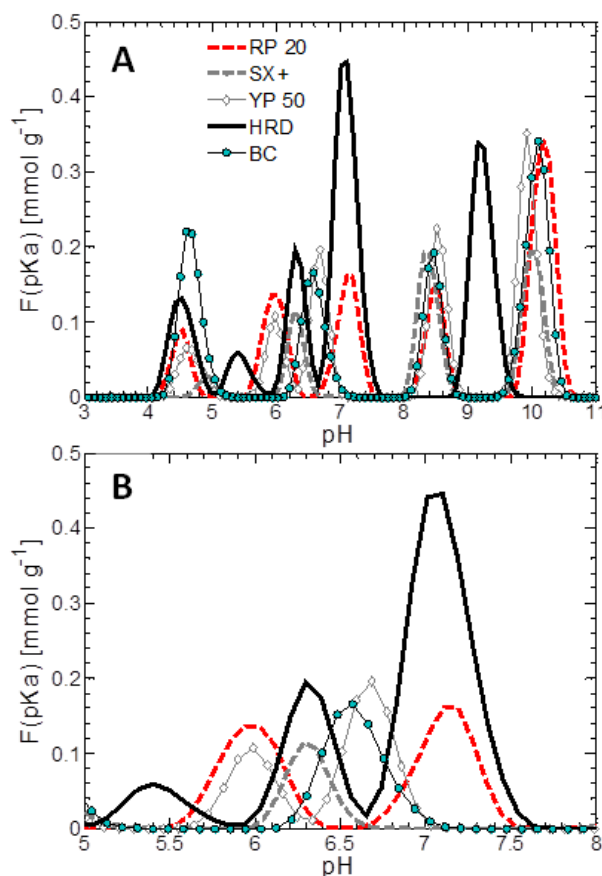


Figure 7.5. Potentiometric titration curves for tested carbons (a) pH range from 4 to 10 (b) zoomed in selection (pH from 5 to 8)

Electrode rise and fall measurements. The different rise potentials (positive and negative electrodes) obtained for the different carbons was found to be well correlated ($P = 10^{-5}$) with the concentration of carboxylic acid groups (**Error! Reference source not found.B**). Carbons with high concentrations of oxygen containing groups (HRD) caused both the positive and negative electrode potentials to decrease when a LC solution was added to the flow cell. Carbons with little oxygen-containing functional groups conversely resulted in the largest individual positive and negative electrode rise potentials which approached 60 mV. By applying a linear regression to the individual electrodes rise/fall potential curve, the projected maximum electrode rise potential could approach 75 mV ($R^2=0.97$; based on the y-intercept). In all cases when the positive and negative electrodes were the same, the whole cell potential rise was minimal ± 15 mV (**Figure 7.6A**). This was due to the similar response of individual electrodes, as has been previously reported (**Figure 7.6B**)²⁶². There was no correlation between the rise/fall potential

magnitude and the micro, meso or macroporous surface area, or micro, meso, or macropore volume (

Figure 7.7. Individual electrode potential rise as a function of (a) total surface area, (b) total pore volume and **Figure 7.8).**

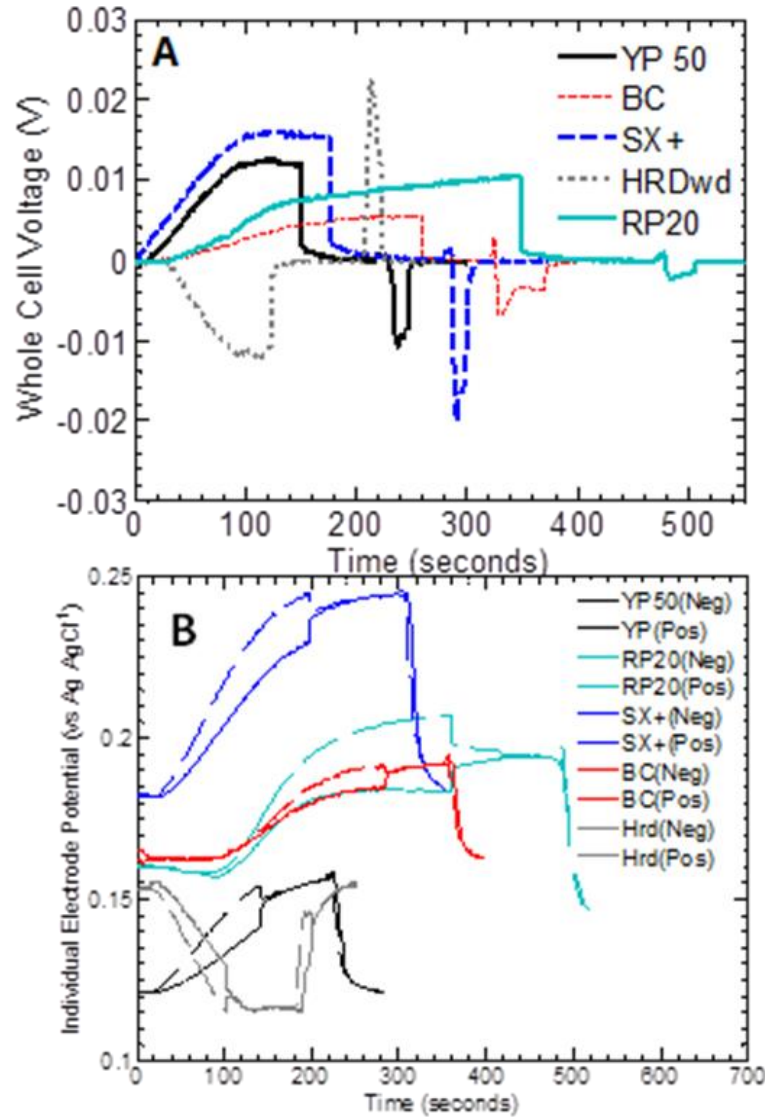


Figure 7.6. (a) Whole cell potential rise during CDLE cycle, and (b) Individual electrode (ϕ^+) and (ϕ^-) potential rise and fall for various activated carbon materials.

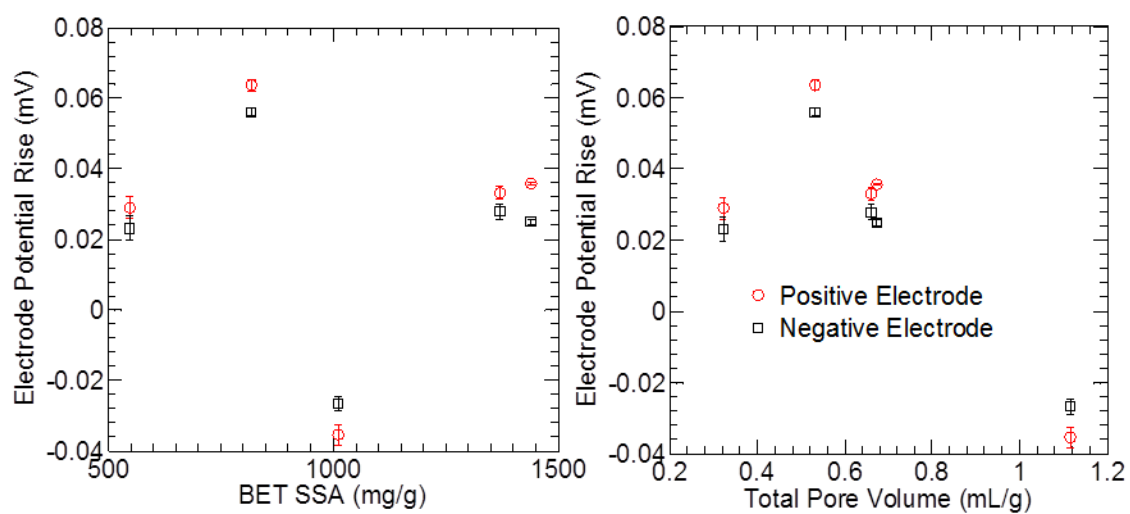


Figure 7.7. Individual electrode potential rise as a function of (a) total surface area, (b) total pore volume.

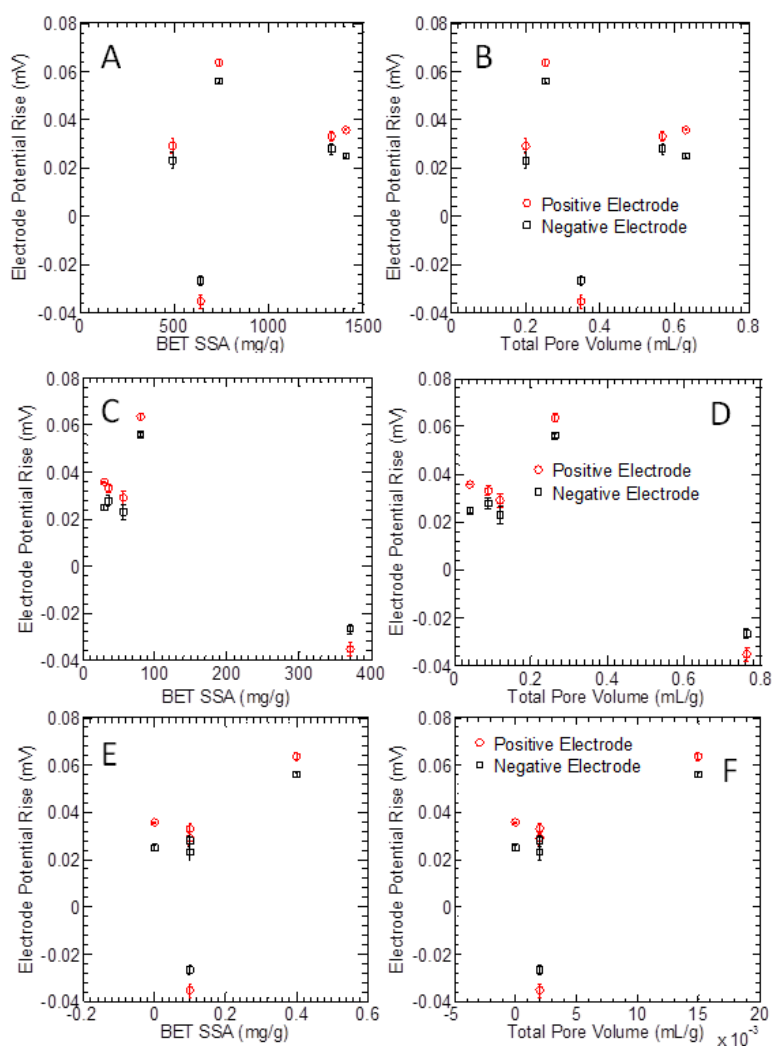


Figure 7.8. Individual electrode potential rise as a function of (a) microporous surface area, (b) microporous volume (c) mesoporous surface area, (d) mesoporous volume (e) macroporous surface area (f) macroporous volume.

The potentiometric titrations of the acidic (HRD) and low acidic (SX+) carbons display charge at the surface of the carbon at various pHs (). The point of zero charge indicates the pH where the charge density at the carbon's surface is zero. This point is displayed in

Figure 7.5. The electrode potential at zero charge can be calculated based on the Nernst equation, $E = E^0 - 0.059pH$. Because the point of zero charge differs by ~ 4.7 pH units, the potential of zero charge for the two electrodes should therefore be shifted by ~ 270 mV. This information can be used to determine the vanishing point for the GCS curves.

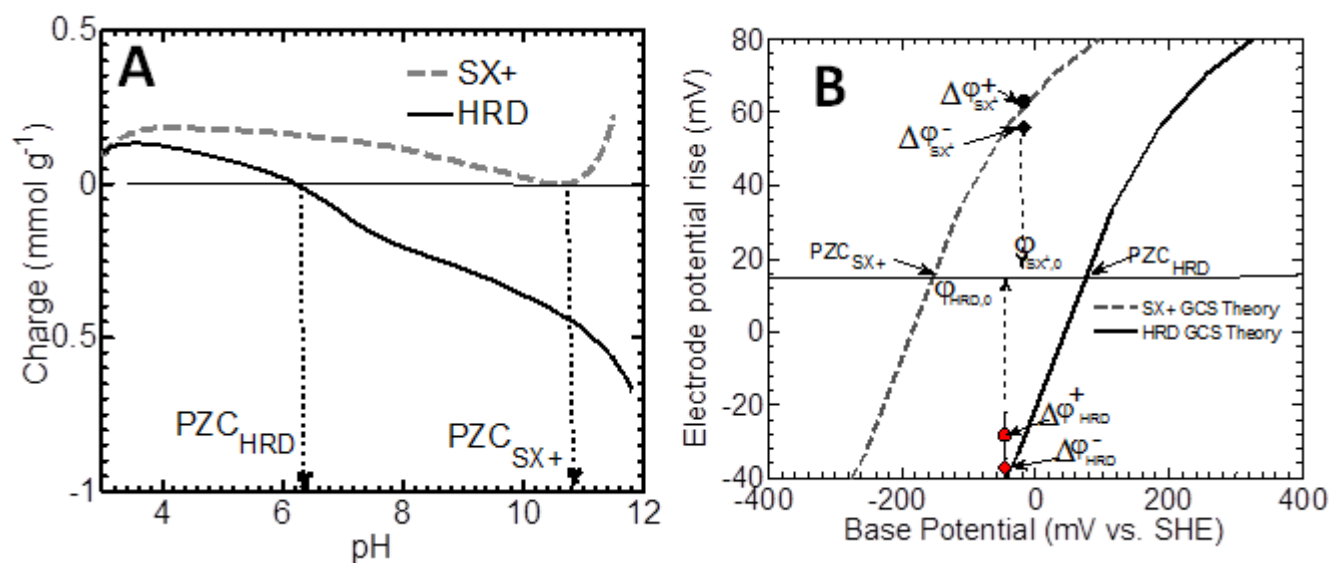


Figure 7.9. (a) Charge versus pH from potentiometric titrations for SX+ and HRD samples, with PZC indicated. (b) GCS modeled potential rise as a function of the base potential for SX+ and HRD samples.

An increase in the concentration of strong acid groups of the carbons was consistent with the shift in the PZC. The SX+ and HRD carbons had PZCs that differed by nearly 5 pH units and ~ 300 mV (**Error! Reference source not found.**A). The GCS curves for HRD and SX+ were calculated by using the PZC as the vanishing point ($\Delta\phi^\pm = 0$). Both the positive and negative

electrode rise/fall potentials for SX+ and HRD were in good agreement with those predicted using the GCS theory. When similar electrodes are used for CDLE, to establish a large potential difference between individual electrodes, the electrodes need to be pushed away from their spontaneous base potentials, along the same GCS curve (**Error! Reference source not found.B**). With dissimilar electrodes (with different PZC) the system is able to operate on two GCS curves, which promotes a potential difference between each individual electrode even at the whole cells spontaneous base potential²⁶². Furthermore, when one electrode's spontaneous base potential is greater than the PZC, and the other electrode's spontaneous base potential is below the PZC (as is the case with SX+ and HRD), it is expected that one electrode will rise and one electrode will fall as the solutions are altered, which is desired. When the electrodes with the two most dissimilar concentrations were examined (SX+ and HRD), the whole cell potential rise reached 86 ± 1.7 mV with the SX+ as the positive electrode and the HRD as the negative electrode (**Figure 7.10**).

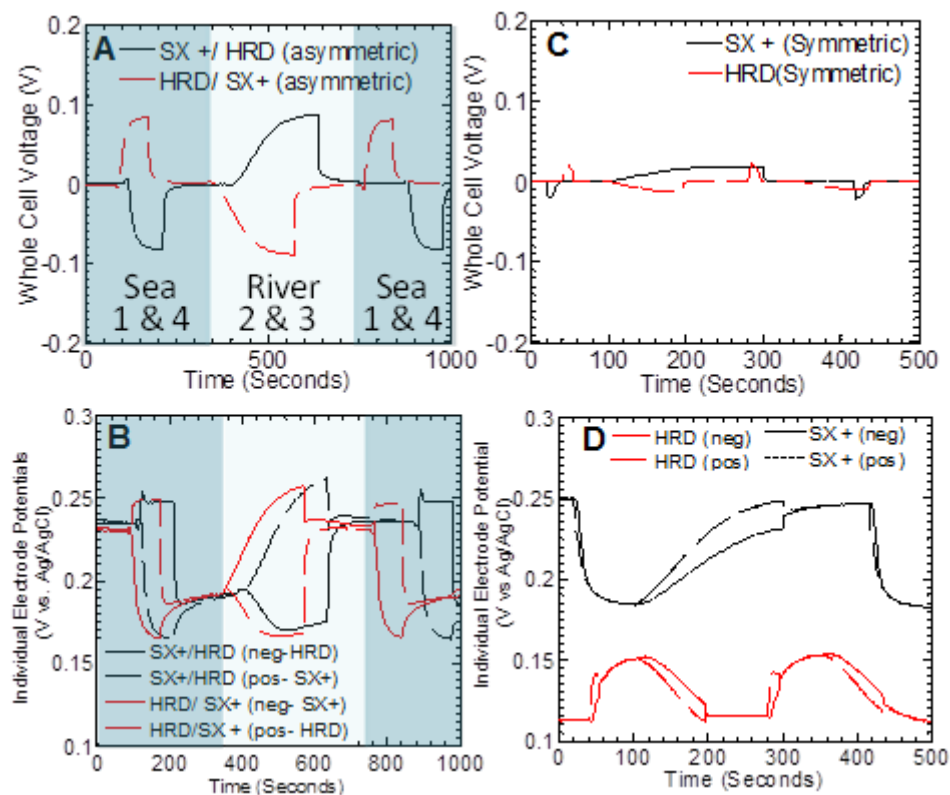


Figure 7.10. (a) Whole cell (ϕ_{cell}) and (b) individual electrode ($\phi_{HRD/SX+}^{\pm}$) potentials for asymmetrical CDLE operation using SX+ and HRD activated carbons. (C) Whole cell (ϕ_{cell}) and (d) individual electrode potentials ($\phi_{SX+/SX+}^{\pm}$ and $\phi_{HRD/HRD}^{\pm}$) for a symmetrical CDLE operation using SX+ and HRD. Blue shaded area indicates when seawater was present in the cell (step 1&4), and red shading indicates when river water was present.

Producing Dissimilar Electrodes Through Chemical Oxidation. The YP50 electrode was oxidized using nitric acid to increase the concentration of positive surface functional groups. This oxidation process, used for treatment of supercapacitors, is known to increase the concentration of strong acid groups by 2-3×, depending on the time and concentration of acid used.^{282, 283} Using the oxidized negative electrode (YP50 ox) with a non-oxidized positive electrode (YP50) increased the whole cell potential from 12 ± 1 mV to 53 ± 1.7 mV (**Error! Reference source not found.A**). This increase was due to the directional differences between the individual electrode rise potentials. The use of this dissimilar configuration produced a whole cell potential rise which was 3-10× greater than that obtained using either of the similar-electrode configurations (YP50/YP50 or YP50ox/YP50ox) (**Error! Reference source not found.B**). Chemical treatment reduced the rise potential of the YP50 from $\Delta\phi_{YP50}^{+} = 46 \pm 2$ mV, to $\Delta\phi_{YP50ox}^{-} = -6 \pm 0.5$ mV (YP50-ox, **Error! Reference source not found.B** and **Error! Reference source not found.C**).

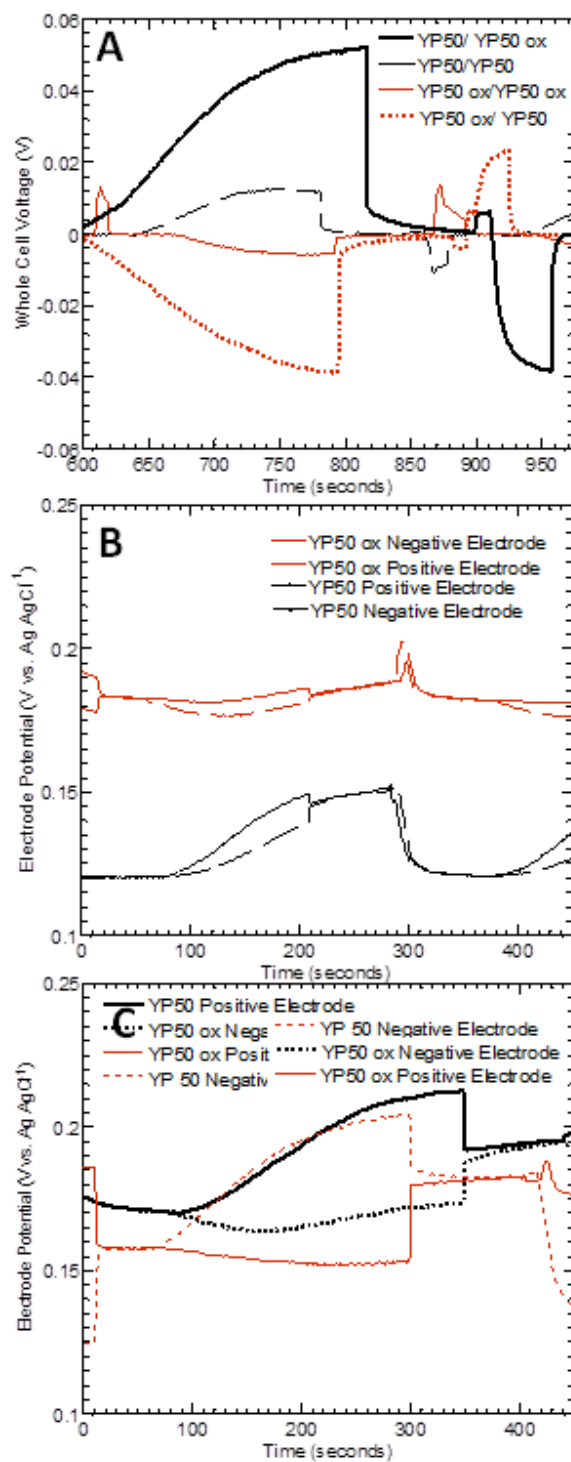


Figure 7.11. (A) Whole cell CDLE performance with similar and dissimilar electrodes YP50/YP50 ox, YP50 ox/YP50, YP50/YP50, and YP50ox/YP50 ox, (B) individual rise and fall

potentials for similar electrodes (YP50/YP50 and YP50 ox/YP50 ox) and (C) individual rise and fall potentials for dissimilar electrodes (YP50/YP50ox and YP50 ox/YP50).

Treating activated carbons to alter surface functional groups may be more preferable than choosing materials with dissimilar concentrations of strong acid groups, because this allows more control over material properties (e.g. exact functional groups, pore distribution, or surface area). YP50 is a typical activated carbon used for supercapacitors because it has a high surface area and a large concentration of micropores, and consequently a high capacitance (**Figure 7.12**). Based on the energy equation [$E_{CDLE} = \frac{1}{2} C (2\phi_{EDL})^2$], if the voltage rise acquired through treatment methods can approach that of dissimilar materials, increasing the capacitance by $2\times$ (as is the case when YP50ox is used instead of the HRD sample) will double the amount of energy extracted from a CDLE cycle (**Figure 7.13**). Thus, the addition of chemical functionality through surface treatments, such as the oxidization process used here, is preferable to selecting materials based on rise potential alone as it ensures that the carbon will also have a high capacitance.

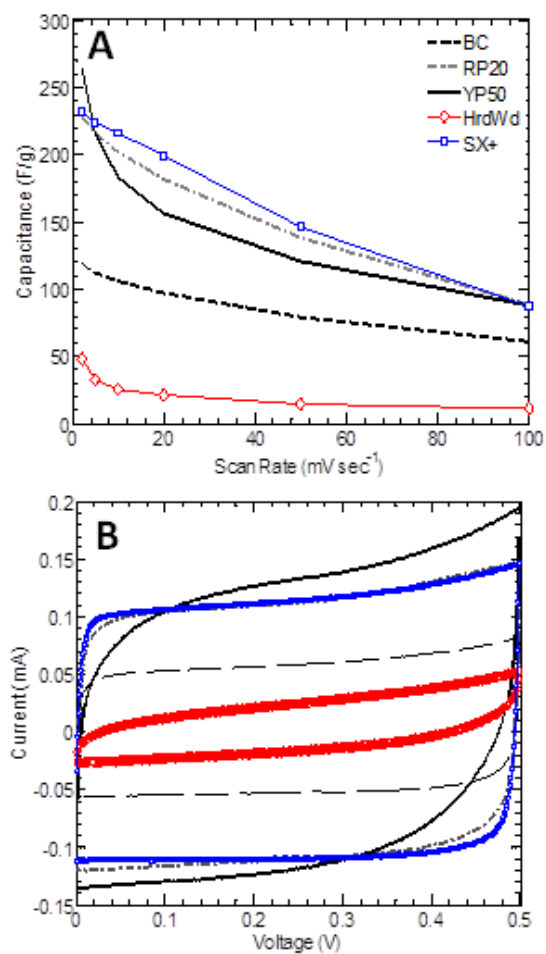


Figure 7.12. (a) Capacitance of various activated carbons as a function of CV scan rate and (b) cyclic voltammogram at 2 mV/sec.

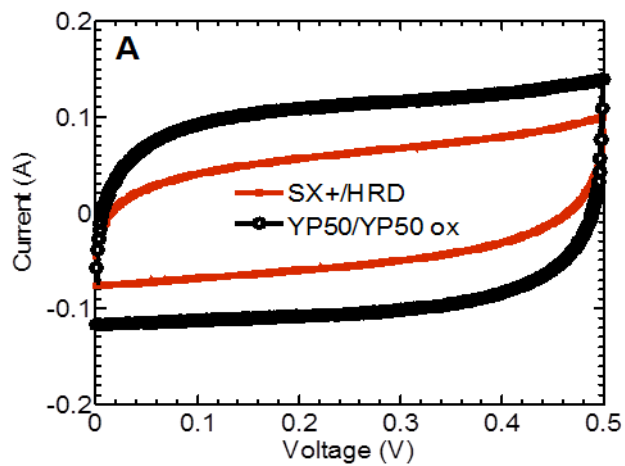


Figure 7.13. Cyclic voltammogram for dissimilar electrodes SX+/HRD and YP50/YP50 ox.

Theoretical results– Evaluation of EDL thickness. PG and GO sheets were examined as positive electrodes in MD simulations by assigning a net charge of 0.1e per atom, or as negative electrodes by assigning $-0.1e$ per atom. The formation of an EDL at the electrodes for the case where PG was the positive electrode and GO was the negative electrode, in the HC electrolyte case, is shown in **Figure 7.1415A**. The ions that were not part of the capacitance or Stern layer (not adsorbed to the electrode) were removed manually to simulate the change from high to low concentration electrolyte (**Figure 7.14B**).

At equilibration, the EDL thickness at the PG electrode increased when changing from the HC to LC electrolyte irrespective of whether PG was the positive electrode or negative electrode. The EDL thickness increased by 0.11 ± 0.05 Å when PG was positive electrode, and 0.10 ± 0.05 Å when PG was the negative electrode. The GO electrode showed the converse behavior, where the EDL thickness decreased on going from the HC to LC electrolyte, with the direction of this response (but not the magnitude) independent of whether GO was simulated as the positive or negative electrode in the cell. The EDL thickness decreased by 0.10 ± 0.06 Å when GO was the positive electrode, and decreased by 0.17 ± 0.05 Å when GO was the negative electrode. The EDL expansion at PG produced a positive-rise electrode potential, and the EDL compression at GO produced a negative-rise potential at the electrode during the CDLE cycle. These simulation results were in agreement with the experimental observations that electrodes with low concentration of strong acid functional groups showed a positive potential rise, and electrodes with high concentration of strong acid functional groups showed a negative potential rise during CDLE cycle, irrespective of whether they were the positive or negative electrode in the cell.

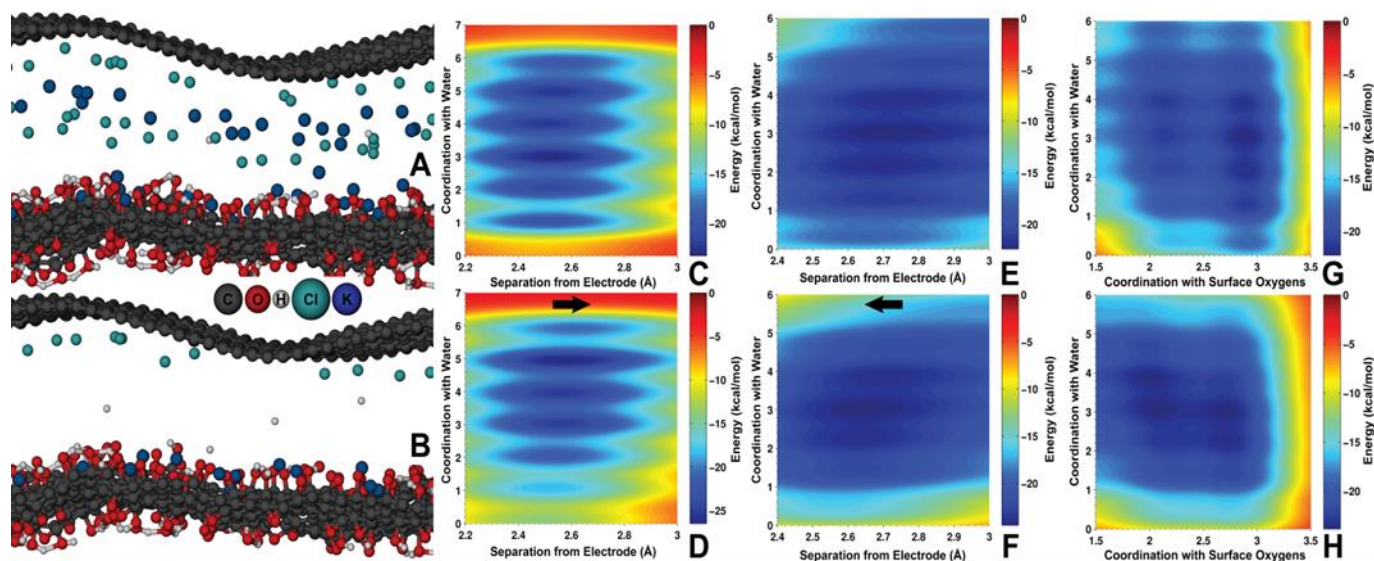


Figure 7.14. Snapshot from a MD simulation showing the electric double layer (EDL) in the (A) high concentration electrolyte and (B) low concentration electrolyte; the water molecules are not shown explicitly. Free-energy surface (FES) for adsorption of chlorine ion on the pristine graphene (PG) electrode as a function of separation from the electrode and coordination with water for the (C) high concentration electrolyte and (D) low concentration electrolyte when PG is the positive electrode in the cell. Free-energy surface (FES) for adsorption of potassium ion on the graphene oxide (GO) electrode as a function of separation from the electrode and coordination with water for the (E) high concentration electrolyte and (F) low concentration electrolyte when GO is the negative electrode in the cell. The arrows indicate the direction of shift of free-energy basins when changing from high to low concentration electrolyte. Free-energy surface (FES) for adsorption of potassium ion on the graphene oxide (GO) electrode as a function of coordination with surface oxygens and coordination with water for the (G) high concentration electrolyte and (H) low concentration electrolyte when GO is the negative electrode in the cell.

To investigate the origins of the dissimilar EDL changes at the PG and GO electrodes we performed metadynamics simulations to investigate the free-energy surface (landscape) of ions with the separation of ions from the electrode and solvation of ions in water as the collective variables. **Figure 7.14C** and **Figure 7.14D** shows the free-energy surface (FES) of chloride ions near the PG electrode for the high concentration electrolyte and low concentration cases respectively when PG is the positive electrode in the cell. From these two figures, we observe that changing the HC to LC moves the position of minimum free-energy of the chloride ion farther away from the PG electrode (x-axis), and that its coordination with water increased from 3 to 5 (y-

axis). In the HC electrolyte the minimum free energy of the chloride ion is at a separation of 2.51 Å from the PG electrode and in the LC electrolyte this increases to a value of 2.59 Å. This suggests that in the LC electrolyte, because of the absence of surrounding ions, the chloride ions were stabilized by moving further into solution and coordinating with more water molecules. This resulted in an EDL expansion, which would produce a positive potential rise at electrodes having a low concentration of strong acid functional groups.

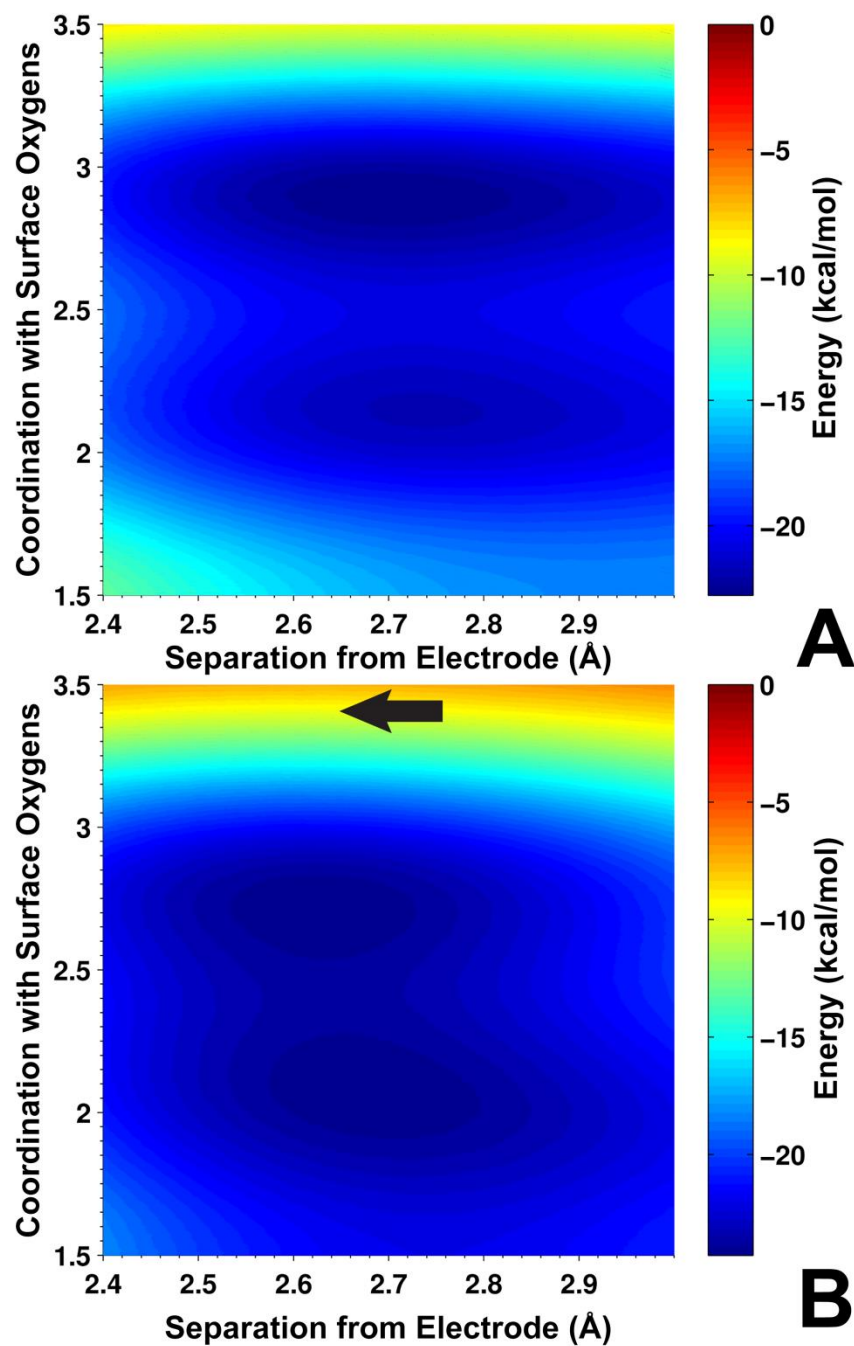


Figure 7.15. Free-energy surface (FES) for adsorption of potassium ion on the graphene oxide (GO) electrode as a function of separation from the electrode and coordination with surface oxygens for the (a) high concentration electrolyte and (b) low concentration electrolyte when GO is the anode in the cell. The arrows indicate the direction of shift of free-energy basins when changing from high to low concentration electrolyte.

With GO as the negative electrode, changing from the HC to LC concentration electrolyte moves the position of minimum free-energy of the potassium ion closer to the GO electrode (x-axis), and its coordination with water remained around 3 (y-axis) (**Figure 7.14E** and **Figure 7.14F**). In the HC electrolyte the minimum free energy of the potassium ion is at a separation of 2.73 Å from the GO electrode and in the low concentration electrolyte this decreases to a value of 2.65 Å. At the GO electrode, ion coordination with surface oxygen atoms was also considered as a collective variable since the surface oxygen atoms could provide part of the solvation shell for the potassium ions near the GO electrode. We can note from **Figure 7.15** that in the LC electrolyte the potassium ion moves closer to the electrode and at the same time its coordination with surface oxygen atoms has decreased slightly from 2.9 to 2.7 (y-axis).

The FES of potassium ions near the GO electrode is shown in **Figure 7.14G** and **Figure 7.14H** as a function of coordination with surface oxygen atoms (x-axis) and coordination with water (y-axis). In the HC electrolyte the free-energy minimum was produced when potassium was coordinated with 3 water and 3 surface oxygen atoms. In the LC electrolyte the potassium ion had closely spaced free-energy basins at (3,3) as well as (2,4) with a barrier of 1.27 kcal mol⁻¹ between the basins. This suggests that in the LC electrolyte the potassium ion can move closer to the electrode and preserve its total coordination of 6. This would produce an EDL compression and thereby a negative potential rise at electrodes with high concentration of strong acid functional groups.

The strong acid functional groups on the electrodes provide part of the solvation shell of the adsorbing ion, and in their presence the adsorbing ion moves closer to the electrode in the LC electrolyte, producing a negative rise potential. In the absence of strong acid functional groups the adsorbing ion moves away from the electrode in the LC electrolyte to increase its solvation in

water producing a positive rise potential. This results in the opposite rise potential trends on electrodes with low and high concentrations of strong acid function groups.

7.4 Summary and Conclusions

CDLE represents a potentially clean, cheap, and sustainable method for extracting energy from salinity gradients, but energy recoveries need to be improved by increasing whole cell voltages. The concentration of strong acid surface functional groups was shown here to strongly correlate with both the direction and magnitude of the individual electrode potential rise/fall. This indicates that carbons can be pre-selected to function as the positive or negative electrodes based on the concentration of strong acid groups. However, the carbons best suited for CDLE must have high capacitance as well as dissimilar rise potentials. Thus, it may be more beneficial to chemically modify high capacitance carbons to obtain highly disparate concentrations of strong acid groups. A carbon with a high rise potential was transformed into a carbon with a low rise potential through chemical oxidation using a strong acid. Additional chemical treatments could be used to tune the type of functionality and the ideal concentration of acidic or basic functionality to improve the potential rise of both the positive and negative electrodes. Methods to chemically modify the carbons to have more positive rise potentials are as yet unidentified. ReaxFF simulations revealed that the rise and fall potential of individual electrodes could be attributed to the EDL expanding or compressing in the LC electrolytes. Additional MD simulations could provide guidance for producing the desired carbon chemistry.

8 Summary and Future Directions

This chapter discussed impacts and future directions of the projects discussed in the dissertation.

Dissociation of Water on Titania Surfaces

1. A fundamental question in this area is whether H₂O molecules adsorbed molecularly or dissociatively on the anatase (101) surface. Until very recently, experimental and theoretical studies consistently promoted the notion that only molecular adsorption occurs on the pristine anatase (101) surface. The DFT study of Vittadini *et al.*⁶⁰ finds molecular adsorption to be energetically favorable over dissociation by 0.44 and 0.28 eV per H₂O molecule (at low and monolayer coverage, respectively). A few years later, combined TPD and XPS experiments⁶⁵ concluded in favor of molecular adsorption. Apart from few exceptions^{84, 146}, most computational studies continue to find molecular adsorption to be energetically favorable²⁸⁴. In contrast with the prevailing view of molecular adsorption of water on anatase, recent high-resolution XPS study⁷⁴ reported the presence of OH groups at the surface and challenged the accepted model of the interface. Analysis of the XPS spectral intensities⁷⁴, proposed that, at monolayer coverage, 23±5% of the water molecules dissociate into a hydroxyl and a proton. Our ReaxFF reactive force field study¹⁴⁶ predicts that 22.3% of water adsorbs dissociatively in agreement with the XPS study⁷⁴. Recent high accuracy (< 0.2 eV) DFT calculations²⁸⁵ of comparison between calculated spectra and experiment provides evidence for the presence of dissociated water in the XPS experiments⁷⁴ on anatase(101) at monolayer (ML) coverage. The study finds that the energetics of H₂O dissociation on anatase is altered when two water molecules are adsorbed on adjacent sites. In these conditions, the energetic cost of dissociation is compensated by the energy gain due to the formation of the HO---H₂O hydrogen bonded complex, and dissociative adsorption becomes possible. The same DFT study proceeds to

discuss how the experimental observations from the earlier combined TPD and XPS study⁶⁵ can be attributed to mixed molecular-dissociative adsorption at the anatase(101)-H₂O interface. Our study corroborates the new experimental and theoretical studies that water dissociation is possible on anatase(101) surface.

2. Theoretical studies of water adsorption on the defect-free rutile(110) surface presented over the years are contradictory. DFT studies predict either molecular or dissociative adsorption on the perfect defect-free surface with results being sensitive to slab thickness, coverage, and exchange-correlation functional^{103, 106, 108, 112, 114, 121, 123, 286}. The most common view expressed in early experimental studies is that at all coverages water adsorbs molecularly on the ideal surface and dissociation does only take place at defect sites^{91, 92, 287, 288}. Recent CTR¹²⁰, SHG²⁸⁹, powder titrations¹¹⁹ and synchrotron radiation photoemission⁹⁷ studies predict mixed molecular-dissociative adsorption at the rutile(110) surface. The percentage of water-dissociation predicted by ReaxFF¹⁴⁶ (22.92%) is in good agreement with CTR¹²⁰ and synchrotron radiation photoemission^{74, 97} (21%) studies. Our study corroborates the new experimental studies that water dissociation is possible on rutile(110) surface.
3. DFT molecular dynamics study by Kumar *et al.*⁹⁹ predict faster proton jump rates on SnO₂ cassiterite (110) surface compared with TiO₂ rutile(110) surface. It is of interest to investigate the proton hopping rates on rutile (110) surface employing the Ti/O/H ReaxFF reactive force field used in our study. A good agreement with the DFT study⁹⁹ will enable extending the study to various rutile and anatase surfaces. Comparison of proton hopping rates between different TiO₂ surfaces can provide insights to the factors affecting the proton jump rates and correlations can likely be drawn to the reactivity and catalytic activity on the various surfaces. Being a force field method, the computational cost will be minimal compared to DFT.

Mechanisms of Oriented Attachment of TiO₂ Nanocrystals

1. To our knowledge, our study is the first to elucidate a detailed and likely general mechanism by which OA could occur in TiO₂ anatase nanocrystals. Our results are consistent with experiment, are likely to be general for aqueous metal-oxide systems, and demonstrate the critical role of solvent in nanocrystal aggregation.
2. Understanding OA-based growth has potential for broader impact as a path to controlled mesoscale structuring of materials with nanoscale functioning units. For example, the branched nanomaterials that can result from this process have large absorption cross-sections²⁹⁰ and short electron mean free paths²⁹¹ for solar cell applications²⁹²⁻²⁹⁴. The energetics of OA are an outcome of the complex interplay between physicochemical parameters such as surface charges/potential, pH, ionic concentrations, saturation state, functional groups at surfaces, and dielectric properties—quantities strongly correlated with microscopic features such as solvent structure and the charge density distribution. Consequently, complete understanding requires correlations over different length scales involved in the energetics between two charged complex interfaces in aqueous electrolytes. Our study involved TiO₂ anatase nanocrystals in aqueous solutions. A future direction to our study will be to investigate the effects of pH, ionic concentrations and effect of different solvents (alcohol, acetic acid, tetrahydrofuran etc.) on OA.
3. Misalignment between attaching nanocrystals results in defects in the final crystal. Perfect alignment can eliminate the interface, but twins and stacking faults are also possible even while maintaining perfect lattice registry^{88, 144, 295-297}. Slight misorientations create defects such as edge or screw dislocations that define grain boundaries in the growing material^{134, 144, 295, 297}. Causes of misoriented aggregation are unknown but could be related to primary particle morphology¹⁴⁴. Because grain boundaries often dominate the physical and transport properties of the resulting material^{298, 299} the short-range forces controlling the degree of co-orientation

upon attachment and any follow-on rearrangement within the particle are important aspects of understanding final OA outcomes. An interesting future work will be to look into the relation between primary particle structure and morphology and defects in the material. We can study OA involving various particle morphologies (smoothly faceted, steps, etc.) and investigate whether OA between different particle structures incorporates defects/dislocations in the material. Predicting microstructure, defect content, and porosity in growing mineral phases requires understanding the extent to which primary particles can align and fill space, as well as the relationship between primary particle structure and morphology and defect incorporation upon attachment.

Li/C ReaxFF Reactive Force Field

1. Development of the Li/C ReaxFF force field in our study paves way for combining the force field with the C/H/O/S/F force field in Islam *et al.*³⁰⁰ to facilitate investigation of Li intercalation in carbon nanostructures in the presence of electrolytes like tetra(ethylene glycol) dimethyl ether (TEGDME), poly(ethylene glycol) dimethyl ether(PEGDME), tetrahydrofuran(THF), 1,2- dimethoxyethane (DME), 1,3-dioxolane(DOXL) etc. Future works involves investigating performance of various carbon nanostructures for applications in batteries and capacitors in the presence of electrolytes.
2. Non-uniform metal deposition and dendrite formation on the negative electrode during repeated cycles of charge and discharge are major hurdles to commercialization of rechargeable lithium, sodium and aluminium metal-based batteries. A long-held view is that unstable electrodeposition is a consequence of inherent characteristics of these metals and their inability to form uniform electrodeposits on surfaces with inevitable defects. Recent experimental studies by Lu *et al.*³⁰¹ finds that simple liquid electrolytes reinforced with halogenated salt blends exhibit stable long-term cycling at room temperature, with no signs of deposition instabilities

over hundreds of charge and discharge cycles. Molecular simulations with ReaxFF reactive force fields can furnish details on the effects of halogenated salts that are not accessible experimentally.

Aqueous Proton Transfer Across Single Layer Graphene

1. Our study predicts that aqueous protons transfer across single layer graphene through hydroxylated atomic defects. Given the limited accuracy with which the defect density can be determined in large (millimetre)-scale graphene, aqueous protons may transfer across single layer graphene not only along the path discussed in our study, but others as well³⁰². Recent transport and mass spectroscopy measurements by Hu *et al.*³⁰² predict proton transport across defect-free single layer graphene under potential bias. However, it needs to be noted that in the study by Hu *et al.*³⁰² there is no rigorous experimental investigation to guarantee that the graphene/Nafion composite film in their study is defect-free after deposition of PdH_x electrodes.

Capacitive Mixing by Double Layer Expansion

1. The graphene oxide sheet employed in our simulations³⁰³ to model electrodes with high concentration of strong acid functional groups contained hydroxyl, carbonyl, carboxyl and ether groups. An interesting future study is to model electrodes with definite concentrations to various functional groups to investigate which functional group maximizes the potential rise at the electrode. ReaxFF simulations can be employed to direct experiments to tune the type of functionality and the ideal concentration of acidic or basic functionality on the electrodes to improve the potential rise of both the positive and negative electrodes.

References

1. van Duin ACT, Dasgupta S, *et al.* ReaxFF: A reactive force field for hydrocarbons. *J Phys Chem A* **105**, 9396-9409 (2001).
2. Janssens GOA, Baekelandt BG, *et al.* Comparison of Cluster and Infinite Crystal Calculations on Zeolites with the Electronegativity Equalization Method (EEM). *J Phys Chem* **99**, 3251-3258 (1995).
3. Mortier WJ, Ghosh SK, *et al.* Electronegativity-equalization method for the calculation of atomic charges in molecules. *J Am Chem Soc* **108**, 4315-4320 (1986).
4. de Vos Burchart E, Verheij VA, *et al.* A consistent molecular mechanics force field for all-silica zeolites. *Zeolites* **12**, 183-189 (1992).
5. de Vos Burchart E. Studies on Zeolites: Molecular Mechanics, Framework Stability and Crystal Growth. Ph.D. thesis, Delft University of Technology, 1992.
6. Chenoweth K, van Duin ACT, *et al.* ReaxFF reactive force field for molecular dynamics simulations of hydrocarbon oxidation. *J Phys Chem A* **112**, 1040-1053 (2008).
7. van Duin ACT, Merinov BV, *et al.* ReaxFF Reactive Force Field for Solid Oxide Fuel Cell Systems with Application to Oxygen Ion Transport in Yttria-Stabilized Zirconia. *The Journal of Physical Chemistry A* **112**, 3133-3140 (2008).
8. Russo MF, Bedrov D, *et al.* Combustion of 1,5-Dinitrobiuret (DNB) in the Presence of Nitric Acid Using ReaxFF Molecular Dynamics Simulations. *The Journal of Physical Chemistry A* **117**, 9216-9223 (2013).
9. Sanderson RT. An Interpretation of Bond Lengths and a Classification of Bonds. *Science* **114**, 670-672 (1951).
10. Kohn W, Becke AD, *et al.* Density Functional Theory of Electronic Structure. *The Journal of Physical Chemistry* **100**, 12974-12980 (1996).
11. Verstraelen T, Ayers PW, *et al.* ACKS2: Atom-condensed Kohn-Sham DFT approximated to second order. *The Journal of Chemical Physics* **138**, - (2013).
12. Cole MW, Kim H-Y, *et al.* Van der Waals interactions: Accuracy of pair potential approximations. *The Journal of Chemical Physics* **137**, - (2012).
13. Gatica S, Cole M. To Wet or Not to Wet: That Is the Question. *J Low Temp Phys* **157**, 111-136 (2009).
14. Gatica SM, Calbi MM, *et al.* Three-body interactions involving clusters and films. *Phys Rev B* **68**, 205409 (2003).
15. Kim H-Y, Cole MW, *et al.* Dispersion interaction between adsorbed linear molecules. *Surf Sci* **198**, 555-570 (1988).
16. Klein JR, Bruch LW, *et al.* Many-body interactions in physisorption: Nonadditivity of film and substrate contributions to the holding potential. *Surf Sci* **173**, 555-564 (1986).
17. Liebrecht M, Cole M. Many-Body Effects in Physical Adsorption. *J Low Temp Phys* **169**, 316-323 (2012).
18. Ruiz VG, Liu W, *et al.* Density-Functional Theory with Screened van~der~Waals Interactions for the Modeling of Hybrid Inorganic-Organic Systems. *Phys Rev Lett* **108**, 146103 (2012).
19. Al-Saidi WA, Voora VK, *et al.* An Assessment of the vdW-TS Method for Extended Systems. *J Chem Theory Comput* **8**, 1503-1513 (2012).
20. Tkatchenko A, DiStasio RA, *et al.* Accurate and Efficient Method for Many-Body van der Waals Interactions. *Phys Rev Lett* **108**, 236402 (2012).
21. Gratzel M. Photoelectrochemical cells. *Nature* **414**, 338-344 (2001).
22. Hoffmann MR, Martin ST, *et al.* Environmental Applications of Semiconductor Photocatalysis. *Chem Rev* **95**, 69-96 (1995).

23. Fujishima A, Honda K. Electrochemical Photolysis of Water at a Semiconductor Electrode. *Nature* **238**, 37-38 (1972).
24. Mills A, Davies RH, *et al.* Water-Purification by Semiconductor Photocatalysis. *Chem Soc Rev* **22**, 417-425 (1993).
25. Kavan L, Gratzel M, *et al.* Electrochemical and photoelectrochemical investigation of single-crystal anatase. *J Am Chem Soc* **118**, 6716-6723 (1996).
26. Chen X, Mao SS. Titanium Dioxide Nanomaterials: Synthesis, Properties, Modifications, and Applications. *Chem Rev* **107**, 2891-2959 (2007).
27. Fu GF, Vary PS, *et al.* Anatase TiO₂ nanocomposites for antimicrobial coatings. *J Phys Chem B* **109**, 8889-8898 (2005).
28. Rajh T, Saponjic Z, *et al.* Charge transfer across the nanocrystalline-DNA interface: Probing DNA recognition. *Nano Lett* **4**, 1017-1023 (2004).
29. Bandura AV, Kubicki JD. Derivation of force field parameters for TiO₂-H₂O systems from ab Initio calculations. *J Phys Chem B* **107**, 11072-11081 (2003).
30. Alimohammadi M, Fichthorn KA. A Force Field for the Interaction of Water with TiO₂ Surfaces. *J Phys Chem C* **115**, 24206-24214 (2011).
31. Hartree DR. The wave mechanics of an atom with a non-Coulomb central field Part I theory and methods. *Math Proc Cambridge Philos Soc* **24**, 89-110 (1928).
32. Fock V. Approximation method for the solution of the quantum mechanical multibody problems. *Z Phys* **61**, 126-148 (1930).
33. Moller C, Plesset MS. Note on an approximation treatment for many-electron systems. *Phys Rev* **46**, 0618-0622 (1934).
34. Kohn W, Sham LJ. Self-consistent equations including exchange and correlation effects. *Phys Rev* **140**, A1133-A1138 (1965).
35. Perdew JP. Density-Functional Approximation for the Correlation-Energy of the Inhomogeneous Electron-Gas. *Phys Rev B* **33**, 8822-8824 (1986).
36. Perdew JP, Chevary JA, *et al.* Atoms, molecules, solids, and surfaces: Applications of the generalized gradient approximation for exchange and correlation. *Phys Rev B* **46**, 6671-6687 (1992).
37. Perdew JP, Burke K, *et al.* Generalized Gradient Approximation Made Simple. *Phys Rev Lett* **77**, 3865-3868 (1996).
38. Hammer B, Hansen LB, *et al.* Improved adsorption energetics within density-functional theory using revised Perdew-Burke-Ernzerhof functionals. *Phys Rev B* **59**, 7413-7421 (1999).
39. Becke AD. Density-functional exchange-energy approximation with correct asymptotic behavior. *Phys Rev A* **38**, 3098-3100 (1988).
40. Lee C, Yang W, *et al.* Development of the Colle-Salvetti correlation-energy formula into a functional of the electron density. *Phys Rev B* **37**, 785-789 (1988).
41. Monti S, van Duin ACT, *et al.* Exploration of the Conformational and Reactive Dynamics of Glycine and Diglycine on TiO₂: Computational Investigations in the Gas Phase and in Solution. *J Phys Chem C* **116**, 5141-5150 (2012).
42. Abolfath RM, van Duin ACT, *et al.* Reactive Molecular Dynamics Study on the First Steps of DNA Damage by Free Hydroxyl Radicals. *J Phys Chem A* **115**, 11045-11049 (2011).
43. Goken EG, Joshi KL, *et al.* Effect of Formic Acid Addition on Water Cluster Stability and Structure. *J Phys Chem A* **115**, 4657-4664 (2011).
44. Rahaman O, van Duin ACT, *et al.* Development of a ReaxFF Reactive Force Field for Aqueous Chloride and Copper Chloride. *J Phys Chem A* **114**, 3556-3568 (2010).
45. Quenneville J, Taylor RS, *et al.* Reactive Molecular Dynamics Studies of DMMP Adsorption and Reactivity on Amorphous Silica Surfaces. *J Phys Chem C* **114**, 18894-18902 (2010).

46. Zhu R, Janetzko F, *et al.* Characterization of the active site of yeast RNA polymerase II by DFT and ReaxFF calculations. *Theor Chem Acc* **120**, 479-489 (2008).
47. Raymand D, van Duin ACT, *et al.* Water adsorption on stepped ZnO surfaces from MD simulation. *Surf Sci* **604**, 741-752 (2010).
48. Raymand D, van Duin ACT, *et al.* Hydroxylation Structure and Proton Transfer Reactivity at the Zinc Oxide-Water Interface. *J Phys Chem C* **115**, 8573-8579 (2011).
49. Aryanpour M, van Duin ACT, *et al.* Development of a Reactive Force Field for Iron-Oxyhydroxide Systems. *J Phys Chem A* **114**, 6298-6307 (2010).
50. van Duin ACT, Bryantsev VS, *et al.* Development and Validation of a ReaxFF Reactive Force Field for Cu Cation/Water Interactions and Copper Metal/Metal Oxide/Metal Hydroxide Condensed Phases. *J Phys Chem A* **114**, 9507-9514 (2010).
51. Russo MF, Jr., Li R, *et al.* Molecular dynamic simulation of aluminum-water reactions using the ReaxFF reactive force field. *Int J Hydrogen Energy* **36**, 5828-5835 (2011).
52. Fogarty JC, Aktulga HM, *et al.* A reactive molecular dynamics simulation of the silica-water interface. *J Chem Phys* **132**, 174704 (2010).
53. Pitman MC, van Duin ACT. Dynamics of Confined Reactive Water in Smectite Clay-Zeolite Composites. *J Am Chem Soc* **134**, 3042-3053 (2012).
54. Soper AK. The radial distribution functions of water and ice from 220 to 673 K and at pressures up to 400 MPa. *Chem Phys* **258**, 121-137 (2000).
55. Mills R. Self-diffusion in normal and heavy water in the range 1-45.deg. *J Phys Chem* **77**, 685-688 (1973).
56. Holz M, Heil SR, *et al.* Temperature-dependent self-diffusion coefficients of water and six selected molecular liquids for calibration in accurate 1H NMR PFG measurements. *PCCP* **2**, 4740-4742 (2000).
57. te Velde G, Bickelhaupt FM, *et al.* Chemistry with ADF. *J Comput Chem* **22**, 931-967 (2001).
58. Tilocca A, Selloni A. Structure and reactivity of water layers on defect-free and defective anatase TiO₂(101) surfaces. *J Phys Chem B* **108**, 4743-4751 (2004).
59. Vittadini A, Casarin M, *et al.* Chemistry of and on TiO₂-anatase surfaces by DFT calculations: a partial review. *Theor Chem Acc* **117**, 663-671 (2007).
60. Vittadini A, Selloni A, *et al.* Structure and energetics of water adsorbed at TiO₂ anatase (101) and (001) surfaces. *Phys Rev Lett* **81**, 2954-2957 (1998).
61. Selloni A, Vittadini A, *et al.* The adsorption of small molecules on the TiO₂ anatase(101) surface by first-principles molecular dynamics. *Surf Sci* **402**, 219-222 (1998).
62. He YB, Tilocca A, *et al.* Local ordering and electronic signatures of submonolayer water on anatase TiO₂(101). *Nat Mater* **8**, 585-589 (2009).
63. Diebold U. The surface science of titanium dioxide. *Surf Sci Rep* **48**, 53-229 (2003).
64. Barnard AS, Curtiss LA. Prediction of TiO₂ nanoparticle phase and shape transitions controlled by surface chemistry. *Nano Lett* **5**, 1261-1266 (2005).
65. Herman GS, Dohnalek Z, *et al.* Experimental investigation of the interaction of water and methanol with anatase-TiO₂(101). *J Phys Chem B* **107**, 2788-2795 (2003).
66. Tilocca A, Selloni A. Vertical and lateral order in adsorbed water layers on anatase TiO₂(101). *Langmuir* **20**, 8379-8384 (2004).
67. Gong X-Q, Selloni A. Role of steps in the reactivity of the anatase TiO₂(101) surface. *J Catal* **249**, 134-139 (2007).
68. Gong X-Q, Selloni A, *et al.* Steps on anatase TiO₂(101). *Nat Mater* **5**, 665-670 (2006).
69. Posternak M, Baldereschi A, *et al.* Dissociation of Water on Anatase TiO₂ Nanoparticles: the Role of Undercoordinated Ti Atoms at Edges. *J Phys Chem C* **113**, 15862-15867 (2009).

70. Sanchez VM, Cojulun JA, *et al.* Dissociation Free Energy Profiles for Water and Methanol on TiO₂ Surfaces. *J Phys Chem C* **114**, 11522-11526 (2010).
71. Sanchez VM, de la Llave E, *et al.* Adsorption of R-OH Molecules on TiO₂ Surfaces at the Solid Liquid Interface. *Langmuir* **27**, 2411-2419 (2011).
72. Sanchez VM, Sued M, *et al.* First-principles molecular dynamics simulations at solid-liquid interfaces with a continuum solvent. *J Chem Phys* **131**, 174108 (2009).
73. Tilocca A, Selloni A. DFT-GGA and DFT+U Simulations of Thin Water Layers on Reduced TiO₂ Anatase. *J Phys Chem C* **116**, 9114-9121 (2012).
74. Walle LE, Borg A, *et al.* Mixed Dissociative and Molecular Water Adsorption on Anatase TiO₂(101). *J Phys Chem C* **115**, 9545-9550 (2011).
75. Mattioli G, Filippone F, *et al.* Reaction intermediates in the photoreduction of oxygen molecules at the (101) TiO₂ (anatase) surface. *J Am Chem Soc* **128**, 13772-13780 (2006).
76. Mattioli G, Filippone F, *et al.* Short hydrogen bonds at the water/TiO₂ (anatase) interface. *J Phys Chem C* **112**, 13579-13586 (2008).
77. Gong XQ, Selloni A. Reactivity of anatase TiO₂ nanoparticles: The role of the minority (001) surface. *J Phys Chem B* **109**, 19560-19562 (2005).
78. Herman GS, Sievers MR, *et al.* Structure determination of the two-domain (1 x 4) anatase TiO₂(001) surface. *Phys Rev Lett* **84**, 3354-3357 (2000).
79. Liang Y, Gan SP, *et al.* Surface structure of anatase TiO₂(001): Reconstruction, atomic steps, and domains. *Phys Rev B* **63**, 235402 (2001).
80. Tanner RE, Sasahara A, *et al.* Formic acid adsorption on anatase TiO₂(001)-(1x4) thin films studied by NC-AFM and STM. *J Phys Chem B* **106**, 8211-8222 (2002).
81. Lazzeri M, Selloni A. Stress-driven reconstruction of an oxide surface: The anatase TiO₂(001)-(1x4) surface. *Phys Rev Lett* **87**, 266105 (2001).
82. Gong XQ, Selloni A, *et al.* Density functional theory study of formic acid adsorption on anatase TiO₂(001): Geometries, energetics, and effects of coverage, hydration, and reconstruction. *J Phys Chem B* **110**, 2804-2811 (2006).
83. Blomquist J, Walle LE, *et al.* Water Dissociation on Single Crystalline Anatase TiO₂(001) Studied by Photoelectron Spectroscopy. *J Phys Chem C* **112**, 16616-16621 (2008).
84. Arrouvel C, Digne M, *et al.* Effects of morphology on surface hydroxyl concentration: a DFT comparison of anatase-TiO₂ and gamma-alumina catalytic supports. *J Catal* **222**, 152-166 (2004).
85. Ignatchenko A, Nealon DG, *et al.* Interaction of water with titania and zirconia surfaces. *J Mol Catal A: Chem* **256**, 57-74 (2006).
86. Homann T, Bredow T, *et al.* Adsorption of small molecules on the anatase(100) surface. *Surf Sci* **555**, 135-144 (2004).
87. Wahab HS, Bredow T, *et al.* Computational investigation of water and oxygen adsorption on the anatase TiO₂ (100) surface. *Journal of Molecular Structure-Theochem* **868**, 101-108 (2008).
88. Penn RL, Banfield JF. Formation of rutile nuclei at anatase {112} twin interfaces and the phase transformation mechanism in nanocrystalline titania. *Am Mineral* **84**, 871-876 (1999).
89. Zhou Y, Fichthorn KA. Microscopic View of Nucleation in the Anatase-to-Rutile Transformation. *J Phys Chem C* **116**, 8314-8321 (2012).
90. Kurtz RL, Stockbauer R, *et al.* Synchrotron Radiation Studies of H₂O Adsorption on TiO₂(110). *Surf Sci* **218**, 178-200 (1989).
91. Hugenschmidt MB, Gamble L, *et al.* The Interaction of H₂O with a TiO₂(110) Surface. *Surf Sci* **302**, 329-340 (1994).
92. Henderson MA. An HREELS and TPD study of water on TiO₂(110): The extent of molecular versus dissociative adsorption. *Surf Sci* **355**, 151-166 (1996).

93. Henderson MA. Structural sensitivity in the dissociation of water on TiO₂ single-crystal surfaces. *Langmuir* **12**, 5093-5098 (1996).
94. Brinkley D, Dietrich M, *et al.* A modulated molecular beam study of the extent of H₂O dissociation on TiO₂(110). *Surf Sci* **395**, 292-306 (1998).
95. Brookes IM, Murny CA, *et al.* Imaging water dissociation on TiO₂(110). *Phys Rev Lett* **87**, 266103 (2001).
96. Krischok S, Hofft O, *et al.* H₂O interaction with bare and Li-precovered TiO₂: studies with electron spectroscopies (MIES and UPS(HeI and II)). *Surf Sci* **495**, 8-18 (2001).
97. Walle LE, Borg A, *et al.* Experimental evidence for mixed dissociative and molecular adsorption of water on a rutile TiO₂(110) surface without oxygen vacancies. *Phys Rev B* **80**, 5 (2009).
98. Zhang CJ, Lindan PJD. Multilayer water adsorption on rutile TiO₂(110): A first-principles study. *J Chem Phys* **118**, 4620-4630 (2003).
99. Kumar N, Kent PRC, *et al.* Faster proton transfer dynamics of water on SnO₂ compared to TiO₂. *J Chem Phys* **134**, 044706 (2011).
100. Lindan PJD, Zhang CJ. Exothermic water dissociation on the rutile TiO₂(110) surface. *Phys Rev B* **72**, 7 (2005).
101. Zhang C, Lindan PJD. Towards a first-principles picture of the oxide-water interface. *J Chem Phys* **119**, 9183-9190 (2003).
102. Vlcek L, Cummings PT. Adsorption of water on TiO₂ and SnO₂ surfaces: Molecular dynamics study. *Collect Czech Chem Commun* **73**, 575-589 (2008).
103. Lindan PJD, Harrison NM, *et al.* Mixed dissociative and molecular adsorption of water on the rutile (110) surface. *Phys Rev Lett* **80**, 762-765 (1998).
104. Lindan PJD, Harrison NM, *et al.* First-principles molecular dynamics simulation of water dissociation on TiO₂(110). *Chem Phys Lett* **261**, 246-252 (1996).
105. Bates SP, Kresse G, *et al.* The adsorption and dissociation of ROH molecules on TiO₂(110). *Surf Sci* **409**, 336-349 (1998).
106. Bredow T, Jug K. Theoretical Investigation of Water-Adsorption at Rutile and Anatase Surfaces. *Surf Sci* **327**, 398-408 (1995).
107. Fahmi A, Minot C. A Theoretical Investigation of Water-Adsorption on Titanium-Dioxide Surfaces. *Surf Sci* **304**, 343-359 (1994).
108. Harris LA, Quong AA. Molecular chemisorption as the theoretically preferred pathway for water adsorption on ideal rutile TiO₂(110). *Phys Rev Lett* **93**, 086105 (2004).
109. Schaub R, Thosttrup P, *et al.* Oxygen vacancies as active sites for water dissociation on rutile TiO₂(110). *Phys Rev Lett* **87**, 266104 (2001).
110. Harris LA, Quong AA. Comment on "Molecular chemisorption as the theoretically preferred pathway for water adsorption on ideal rutile TiO₂(110)" - Harris and Quong reply. *Phys Rev Lett* **95**, 029602 (2005).
111. Bandura AV, Kubicki JD, *et al.* Comparisons of Multilayer H₂O Adsorption onto the (110) Surfaces of α -TiO₂ and SnO₂ as Calculated with Density Functional Theory. *J Phys Chem B* **112**, 11616-11624 (2008).
112. Bandura AV, Sykes DG, *et al.* Adsorption of water on the TiO₂ (rutile) (110) surface: A comparison of periodic and embedded cluster calculations. *J Phys Chem B* **108**, 7844-7853 (2004).
113. Hammer B, Wendt S, *et al.* Water Adsorption on TiO₂. *Top Catal* **53**, 423-430 (2010).
114. Zhang W, Yang J, *et al.* Quantum molecular dynamics study of water on TiO₂(110) surface. *J Chem Phys* **129**, 064703 (2008).
115. Mamontov E, Vlcek L, *et al.* Dynamics and structure of hydration water on rutile and cassiterite nanopowders studied by quasielastic neutron scattering and molecular dynamics simulations. *J Phys Chem C* **111**, 4328-4341 (2007).

116. Cheng J, Sprik M. Acidity of the Aqueous Rutile TiO₂(110) Surface from Density Functional Theory Based Molecular Dynamics. *J Chem Theory Comput* **6**, 880-889 (2010).
117. Koparde VN, Cummings PT. Molecular dynamics study of water adsorption on TiO₂ nanoparticles. *J Phys Chem C* **111**, 6920-6926 (2007).
118. Predota M, Bandura AV, *et al.* Electric double layer at the rutile (110) surface. 1. Structure of surfaces and interfacial water from molecular dynamics by use of ab initio potentials. *J Phys Chem B* **108**, 12049-12060 (2004).
119. Zhang Z, Fenter P, *et al.* Ion adsorption at the rutile-water interface: Linking molecular and macroscopic properties. *Langmuir* **20**, 4954-4969 (2004).
120. Zhang Z, Fenter P, *et al.* Structure of rutile TiO₂ (110) in water and 1 molal Rb⁺ at pH 12: Inter-relationship among surface charge, interfacial hydration structure, and substrate structural displacements. *Surf Sci* **601**, 1129-1143 (2007).
121. Wesolowski DJ, Sofo JO, *et al.* Comment on "Structure and dynamics of liquid water on rutile TiO₂(110)". *Phys Rev B* **85**, 5 (2012).
122. Perron H, Vandenborre J, *et al.* Combined investigation of water sorption on TiO₂ rutile (110) single crystal face: XPS vs. periodic DFT. *Surf Sci* **601**, 518-527 (2007).
123. Kumar N, Neogi S, *et al.* Hydrogen Bonds and Vibrations of Water on (110) Rutile. *J Phys Chem C* **113**, 13732-13740 (2009).
124. Luzar A, Chandler D. Effect of Environment on Hydrogen Bond Dynamics in Liquid Water. *Phys Rev Lett* **76**, 928-931 (1996).
125. Luzar A, Chandler D. Hydrogen-bond kinetics in liquid water. *Nature* **379**, 55-57 (1996).
126. Kavathekar RS, English NJ, *et al.* Spatial distribution of adsorbed water layers at the TiO₂ rutile and anatase interfaces. *Chem Phys Lett* **554**, 102-106 (2012).
127. Levchenko AA, Kolesnikov AI, *et al.* Dynamics of Water Confined on a TiO₂ (Anatase) Surface. *J Phys Chem A* **111**, 12584-12588 (2007).
128. Spencer EC, Levchenko AA, *et al.* Inelastic Neutron Scattering Study of Confined Surface Water on Rutile Nanoparticles. *J Phys Chem A* **113**, 2796-2800 (2009).
129. Politi Y, Arad T, *et al.* Sea urchin spine calcite forms via a transient amorphous calcium carbonate phase. *Science* **306**, 1161-1164 (2004).
130. Killian CE, Metzler RA, *et al.* Mechanism of Calcite Co-Orientation in the Sea Urchin Tooth. *J Am Chem Soc* **131**, 18404-18409 (2009).
131. Cölfen H, Antonietti M. Mesocrystals: Inorganic Superstructures Made by Highly Parallel Crystallization and Controlled Alignment. *Angew Chem Int Ed* **44**, 5576-5591 (2005).
132. Schliehe C, Juarez BH, *et al.* Ultrathin PbS Sheets by Two-Dimensional Oriented Attachment. *Science* **329**, 550-553 (2010).
133. Pacholski C, Kornowski A, *et al.* Self-Assembly of ZnO: From Nanodots to Nanorods. *Angew Chem Int Ed* **41**, 1188-1191 (2002).
134. Penn RL, Banfield JF. Morphology development and crystal growth in nanocrystalline aggregates under hydrothermal conditions: Insights from titania. *Geochim Cosmochim Acta* **63**, 1549-1557 (1999).
135. Cho K-S, Talapin DV, *et al.* Designing PbSe Nanowires and Nanorings through Oriented Attachment of Nanoparticles. *J Am Chem Soc* **127**, 7140-7147 (2005).
136. Yu JH, Joo J, *et al.* Synthesis of Quantum-Sized Cubic ZnS Nanorods by the Oriented Attachment Mechanism. *J Am Chem Soc* **127**, 5662-5670 (2005).
137. Bailey JK, Brinker CJ, *et al.* Growth Mechanisms of Iron Oxide Particles of Differing Morphologies from the Forced Hydrolysis of Ferric Chloride Solutions. *J Colloid Interface Sci* **157**, 1-13 (1993).
138. Zhang G, Wang W, *et al.* Solvothermal Synthesis of V–VI Binary and Ternary Hexagonal Platelets: The Oriented Attachment Mechanism. *Cryst Growth Des* **9**, 145-150 (2008).

139. Liu Z, Zhou H, *et al.* Synthesis of Silver Nanoplates by Two-Dimensional Oriented Attachment. *Langmuir* **28**, 9244-9249 (2012).
140. Halder A, Ravishankar N. Ultrafine Single-Crystalline Gold Nanowire Arrays by Oriented Attachment. *Adv Mater* **19**, 1854-1858 (2007).
141. Zitoun D, Pinna N, *et al.* Single Crystal Manganese Oxide Multipods by Oriented Attachment. *J Am Chem Soc* **127**, 15034-15035 (2005).
142. Heiligttag FJ, Rossell MD, *et al.* Template-free co-assembly of preformed Au and TiO₂ nanoparticles into multicomponent 3D aerogels. *J Mater Chem* **21**, 16893-16899 (2011).
143. Yang HG, Zeng HC. Self-Construction of Hollow SnO₂ Octahedra Based on Two-Dimensional Aggregation of Nanocrystallites. *Angew Chem Int Ed* **43**, 5930-5933 (2004).
144. Penn RL, Banfield JF. Imperfect oriented attachment: Dislocation generation in defect-free nanocrystals. *Science* **281**, 969-971 (1998).
145. Kim S-Y, Kumar N, *et al.* Development of a ReaxFF Reactive Force Field for Titanium Dioxide/Water Systems. *Langmuir* **29**, 7838-7846 (2013).
146. Raju M, Kim S-Y, *et al.* ReaxFF Reactive Force Field Study of the Dissociation of Water on Titania Surfaces. *J Phys Chem C* **117**, 10558-10572 (2013).
147. Russo Jr MF, van Duin ACT. Atomistic-scale simulations of chemical reactions: Bridging from quantum chemistry to engineering. *Nucl Instrum Methods Phys Res, Sect B* **269**, 1549-1554 (2011).
148. Lazzeri M, Vittadini A, *et al.* Structure and energetics of stoichiometric TiO₂ anatase surfaces. *Phys Rev B* **63**, 155409 (2001).
149. Alimohammadi M, Fichthorn KA. Molecular Dynamics Simulation of the Aggregation of Titanium Dioxide Nanocrystals: Preferential Alignment. *Nano Lett* **9**, 4198-4203 (2009).
150. Yuwono VM, Burrows ND, *et al.* Oriented Aggregation: Formation and Transformation of Mesocrystal Intermediates Revealed. *J Am Chem Soc* **132**, 2163-2165 (2010).
151. Li D, Nielsen MH, *et al.* Direction-Specific Interactions Control Crystal Growth by Oriented Attachment. *Science* **336**, 1014-1018 (2012).
152. Wang H-W, Wesolowski DJ, *et al.* Structure and Stability of SnO₂ Nanocrystals and Surface-Bound Water Species. *J Am Chem Soc* **135**, 6885-6895 (2013).
153. Liao H-G, Cui L, *et al.* Real-Time Imaging of Pt₃Fe Nanorod Growth in Solution. *Science* **336**, 1011-1014 (2012).
154. Lee EJH, Ribeiro C, *et al.* Oriented Attachment: An Effective Mechanism in the Formation of Anisotropic Nanocrystals. *J Phys Chem B* **109**, 20842-20846 (2005).
155. Meyer B, Marx D, *et al.* Partial Dissociation of Water Leads to Stable Superstructures on the Surface of Zinc Oxide. *Angew Chem Int Ed* **43**, 6641-6645 (2004).
156. Machesky ML, Předota M, *et al.* Surface Protonation at the Rutile (110) Interface: Explicit Incorporation of Solvation Structure within the Refined MUSIC Model Framework. *Langmuir* **24**, 12331-12339 (2008).
157. Kosmulski M. pH-dependent surface charging and points of zero charge: III. Update. *J Colloid Interface Sci* **298**, 730-741 (2006).
158. Holmberg JP, Ahlberg E, *et al.* Surface charge and interfacial potential of titanium dioxide nanoparticles: Experimental and theoretical investigations. *J Colloid Interface Sci* **407**, 168-176 (2013).
159. Sprycha R. Surface charge and adsorption of background electrolyte ions at anatase/electrolyte interface. *J Colloid Interface Sci* **102**, 173-185 (1984).
160. Machesky ML, Wesolowski DJ, *et al.* On the Temperature Dependence of Intrinsic Surface Protonation Equilibrium Constants: An Extension of the Revised MUSIC Model. *J Colloid Interface Sci* **239**, 314-327 (2001).

161. Předota M, Machesky ML, *et al.* Electric Double Layer at the Rutile (110) Surface. 4. Effect of Temperature and pH on the Adsorption and Dynamics of Ions. *J Phys Chem C* **117**, 22852-22866 (2013).
162. Patwardhan SV, Emami FS, *et al.* Chemistry of Aqueous Silica Nanoparticle Surfaces and the Mechanism of Selective Peptide Adsorption. *J Am Chem Soc* **134**, 6244-6256 (2012).
163. Polleux J, Pinna N, *et al.* Ligand Functionality as a Versatile Tool to Control the Assembly Behavior of Preformed Titania Nanocrystals. *Chem--Eur J* **11**, 3541-3551 (2005).
164. Zhang Q, Liu S-J, *et al.* Recent advances in oriented attachment growth and synthesis of functional materials: concept, evidence, mechanism, and future. *J Mater Chem* **19**, 191-207 (2009).
165. Dresselhaus MS, Dresselhaus G. Intercalation compounds of graphite. *Advances in Physics* **51**, 1-186 (2002).
166. Paulo VCM, Mota FdB, *et al.* Adsorption of monovalent metal atoms on graphene: a theoretical approach. *Nanotechnology* **21**, 115701 (2010).
167. Yang C-K. A metallic graphene layer adsorbed with lithium. *Appl Phys Lett* **94**, 163115 (2009).
168. Wang X, Zeng Z, *et al.* First-principles study on the enhancement of lithium storage capacity in boron doped graphene. *Appl Phys Lett* **95**, 183103 (2009).
169. Persson K, Hinuma Y, *et al.* Thermodynamic and kinetic properties of the Li-graphite system from first-principles calculations. *Phys Rev B* **82**, 125416 (2010).
170. Persson K, Sethuraman VA, *et al.* Lithium Diffusion in Graphitic Carbon. *J Phys Chem Lett* **1**, 1176-1180 (2010).
171. Guerard D, Herold A. Intercalation of lithium into graphite and other carbons. *Carbon* **13**, 337-345 (1975).
172. Ohzuku T, Iwakoshi Y, *et al.* Formation of Lithium-Graphite Intercalation Compounds in Nonaqueous Electrolytes and Their Application as a Negative Electrode for a Lithium Ion (Shuttlecock) Cell. *J Electrochem Soc* **140**, 2490-2498 (1993).
173. Dahn JR. Phase diagram of Li_xC_6 . *Phys Rev B* **44**, 9170-9177 (1991).
174. Zhao X, Hayner CM, *et al.* In-Plane Vacancy-Enabled High-Power Si-Graphene Composite Electrode for Lithium-Ion Batteries. *Advanced Energy Materials* **1**, 1079-1084 (2011).
175. Liu M, Kutana A, *et al.* First-Principles Studies of Li Nucleation on Graphene. *J Phys Chem Lett* **5**, 1225-1229 (2014).
176. Liu Y, Artyukhov VI, *et al.* Feasibility of Lithium Storage on Graphene and Its Derivatives. *J Phys Chem Lett* **4**, 1737-1742 (2013).
177. Xu C, Xu B, *et al.* Graphene-based electrodes for electrochemical energy storage. *Energy & Environmental Science* **6**, 1388-1414 (2013).
178. Ganesh P, Kim J, *et al.* Binding and Diffusion of Lithium in Graphite: Quantum Monte Carlo Benchmarks and Validation of van der Waals Density Functional Methods. *J Chem Theory Comput* **10**, 5318-5323 (2014).
179. Xiao S, Zhu H, *et al.* Enhancing the efficiency of lithium intercalation in carbon nanotube bundles using surface functional groups. *PCCP* **16**, 16003-16012 (2014).
180. Song B, Yang J, *et al.* Intercalation and diffusion of lithium ions in a carbon nanotube bundle by ab initio molecular dynamics simulations. *Energy & Environmental Science* **4**, 1379-1384 (2011).
181. Meng YS, Arroyo-de Dompablo ME. First principles computational materials design for energy storage materials in lithium ion batteries. *Energy & Environmental Science* **2**, 589-609 (2009).
182. Dahn JR, Zheng T, *et al.* Mechanisms for Lithium Insertion in Carbonaceous Materials. *Science* **270**, 590-593 (1995).
183. Plimpton S. Fast Parallel Algorithms for Short-Range Molecular Dynamics. *J Comput Phys* **117**, 1-19 (1995).

184. Yang H, Huang X, *et al.* Self-weakening in lithiated graphene electrodes. *Chem Phys Lett* **563**, 58-62 (2013).
185. Huang X, Yang H, *et al.* Lithiation induced corrosive fracture in defective carbon nanotubes. *Appl Phys Lett* **103**, 153901 (2013).
186. Grimme S. Semiempirical GGA-type density functional constructed with a long-range dispersion correction. *J Comput Chem* **27**, 1787-1799 (2006).
187. Kresse G, Hafner J. Ab initio molecular dynamics for liquid metals. *Phys Rev B* **47**, 558-561 (1993).
188. Kresse G, Hafner J. Ab initio molecular-dynamics simulation of the liquid-metal–amorphous-semiconductor transition in germanium. *Phys Rev B* **49**, 14251-14269 (1994).
189. Lee E, Persson KA. Li Absorption and Intercalation in Single Layer Graphene and Few Layer Graphene by First Principles. *Nano Lett* **12**, 4624-4628 (2012).
190. Frisch MJ, Trucks GW, *et al.* Gaussian 09. Wallingford, CT, USA: Gaussian, Inc.; 2009.
191. Fan X, Zheng WT, *et al.* Adsorption and Diffusion of Li on Pristine and Defective Graphene. *ACS Appl Mater Interfaces* **4**, 2432-2438 (2012).
192. Takami N, Satoh A, *et al.* Structural and Kinetic Characterization of Lithium Intercalation into Carbon Anodes for Secondary Lithium Batteries. *J Electrochem Soc* **142**, 371-379 (1995).
193. Imai Y, Watanabe A. Energetic evaluation of possible stacking structures of Li-intercalation in graphite using a first-principle pseudopotential calculation. *J Alloys Compd* **439**, 258-267 (2007).
194. Datta D, Li J, *et al.* Enhanced lithiation in defective graphene. *Carbon* **80**, 305-310 (2014).
195. Mukherjee R, Thomas AV, *et al.* Defect-induced plating of lithium metal within porous graphene networks. *Nat Commun* **5**, (2014).
196. Bonomi M, Branduardi D, *et al.* PLUMED: A portable plugin for free-energy calculations with molecular dynamics. *Comput Phys Commun* **180**, 1961-1972 (2009).
197. Nadler MR, Kempier CP. Crystallographic Data 186. Lithium. *Anal Chem* **31**, 2109-2109 (1959).
198. Ganesh P, Kent PRC, *et al.* Solid–Electrolyte Interphase Formation and Electrolyte Reduction at Li-Ion Battery Graphite Anodes: Insights from First-Principles Molecular Dynamics. *J Phys Chem C* **116**, 24476-24481 (2012).
199. Liu Y, Artyukhov VI, *et al.* Feasibility of Lithium Storage on Graphene and Its Derivatives. *The Journal of Physical Chemistry Letters* **4**, 1737-1742 (2013).
200. Ganesh P, Kent PRC, *et al.* Formation, characterization, and dynamics of onion-like carbon structures for electrical energy storage from nanodiamonds using reactive force fields. *J Appl Phys* **110**, - (2011).
201. Pech D, Brunet M, *et al.* Ultrahigh-power micrometre-sized supercapacitors based on onion-like carbon. *Nat Nano* **5**, 651-654 (2010).
202. Joshi RK, Carbone P, *et al.* Precise and Ultrafast Molecular Sieving Through Graphene Oxide Membranes. *Science* **343**, 752-754 (2014).
203. Mi B. Graphene Oxide Membranes for Ionic and Molecular Sieving. *Science* **343**, 740-742 (2014).
204. Gao W, Wu G, *et al.* Ozonated Graphene Oxide Film as a Proton-Exchange Membrane. *Angew Chemie Int Ed* **53**, 1-6 (2014).
205. Nair RR, Wu HA, *et al.* Unimpeded Permeation of Water Through Helium-Leak–Tight Graphene-Based Membranes. *Science* **335**, 442-444 (2012).
206. Guo F, Silverberg G, *et al.* Graphene-based environmental barriers. *ES&T* **46**, 7717-7724 (2012).
207. Hauser AW, Schwerdtfeger P. Nanoporous Graphene Membranes for Efficient ³He/⁴He Separation. *J Phys Chem Lett* **3**, 209-213 (2011).
208. Banerjee S, Shim J, *et al.* Electrochemistry at the Edge of a Single Graphene Layer in a Nanopore. *ACS Nano* **7**, 834-843 (2013).
209. Wang XD, Wng Q, *et al.* Atomistic Origins of High Rate Capability and Capacity of N-Doped Graphene for Lithium Storage. *Nano Lett* **14**, 1164-1171 (2014).

210. Bunch JS, Verbridge SS, *et al.* Impereable Atomic Membranes from Graphene Sheets. *Nano Lett* **8**, 2458-2462 (2008).
211. Miao M, Nardelli MB, *et al.* First principles study of the permeability of graphene to hydrogen atoms. *PCCP* **15**, 16132-16137 (2013).
212. Jiang D, Cooper VR, *et al.* Porous graphene as the ultimate membrane for gas separation. *Nano Lett* **9**, 4019-4024 (2009).
213. Achtyl JL, Vlassiuk IV, *et al.* Free Energy Relationships in the Electrical Double Layer over Single-Layer Graphene. *J Am Chem Soc* **135**, 979-981 (2013).
214. Vlassiuk I, Smirnov S, *et al.* Graphene Nucleation Density on Copper: Fundamental Role of Background Pressure. *The Journal of Physical Chemistry C* **117**, 18919-18926 (2013).
215. Ong S, Zhao X, *et al.* Polarization of water molecules at a charged interface; second harmonic studies of the silica/water interface. *Chem Phys Lett* **191**, 327-335 (1992).
216. Gibbs-Davis JM, Kruk JJ, *et al.* Jammed Acid-Base Chemistry at Interfaces. *J Am Chem Soc* **130**, 15444-15447 (2008).
217. Konek CT, Musorrafiti MJ, *et al.* Interfacial Acidities, Charge Densities, Potentials, and Energies of Carboxylic Acid-Functionalized Silica/Water Interfaces Determined by Second Harmonic Generation. *J Am Chem Soc* **126**, 11754-11755 (2004).
218. Stumm W, Morgan JJ. *Aquatic Chemistry, Chemical Equilibria and Rates in Natural Waters*, 3rd edn. John Wiley & Sons: New York, 1996.
219. Higgins SR, Stack, A.G., Knauss, K.G., Eggleston, C.M., Jordan, G. Probing molecular-scale adsorption and dissolution-growth processes using nonlinear optical and scanning probe methods suitable for hydrothermal applications. *Geochemical Society Special Publication No. 7*, 111 (2002).
220. Azam MS, Weeraman CN, *et al.* Halide-Induced Cooperative Acid–Base Behavior at a Negatively Charged Interface. *J Phys Chem C* **117**, 8840-8850 (2013).
221. Duval Y, Mielczarski JA, *et al.* Evidence of the Existence of Three Types of Species at the Quartz-Aqueous Solution Interface at pH 0-10: XPS Surface Group Quantification and Surface Complexation Modeling. *J Phys Chem B* **106**, 2937-2945 (2002).
222. Hayes PL, Malin JN, *et al.* Interaction of Nitrate, Barium, Strontium and Cadmium Ions with Fused Quartz/Water Interfaces Studied by Second Harmonic Generation. *J Phys Chem A* **112**, 660-668 (2008).
223. Hayes PL, Gibbs-Davis JM, *et al.* Environmental Biogeochemistry Studied by Second-Harmonic Generation: A Look at the Agricultural Antibiotic Oxytetracycline *The Journal of Physical Chemistry C* **111**, 8796-8804 (2007).
224. Musorrafiti MJ, Konek CT, *et al.* Interaction of Chromium(VI) with the α -Aluminum Oxide–Water Interface. *The Journal of Physical Chemistry C* **112**, 2032-2039 (2008).
225. Al-Abadleh HA, Mifflin AL, *et al.* Kinetic Studies of Chromium (VI) Binding to Carboxylic Acid- and Methyl Ester-Functionalized Silica/Water Interfaces Important in Geochemistry. *J Phys Chem B* **109**, 16852-16859 (2005).
226. Achtyl JL, Vlassiuk IV, *et al.* Interaction of Magnesium Ions with Pristine Single-Layer and Defected Graphene/Water Interfaces Studied by Second Harmonic Generation. *J Phys Chem B ACS ASAP* (2014).
227. Kresse G, Joubert D. From ultrasoft pseudopotentials to the projector augmented-wave method. *Phys Rev B* **59**, 1758 (1999).
228. Stack AG, Higgins SR, *et al.* Point of zero charge of a corundum-water interface probed with optical second harmonic generation (SHG) and atomic force microscopy (AFM): New approaches to oxide surface charge. *Geochim Cosmochim Acta* **65**, 3055-3063 (2001).

229. Petersen MK, Voth GA. Characterization of the Solvation and Transport of the Hydrated Proton in the Perfluorosulfonic Acid Membrane Nafion. *J Phys Chem B* 18594-18600 (2006).
230. Junge W, McLaughlin S. The role of fixed and mobile buffers in the kinetics of proton movement. *Biochim Biophys Acta* **890**, 1-5 (1987).
231. Eikerling M, Kornyshev AA, *et al.* Mechanisms of Proton Conductance in Polymer Electrolyte Membranes. *J Phys Chem B* **105**, 3646-3662 (2001).
232. Choi P, Jalani NH, *et al.* Thermodynamics and Proton Transport in Nafion II. Proton Diffusion Mechanisms and Conductivity. *J Electrochem Soc* **152**, E123-E130 (2005).
233. Hashimoto A, Suenaga K, *et al.* Direct evidence for atomic defects in graphene layers. *Nature* **430**, 870-873 (2004).
234. Meyer JC, Kisielowski C, *et al.* Direct Imaging of Lattice Atoms and Topological Defects in Graphene Membranes. *Nano Lett* **8**, 3582-3586 (2008).
235. Meyer JC, Eder F, *et al.* Accurate Measurement of Electron Beam Induced Displacement Cross Sections *Phys Rev Lett* **108**, 196102 (2012).
236. Kresse G, Furthmuller J. Efficient iterative schemes for abinitio total-energy calculations using a plane-wave basis set. *Phys Rev B* **54**, 11169-11186 (1996).
237. van Duin AC, Dasgupta S, *et al.* ReaxFF: A Reactive Force Field for Hydrocarbons. *J Phys Chem A* **105**, 9396-9409 (2001).
238. Baustian KJ, Cziczo DJ, *et al.* Importance of aerosol composition, mixing state, and morphology for heterogeneous ice nucleation: A combined field and laboratory approach. *Journal of Geophysical Research-Atmospheres* **117**, (2012).
239. de Grotthuss CJT. Sur la décomposition de l'eau et des corps qu'elle tient en dissolution à l'aide de l'électricité galvanique. *Ann Chim* **58**, 54-73 (1806).
240. Light TS, Licht S, *et al.* The Fundamental Conductivity and Resistivity of Water. *Electrochem Solid-State Lett* **8**, E16-E19 (2005).
241. Voth GA. Computer Simulation of Proton Solvation and Transport in Aqueous and Biomolecular Systems. *Account of Chemical Research* **39**, 143 (2006).
242. Fogarty JC, Aktulga HM, *et al.* A reactive molecular dynamics simulation of the silica-water interface. *Journal of Chemical Physics* **132**, 174704/174701-174704/174710 (2010).
243. van Duin ACT, Zou C, *et al.* A ReaxFF reactive force field for proton transfer reactions in bulk water and its applications to heterogeneous catalysis, vol. Computational Catalysis. Royal Society of Chemistry: Cambridge, 2013.
244. Duval Y, Mielczarski JA, *et al.* Evidence of the Existence of Three Types of Species at the Quartz–Aqueous Solution Interface at pH 0–10: XPS Surface Group Quantification and Surface Complexation Modeling. *The Journal of Physical Chemistry B* **106**, 2937-2945 (2002).
245. Lee SH, Rasaiah CJ. Proton transfer and the mobilities of the H⁺ and OH[–] ions from studies of a dissociating model for water. *Journal of Chemistry and Physics* **135**, 124505.
246. Cicero G, Grossman JC, *et al.* Water Confined in Nanotubes and between Graphene Sheets: A First Principle Study. *J Am Chem Soc* **130**, 1871-1878 (2008).
247. Zhou H, Ganesh P, *et al.* Understanding controls on interfacial wetting at epitaxial graphene: Experiment and theory. *Phys Rev B* **85**, 035406 (2012).
248. Ramon GZ, Feinberg BJ, *et al.* Membrane-based production of salinity-gradient power. *Energy & Environmental Science* **4**, 4423-4434 (2011).
249. Weinstein JN, Leitz FB. Electric power from differences in salinity: the dialytic battery. *Science* **191**, 557 (1976).
250. Puttamraju P, SenGupta AK. Evidence of Tunable On–Off Sorption Behaviors of Metal Oxide Nanoparticles: Role of Ion Exchanger Support. *Ind Eng Chem Res* **45**, 7737-7742 (2006).

251. Sylvester PW, P.; Möller, T.; Badruzzaman, M.; Boyd, O.; . A Hybrid Sorbent Utilizing Nanoparticles of Hydrous Iron Oxide for Arsenic Removal from Drinking Water. *Environ Eng Sci* **24**, 104-112 (2007).
252. Loeb S. Production of energy from concentrated brines by pressure-retarded osmosis : I. Preliminary technical and economic correlations. *J Membr Sci* **1**, 49-63 (1976).
253. Loeb S, Van Hessen F, *et al.* Production of energy from concentrated brines by pressure-retarded osmosis : II. Experimental results and projected energy costs. *J Membr Sci* **1**, 249-269 (1976).
254. Veerman J, Saakes M, *et al.* Reverse electrodialysis: A validated process model for design and optimization. *Chem Eng J* **166**, 256-268 (2011).
255. Veerman J, Saakes M, *et al.* Reverse electrodialysis: evaluation of suitable electrode systems. *J Appl Electrochem* **40**, 1461-1474 (2010).
256. Veerman J, de Jong RM, *et al.* Reverse electrodialysis: Comparison of six commercial membrane pairs on the thermodynamic efficiency and power density. *J Membr Sci* **343**, 7-15 (2009).
257. Veerman J, Saakes M, *et al.* Reverse electrodialysis: Performance of a stack with 50 cells on the mixing of sea and river water. *J Membr Sci* **327**, 136-144 (2009).
258. Post JW, Veerman J, *et al.* Salinity-gradient power: Evaluation of pressure-retarded osmosis and reverse electrodialysis. *J Membr Sci* **288**, 218-230 (2007).
259. Hatzell MC, Logan BE. Evaluation of Flow Fields on Bubble Removal and System Performance in an Ammonium Bicarbonate Reverse Electrodialysis Stack. *J Membr Sci* **446**, 449-455 (2013).
260. Hatzell MC, Cusick RD, *et al.* Comparison of hydrogen production and electrical power generation for energy capture in closed-loop ammonium bicarbonate reverse electrodialysis systems. *PCCP* **16**, 1632-1638 (2014).
261. Brogioli D, Ziano R, *et al.* Capacitive mixing for the extraction of energy from salinity differences: Survey of experimental results and electrochemical models. *J Colloid Interface Sci* **407**, 457-466 (2013).
262. Brogioli D, Ziano R, *et al.* Exploiting the spontaneous potential of the electrodes used in the capacitive mixing technique for the extraction of energy from salinity difference. *Energy & Environmental Science* **5**, 9870-9880 (2012).
263. Brogioli D, Zhao R, *et al.* A prototype cell for extracting energy from a water salinity difference by means of double layer expansion in nanoporous carbon electrodes. *Energy & Environmental Science* **4**, 772-777 (2011).
264. Brogioli D. Extracting Renewable Energy from a Salinity Difference Using a Capacitor. *Phys Rev Lett* **103**, 058501 (2009).
265. Rica RIA, Brogioli D, *et al.* Ions transport and adsorption mechanisms in porous electrodes during capacitive-mixing double layer expansion (CDLE). *The Journal of Physical Chemistry C* **116**, 16934-16938 (2012).
266. Rica R, Ziano R, *et al.* Thermodynamic relation between voltage-concentration dependence and salt adsorption in electrochemical cells. *Phys Rev Lett* **109**, 156103 (2012).
267. Rica RA, Ziano R, *et al.* Electro-diffusion of ions in porous electrodes for capacitive extraction of renewable energy from salinity differences. *Electrochim Acta* **92**, 304-314 (2013).
268. Iglesias GR, Fernández MM, *et al.* Materials selection for optimum energy production by double layer expansion methods. *J Power Sources* **261**, 371-377 (2014).
269. Porada S, Zhao R, *et al.* Review on the Science and Technology of Water Desalination by Capacitive Deionization. *Prog Mater Sci* **58**, 1388-1442 (2013).
270. Biesheuvel P. Thermodynamic cycle analysis for capacitive deionization. *J Colloid Interface Sci* **332**, 258-264 (2009).

271. Anderson MA, Cudero AL, *et al.* Capacitive deionization as an electrochemical means of saving energy and delivering clean water. Comparison to present desalination practices: Will it compete? *Electrochim Acta* **55**, 3845-3856 (2010).
272. Hatzell KB, Iwama E, *et al.* Capacitive deionization concept based on suspension electrodes without ion exchange membranes. *Electrochem Commun* **43**, 18-21 (2014).
273. Suss ME, Baumann TF, *et al.* Capacitive desalination with flow-through electrodes. *Energy & Environmental Science* **5**, 9511-9519 (2012).
274. Sales BB, Saakes M, *et al.* Direct Power Production from a Water Salinity Difference in a Membrane-Modified Supercapacitor Flow Cell. *Environ Sci Technol* **44**, 5661-5665 (2010).
275. Hatzell MC, Cusick RD, *et al.* Capacitive Mixing Power Production from Salinity Gradient Energy Enhanced through Exoelectrogen-Generated Ionic Currents. *Energy & Environmental Science* (2014).
276. Watson VJ, Nieto Delgado C, *et al.* Influence of chemical and physical properties of activated carbon powders on oxygen reduction and microbial fuel cell performance. *Environ Sci Technol* (2013).
277. Bagri A, Mattevi C, *et al.* Structural evolution during the reduction of chemically derived graphene oxide. *Nat Chem* **2**, 581-587 (2010).
278. Rahaman O, van Duin ACT, *et al.* Development of a ReaxFF Reactive Force Field for Glycine and Application to Solvent Effect and Tautomerization. *The Journal of Physical Chemistry B* **115**, 249-261 (2010).
279. Rahaman O, van Duin ACT, *et al.* Development of a ReaxFF Reactive Force Field for Aqueous Chloride and Copper Chloride. *The Journal of Physical Chemistry A* **114**, 3556-3568 (2010).
280. Bonomi M, Branduardi D, *et al.* PLUMED: A portable plugin for free-energy calculations with molecular dynamics. *Comput Phys Commun* **180**, 1961-1972 (2009).
281. Goldberg S. Surface Complexation Modeling. In: Elsevier (ed). USDA-ASR: Riverside, CA, 2013.
282. Noh JS, Schwarz JA. Effect of HNO₃ treatment on the surface acidity of activated carbons. *Carbon* **28**, 675-682 (1990).
283. Hulicova-Jurcakova D, Seredych M, *et al.* Combined Effect of Nitrogen-and Oxygen-Containing Functional Groups of Microporous Activated Carbon on its Electrochemical Performance in Supercapacitors. *Adv Funct Mater* **19**, 438-447 (2009).
284. Sun CH, Liu LM, *et al.* Titania-water interactions: a review of theoretical studies. *J Mater Chem* **20**, 10319-10334 (2010).
285. Patrick CE, Giustino F. Structure of a Water Monolayer on the Anatase TiO₂(101) Surface. *Physical Review Applied* **2**, 014001 (2014).
286. Kowalski PM, Meyer B, *et al.* Composition, structure, and stability of the rutile TiO₂(110) surface: Oxygen depletion, hydroxylation, hydrogen migration, and water adsorption. *Phys Rev B* **79**, 115410 (2009).
287. Diebold U. Structure and properties of TiO₂ surfaces: a brief review. *Applied Physics a-Materials Science & Processing* **76**, 681-687 (2003).
288. Allegretti F, O'Brien S, *et al.* Adsorption bond length for H₂O on TiO₂(110): A key parameter for theoretical understanding. *Phys Rev Lett* **95**, 4 (2005).
289. Fitts JP, Machesky ML, *et al.* Second-harmonic generation and theoretical studies of protonation at the water/ α -TiO₂ (110) interface. *Chem Phys Lett* **411**, 399-403 (2005).
290. Kuno M. An overview of solution-based semiconductor nanowires: synthesis and optical studies. *PCCP* **10**, 620-639 (2008).
291. Suyatin DB, Sun J, *et al.* Electrical Properties of Self-Assembled Branched InAs Nanowire Junctions. *Nano Lett* **8**, 1100-1104 (2008).

292. Bierman MJ, Jin S. Potential applications of hierarchical branching nanowires in solar energy conversion. *Energy & Environmental Science* **2**, 1050-1059 (2009).
293. Filipe V, Hawe A, *et al.* Critical Evaluation of Nanoparticle Tracking Analysis (NTA) by NanoSight for the Measurement of Nanoparticles and Protein Aggregates. *Pharm Res* **27**, 796-810 (2010).
294. James AE, Driskell JD. Monitoring gold nanoparticle conjugation and analysis of biomolecular binding with nanoparticle tracking analysis (NTA) and dynamic light scattering (DLS). *Analyst* **138**, 1212-1218 (2013).
295. Banfield JF, Welch SA, *et al.* Aggregation-Based Crystal Growth and Microstructure Development in Natural Iron Oxyhydroxide Biomineralization Products. *Science* **289**, 751-754 (2000).
296. Huang F, Zhang H, *et al.* The Role of Oriented Attachment Crystal Growth in Hydrothermal Coarsening of Nanocrystalline ZnS. *The Journal of Physical Chemistry B* **107**, 10470-10475 (2003).
297. Penn RL, Banfield JF. Oriented attachment and growth, twinning, polytypism, and formation of metastable phases; insights from nanocrystalline TiO₂. *Am Mineral* **83**, 1077-1082 (1998).
298. Echigo T, Monsegue N, *et al.* Nanopores in hematite (α -Fe₂O₃) nanocrystals observed by electron tomography. *Am Mineral* **98**, 154-162 (2013).
299. Sivula K, Le Formal F, *et al.* Solar Water Splitting: Progress Using Hematite (α -Fe₂O₃) Photoelectrodes. *ChemSusChem* **4**, 432-449 (2011).
300. Islam MM, Bryantsev VS, *et al.* ReaxFF Reactive Force Field Simulations on the Influence of Teflon on Electrolyte Decomposition during Li/SWCNT Anode Discharge in Lithium-Sulfur Batteries. *J Electrochem Soc* **161**, E3009-E3014 (2014).
301. Lu Y, Tu Z, *et al.* Stable lithium electrodeposition in liquid and nanoporous solid electrolytes. *Nat Mater* **13**, 961-969 (2014).
302. Hu S, Lozada-Hidalgo M, *et al.* Proton transport through one-atom-thick crystals. *Nature* **516**, 227-230 (2014).
303. Hatzell MC, Raju M, *et al.* Effect of Strong Acid Functional Groups on Electrode Rise Potential in Capacitive Mixing by Double Layer Expansion. *Environ Sci Technol* **48**, 14041-14048 (2014).

VITA

Muralikrishna Raju

Education

- **The Pennsylvania State University** University Park, Pennsylvania
Ph.D. Physics 2007 – Present
- **Indian Institute of Technology – Roorkee** Roorkee, India
M.S. Physics 2005 – 2007
- **Sri Sathya Sai Institute of Higher Learning** Bangalore, India
B.S. Physics (Hons.) 2002-2005

Publications (<http://scholar.google.com/citations?user=HO3EQTkAAAAJ&hl=en>)

- Raju M, van Duin ACT, Fichthorn KA. **Nano Letters** *14*, 1836-1842 (2014).
- Raju M, Kim S-Y, van Duin ACT, Fichthorn KA. **The Journal of Physical Chemistry C** *117*, 10558-10572 (2013).
- Marta C. Hatzell, Muralikrishna Raju, Valerie J. Watson, Andrew G. Stack, Adri C. T. van Duin, Bruce E. Logan. The role of strong acid functional groups on capacitive mixing by double layer modulation. **Environ. Sci. Tech.** (accepted Nov 2014).
- Feifei F, Shan H, Hui Y, Muralikrishna R, Dibakar D, Vivek BS, Adri CTvD, Sulin Z, Ting Z. **Modelling and Simulation in Materials Science and Engineering** *21*, 074002 (2013).
- Huang X, Yang H, Liang W, Raju M, Terrones M, Crespi VH, van Duin ACT, Zhang S. **Applied Physics Letters** *103*, 153901-153904 (2013).
- Yang H, Huang X, Liang W, van Duin ACT, Raju M, Zhang S. **Chemical Physics Letters** *563*, 58-62 (2013).
- Jennifer L. Achtyl, Raymond R. Unocic, Yu Cai, Raju M, Pasquale F. Fulvio, Hua Zhou, Paul A. Fenter, David J. Wesolowski, Sheng Dai, Adri Van Duin, Matthew Neurock, Franz M. Geiger. Water-Mediated Proton Transfer across Single Layer Graphene. **Nat. Commun.** (under consideration).
- Muralikrishna Raju, P. Ganesh, P. R. C. Kent, Adri C. T. van Duin. A Reactive Force Field for Li/C Systems. **Enegy. Environ. Sci.** (under consideration).
- Y. W. Yin, M. Raju, W. J. Hu, John David Burton, Y-M. Kim, A. Y. Borisevich, Steve J. Pennycook, S. M. Yang, T.W. Noh, Alexei Grouverman, X.G. Li, Zhidong Zhang, Evgeny Y. Tsymbal. Multiferroic Tunnel Junctions and Ferroelectric Control of Magnetic State at Interface. **Journal of Applied Physics** (accepted, Oct 2014).
- Yin YW, Raju M, Hu WJ, Weng XJ, Li XG, Li Q. **Journal of Applied Physics** *109*, 07D915 (2011).
- Yin Y-W, Raju M, Hu W-J, Weng X-J, Zou K, Zhu J, Li X-G, Zhang Z-D, Li Q. **Frontiers of Physics** *7*, 380-385 (2012).